Turbulence in the sea ice impacted Southern Ocean and its implications for primary production and carbon export

Isabelle Sindizwa Nunes da Costa (née Giddy)

Supervised by Professor Sebastiaan Swart, Dr Sarah-Anne Nicholson and Professor Isabelle Ansorge

UNIVERSITY OF CAPE TOWN
IYUNIVESITHI YASEKAPA • UNIVERSITEIT VAN KAAPSTAD

UNIVERSITY OF GOTHENBURG

Dissertation for the degree of Philosophiae Doctor (PhD)

Department of Marine Sciences, University of Gothenburg
&
Department of Oceanography, University of Cape Town

2022

Turbulence in the sea ice impacted Southern Ocean and its implications for primary production and carbon export

ISBN 978-91-8009-769-7 (printed)
ISBN 978-91-8009-770-3 (pdf)

This book was typeset by the author using LaTeX.

Front cover: © Federico & Patti Soriano

Back cover photo: The author. Photo credit: Ornella Atwell

Quote on opposite page: J.M. Coetzee, Age of Iron, 1990

Printed by: Stema Specialtryck AB, Borås, 2022

Keywords: Southern Ocean, sea ice, submesoscale, diapycnal mixing, heat fluxes, primary production, carbon export, gliders.

to the latitudes where albatrosses fly

Declaration

I know the meaning of plagiarism and declare that all of the work in the dissertation (or thesis), save for that which is properly acknowledged, is my own.

I confirm that I have been granted permission by the University of Cape Town's Doctoral Degrees Board to include the following publication(s) in my PhD thesis, and where co-authorships are involved, my co-authors have agreed that I may include the publication(s):

Swart, S., M. du Plessis, A.F. Thompson, L. Biddle, **I. Giddy**, T. Linders, M. Mohrmann, S-A. Nicholson, 2020. Submesoscale Fronts in the Antarctic Marginal Ice Zone and Their Response to Wind Forcing. *Geophysical Research Letters*, 47 (6), e2019GL086649. https://doi.org/10.1029/2019GL086649

Giddy, I., S. Swart, M. du Plessis, A.F. Thompson, S-A Nicholson. (2021). Stirring of Sea-Ice Meltwater Enhances Submesoscale Fronts in the Southern Ocean. *Journal of Geophysical Research: Ocean*, 126(4), e2020JC016814

Giddy, I., I. Fer, S. Swart, S-A Nicholson. (*manuscript, 2022).* Vertical convergence of turbulent and double diffusive heat flux drives warming and erosion of Antarctic Winter Water in summer. (in prep for submission to Journal of Physical Oceanography)

Giddy, I., S-A Nicholson, B. Y. Queste, S. Thomalla, S. Swart. (*in review*, 2022). Sea-ice impacts inter-annual variability in phytoplankton phenology and carbon export in the Weddell Sea. *Geophysical Research Letters*

Signature: Date: 20/01/2023

Student Name: Isabelle Sindizwa Giddy Nunes da Costa Student Number: GDDISA001

Contents

Preface

> Here I am sitting on the golden-silver sand of the beach, casuarinas trees murmuring behind me, the reef rumbling to comfort me in the distance, a lagoon turning from turquoise to orange as I look out at what promises to be a magnificent sunset, asking myself how far I am seeing when I look out to sea. [...] if I look down to my left, would I, if I went straight, get to the South Pole?
>
> *Collen, 2005, p. 71*

Many mornings during the writing of this PhD, I went down to the beach and gazed south towards the horizon over the rippling swell. Beyond sight, expands the Southern Ocean. The story of western discovery of the Southern Ocean begins on the 13^{th} July 1772, when Captain James Cook's ships, Adventure and Resolution, sailed from Portsmouth, England, on his second voyage to search for the fabled southern continent, Tierra Australis Incognito. Upon his return, he logged an abundance of fur seals and whales, opening the doors for their exploitation further south (*Hofman*, 2017). Indeed, the Weddell Sea, takes its name from the sealer, James Weddell, who reached the southernmost latitude at the time in the 1820's (pictured in the image below).

In the early 1900's, Antarctica and the Southern Ocean caught the imagination of explorers, leading to a resurgence of expeditions. In the midst of sea ice in the eastern Weddell Sea is where the recently discovered "Endurance" of Shackleton was engulfed, now sitting on the seafloor, sailing through time. A memory of a tale of courage, strength and hope.

Figure 1: To James Weddell, Esqr R.N... the brig Jane and cutter Beaufoy on 20^{th} February 1823, bearing up in $74°15'$ (Being the highest Southern Latitude ever reached). Hand-coloured. National Maritime Museum, Greenwich, London.

The Southern Ocean is the only ocean around which waters circulate unbounded by landmasses. It is this feature that creates the conditions in which the Southern Ocean plays a central role in regulating the global climate system. Some 30 million years ago the circum-Antartic oceanic belt was formed as the Drake Passage widened, thermally isolating Antarctica and chilling the global climate (*Scher and Martin*, 2006). Without this deep interoceanic link, global climate would be sharply different from what we have today. The Southern Ocean not only promotes

exchange between ocean basins, but it is also the site of major deep-ocean overturning, driven by the sinking of dense upper waters that are formed along the continental margins. Upon reaching great depths and moving northward, this dense water of Antarctic origin cools and ventilates the abyssal layer of the world ocean, affecting oceanic CO_2 storage. It hosts some of the strongest winds, and is known for the roaring forties and furious fifties, making it daunting even for modern maritime traffic and science research vessels. Scientific discovery is especially challenging within the harsh wind, wave and sea ice conditions that dominate the Southern Ocean. Impressive pioneering ship-based oceanographic surveys of the Weddell Sea were carried out since the 1950s; the first through a collaboration between the US and Russia (*Gordon*, 2012), and since the early 2000s, the Good Hope line, running mostly along the Greenwich Meridian and through the Weddell Sea to the Antarctic Continent, has been maintained by multiple national efforts, including South Africa, France and the USA (*Ansorge et al.*, 2005). It was on one of these cruises in 2010 that I first experienced the thrill of scientific discovery aboard the South African vessel, the *RV SA Agulhas* to the almost other-worldly Southern Ocean and Antarctica. It is so remote, that one might wonder why study this ocean so far from human habitation. This was a question I contemplated at the time, given the continuing and pressing structural and socioeconomic injustices in my home country, South Africa, and the need for action in the light of the current climate crisis. Yet, it is here that key climate regulatory processes occur (*Moore et al.*, 2018) where 65% of the world's ocean last makes contact with the atmosphere (*De Vries and Primeau*, 2011). It is here that the world's oceans are replenished of nutrients, maintaining ecosystems and a global fishery (*Sarmiento et al.*, 2004). And so I began to see the link between Africa and Antarctica, and learn of its untold perspectives (*Lavery*, 2019).

In the recent Inter-governmental Panel on Climate Change Special Report on the Ocean and Cryosphere in a Changing Climate (*Meredith et al.*, 2019), the main findings are summarised :

"The polar regions are losing ice, and their oceans are changing rapidly. The consequences of this polar transition extend to the whole planet, and are affecting people in multiple ways"

Building understanding of the processes that occur in these sensitive regions can improve predictions and inform decision-makers. Bringing focus to this unseen world can further motivate rapid action to avert the climate crisis. The innovation of autonomous underwater vehicles (e.g. gliders) has opened the door to low-carbon, sustained, high spatio-temporal resolution observations of the ocean (*Rudnick*, 2016). Pertinently for the remote regions such as the seasonally ice covered Southern Ocean, gliders enable the novel observation of oceanographic processes that are undersampled in time and space. It is with these platforms that I seek to investigate the role of sea ice on regulating upper ocean properties and biological primary production, with the intention to improve the current interpretation of ocean variability and predictions of future ocean and climate conditions. It is my hope that in this way, the body of work presented in this thesis makes a contribution not only to the advancement of science but also to the greater good.

Scientific environment

The research for this dissertation was completed through a double degree agreement between the University of Gothenburg (GU) with the Polar Gliders research group and the University of Cape Town, through which I was affiliated with the Southern Ocean Carbon and Climate Observatory, CSIR. Being part of both of these research groups hosted many an interesting discussion and created an incredibly supportive environment in which to carry out my research. During my PhD I also undertook a research exchange to the University of East Anglia through the Tyndyll Center for Climate Research. A combination of courses and summer schools enriched my experience and provided inspiration and knowledge that drove much of the analysis presented in this thesis. I began my PhD by participating in the GU course "Observing the Ocean from Macro to Micro scale". In many ways, the ideas in this course motivated my approach to this thesis in considering the importance of interactions across scales in the ocean. The foundations for my understanding of turbulence in the ocean were set in the WHOI GFD summer series lectures on turbulence in a stratified ocean, which I attended as a guest student, together with the Masters course, Introduction to Turbulence in the Ocean and Atmosphere, offered at the University of Bergen. The Fluid Dynamics for Sustainability and the Environment summer school hosted by Ecole Polytechnique forged long lasting friendships and broadened my knowledge. The OceanHackWeek virtual summer school, introduced me to collaborative coding and open-source code for science. Finally, a Time Series Analysis course with Jonathan Lilly, beyond building my intuition for spectral analysis which I had been struggling with for a number of years before, gave me new perspectives to data analysis and the undertaking of scientific enquiry at large. The participation in the SCALE cruise during my PhD was a fantastic training opportunity where I deployed autonomous platforms and countless CTDs. This experience also helped to build my intuition for the region that this dissertation is based upon. SEAmester, the South African at sea learning and teaching cruise, was a wonderful way to meet and forge deep relationships with other South African students and scientists. In addition, I had the opportunity to participate in meetings that also developed my whole person. These included Polar Gliders annual research retreats at Börno, a Time to Think workshop and the Life Skills for Young Scientists (LiSYS) meetings with Johnathan Lilly.

Figure 2: A snow petrel fishing in between open-ocean and sea ice during the SCALE cruise, 2019. Photo Credit: Derek Engelbrecht

Acknowledgements

The making of this thesis has been a community effort. I have thoroughly enjoyed the last four years and I thank everyone that was part of the journey.

Seb and Sarah, your enthusiasm for this work is contagious. Thank you for trusting me to take your ideas forward and dive into my own. It has been really wonderful to work you both, thank you for all the great discussions. Seb, I especially thank you for your blue skies thinking and for giving me the space to grow as an independent researcher. Sarah, thank you for inspiring and encouraging me to explore the fascinating world of turbulent flows. Isabelle, thank you for your mentorship and your support to seek out opportunities. I would also like to thank my collaborators during different parts of my PhD: Andy Thompson, Marcel du Plessis, Sandy Thomalla, Bastien Queste and Ilker Fer; I have learnt so much from each of you. Anna Wåhlin, our brief discussions over the years and your guidance went a long way and I am grateful for your input. Importantly, none of the glider deployments would have been possible without the captain and crew of the *RV SA Agulhas II* for which I am incredibly grateful.

I have been lucky to be part of two research groups throughout my PhD. The Polar Gliders research group, it has been so nice to grow along with you, to share our positive thoughts during Monday morning meetings, and to know that you have my back. To everyone at the Southern Ocean Carbon-Climate Observatory, your inputs have always been valuable. Thank you for creating a space that is so warm and welcoming.

To my family, you have cheered me on at every step of the way, in so many ways. To the cabbage patch crew, you were there from the very beginnings of my venture into Oceanography and make my life joyful. Paulo, you are my anchor and my sail. Thank you for being my biggest support during the tough moments and equally, sharing in the excitement of my discoveries. And, of course, I couldn't have done it without my loyal desk mates during the hours spent at home while writing this thesis, Wizard and Misty.

Isabelle Giddy
Cape Town, May 2022

Funding Statement

This thesis was made possible through the generous support of a number of funding agencies. My time at the University of Cape Town was funded by the Oppenheimer Memorial Trust, NRF-SANAP (SNA170506229906), iAtlantic Horizon 2020 grant (818123), UCT Postgraduate Funding Office, UCT Doctoral Research Scholarship and VC Research Scholarship. My travel and research at the University of Gothenburg was funded through the STINT-NRF Mobility Grant (STNT180910357293). A 2-month research visit to the University of East Anglia was funded by the UCT-UEA Newton Climate Fellowship. The field campaigns and research projects within which this thesis was carried out was funded by the grants of S. Swart: Wallenberg Academy Fellowship (WAF 2015.0186), Swedish Research Council (VR 2019-04400); and the grants of S-A. Nicholson and S. Swart: NRF-SANAP (SNA170522231782, SANAP200324510487).

Abstract

The sea-ice impacted Southern Ocean, south of the Antarctic Circumpolar Current, is one of the most important regions on earth for the cycling of carbon and distribution of heat and freshwater around the globe. Here, along-isopycnal upwelling of warm, carbon-rich circumpolar deep water coincides with the annual growth and melt of Antarctic sea ice that represents one of the worlds largest surface water transformations. The air-sea-ice buoyancy exchanges and biological processes that change the surface water properties therefore have global consequences, as they set the properties of downwelling intermediate waters that enter the upper branch of the global thermohaline circulation. The region hosts some of the largest uncertainties in global climate models. The reason for this stems from two sources. Firstly, the spatio-temporal resolution of global climate models is limited by computational constraints such that smaller scale processes need to be parameterized. Secondly, the challenges associated with making observations in or near sea ice and in the harsh and remote conditions of the Southern Ocean means that the region is sparsely sampled, and as such, the parameterizations of the small scale and turbulent terms in global climate models are validated based only on a few *in situ* samples. This thesis concerns the observation and interpretation of (sub)meso- to micro scale turbulence and its implications in the sea ice impacted Southern Ocean. I aimed to understand the 0.01-1 km scale physical and biological processes that drive changes in the properties of the upper ocean following sea ice melt, using groundbreaking sustained high temporal and spatial resolution observations made by gliders. There are three main findings. Firstly, we find that sea ice melt by introducing a lateral freshwater gradient enhances stirring of submesoscale flows (0.1-10 km) and therefore lateral variability in the upper ocean, but simultaneously constrains vertical fluxes between the ocean interior and surface by enhancing stratification. Secondly, turbulent diapycnal mixing and double diffusive convection (0.1-1 m scales) drive the warming of the subsurface winter water, therefore mediating fluxes between the ocean interior and surface. Finally, phytoplankton respond favourably to larger volume sea ice that enhances winter mixing of nutrients from the deep reservoir and to upper ocean stratification in the summer. The preliminary evidence from this study suggests that the resultant higher intensity phytoplankton bloom translates to enhanced short term carbon export but not necessarily long term export. Overall, we show, using observations, that the variability and transport of heat and freshwater flux in the sea ice impacted Southern Ocean are sensitive to sea ice, with downstream impacts on phytoplankton, the biological carbon pump and ultimately the upper cell of the meridional overturning circulation.

Sammanfattning

Den säsongsbetonade havsisen i Södra oceanen är globalt viktig för distributionen av värme, färskvatten, koldioxid och näringsämnen. Bidragande till detta är kombinationen av två speciella fenomen: uppvällning av varmt, koldioxidrikt vatten, och ett ythav som påverkas av stor tillväxt och smätning av havsis . De turbulenta processerna som förmedlar utbyte och blandning av vattenegenskaper mellan det uppvällda djupvattnet och det havsispåverkade ytskiktet bestämmer egenskaperna hos vattnet som kommer in i den globala cirkulationen. Det finns dock stora osäkerheter om vilken roll småskaliga turbulenta processer spelar i globala klimatmodeller på grund av modellernas beräkningsbegränsningar, i kombination med sparsam provtagning i avlägsna och svåra förhållanden som är karakteristiska för havsisregionen i Södra oceanen. Denna avhandling handlar om att observera och förstå turbulens från centimeter- till kilometerskala. Det särskilda syftet är att förstå vad som händer i det övre havet efter att havsis smälter, när det gäller blandning av vattenegenskaper och primärproduktion av alger. Vi uppnår detta med hjälp av undervattensdrönare som kan samla in data i havet med hög upplösning i både rum och tid under långa perioder. Det finns tre huvudsakliga fynd: (1) Vi finner att smältningen av havsis ökar horisontella förändringar i kilometerskala i salthalt och temperatur. Havsissmältandet ökar dock också stabiliteten för det blandade ytskiktet, vilket förhindrar vertikal transport av värme och färskvatten mellan havets inre och ythav i de regioner där havsisen smälter. (2) Blandning av värme i centimeterskala i vintervattnet under ytan driver den säsongsbetonade uppvärmningen av detta lager, vilket förmedlar omvandlingen under ytan av det varma och salta djupvattnet. (3) Algtillväxten ökar i förhållande till mängden havsis som växer, främst på grund av att havsisen växer under vintern och kan driva medbringandet av begränsande näringsämnen och mineraler från djuphavsreservoaren till ythavet.

Outline

This thesis is based on four scientific papers referred to in the text by their roman numerals as listed below. The thesis consists of an introductory part, a synopsis of the observations, an introduction to each paper, and the conclusions followed by the scientific papers.

The papers included in this thesis (**chapter 9**) are:

I: Swart, S., M. du Plessis, A.F. Thompson, L. Biddle, **I. Giddy**, T. Linders, M. Mohrmann, S-A. Nicholson, 2020. Submesoscale Fronts in the Antarctic Marginal Ice Zone and Their Response to Wind Forcing. *Geophysical Research Letters*, **47 (6), e2019GL086649**. https://doi.org/10.1029/2019GL086649

II: **Giddy, I.**, S. Swart, M. du Plessis, A.F. Thompson, S-A Nicholson. (2021). Stirring of Sea-Ice Meltwater Enhances Submesoscale Fronts in the Southern Ocean. *Journal of Geophysical Research: Oceans*, **126(4), e2020JC016814**

III: **Giddy, I.**, I. Fer, S. Swart, S-A Nicholson. (*manuscript*, 2022). Vertical convergence of turbulent and double diffusive heat flux drives warming and erosion of Antarctic Winter Water in summer. *in prep for submission to Journal of Physical Oceanography*

IV: **Giddy, I.**, S-A Nicholson, B. Y. Queste, S. Thomalla, S. Swart. (*in review*, 2022). Sea-ice impacts inter-annual variability in phytoplankton phenology and carbon export in the Weddell Sea. *Geophysical Research Letters*

Paper I presents the first data collected as part of this thesis. In **Paper I**, I assisted with the plotting of Figure 2, and computed the surface density spectra plotted in Figure 3b. I also provided input on the uncertainty introduced to lateral gradient approximations given errors in salinity due to uncorrected thermal inertia of the conductivity cell. In **Paper II**, I formulated the research question, performed the data analysis and led the writing and reviewing of the manuscript. I participated in the piloting of the glider that collected the data for the analysis primarily through developing and maintaining a data visualisation website (`www.roammiz.com`). In **Paper III**, I processed the data, formulated the research question, performed the analysis and wrote the manuscript. In **Paper IV**, I deployed one of the gliders used in the analysis (SG640) and participated in at-sea fieldwork as part of the Southern oCean seAsonaL Experiment (SCALE). I formulated the research questions, carried out the data analysis, and wrote the manuscript.

Other works not included in this thesis:

du Plessis, M.D., Swart, S., Biddle, L.C., **Giddy, I.S.**, Monteiro, P.M.S., Reason, C.J.C., Thompson, A.F. and Nicholson, S.A., The daily resolved Southern Ocean mixed layer: Regional contrasts assessed using glider observations. *Journal of Geophysical Research: Oceans*, **p.e2021JC017760**. https://doi.org/10.1029/2021JC017760

In this paper, I contributed to the interpretation of the analysis pertaining to the marginal ice zone, editing of the manuscript, and response to the reviewers.

Gregor, L., T. Ryan-Keogh, S-A. Nicholson, M. du Plessis, **I. Giddy**, S. Swart. (2019). GliderTools: A python toolbox for processing underwater glider data. *Frontiers in Marine Science*. https://doi.org/10.3389/fmars.2019.00738

In this paper, I contributed to the development of the objective mapping component incorporated into GliderTools.

Giddy, I, S. Thomsen, and co-authors. Ocean Gliders Salinity SOP. `https://oceangliderscommunity.github.io/Salinity_SOP/README.html`

I am leading this SOP together with S. Thomsen, collating ideas from co-authors and contributors and maintaining the gitHub repository.

Chapter 1

Motivation

The Southern Ocean acts as a globally important buffer to climate change through its capacity to absorb excess heat (∼75%, *Frölicher et al.*, 2015) and carbon (∼50% *De Vries et al.*, 2017). However, both heat and carbon uptake estimates are model-dependent and have substantial temporal and spatial biases when compared with observations (*Sallée et al.*, 2013). Large discrepancies between global climate models are particularly evident in the seasonally covered sea ice region of the Southern Ocean, where regional and temporal variability of heat and carbon fluxes are poorly constrained (*Gruber et al.*, 2009; *Roden et al.*, 2016). A major control of these fluxes is associated with mixing in the surface ocean boundary layer and the depth of the mixed layer, which modulates the exchange of ocean properties between the surface and ocean interior. If the processes that drive mixing and the depth of the mixed layer are not resolved or are inadequately parameterized in global climate models, the modelled flux of ocean properties will be incorrect.

Ocean circulation in models is based on the continuum equations of motion for seawater (e.g. Navier-Stokes equations), however, due to computational limitations, present ocean models discretize the continuum equations and parameterize unresolved processes, such as submesoscale, O(0.1-10) km, flows (*Fox-Kemper et al.*, 2019). Moreover, a computer model does not indicate if processes are omitted, it simply resolves an incorrect answer. Therefore, experiments and observations are needed in order to determine model biases and unrepresented processes. The bias in mixed layer depth improves with model resolution, highlighting the contribution of ocean circulation (advection and air-sea fluxes) to deep mixing (*Small et al.*, 2021), and hinting to an important role of submesoscale ageostrophic processes. The seasonally sea ice-covered Southern Ocean is remote and inhospitable; a challenging location for observational oceanography. Because of this, observations are sparse (*Lenton et al.*, 2013; *Swart et al.*, 2019). This means that there is little data to validate and improve ocean models.

Given the rapidly changing atmospheric forcing and circulation in the Southern Ocean (Figure 1.1), as outlined in the IPCC Special report (*Meredith et al.*, 2019) on the Ocean and Cryosphere, and the disproportionate role of the Southern Ocean on the climate system, we can infer that even small inaccuracies in its representation in global climate models can have potentially large implications.

This thesis contributes to the existing and growing body of literature by addressing the mechanisms that impact the transport and redistribution of heat, freshwater

and carbon in the sea ice impacted Southern Ocean at scales of centimeters to kilometers (micro- to (sub)mesoscales) using *in situ* observations by autonomous surface and underwater vehicles. It marks the first time that upper ocean variability in the sea ice impacted Southern Ocean has been observed at spatio-temporal resolutions that resolve the evolution of physical and biological phenomena at the submesoscale and below.

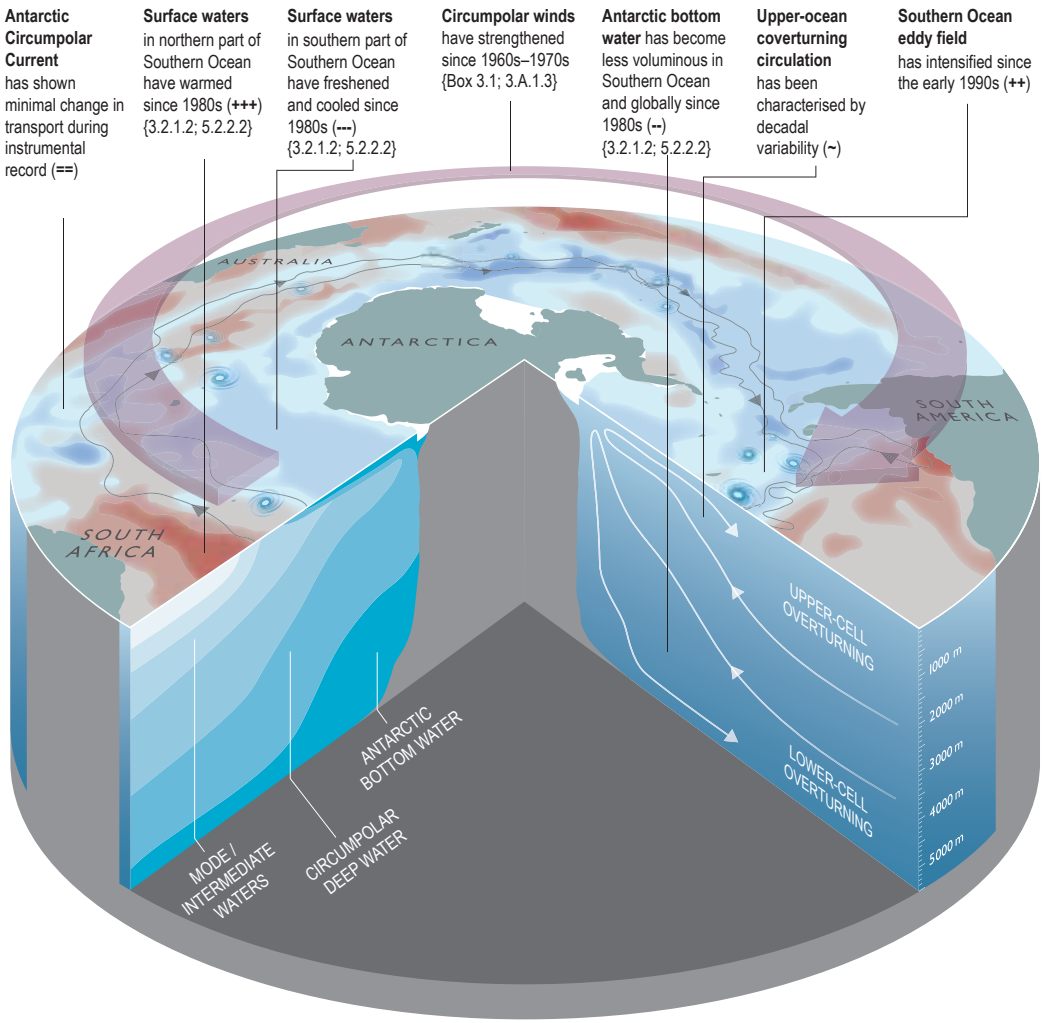

Figure 1.1: The major Southern Ocean changes assessed in the IPCC Special Report on the Ocean and Cryosphere (Meredith et al., 2019). The circumpolar circulation together with the prevailing westerly winds are highlighted. We draw attention to the major water masses and their link to the overturning circulation. Recent (since the 1980s) surface ocean trends (cooling and freshening of the subpolar ocean, warming in the northern Southern Ocean) are illustrated with the blue and red coloring around Antarctica.

Chapter 2

Background

2.1 The importance of Antarctic sea ice

The subpolar region of the Southern Ocean, south of the Polar Front, influences the global climate system over a broad range of space and timescales through the intersection of sea ice formation and melt with sites of deep-water formation and ventilation. Annually, sea ice cover ranges from $\sim$19 million km^2 in austral winter to $\sim$3-4 million km^2 in austral summer (*Parkinson*, 2019). Its distribution and extent is dynamic, with high inter-annual and regional variability and is sensitive to a range of air-sea feedback mechanisms (e.g. wind-driven sea ice drift, Atlantic warming; *Eayrs et al.*, 2019; *Holland and Kwok*, 2012; *Li et al.*, 2014). The transformation of the upper ocean by sea ice growth and melt plays a crucial role in modulating the radiative and thermodynamic properties of the ocean surface, the exchanges of heat, gases and momentum between the ocean and atmosphere, the meridional overturning circulation (*Abernathey et al.*, 2016), and ocean productivity (*Arrigo et al.*, 2008) that supports vast phytoplankton blooms, ecologically important krill, whales and seabirds (*Massom and Stammerjohn*, 2010).

Since the beginning of the satellite observation period in 1979, Antarctic sea ice exhibited a slight increasing trend until 2016 when sea ice was first observed to decline. The slight increase in sea ice extent has been linked with cold sea surface temperatures (*Comiso et al.*, 2017), with enhanced westerly winds driving northward sea ice transport and cooling the sea surface (*Haumann et al.*, 2020). The decline in sea ice since 2016 has been linked to a warmer upper ocean as a result of a shift in atmospheric forcing driving enhanced upwelling of deeper warm water (*Meehl et al.*, 2019). Thus, Antarctic sea ice is sensitive to both atmospheric and oceanic variability that changes the distribution of heat in the Southern Ocean.

A significant long-term decline in Antarctic sea ice remains to be observed, but appears in climate models predicting a warmer climate with warmer ocean surface temperatures (*Roach et al.*, 2020). The decline of Antarctic sea ice will likely have widespread ramifications, however, because of the multiple interacting processes across different time and space scales, the climate response remains an area of uncertainty. For example, recently the albedo effect of only three years of observed sea ice decline in the Southern Ocean between 2016-2018 alone, reversed the global sea ice-albedo climate feedback from a cooling trend to a warming trend (*Riihelä et al.*, 2021). This suggests that Antarctic sea ice decline will enhance global warming. In contrast, a

decrease in sea ice cover may result in enhanced net primary productivity in the ocean surface which could offset carbon in the atmosphere (*Barnes*, 2015; *Henson et al.*, 2022; *Tagliabue et al.*, 2021), and mediate warming.

Atmospheric and intrinsic ocean variability influences the annual growth of sea ice through its role in the variability of buoyancy, stratification (*Pellichero et al.*, 2018; *Wilson et al.*, 2019) and lateral gradients (*Biddle and Swart*, 2020) in the upper ocean. Sea ice is central to the modulation of upper ocean turbulence, the extent of surface mixing (mixed layer depths), and the transport of water properties between the surface and ocean-interior, thus setting up a tight feedback mechanism between the atmosphere, ice and ocean.

2.2 Circulation in the subpolar Southern Ocean

In considering the role of sea ice in modulating fine-scale (centimeter to kilometer scale) ocean dynamical and the linked biological processes, it is necessary to consider the water masses and general circulation of the Southern Ocean south of the Antarctic Polar Front (Figure 2.1), within which these processes occur.

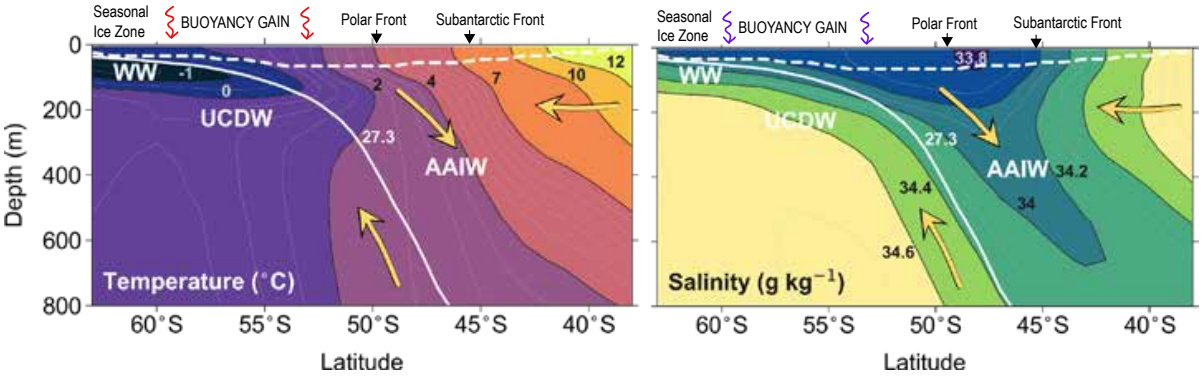

Figure 2.1: Meridional sections of (left) Temperature and (right) Salinity in the Southern Ocean, showing the approximate position and properties of Antarctic winter water (WW), Upper Circumpolar Deep Water (UCDW) and Antarctic Intermediate Water (AAIW), and Southern Ocean fronts. Surface layer buoyancy gain through heat and freshwater flux into the ocean is indicated. Adapted from du Plessis et al. (2022)

The subpolar Southern Ocean is one of the most important regions on earth for the cycling of carbon and distribution of heat and freshwater around the globe (*Abernathey et al.*, 2016; *Hoppema*, 2004; *MacGilchrist et al.*, 2019). It is a region where dense waters return to the surface in nearly adiabatic pathways along tilted density surfaces. The persistent, strong band of westerly winds drives surface divergence that results in upwelling polewards of the zonal surface-wind maximum and downwelling equatorwards of the maximum. When warm, salty, CO_2-rich Upper Circumpolar Deep Water (UCDW) comes into contact with the surface waters and atmosphere exchange of water properties occurs such that its buoyancy increases. Wind-driven Ekman transport advects this water northward, which then subducts as Antarctic Intermediate Water (AAIW), entering the upper limb of the meridional overturning circulation (MOC, *Marshall and Speer*, 2012; *Speer et al.*, 2000, Figure 2.1). The buoyancy gain required

for the transformation of UCDW to AAIW is a topic of relatively recent discussion. Initially, it was understood that the water mass transformation was dependent on the location of upwelling relative to the time-mean air-sea ice buoyancy flux (*Marshall and Speer*, 2012). It has also been argued that buoyancy gain in upwelled UCDW is achieved through the propagation of the surface freshwater via vertical mixing at the base of the mixed layer (*Iudicone et al.*, 2008). Indeed, the buoyancy of the subpolar Southern Ocean is largely determined by the seasonality of sea ice and its associated freshwater fluxes (*Pellichero et al.*, 2017). The seasonal role of sea ice in water mass transformation was suggested by *Abernathey et al.* (2016), where the relative influence of atmospheric, sea ice, and glacial freshwater fluxes, heat fluxes, and upper-ocean mixing in buoyancy transformation within the upper branch of the MOC were assessed. Freshwater input from northwards advected sea ice emerged as a dominant term, emphasising the sensitivity of water mass transformation to changes in winds and wind-driven sea ice transport. These results were confirmed in a similar analysis using observations (*Pellichero et al.*, 2018).

The upwelling deep water is preconditioned for transformation by initially becoming colder and fresher via subsurface diapycnal mixing driven by by gravitational instabilities and convection during winter ocean heat loss (*Tamsitt et al.*, 2018). *Evans et al.* (2018a) corroborate this result in showing how the seasonal mixing of winter water (saltier and denser in winter, fresher and warmer in summer) acts as a conduit for the transformation of deep water to intermediate water. They propose cabbeling instabilities (when two water masses mix to form a denser water mass), a process that is linked with brine rejection by sea ice formation, as a primary mechanism driving the mixing of UCDW with the overlying winter water. In addition to these vertical processes, lateral variability in density from heterogeneous ice formation and melt creates the potential for submesoscale instabilities and flows to grow, thereby efficiently transporting water between the subsurface and surface resulting in the rapid restratification of the upper ocean (*Biddle and Swart*, 2020; *Manucharyan and Thompson*, 2017; *Thomas et al.*, 2008). Thus, sea ice mediates the turbulent processes in the upper ocean that can lead to the exchange of properties between the ocean interior-surface and atmosphere. High resolution observations of temperature, salinity and turbulent dissipation are used to progress our understanding of these sea ice mediated turbulent flows and their link to water mass transformation in *Papers II and III*.

2.3 Turbulence in the seasonal ice zone

One of the most important places for ocean turbulence is the ocean surface boundary layer. Because of the direct connection between the surface boundary layer and the upwelled UCDW (Figure 2.1), mixing processes that occur in this layer, such as advection, stirring, turbulent diffusion, and convection, mediate the exchange of heat, freshwater and CO_2 between the atmosphere and ocean interior. The ocean surface boundary layer is characterized by a mixing layer that is formed through active turbulent mixing either by winds or convection, and a mixed layer, representing the mixing that has recently occurred where ocean properties are well mixed and relatively homogeneous with depth.

Looking at the Sentinel1 radar image of the surface ocean (Figure 2.2a), a field of

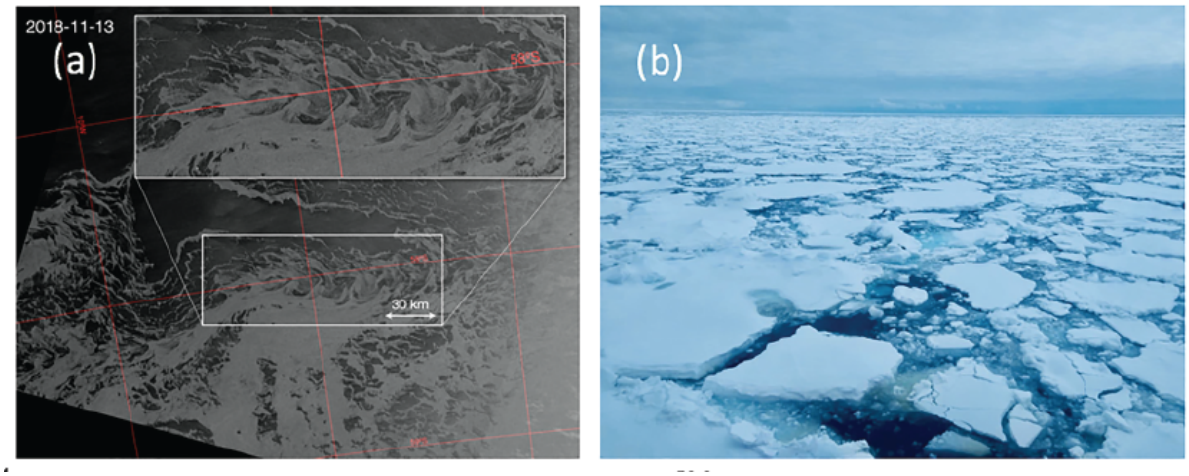

Figure 2.2: (a) Sentinel1 synthetic aperture radar image from 13 November 2018 (1 month prior to robotic deployments) suggesting ocean submesoscale features present at the sea ice margins of O(5-10 km). (b) Photo taken from the RV SA Agulhas II (15 December 2018; 61.07°S, 0.05°E) showing sea ice conditions ∼100 km south of the study location. Image from Swart et al. (2020).

filaments of varying length-scales form patterns in the sea ice, reflecting the underlying fluid motions. This thesis focuses on turbulent processes from the submeso to microscale that act to mediate the properties of the upper ocean following sea ice melt. Before addressing each of these processes and their driving mechanisms, we broadly introduce the scales of turbulent motion in the ocean.

Gradients in the ocean are stirred, strained and sharpened by a range of ocean flows forced by fluxes of momentum, heat and freshwater at the ocean surface (from ocean gyres, mesoscale and submesoscale eddies, internal waves) to small enough scales where 3-dimensional turbulent dissipation and molecular diffusion act to mix ocean properties. This cascade of ocean gradients represents the underlying processes in which energy is transferred across lengthscales via a turbulence cascade until reaching the lengthscale at which dissipation becomes dominant (Kolmogorov lengthscale, *Kolmogorov*, 1941). In the ocean interior, the mesoscale motions with scales $O(10)$ km or more, are described by balanced sub-inertial quasi-geostrophic dynamics in which there is an inverse cascade of energy (*Charney*, 1971; *Kraichnan*, 1967). At the smallest scales (less than $O(10)$ m), shear instabilities, convection and breaking internal waves produce isotropic 3-dimensional turbulence that effectively and irreversibly mixes ocean property gradients in the ocean. Submesoscale flows with characteristic scales of $O(0.1\text{-}10)$ km occupy the intermediate space and timescales between geostrophic mesoscale eddies and the fully 3-dimensional turbulence and are a key intermediary in the cascade of kinetic energy from mesoscales towards microscales (*McWilliams*, 2016). The irreversible mixing across isopycnals of water properties is the result of dissipation at centimeter scales. It is this mixing that ultimately results in the transfer of heat, salt, gases and nutrients between water masses. Thus, while it is large scale processes that drive the transport of ocean properties and the rate of dissipation, through their mediation of ocean mixing, these small-scale processes are strongly linked to large scale dynamics.

2.3.1 Submesoscale macro-turbulence

Submesoscale ocean dynamics and instabilities are ubiquitous in the world's oceans, generally constrained but not limited to boundary layers (both the surface and bottom boundary) (*McWilliams*, 2016). Submesoscale flows that grow in the ocean surface boundary layer (property homogeneous mixed ocean layer that is in contact with the atmosphere at the top and interior ocean below) can play a critical role in setting the oceans surface boundary layer thickness and associated density stratification. Submesoscale instabilities contribute to lateral stirring and tracer dispersal. In the ocean, they have horizontal scales of O(0.1 - 10 km) and timescales of hours to weeks (*McWilliams*, 2016; *Thomas et al.*, 2008). At these scales, the flows are less constrained by Earth's rotation than mesoscale dynamics but more constrained than more 3-dimensional structures. Dynamically, submesoscale processes are characterised by order one Rossby and Richardson numbers (*Thomas et al.*, 2008). The Rossby number, arising from the relative scaling of the inertial and Coriolis terms in the equations of motion, is defined as $R_o = U/fL$, where U is the characteristic horizontal velocity scale, f is the local Coriolis frequency and L is the characteristic horizontal length scale. The Richardson number describes the ratio of stratification to vertical shear, $Ri = N^2/S^2$.

Upper ocean turbulence in submesoscale fronts, eddies and filaments can be associated with strong vertical velocities, transporting water (and its properties; heat, inorganic and organic carbon, and nutrients) between the ocean interior and surface (*Freilich and Mahadevan*, 2021; *Lévy et al.*, 2018; *Su et al.*, 2018). Mixed Layer Eddies, a class of submesoscale flows (*Fox-Kemper et al.*, 2008), arise from baroclinic mixed-layer instabilities and, given sufficient potential energy (i.e. deep mixed layers and strong lateral gradients), can rapidly restratify the upper ocean (*Boccaletti et al.*, 2007; *Mahadevan et al.*, 2012). Winds that blow over submesoscale fronts advect density such that either water column stratification (via isopycnal slumping) is enhanced or, conversely, turbulent overturns at the front are energized (through shear production of turbulence), maintaining the frontal structure and delaying isopycnal slumping and restratification (e.g. *D'Asaro et al.*, 2011; *du Plessis et al.*, 2019). Submesoscale flows further act to advect and redistribute ocean properties including phytoplankton communities (*Lévy et al.*, 2018), and sea ice (*Manucharyan and Thompson*, 2017). The interaction of Mixed Layer Eddies with mechanical wind forcing is illustrated in Figure 2.3. While lighter water will tend to slump over heavier water, resulting in eddy overturning, winds that are oriented down-current will advect

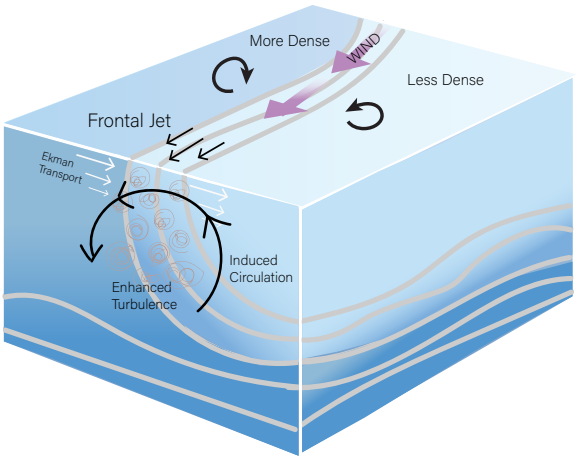

Figure 2.3: Schematic of the flow induced by submesoscale Mixed Layer Eddies and Ekman Buoyancy Flux when the winds are down-front. In this case, frontal slumping is prevented by the opposing ekman transport of heavy water (dark blue, saltier) over light water (light blue, fresher) that enhances turbulence at the front. Adapted for the Southern Hemisphere sea-ice impacted ocean from Mahadevan (2016).

water to the left in the Southern Hemisphere, pushing heavier water over lighter water. This introduces instabilities that maintain the front, and arrest restratification by Mixed Layer Eddies.

At the edge of the sea ice extent and in the regions of active sea ice melt, heterogeneous ice melt and ice formation introduce lateral density gradients that provide energy for submesoscale instabilities and mixed layer overturns (e.g. *Manucharyan and Thompson*, 2017). While there is evidence of submesoscale features in the seasonal ice zone year round (*Biddle and Swart*, 2020), their impact on upper ocean stratification and water mass transport is an area of active research. The role of submesoscale flows in the mixed layer of the ice-impacted Southern Ocean is addressed in *Paper I and II*.

2.3.2 Microscale turbulence

The action of turbulent eddies is to disperse particles by stirring which increases concentration gradients and homogenizes fluid properties through diffusion. These two processes lead to efficient mixing at the molecular scale. Mixing across isopycnals (diapycnal mixing) results in the irreversible transfer of heat, freshwater and tracers, a key process in the exchange of water properties and transformation of water masses. The resulting turbulent-enhanced mixing (eddy diffusivity) can be approximated from the rate of turbulent dissipation following the *Osborn* (1980) model. Under steady state turbulence with no transport, the rate of dissipation of Turbulent Kinetic Energy (TKE) is balanced by shear production and buoyancy flux:

$$\underbrace{\varepsilon}_{\text{Viscous dissipation}} = \underbrace{-\overline{u'w'}\frac{d\overline{U}}{dz}}_{\text{shear production}} - \underbrace{\overline{w'b'}}_{\text{buoyancy production}}, \tag{2.1}$$

where z is the depth, $\overline{U}$ is the mean velocity, and $\overline{u'w'}$ is the Reynolds stress. While shear production will always act to create TKE, buoyancy flux can be either stabilizing or destabilizing. As such, processes that either enhance shear production or induce stabilizing or destabilizing buoyancy fluxes can change the rate of dissipation of TKE and therefore the rate of turbulent mixing and transfer of ocean properties.

In the sea ice impacted Southern Ocean these processes include: 1) deep winter mixing driven by brine rejection (*Evans et al.*, 2018a; *McPhee and Morison*, 2001; *Wilson et al.*, 2019) that induces convection and 2) wind and wave-driven shear production of turbulence which is important year-round (*Belcher et al.*, 2012) and plays a key role in the exchange of nutrients and CO_2 across the pycnocline (*Nicholson et al.*, 2019, 2022). Another source of turbulence by which water properties are exchanged is through double diffusive convection (DDC). DDC occurs as a result of the different molecular diffusivities of heat and salt. When cold, fresh water overlies salty, warm water, if a parcel of water is displaced downwards, for example, it will quickly gain heat, and, when returning through the water column with increased buoyancy, will overshoot its original position. This process leads to oscillatory overturns that grow in amplitude and are observed as layering in the ocean. Evidence of enhanced subsurface mixing that results from DDC has been observed in the Ross Sea in winter (*Bebieva and Speer*, 2019) and in the Weddell Sea (*Muench et al.*, 1990; *Shaw and Stanton*, 2014), with a substantial contribution to upwards heat flux observed at Maud Rise. Nevertheless, a global

analysis of DDC suggests that the contribution of DDC to the global energy balance is negligible (*van der Boog et al.*, 2021). This analysis was, however, based on the presence of thermohaline staircases from course resolution data. In *Paper III*, we use high resolution direct observations of dissipation to attribute the oceanic processes driving vertical heat fluxes in the summertime, with particular focus on shear-production of turbulence and double diffusive convection.

2.4 Primary production and carbon export in the seasonal ice zone

Biological activity in the upper ocean takes up CO_2 from the atmosphere and converts it to carbon, making it available as food to support higher trophic levels and bacterial communities. About 10% of this carbon is exported into the deep ocean, maintaining a vertical gradient in dissolved CO_2 and allowing for the ocean to continue to absorb natural and anthropogenic CO_2 via the solubility pump (*Sarmiento and Gruber*, 2006). Without this process, it is estimated that CO_2 levels in the atmosphere would be two-fold higher (*Maier-Reimer et al.*, 1996). The sea ice impacted Southern Ocean supports a unique balance between ocean mixing (supply of nutrients) and stratification (light availability), making it one of the most productive oceans regions (*Ardyna et al.*, 2017; *Arrigo et al.*, 2008). Mixing draws up nutrients, while stratification maintains phytoplankton in favourable light conditions. Primary production in this region supports a diverse food-web dominated by krill, marine birds, seals and whales (*Massom and Stammerjohn*, 2010) and drives the biological carbon pump, through the downward transport of particulate organic carbon from the surface ocean to the interior.

The interplay between limiting nutrients and trace minerals, light and predation regulates net primary production across the Southern Ocean (*Arteaga et al.*, 2020; *Tagliabue et al.*, 2014; *Thomalla et al.*, 2011). The sea ice impacted phytoplankton blooms have the strongest seasonal response to light in the Southern Ocean, through the seasonal cycle of solar irradiance, sea ice cover (limiting light) and sea ice melt (enhancing light available by increased stratification) (*Ardyna et al.*, 2017).

The amount of carbon that is exported to the ocean interior is modulated by both biological and physical processes. Direct transport by the physical injection pump (*Boyd et al.*, 2019), which includes that of submesoscale vertical transport (e.g. *Freilich and Mahadevan*, 2021; *Omand et al.*, 2015; *Siegelman et al.*, 2020) has been observed in regions with high eddy kinetic energy. However, the biological gravitational pump is thought to account for the vast majority of carbon export in the world's oceans (*Henson et al.*, 2019; *Martin et al.*, 1987). The efficiency of this export is regulated by the complex interactions of multiple processes, including particle formation and rates of sinking (aggregation, fragmentation, ballasting, senescence, grazing, viral lysis) and remineralization (microbial activity, chemical dissolution), themselves factors that largely depend on rates of primary production and the community composition. It is in part because of this complexity that there remains high uncertainty in future predictions of carbon export throughout the world's oceans (*Henson et al.*, 2022). Because sea ice impacts the stratification and mixing characteristics of the upper ocean, changes in sea ice will have direct implications to the magnitude, duration and community composition of phytoplankton, which will in turn impact carbon flux to depth. Sinking organic

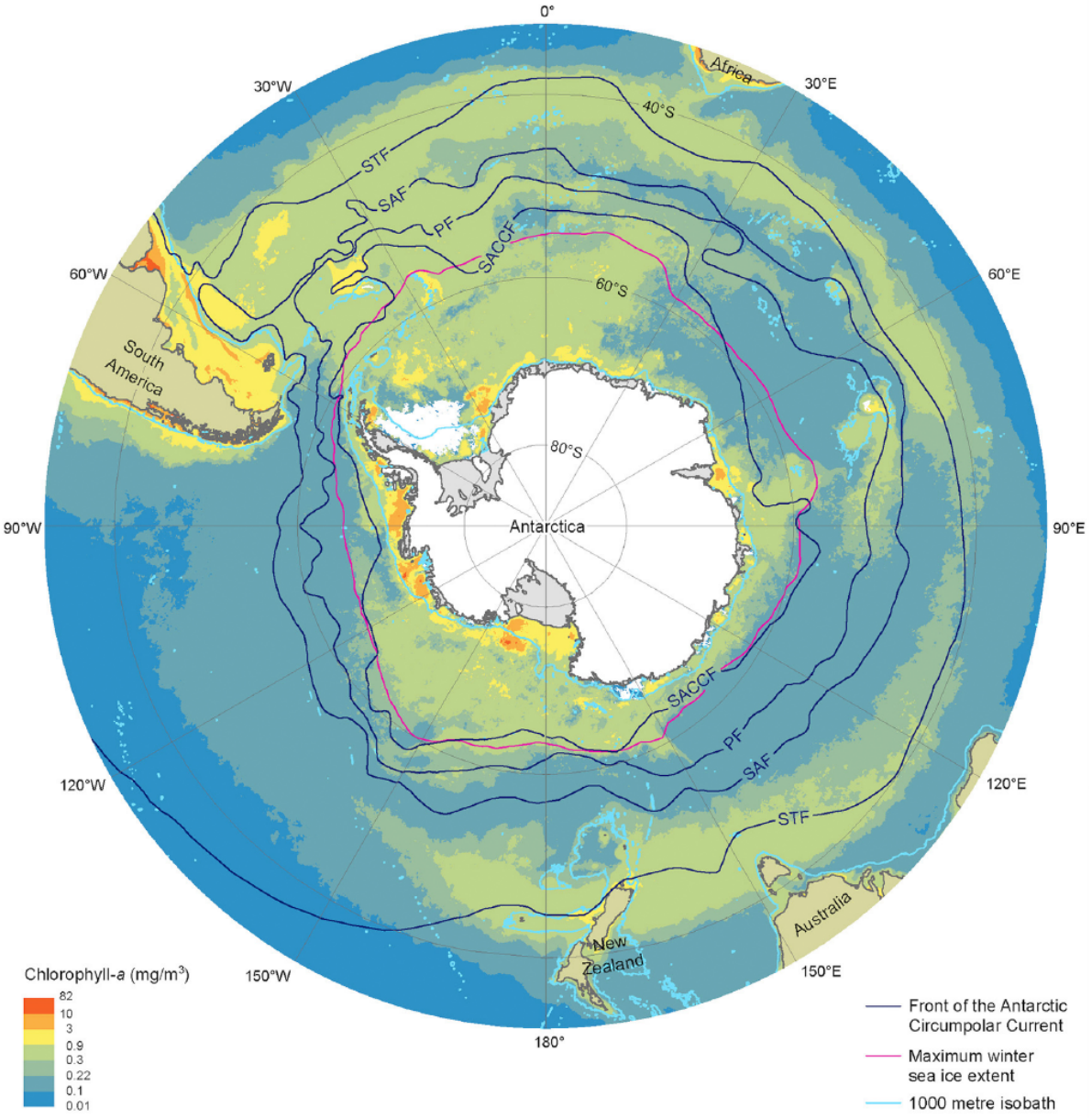

Figure 2.4: Average distribution of Chlorophyll a *in the Southern Ocean. The maximum winter sea ice extent in marked with a red contour line. Image from Deppeler and Davidson (2017)*

.

carbon that is remineralized within the circulating Circumpolar Deep Water layer currently accounts for about half of the carbon sink in the Weddell Gyre (*Hoppema*, 2004; *MacGilchrist et al.*, 2019; *Naveira Garabato et al.*, 2017), suggesting that changes in the biological carbon pump here (and likely in other subpolar gyres) can have a disproportionate impact on the global carbon cycle (i.e. the soft carbon component of the carbon cycle is enhanced in this region).

While supporting large phytoplankton blooms during austral summer (Figure 2.4 *Deppeler and Davidson*, 2017), the sea-ice impacted Southern Ocean would be expected to be sensitive to the changing climate. CMIP6 models predict that both net primary production and carbon export will increase in the Southern Ocean in a warmer climate (*Henson et al.*, 2022; *Tagliabue et al.*, 2021). However, model agreement does not equate to a valid prediction and *in situ* observational validation is important. A recent float based study suggested that net primary production will decrease as a result of either reduced nutrient and mineral availability due to increased stratification (*Arteaga et al.*, 2020). Another study suggests reduced light availability due to enhanced winds may decrease net primary production in the ice-impacted Southern Ocean (*Deppeler and Davidson*, 2017). In *Pinkerton et al.* (2021), depending on the primary production model applied to satellite data, the observed trend in net primary production differed in direction. How any of these changes translate mechanistically to carbon export remains to be quantified as primary production is not necessarily linearly related to carbon export flux (*Henson et al.*, 2019). How phytoplankton respond to the changes in the upper ocean that result from variations in sea ice formation and melt, and how this translates to short and long term carbon storage, is considered through an empirical analysis in *Paper IV*.

Chapter 3

Objectives

The overarching aim of this thesis is to advance the understanding of upper ocean turbulence in the sea ice impacted Southern Ocean using novel, high-resolution observations. The thesis is comprised of four scientific papers that address three distinct topics, each with its own series of research questions. The first three papers focus on mixing processes that modify the properties of water in the upper ocean. The fourth paper assesses the impact of sea ice and associated mixing processes on primary production and carbon export.

1. Submesoscale flows in the sea ice impacted Southern Ocean

    - How does sea ice melt impact upper ocean stratification?
    - Does sea ice melt enhance submesoscale instabilities?
    - Do submesoscale mixed layer fronts vary seasonally?

    Paper I presents the first direct observations of submesoscale lateral gradients in the ice-impacted Southern Ocean using twinned surface and subsurface autonomous platforms. *Paper II* uses three months of glider observations made directly following sea ice melt, to quantify the length scales and strength of submesoscale fronts in the mixed layer and their seasonal progression.

2. Diapycnal mixing in the sea ice impacted Southern Ocean under stable buoyancy forcing

    - What are the characteristics of turbulent dissipation in the ice-impacted Southern Ocean during summer?
    - What are the drivers of surface and subsurface mixing in the ice-impacted Southern Ocean?
    - Do diapycnal fluxes of heat contribute substantially to the seasonal erosion of the subsurface Antarctic winter water layer?

    Paper III uses measurements of microstructure together with glider observations of temperature and salinity that were made during austral summer to investigate the dominant drivers, characterise turbulent dissipation and quantify the contribution to diapycnal mixing to heat fluxes across the winter water layer.

3. Primary Production and Carbon Export in the Weddell Sea

    - To what extent does sea ice drive phytoplankton bloom amplitude and duration in the Weddell Sea?
    - Can bloom amplitude predict carbon export?

    Paper IV addresses these questions using a combination of satellite observations, biogeochemical Argo floats and gliders observations. The Weddell Sea is a focus region because primary production and carbon export are spatially heterogeneous, warranting a case-study approach.

Chapter 4

Observations

4.1 Overview of the Field Campaigns

In situ oceanographic observations form the keystone datasets used in this thesis. Novel, high resolution observations of the seasonal ice zone are collected through two projects: 1) The Robotic Observations and Modeling of the Marginal Ice Zone (ROAM-MIZ) project (2018-2022) and 2) the SOSCEx-STORM experiment (Figure 4.1a) that involve field campaigns set at the northern reach of the Antarctic Marginal Ice Zone (defined broadly as the transition zone from pack ice to open water) and south of the Antarctic Circumpolar Current. Measurements were carried out between 2018-2020. This comprised of one Sailbuoy deployment (*Paper I*) and three glider deployments: two Seagliders (*Paper I, II, IV*) and one Slocum (*Paper III*). The Slocum was fitted with a turbulence instrument package MicroRider-1000LP (MR). The distribution of each of the glider sampling patterns is shown in Figure 4.1b,c,d, with sampling concentrated at 60°S; 0°E. The region that the gliders sampled was covered with sea ice during the winter (Figure 4.1a); however the gliders were intentionally deployed directly following the melt of sea ice (e.g. in 2018 SG643 was deployed 4 days after the local melt of sea ice), which occurred towards the end of November and beginning of December, to capture the sea ice driven modifications to the surface oceans and its evolution through summer (Figure 4.1e). During the measurement period, the mean heat flux into the ocean was positive in the daytime (stabilizing conditions), which gradually decreased towards the end of each deployment during the onset of austral autumn. Table 4.1 summarises the respective autonomous platform deployments. In addition to these observations a number of openly available datasets were used (satellite observations, reanalysis and floats) and are detailed in the sections that follow.

Table 4.1: List of autonomous platforms used in the thesis, detailing respective deployment and retrieval dates, sampling pattern and the paper that the data is used in. All deployments were centered at 0°E; 60°S.

name	deployed	retrieved	days	sampling pattern	paper
Sailbuoy	15 Dec 2018	1 Mar 2019	90	mesoscale transects	I
SG643	14 Dec 2018	26 Mar 2019	102	submesoscale bowtie	II, IV
SG640	20 Oct 2019	18 Feb 2020	125	mesoscale transects	IV
Slocum	16 Dec 2019	18 Feb 2020	64	submesoscale bowtie	III

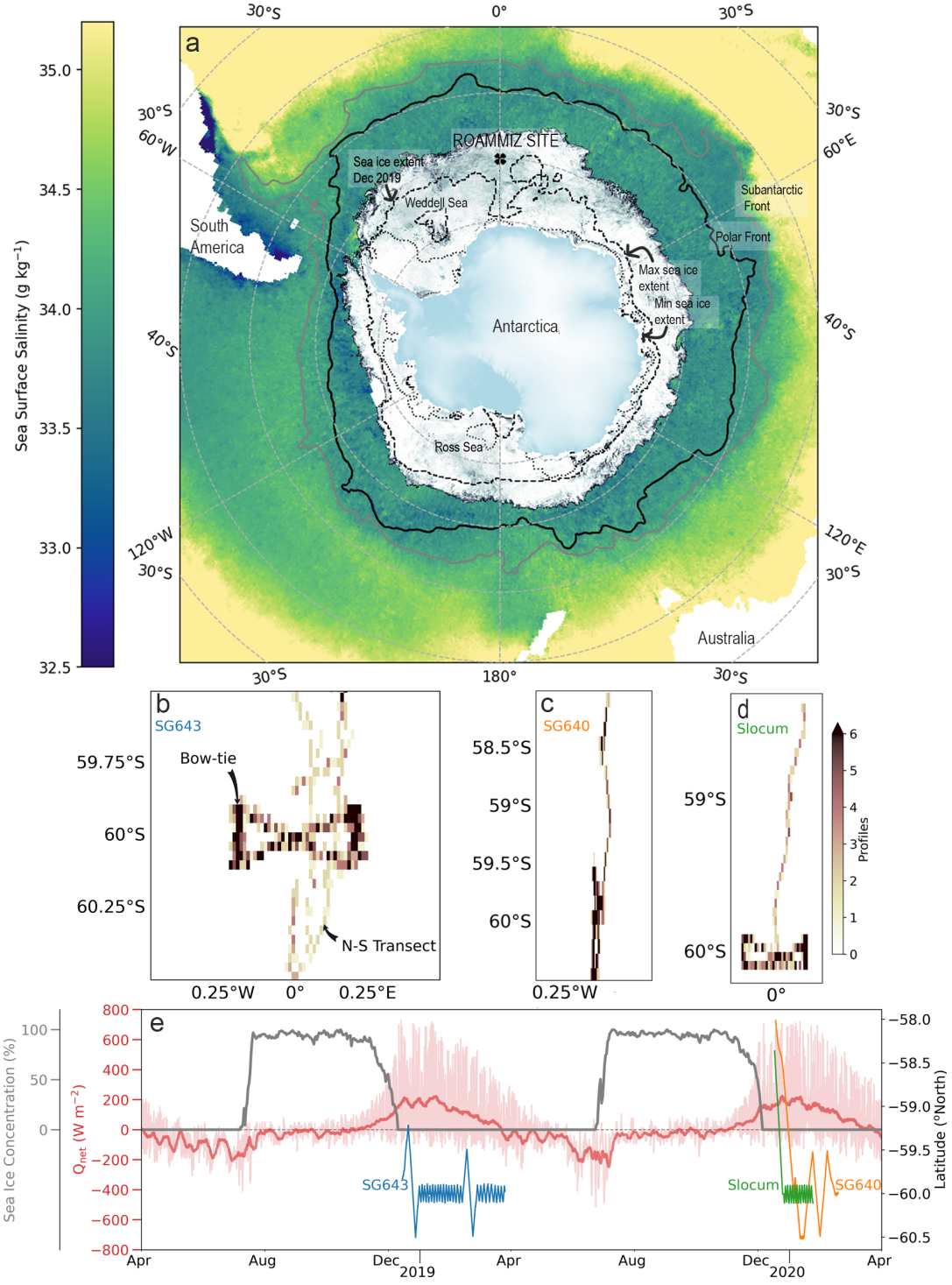

Figure 4.1: Overview of the study region and glider sampling strategy. a) Map of the study region showing the maximum (sea ice colormap) and minimum (dotted line) extents of sea ice and the extent of sea ice at the time of glider deployment (dashed line) in the 2019-2020 annual cycle; the mean location of the Antarctic Polar Front (blue contour) and the Subantarctic Front (grey contour); the ROAMMIZ study site at 60°S; 0°E is marked with an X. The colormap is the average Sea Surface Salinity (SSS) in December 2019 (ESA SSS Climate Change Initiative). Sampling distributions and location of b) SG643, c) SG640 and d) the Slocum glider. e) Time series of sea ice concentration (grey line, Spreen et al., 2008) and net heat flux (red line, ECMWF ERA5) at 60°S; 0°E, together with the latitudinal transects completed by gliders SG643 (blue), Slocum (green) and SG640 (orange).

4.2 Autonomous platforms

4.2.1 Sailbuoy

Sailbuoys are wind propelled with solar panels powering the scientific sensors and navigation systems, allowing them to remain at sea for many months. From 15 December 2018 to 1 March 2019, the Sailbuoy maintained a north-south transect of ∼100 km during which time surface sea water salinity and temperature were measured at 0.5 m depth. Simultaneously, wind speed, wind gust and direction, barometric pressure and air temperature were measured at 0.7 m above sea level. In this thesis (*Paper I*), we focus on the surface measurements of sea water temperature and salinity, and the wind observations.

4.2.2 Gliders

Underwater gliders are a class of autonomous underwater vehicles (AUVs) that profile vertically through the water column by changing their buoyancy and achieve horizontal motion through lift provided by wings. In combination, this results in a characteristic "sawtooth" profiling pattern illustrated in Figure 4.2c. The potential for instruments, such as gliders, in spear-heading future oceanographic observations was imagined in a narrative piece by Henry Stommel (*Stommel*, 1989), where he presents a future scenario of oceanographic observations in which the world's oceans are patrolled by gliders, collecting thousands of ocean profiles a year and likened to the satellite coverage of the ocean surface. While this has not yet come to be, gliders are used extensively in oceanographic research, extending the reach of research vessels in space and time. Gliders can perform sustained, autonomous sampling of the upper 1 km of the ocean. The ability to direct the movement of the glider separates gliders from profiling floats (such as Argo floats) and further allows for the design of unique observational experiments. The high spatio-temporal resolution (2-4 hour; 0.3-4 km; 1 m in the vertical) measurements by gliders build the basis observations for this thesis. Underwater gliders are especially effective for making high resolution observations over longer time periods (weeks - months) because they propel themselves using buoyancy changes and therefore have efficient battery consumption. Their active navigation allows for profiling across currents and fronts in contrast to profiling floats. They allow cross-front measurements to help resolve lateral gradients, while also profiling with depth. In this work the gliders are either piloted to complete "submesoscale bowties" (∼20 km) or "mesoscale transects" (∼100 km) (Figure 4.1). The addition of mesoscale transects, allowed us to evaluate the larger scale ocean gradients within which the submesoscale flows were active. The 'bowtie' pattern is selected in order to build statistically robust sampling of the fronts at the submesoscale. Given that the gliders do not perfectly sample the front perpendicularly can result in a bias, which results in underestimating the lateral gradients from which submesoscale parameterizations are approximated (*Thompson et al.*, 2016).

Seagliders

Two Seagliders (Figure 4.2a) were deployed in consecutive years, austral summer 2018-2019 and 2019-2020 from the *RV SA Agulhas II*. The gliders (SG643 and SG640) sampled temperature, conductivity (salinity), dissolved oxygen, 470 and 700 nm optical backscatter, chlorophyll *a* fluorescence, and Photosynthetically Active Radiation (PAR; only SG643) nominally

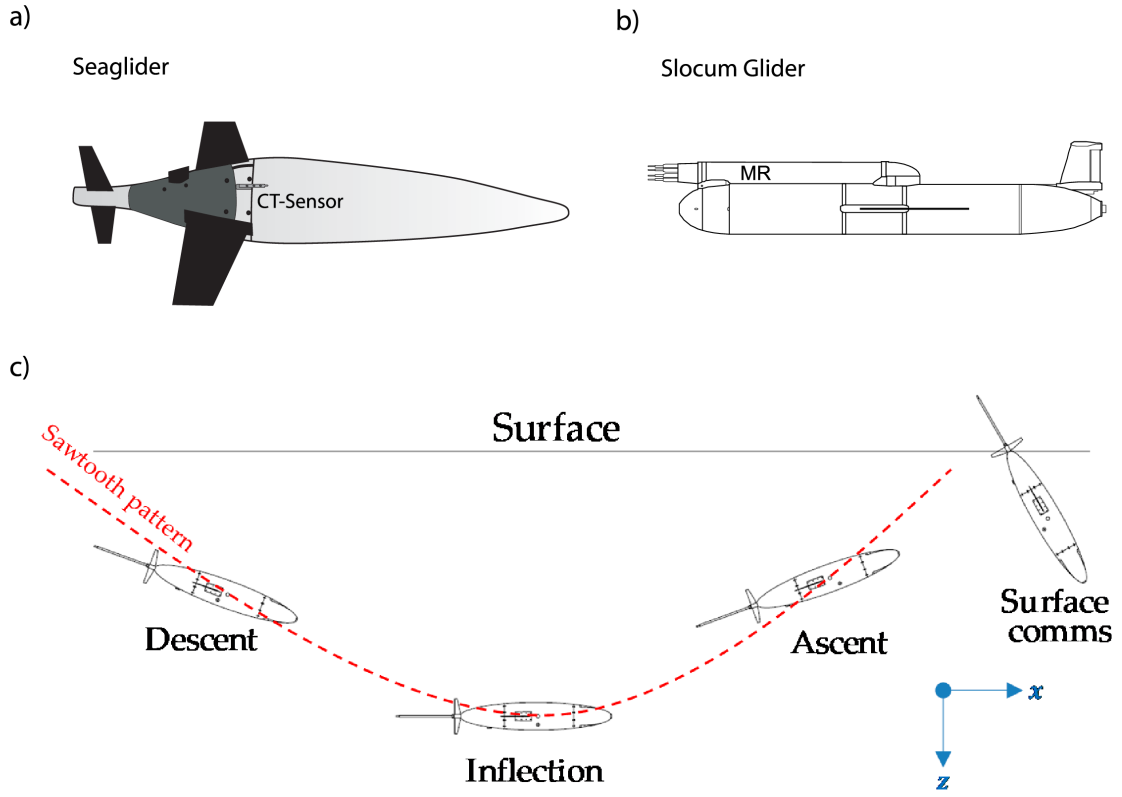

Figure 4.2: Schematics of the two gliders used in this thesis a) Seaglider with the CT sensor labelled and b) Slocum glider with mounted microrider (Fer et al., 2014). c) Typical "sawtooth" glide profile through the water (Orozco-Muñiz et al., 2020).

at 0.2 Hz resulting in a vertical resolution of 0.2-1.5 m in the upper 400 m.

In *Paper II*, SG643 was linearly gridded to 1-km horizontal resolution and 1-m vertical resolution, while in *Paper IV*, both SG643 and SG640 were gridded by profile in the horizontal and binned to 1-m resolution in the vertical. The different choices in gridding pertain to the different research questions that are addressed in each of these papers.

Slocum

A 1000-m-rated Teledyne Webb Research (TWR) Slocum electric glider, G2 (Figure 4.2b), was deployed from the *RV SA Agulhas II* at 58°S, 0°E on the 17^{th} December 2019. The glider then transited directly south for 10 days, completing a mesoscale transect ($\sim$224 km), until it reached 60°S on the 25^{th} December (Figure 4.1). Thereafter, the glider completed a bow-tie pattern of shorter submesoscale transects ($\sim$20-60 km) until it was retrieved on the 18^{th} February 2020. The Slocum sampled temperature, conductivity (salinity), dissolved oxygen, 470 and 700 nm optical backscatter and chlorophyll *a* fluorescence. The sampling frequency was 1 Hz, with an average flight speed of 0.3 m s^{-1}, resulting in a vertical resolution of 0.2 m. In addition, the glider was fitted with a neutrally buoyant, lowpower, self-contained turbulence instrument package MicroRider-1000LP (MR), manufactured by Rockland Scientific International. It was equipped with two orthogonal airfoil velocity shear probes (SPM-38), a pressure transducer, a two-axis vibration sensor (a pair of piezo-accelerometers), and a high-accuracy dual-axis inclinometer, from which turbulent dissipation was derived (detailed in *Paper III*). The sampling frequency is 512 Hz on all turbulence channels (vibration, shear) and 64 Hz for the other channels (pitch, roll, and pressure). The Slocum glider data were processed and corrected for thermal inertia using the software kindly provided by Dr. Gerd Krahmann (GEOMAR, Germany). The software included a hydrodynamic model from which the angle of attack and flow rate past the sensor are computed.

All glider data was further prepared for analysis using GliderTools (*Gregor et al.*, 2019).

4.3 Thermal Lag Correction of Salinity

Salinity derived from temperature and conductivity is prone to dynamic errors that are a result of profiling in a dynamic environment characterised by spatial temperature and salinity gradients. While dynamic errors in conductivity and temperature are usually small relative to natural variations, they can compound into large relative errors in derived salinity. This is because, in many regions of the ocean salinity does not vary as much as conductivity and temperature. Dynamic errors can, for example, create false density instability in profiles and false variations in mixed layer depths. This is particularly important in beta oceans (like the subpolar Southern Ocean), where density is set by salinity variations. While there are algorithms that correct for thermal inertia, it is not always possible to correct for all the error (see residual error in Figure 4.3 below). In *Papers I and II* I use density to compute lateral gradients and estimate the activity of submesoscale flows. In these cases, errors due to thermal inertia can propagate to the estimates of lateral density gradients. In *Paper II*, Figure 3, we propose a method to approximate the error by comparing dive-climb and climb-dive plots and then take the root mean square error of the difference from zero.

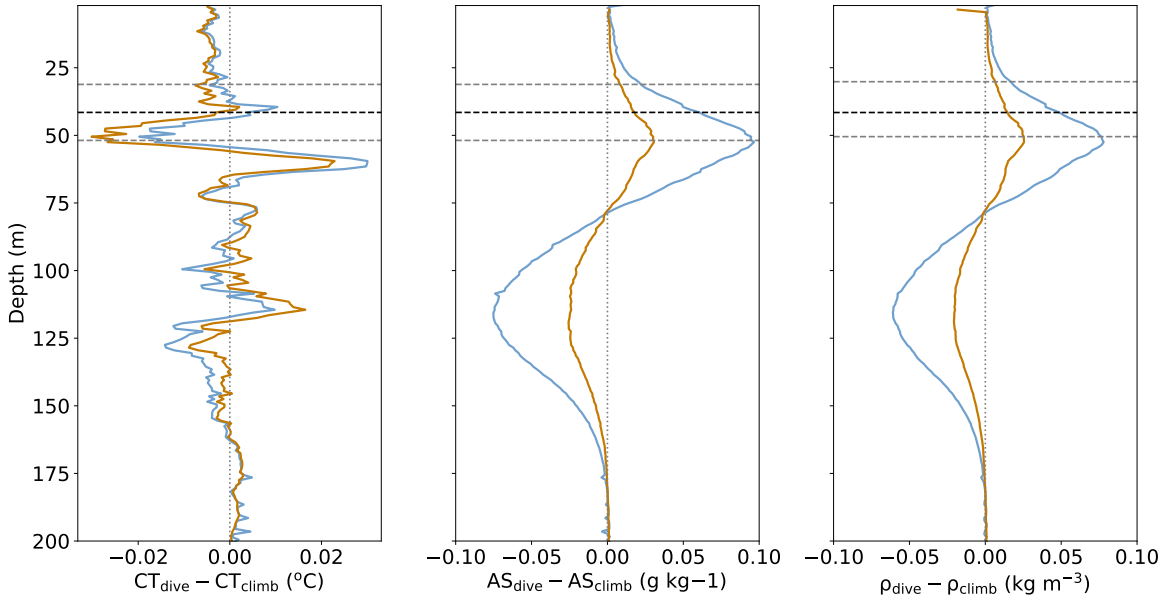

*Figure 4.3: Example of uncorrected (blue) and corrected (orange) Conservative Temperature (CT), Absolute Salinity (AS) and Potential Density (ρ) between consecutive dives and climbs (*Paper II*). The time-averaged mixed layer depth and one standard deviation are shown in the dashed black and grey lines respectively.*

4.4 Microstructure

Direct measurements of microstructure shear variance are used to derive the viscous dissipation rate of turbulent kinetic energy per unit mass, ε (W kg^{-1}). Velocity variance is measured with shear probes that are orthogonal to each other to measure the transverse and vertical components of the along-path shear. Dissipation is then derived from the shear microstructure following *Fer et al.* (2014) using an adaption of the Rockland Scientific ODAS v4.4.04 software. After taking the fast fourier transform (FFT) of the shear (segmented into 30 second intervals, a time scale based on the length of the platform, 1.8 m) and converting it to a wavenumber spectrum using Taylor's frozen field hypothesis, the dissipation rate for each FFT segment is calculated, assuming isotropic turbulence, by integrating the wavenumber spectrum as:

$$\varepsilon_j = \frac{15}{2}\nu\overline{(\frac{\partial u_j}{\partial x})^2} \approx \frac{15}{2}\nu\int_{k_l}^{k_u}\Psi(k)dk, \tag{4.1}$$

where $\frac{\partial u_j}{\partial x}$ is the turbulent scale shear component measured along the glider's along-path coordinate x, j identifies the shear probe number oriented orthogonal to measure the transverse and vertical components of the along-path shear, ν is the kinematic viscosity of seawater, which is a function of the local water temperature, and the overbar denotes averaging. The shear wavenumber spectrum is integrated between k_l, set by the window length and k_u, the minimum in a curve fit to the shear spectrum, that is unaffected by noise. The empirical model for the turbulence spectrum determined by *Nasmyth* (1970) is used to correct for unresolved variance. A number of quality control steps are applied (detailed in Appendix A.1 of *Paper III*), finally taking the average of the quality controlled dissipation estimates from both shear probes. An example of the mean shear wavenumber spectra for dissipation values of

1×10^{-8} W kg^{-1} measured by each orthogonal shear probe is given in Figure 4.4.

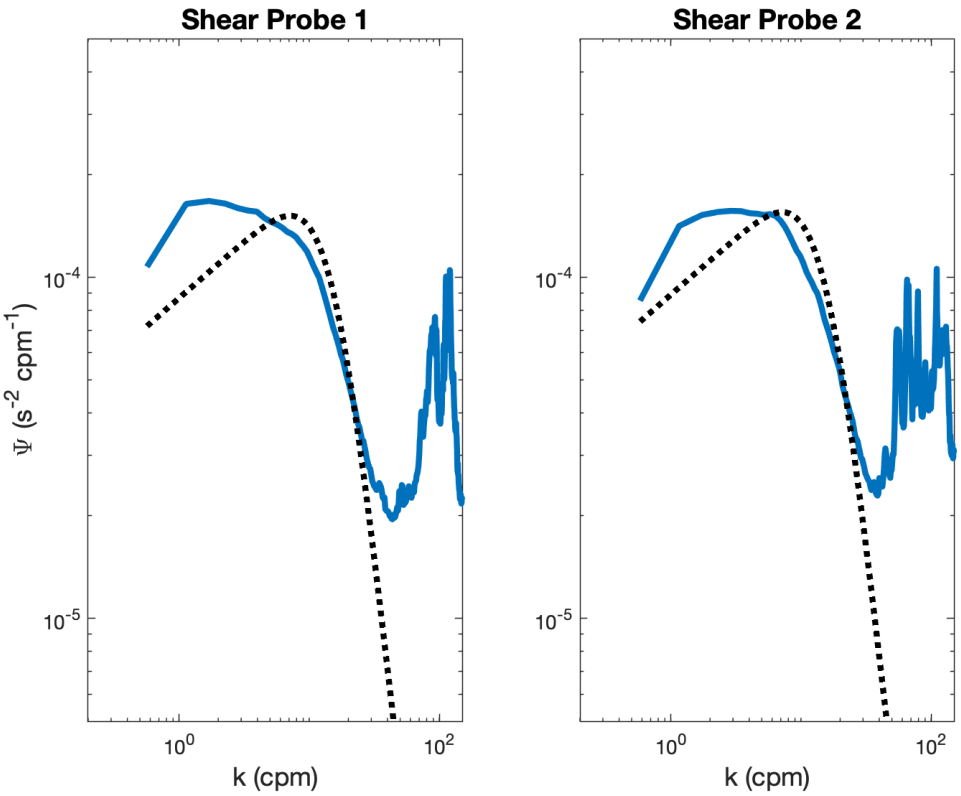

Figure 4.4: Example mean shear spectra measured by each probe for a mean dissipation rate of 1×10^{-8} W kg^{-1}. The corresponding Nasmyth spectrum is overlain with the dotted black line.

4.5 Floats

In this thesis I use Biogeochemical Argo (BGC-Argo) floats, made available by Southern Ocean Carbon and Climate Observations and Modeling (SOCCOM) project. These floats are robotic drifters that move with ocean currents profiling the ocean from the surface to mid-level (2000 m) through adjusting their buoyancy. At depth they drift with the currents, generally programmed to return to the surface once every 10 days. They are equipped with sensors that measure sea water temperature and salinity, and biogeochemical variables, of which I use chlorophyll *a* fluorescence and optical backscatter. In particular, I use two BGC-Argo floats that profiled in proximity to the ROAMMIZ study site from December 2014 to July 2019 (WMO ID: 5094467) and January 2015 to February 2020 (WMO ID: 509397, e.g. Figure 4.5b). For all the float variables only data with a quality control flag of 1 or 2 were used (good or probably good). Potential density was derived from Absolute Salinity and Conservative Temperature (example time-series provided in Figure 4.5a) using the Gibbs Sea Water TEOS-10 Toolbox (*McDougall and Barker*, 2011). Data from these floats is used in *Papers II, III, and IV*.

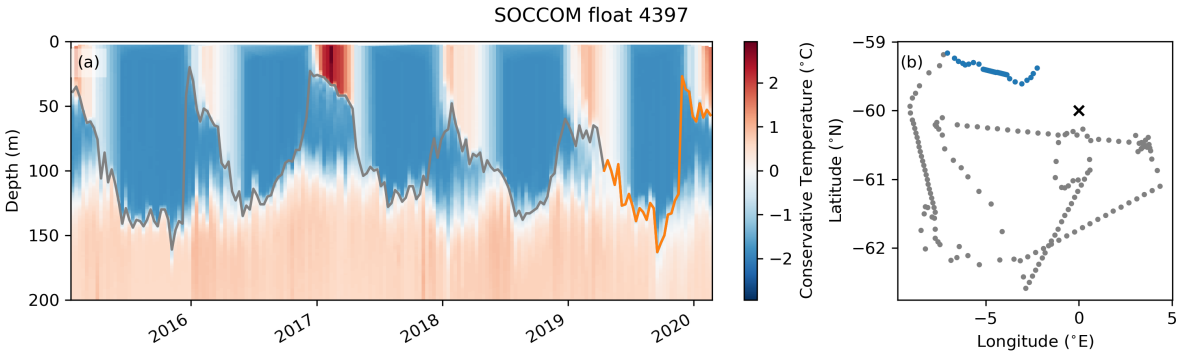

Figure 4.5: (a) Timeseries of Conservative Temperature measured by SOCCOM float 5094397 used in Paper III *to identify the base of the winter water layer. The mixed layer depth is overlain in grey, with the year 2019-2020 in orange. (b) the drift path of the SOCCOM float, with the final year in orange. The study site at 60°S, 0°E is marked.*

4.6 Satellite and Reanalysis Data

Surface heat fluxes, freshwater fluxes (Evaporation - Precipitation), 10 m winds and sea ice concentration are used together with glider data throughout this thesis. In *Paper II*, surface heat and freshwater fluxes and 10 m winds are used in particular for the calculation and interpretation of submesoscale parameterizations. In *Paper III*, these variables are used to interpret the variability of subsurface turbulent heat fluxes. For the calculation of friction velocity (u_*), we use the instantaneous turbulent surface stress product from ERA5, which has similar variability but slightly higher magnitudes than wind stress derived from 10 m winds. In *Paper I*, we show that this product is in good agreement with *in situ* winds observed by the Sailbuoy, providing confidence in the use of ERA5 winds, The shortwave component of the total heat flux is incorporated in the Winter Water temperature budget. Net heat fluxes are used to compute surface buoyancy that is used to interpret the relationship between observed and prediction dissipation as well as the mixing layer depth in *Paper III*. In *Paper IV*, surface heat fluxes and winds are used to interpret phytoplankton bloom phenology. Hourly (*Paper I,II,III*) and six-hourly (*Paper IV*) atmospheric reanalysis fields are obtained from the latest European Centre for Medium-Range Weather Forecasts (ECMWF) climate reanalysis product, ERA5, with a 0.25° x 0.25° resolution (*Hersbach et al.*, 2018).

Sea ice concentration and extent is used to contextualise the results in *Papers II and III*. In particular, sea ice concentration estimates over 20 years are used to investigate phytoplankton bloom phenology and sea ice concentration together with thickness is used to develop a metric for sea ice volume in *Paper IV*. Daily sea ice concentration products OSI-450 (1997-2015) (*OSI-450.*, 2017) and OSI-430-b (2016-2019) (*OSI-430-b*, 2019), distributed by EUMETSAT Ocean and Ice Satellite Application Facility (*Lavergne et al.*, 2019), with a spatial resolution of 25 km. Daily thin sea ice thickness, distributed by the University of Bremen, was extracted for the time period (2011-2020) at 40 km spatial resolution. The product is retrieved from observations of the L-band microwave sensor SMOS (Soil Moisture and Ocean Salinity) (*Huntemann et al.*, 2014). The maximum and minimum sea ice extents in 2019 and 2020 are taken from the Sea Ice Index data product, provided by the National Snow and Ice Data Center.

In *Paper IV*, Chl *a* was extracted at 8-daily resolution from the Ocean Color Climate Change Initiative (OC-CCI) v5.0 product, distributed by the European Space Agency (*Sathyendranath et al.*, 2019). MODIS 8-Daily Mean PAR was extracted from the 8-daily 4 km resolution product from 2002 to 2020. The daily product was used from 2019 to 2020 and

co-located with the glider positions and was in good agreement with glider observed integrated daily PAR.

Chapter 5

Submesoscale flows in the sea ice impacted Southern Ocean

Paper I: Submesoscale Fronts in the Antarctic Marginal Ice Zone and Their Response to Wind Forcing.

Paper I was published in *Geophysical Research Letters* in 2020, with coauthors Sebastiaan Swart, Marcel du Plessis, Andrew Thompson, Louise Biddle, Torsten Linders, Martin Mohrmann and Sarah-Anne Nicholson. This paper uses an autonomous surface vehicle coupled with a glider to observe submesoscale lateral gradients in the sea ice impacted Southern Ocean during austral summer. Special thanks for Martin Mohrmann who deployed the platforms and to the Caltech group under Andy Thompson who piloted SG643.

Paper II: Stirring of Sea-ice Meltwater Enhances Submesoscale Fronts in the Southern Ocean

Paper II was published in the *Journal of Geophysical Research: Oceans* in 2021, with coauthors Sebastiaan Swart, Marcel du Plessis, Andrew Thompson and Sarah-Anne Nicholson. I thank Dhruv Balwada and an anonymous reviewer for their valuable input on the development of this manuscript. This paper combines glider observations with atmospheric reanalysis data to investigate the influence of submesoscale flows on the upper ocean and its interaction with surface boundary layer forcing following the melt of sea ice.

In the following, I contextualise *Papers I and II* within the framework of the thesis and summarize the results. The reader is referred to the full papers in chapter 9.

5.1 Context

At high-latitudes, the first baroclinic Rossby Radius of deformation falls below 10 km (*Chelton et al.*, 1998). This is pertinent to the work that follows as it is a key motivation for observing upper ocean variability with autonomous surface and underwater vehicles. Autonomous surface and underwater vehicles (as introduced in chapter 4.2), sample the ocean at 0.1-4 km horizontal scales, therefore enabling one to resolve the scales at which flows become ageostrophic. Prior to this body of work, evidence for submesoscale flows (refer to the definition in chapter

2.3) within sea ice impacted oceans was demonstrated in the Arctic through theoretical work and numerical simulations (*Horvat et al.*, 2016; *Manucharyan and Thompson*, 2017), as well as in observations (*Brenner et al.*, 2020; *Koenig et al.*, 2020; *Timmermans and Winsor*, 2013; *von Appen et al.*, 2018). In the Southern Ocean, a statistical analysis of seal-tag CTD data (Marine Mammals Exploring the Oceans Pole to Pole, MEOP, *Biddle and Swart*, 2020) indicated submesoscale flows persist through all seasons and within sea ice covered regions. In *Paper I* we show, using high-resolution (horizontal scales of 10-100 m) surface observations, that submesoscale fronts were prevalent in summer (when the Rossby Radius was estimated to be $\sim$2 km) following sea ice melt, suggesting that sea ice melt water fronts can energize submesoscale instabilities. In *Paper II*, we used three months of glider observations to quantify the impact and seasonal evolution of these observed mixed layer submesoscale fronts on upper ocean stability and their potential to mediate vertical fluxes of water properties.

5.2 Summary of the results

Within this work, we address the **first objective of the thesis that considers the impact of submesoscale flows in the seasonal ice zone of the Southern Ocean**. Observations of the upper ocean were undertaken in summer thus, the findings are specific to ice-free stabilizing buoyancy forcing conditions. We observe fine scale lateral gradients (fronts) in the surface mixed layer. Haline fronts exceeding 0.5 g kg^{-1} km^{-1} were observed with a Sailbuoy sampling the ocean at a horizontal resolution of 100-300 m (*Paper I*). Similarly, haline fronts of 0.02 g kg^{-1} km^{-1} were observed within the mixed layer with a glider (sampling at a horizontal resolution of 0.5-4 km) (*Paper II*). These fronts are suggested to be formed by strain resulting from stirring mesoscale sea ice melt fronts. When the larger scale mesoscale gradient in salinity decreases later in the summer season, the submesoscale fronts are also observed to weaken (*Paper II*, Figure 6). The difference in magnitudes of the observed fronts is attributed to the higher sampling resolution of the Sailbuoy compared to the glider, and due to the reduction in lateral gradients with depth (shown in *Paper I*, Figure 4).

In *Paper I* the fronts are observed to respond to wind forcing, with strong winds ($\geq$0.3 N m^{-2}) dispersing lateral gradients. Here we proposed that thermohaline shear dispersion following frontal slumping due to baroclinic instabilities weakened lateral gradients. A tracer dye experiment in the Gulf Stream tracked the dispersion of fronts by winds (*Wenegrat et al.*, 2020), providing a direct observation of this process. The analysis of Ekman Buoyancy Fluxes in *Paper II* further supports the finding that there is a strong response of the upper ocean and lateral density gradients to mechanical forcing by winds in this region. The potential for submesoscale baroclinic instabilities to grow is assessed by estimating the equivalent heat flux (buoyancy input by slumping submesoscale fronts) by Mixed Layer Eddies following (*Fox-Kemper et al.*, 2008). We find a weak contribution by Mixed Layer Eddies (Q_{MLE} = 5 - 20 W m^{-2}). Q_{MLE} is weak as a result of the strong stratification by sea ice melt that maintains shallow mixed layers. As such, while submesoscale fronts are formed by stirring of mesoscale sea ice meltwater fronts, submesoscale vertical fluxes are limited to within the mixed layer. Nevertheless, surface enhanced fronts increase the potential for Ekman-driven cross-frontal flow to modulate the stability of the mixed layer and mixed layer properties (with estimates of Ekman Buoyancy Fluxes varying between 100-1000 W m^{-2}).

Wavenumber spectra are used to describe the horizontal density variance in the mixed layer and analyze the seasonal timescale of active scales of energy variance. The average slope of

the spectra computed from the glider measurements (5 m depth, horizontal resolution of 0.5-4 km) ranges from k=2.1-3.6, and from the Sailbuoy measurements the mean slope is k=-2.4, (0.5 m, horizontal resolution of 100-300 m). The approximated slopes are steeper than surface quasi-geostrophic theory but not as steep as that predicted by interior quasi-geostrophic turbulence theory. Acknowledging the uncertainties involved with these calculations, the results suggest that the surface ocean variance in horizontal density is driven by submesoscale dynamics (with shallower slopes representing energy at small scales). If we assume density spectra as a proxy for Potential Energy, we find that the total Potential Energy in the system decreases towards late summer, indicating that the sea ice meltwater, which is exhausted later in summer, may be related to the change in Potential Energy. The density spectral slopes steepen later in the summer season, in accordance with the idea that there is a decrease in the source of mesoscale stirring by sea ice meltwater. However, we acknowledge that the change in slope may be attributed to noise and errors associated with applying spectral analysis to measurements that are not uniformly spaced. Part could also be attributed to sampling resolution. Furthermore, the scales of submesoscale flows might be expected to decrease during late summer as the ocean becomes more stratified, thus requiring even higher resolution observations.

Finally, a major result of *Paper II* is that the strong stratification, also most likely a result of recently melted *in situ* and advected sea ice, reduces the Potential Energy available for submesoscale associated vertical fluxes. This suggests that the subduction of modified waters by sea ice does not occur in the location of sea ice melt. Subduction 'hotspots' in the Southern Ocean have since been observed further north near the Antarctic Polar Front in regions of higher eddy kinetic energy (*Dove et al.*, 2021). However, we found that entrainment events contribute to substantial heat loss in the mixed layer during summer (*du Plessis et al.*, 2022). The role of diapycnal mixing in driving the vertical exchange of water properties in the sea ice impacted Southern Ocean is addressed in the *Paper III*.

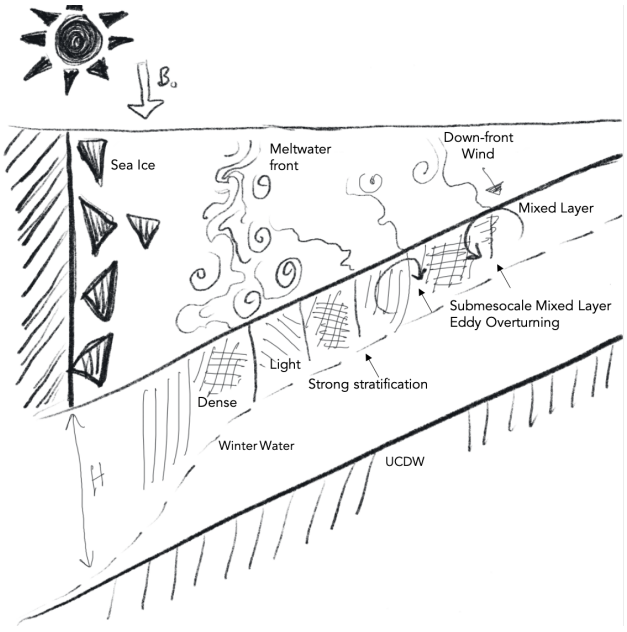

Figure 5.1: Sketch of meltwater dispersion by submesoscale mixed layer eddies and wind-front interactions under positive buoyancy forcing, highlighting the vertical structure of the water column following ice melt.

Through this work, we propose a mechanism through which sea-ice meltwater is dispersed during austral summer (Illustrated in the schematic below). Low density meltwater is introduced into the upper ocean following sea ice melt. This process rapidly restratifies the mixed layer. We observe however, that the meltwater is not uniformly distributed, but rather observed as a series of meltwater fronts and eddies ranging in horizontal scales, but limited by the strong

meltwater induced vertical stratification to the vertical scale of the mixed layer. We observe the frequency and intensity of these fronts to weaken with distance and time from the sea-ice melt region (Paper II) and propose that submesoscale mixed layer eddies and their interaction with winds are acting to stir and disperse the meltwater northwards. These findings imply that the water that is transformed by mixing with the cold and fresh meltwater is not subducted in the same region that it is transformed.

Large uncertainty remains in the projections by Global Climate Models (GCMs) of the Southern Ocean and its role in the global overturning circulation (*Fox-Kemper et al.*, 2021). Small-scale processes can have a substantial impact on high-impact low likelihood events that are characteristic of regions in the Southern Ocean (*Hewitt et al.*, 2022) and thus essential to capture for better climate predictions. But, explicitly resolving these processes will remain challenging for decades to come (*Fox-Kemper et al.*, 2019). One avenue has been to parameterize these processes and an earlier assessment of GCMs showed that GCMs that parameterize submesoscale eddies increases global mean SST by 0.1∘C (*Fox-Kemper et al.*, 2011). However, parameterizations are not designed to represent all processes and these features are not ubiquitously distributed in the ocean. For example, the submesoscale parameterization of *Fox-Kemper et al.* (2008) accounts only for the restratifying effects of mixed layer eddies - a feature we observed to be weak in the quiescent summer time ice edge that was the focus of this thesis. On the other hand, our results pointed to the role of wind-front interactions in introducing small-scale variability to the region and modulating turbulence - a parameterization that was only recently developed and remains to be widely tested and implemented (*Bodner et al.*, 2022).

Chapter 6

Diapycnal mixing across Antarctic Winter Water

Paper III: Vertical convergence of turbulent and double diffusive heat flux drives warming and erosion of Antarctic Winter Water in summer

This manuscript is currently being prepared for submission to the Journal of Physical Oceanography and was developed with the support of coauthors Ilker Fer, Sebastiaan Swart, and Sarah-Anne Nicholson. I thank Gerd Krahmann for the additional support in processing the Slocum glider data and Sea Technology Services for the assistance in deploying, piloting and retrieving the glider. In the following, the paper is contextualised and a summary of the results is presented. The reader is referred to the manuscript in Chapter 9 for a full discussion.

6.1 Context

After summertime sea ice melt, the mixed layer of the subpolar Southern Ocean largely experiences stabilizing buoyancy forces (freshwater input from meltwater, either from direct 1-dimensional melt or via advection, and incoming solar radiation; *Paper II*). The resulting enhanced stratification dampens submesoscale vertical fluxes and, in *Paper II*, we posit that the subduction of surface transformed waters does not necessarily occur in the same region as where sea ice melts. In that work, we did not consider the subsurface layer, referred to as "winter water" that is capped between the stratified mixed layer and the warm and saline Upper Circumpolar Deep Water (UCDW) beneath. However, in *Paper III*, we show that the winter water thins and warms over the summer season. This was similarly observed in *du Plessis et al.* (2022) where we note that entrainment of winter water cools the mixed layer. *Evans et al.* (2018a) show that mixing between the winter water layer and UCDW is an important step in the the transformation of the deep water mass, UCDW to intermediate water (Antarctic Intermediate Water, AAIW) that forms the upper branch of the Meridional Overturning Circulation. They suggest that this summer transformation occurs through the input of positive buoyancy (from meltwater and solar radiation). In *Paper III*, we use direct observations of the viscous dissipation rate of turbulent kinetic energy (TKE), hereafter "dissipation", to determine the mixing processes that mediate the exchange of properties between the surface, subsurface and ocean interior.

6.2 Summary of the results

In *Paper III*, we address the **second objective of this thesis that considers diapycnal mixing in the sea ice impacted Southern Ocean**. Using direct measurements of microstructure shear, we characterize the time-averaged levels of dissipation and diffusivity in the subpolar Southern Ocean following sea ice melt. We identify two regions of enhanced mixing: Firstly, in the surface mixing layer, of which 84% of the observed dissipation is explained by wind-driven turbulence. Secondly, at the base of the winter water layer, which we attribute to double diffusive convection (DDC). The enhanced dissipation in the subsurface is most likely a result of DDC given that the winter water is distinguished as colder, and fresher, than the underlying warmer, and saltier, UCDW. Such profiles are associated with Turner Angles (that provides a metric of the relative contribution of temperature and salinity to the local stability of the water column) between $-\pi/2$ and $-\pi/4$. In addition, we observe temperature staircases (*Kelley*, 1990) that occur as a result of DDC and a band of high spice variance (*Middleton et al.*, 2021). We emphasise that DDC is associated with higher rates of eddy diffusivity (turbulence-enhanced mixing) because, unlike mechanically-driven mixing where a portion of the energy is lost to raising the potential energy of the system, in DDC, all the energy is converted to a buoyancy flux. The observed background mixing is attributed to shear-driven turbulence resulting from the steepening of isopycnals by internal waves.

In *du Plessis et al.* (2022), we assessed the mixed layer temperature budget in the Weddell Sea within the broader context of the Southern Ocean, concluding, in agreement with *Paper II*, that variability within the mixed layer cannot be solely explained by 1-dimensional processes alone. In *Paper III*, we developed a subsurface winter water temperature-tendency budget to determine the contribution of mixing processes to the observed warming and thinning of the layer, considering only 1-dimensional processes in the subsurface winter water layer. We find that the observed temperature is well represented by three components: solar radiation, diapycnal mixing and entrainment. The winter water warming trend is explained by the vertical convergence of turbulent and double-diffusive heat fluxes. Notably, 22% of this winter water warming is due to DDC and excluding the enhanced eddy diffusivity compared to that approximated when mechanically-driven turbulent mixing is assumed would underestimate the warming of the winter water layer and therefore water mass transformation in this region.

Chapter 7

Sea ice impact on primary production and carbon export

Paper IV: Sea ice impacts inter-annual variability in phytoplankton phenology and carbon export in the Weddell Sea

Paper IV is currently under review for publication in *Geophysical Research Letters*, with coauthors Sebastiaan Swart, Bastien Queste, Sandy Thomalla and Sarah-Anne Nicholson. I thank especially Louise Biddle as well as Hannah Rosenthal and Johan Edholm who were all on the polar gliders SCALE team onboard the *RV SA Agulhas II*, when together we deployed SG640, the data from which is used in *Paper IV*. I also thank an anonymous reviewer for their valuable input. Here, I introduce and contextualise the paper, expand on some of the methods applied and summarize the results. I refer the reader to the full paper in Chapter 9.

7.1 Context

In the first three papers of this thesis, we focused on the role of sea ice on mediating observed variability in upper ocean turbulence. Here, we shift focus to the role of sea ice in modulating primary production and carbon export through its impact on upper ocean turbulence.

Phytoplankton form the base of the Southern Ocean biological carbon pump. The carbon produced by primary production is either transferred to higher trophic levels, which sustain the foodweb, or directly fluxed to the deep ocean. Carbon may also enter the deep ocean later in the trophic cascade. Biological carbon export in the subpolar gyres, and especially the Weddell Gyre, substantially contributes to the carbon cycle via lateral transport in the Upper Circumpolar Deep Water (*Hoppema*, 2004; *MacGilchrist et al.*, 2019).

While primary production in the Southern Ocean is on average increasing, the response of phytoplankton in the sea ice impacted Southern Ocean is not certain (*Deppeler and Davidson*, 2017). Phytoplankton biomass (chlorophyll *a*) in the seasonally ice-covered Southern Ocean has, until recently, been largely undersampled because satellite observations are impeded by sea ice and cloud cover (*Thomalla et al.*, 2011). Under ice, Biogeochemical Argo floats have allowed for annual observations of chlorophyll *a* (*Arteaga et al.*, 2020) at $\sim$10-day resolution. However, high resolution, seasonal studies remain sparse. It is known that primary production and carbon export flux are not necessarily proportionally related to each other and display high regionality (*Henson et al.*, 2019), with external interacting factors influencing them both

(*Henson et al.*, 2022; *Pinkerton et al.*, 2021). With this work, we simultaneously analyse the variability in primary production and carbon export at sub-daily resolution in order to observe the link between the two and understand how they respond to sea ice and sea ice-induced turbulence.

7.2 Methods

Paper IV applies glider measurements of both physical (temperature and salinity) and biological (chlorophyll *a* and optical backscatter) variables to simultaneously quantify primary production, carbon export, and water column density at scales of hours to days. These metrics, along with Biogeochemical Argo and satellite observations, were used to reveal the response of phytoplankton to ocean processes associated with sea ice growth and melt. One of the main analyses in *Paper IV* assesses the differences in carbon export and transfer efficiencies between two years of glider observations. Carbon export is defined as the ratio between primary production at the surface and carbon flux at the base of the mixed layer. Transfer efficiency is defined as the ratio of carbon flux at the base of the mixed layer to carbon flux at a deeper depth, which we take as the average depth of the deepest winter mixed layer. In this section, I expand on the methods and uncertainties in estimating carbon export and transfer efficiency. It is well known that there is regional variability in the export and transfer efficiency (*Henson et al.*, 2019), however, temporal variability and long term trends are less certain (*Henson et al.*, 2022). With this analysis, we look at the processes which may cause biological carbon export flux to change.

In the absence of *in situ* incubation experiments, primary production is necessarily modelled. The modeling of primary production has been spear-headed by the satellite optics community (*Behrenfeld et al.*, 2005; *Platt and Sathyendranath*, 1993), but the models have been adapted for underwater profiling floats and gliders (e.g. *Arteaga*, 2021; *Hemsley et al.*, 2015). There are two main approaches to estimating primary production. The first is based on chlorophyll *a*, with growth rate estimated as a function of chl *a* and irradiance, the Platt Model (*Platt and Sathyendranath*, 1993), and the Vertically Generalized Production Model, (VGPM; *Behrenfeld and Falkowski*, 1997). VGPM assumes nitrogen limited primary production, which may not hold in the Southern Ocean. The second approach to modeling primary production is a carbon-based approach that makes predictions on phytoplankton growth rate based on the ratio of chlorophyll *a* to carbon, of which there are two variations: the standard CbPM, (*Behrenfeld et al.*, 2005) and the spectrally-resolved CbPM, (*Westberry et al.*, 2008). The long-term trends in Primary Production observed by satellites result in an increasing trend if VGPM is applied and a decreasing trend if CbPM is applied *Pinkerton et al.* (2021). Here, we compare these models using glider observations (*Paper IV*, Figure S9) and find them, at least for the period of observation, to co-vary even though the magnitudes are different (with VGPM and Platt estimates lower than that of CbPM). Estimates of vertically integrated CbPM, based on glider observations, are slightly higher in magnitude, but comparable to the surface only estimates. This implies that assumptions of vertically homogeneous phytoplankton distribution, at least for our period of observation and this region, are reasonable. Estimates of primary production from the above models when blooms are dominated by deep chlorophyll maxima (*Baldry et al.*, 2020), possibly later in the season under nutrient limiting conditions, may not be as comparable to vertically-resolved glider based estimates.

Similarly, there are several ways by which downward fluxes of carbon can be estimated.

These are either made as direct measurements from sediment traps (*Lampitt et al.*, 2008) or via indirect estimates. For the latter, there are multiple methods: nutrient uptake (*Moreau et al.*, 2020; *Sanders et al.*, 2005), oxygen utilization (*Jenkins*, 1982; *Kheireddine et al.*, 2020), radioisotopes (*Buesseler*, 1998; *Le Moigne et al.*, 2013), quantifying spikes in optical backscatter profiles (*Briggs et al.*, 2011). Indirect estimate methods were used in this analysis. The range of export flux to 100 m based on the *Briggs et al.* (2011) method that we applied in *Paper IV* was comparable to previous estimates in the same region (*Moreau et al.*, 2020; *van der Loeff et al.*, 2011).

All the above indirect methods of estimating primary production and carbon export contain a degree of uncertainty. Taking this into account, we emphasize the relative differences in primary production and carbon export between the two years in comparison rather than their absolute values.

7.3 Summary of the results

With *Paper IV*, we address the **third objective of this thesis that sets out to assess the impact of sea ice on primary production and carbon export in the Weddell Sea**. We find empirical evidence using 10 years of satellite observations together with Biochemical Argo floats that shows that in parts of the sea ice impacted Southern Ocean (e.g. Weddell Sea, Ross Sea), enhanced winter growth of sea ice drives deeper winter mixing and, therefore, increased vertical fluxes of limiting nutrients which support larger magnitude blooms in the following summer. The two sequential summer seasons of glider data provide preliminary evidence that more intense blooms (higher amplitude) lead to higher carbon export, suggesting a potential positive impact of sea ice volume on the biological carbon pump. However, higher export below 100 m was attenuated more quickly with depth and did not translate to substantially higher export past 170 m, the depth of deepest winter mixing. This suggests that more intense blooms and carbon export events may not lead to enhanced long-term carbon storage. It should be acknowledged that we interpret changes in primary production based on one changing variable: sea ice volume/winter mixed layer depth. However, phytoplankton respond to many interacting factors (e.g. nutrients and trace metal variability, irradiance, grazing and their interactions). But without an *in situ* process-study measuring multiple variables or a model that resolves them, it remains challenging to elucidate the exact driver(s) of the variability observed.

We consider three explanations for the decrease in carbon export with depth. Large cells (notably diatoms with additional ballast; *Tréguer et al.*, 2018), would be expected to sink faster, escaping microbial degradation and hence drive a higher transfer efficiency and lower attenuation rate. Although we did not directly measure community composition, chl a:C_{phyto} ratios have been used to infer changes in community composition, with a higher chl a:C_{phyto} typically indicating a larger proportion of diatoms (*Cetini et al.*, 2015). As such, there were likely more diatoms in the community during the 2019-20 summer season (when high chl a was observed) than during the 2018-19 summer season (when low chl a was observed). Alternatively, the higher chl a:C_{phyto} may also represent a higher ratio of fresh, labile phytoplankton in 2019-20 compared to "older", more refractory particulate matter, in 2018-19. Refractory particulate matter does not remineralize as fast as fresher cells and could explain the observed higher transfer efficiency compared to the following year (*Cavan et al.*, 2018). Changes in density with depth can also influence the sinking rate of particles and therefore the flux attenuation rates. The strongly stratified thermocline that was observed during the 2019-20 summer

season might have retained particles within the thermocline, exposing the sinking particulate matter to a longer period of remineralization in the upper ocean, and thus reducing export to depth. Finally, remineralization rates and flux attenuation may be influenced by bacterial load and grazing (e.g. *Cavan et al.*, 2015). Thus, the faster remineralization rates observed in 2019-20 could be a result of higher grazing pressure within the upper 200 m. In conclusion, an outstanding finding is that the export of carbon cannot be directly explained by physics alone, however more observations are required to confirm the results of this investigation.

Chapter 8

Conclusions and Perspectives

8.1 Summary

Sea ice formation and melt in the Southern Ocean accounts for one of the largest phenomena of surface transformation on the planet. Changing, within an annual cycle, from an area of $\sim$19 million km^2 of sea ice covered ocean in the winter months to one of $\sim$3 million km^2 during the summer months (*Parkinson*, 2019). At the northern extent of the sea ice, warm carbon-rich circumpolar deep water upwells (Figure 2.1), such that processes controlling the transformation of water at the surface in the subpolar Southern Ocean have a disproportionate control on the climate system. It has been shown in model and observational data, that sea ice melt exerts a primary control on the transformation of deep water to intermediate water (*Abernathey et al.*, 2016; *Pellichero et al.*, 2018) and temperature trends in the surface and subsurface layers of the subpolar Southern Ocean (*Haumann et al.*, 2020). However, the scarcity of observations has limited the understanding, in particular, of small-scale processes in modulating upper ocean properties and therefore the exchange of climate important variables: heat and carbon. This background broadly forms the motivation for this thesis.

We have illustrated, through high-resolution observations in the subpolar Southern Ocean, the profound role of sea ice in modulating turbulent processes occurring at scales of kilometers to centimeters. These processes, in turn, mediate the upper ocean physical, chemical and biological properties with local and remote implications.

Directly following the austral-summer melt of sea ice, very cold waters together with large freshwater fluxes set the density characteristics of the upper ocean. Within this seascape, we observe lateral gradients over 0.1-10 km in the surface mixed layer, (*Paper I*), that are likely representative of a mixture of submesoscale Mixed Layer Eddies and filaments as well as fronts formed through stirring mesoscale eddies (*Paper II*). The scale and frequency of these features decreases towards the end of the summer season as does the salinity control on mixed layer density. Incoming solar radiation that warms the upper ocean, together with the stirring of sea ice melt water and the increasing stratification, limits the Potential Energy available for mixed layer instabilities (*Paper II*). But the shallow mixed layer means that upper ocean responds readily to wind forcing. Prevailing winds drive vertical mixing (*Paper III*) and wind-front interactions introduce variability to the stability of the mixed layer (*Paper I, II*). While the mixed layer was characterised by lateral heterogeneity in temperature and salinity, the temperature variability in the underlying winter water was largely explained by 1-dimensional vertical processes alone (*Paper III*). Mixing at the base of the mixed layer is attributed to wind-driven

shear production of turbulence, but is again limited by buoyancy effects that are likely introduced by recent sea ice melt. At the base of the winter water, enhanced turbulent mixing is attributed to double-diffusive convection. The rate of mixing at the base of the mixed layer and the base of the winter water contribute to the rate of heat flux convergence into the subsurface winter water layer, its erosion and thus enabling a pathway for exchange of water properties between the ocean interior and the surface and their associated transformation.

Superimposed onto the dynamical flows of the upper ocean in this region, communities of phytoplankton and the ecosystems that they support are actively responding to changes in the environment. On climate relevant scales, they provide a biological medium through which carbon is transferred from the surface to the ocean interior (via the biological carbon pump). In *Paper IV*, we find empirical evidence, using 10 years of satellite observations together with BGC-Argo floats, that increased sea ice formation in winter drives deeper vertical mixing resulting in the entrainment of limiting nutrients and minerals. This translates to enhanced primary production the following summer season in the northeast Weddell Sea.

von Berg et al. (2020) similarly show that enhanced mineral supply from Maud Rise supports greater bloom amplitudes, however, anomalous deep mixing during a polyna event did not substantially enhance the subsequent bloom. The largest observed bloom occurred during an anomalously shallow spring mixed layer that deepened during the summer suggesting that light and summer iron supply are also important in this region. These findings concur with that of *Ardyna et al.* (2017), where light is identified as a major driver of bloom phenology. Deeper mixing (up to 150 m) during winter is observed to increase the subsequent bloom likely through enhancing iron supply. However deeper mixing also results in deeper summer mixed layers, introducing further light limitation and reducing bloom magnitudes. As such, in regions where winter mixing is the primary limit on available trace minerals for photosynthesis, primary production may be enhanced following deeper winter mixing up to a threshold. The possibility of such a mechanism was observed over two years of glider observations

Using two years of glider observations of two contrasting seasonal cycles of primary production show that higher surface primary production leads to higher short term carbon export beneath the mixed layer. However, higher short term export does not necessarily imply higher long term export. We find that the efficiency of carbon transfer to depths deeper than the average winter mixed layer maximum in the year of higher primary production is lower compared to the year that experienced lower rates of primary production. The reasons for this fall into two broad categories that require further research. The first is a physics perspective explanation and the second is a biology perspective explanation. Firstly, greater sea ice formation and thus, deeper winter mixing, increased nutrients in the surface waters and stronger bloom, could also lead to higher stratification during the summer, increasing the retention time of particles in the upper ocean and therefore the attenuation rate with depth. Secondly, differing community compositions associated with the different base conditions of the two blooms observed may result in different remineralization rates.

8.2 Implications

Prior to this work, most observational and modelling studies of upper ocean turbulence in seasonal sea ice zones have been focused in the Arctic Ocean (*Appen et al.*, 2018; *Brenner et al.*, 2020; *Scheifele et al.*, 2021; *Timmermans and Jayne*, 2016; *Timmermans and Winsor*, 2013; *Timmermans et al.*, 2012). While the Arctic Ocean shares some similarities with the Southern

Ocean (sea ice presence and high seasonality), the Southern Ocean sea ice zone, in which the sea ice is relatively thin ($\sim$0.5 m) and multi-year ice is uncommon, is unique in its circumpolar extent and the persistent and strong winds maintain a relatively weakly stratified upper ocean. We observed slightly weaker lateral fronts (*Timmermans and Winsor*, 2013) and stronger turbulence (*Scheifele et al.*, 2021) than that observed in Arctic ice-free conditions. While the evidence suggests that submesoscale flows are not driving vertical exchange of water properties in the summertime, the associated eddies are indeed responsible for a lateral component in the mixed layer temperature and salinity budgets, such that the mixed layer budget cannot be predicted by 1-dimensional processes alone (*du Plessis et al.*, 2022). The observation of variable Ekman-driven cross frontal flow has the potential to modulate the stability of the mixed layer. The inclusion of submesoscale flows is therefore a necessary parameterization in coupled-climate models to accurately represent mixed layer heat and freshwater transport.

Turbulent dissipation in the sea ice impacted Southern Ocean is often assumed constant in mixed layer budget studies or not included at all (*du Plessis et al.*, 2022; *Pellichero et al.*, 2017). To a large extent, this assumption is due to the unavailability of direct observations. However, the results of *Paper III* present the first observations of turbulent dissipation in the sea ice impacted Weddell Sea of the Southern Ocean. The observations confirm the sensitivity of the mixed layer to wind forcing that was observed in *Papers I and II*. In *du Plessis et al.* (2022), we highlight that in the sea ice impacted Southern Ocean, vertical entrainment of winter water can cool the mixed layer sufficiently to offset winter entrainment of heat from the underlying Upper Circumpolar Deep Water. The winter water temperature tendency analysis in *Paper III* shows that diapycnal mixing is a key term in driving the seasonal warming of this layer and therefore central to the transformation of UCDW to AAIW. The misrepresentation, therefore, of dissipation rates and turbulent-enhanced mixing (eddy diffusivity) has implications for the upper ocean heat budget and water mass transformation. Furthermore, these findings point to the potential for turbulent-enhanced mixing to increase under increased wind intensity (*Young and Ribal*, 2019). This could accelerate the demise of sea ice through enhanced subsurface warming and winter water erosion.

The transport of sea ice and its 1-dimensional impact on mixed layer buoyancy has been emphasised in the literature as an important regulator of water mass transformation in the high-latitude Southern Ocean (*Abernathey et al.*, 2016; *Pellichero et al.*, 2018). The overarching lines of evidence presented in *Papers I, II and III* point to a key role of sea ice linked submeso-microscale processes in setting upper ocean water properties, water mass transformation, and thereby, the global overturning circulation at the macroscale (*Hewitt et al.*, 2022). The findings of this work provide evidence of (sub)mesoscale processes (or subgrid-scale) in the sea-ice impacted Southern Ocean which will allow for improved interpretation of observed and modelled variability of the large scale response of the climate system through their likely impact on sea ice growth and decline, mixed layer depths, heat and freshwater fluxes and water mass transformation in this region - all which have previously shown to change when model resolution is changed (*Belcher et al.*, 2012; *Chassignet et al.*, 2020; *Fox-Kemper et al.*, 2021)

Quantifying the ocean's role in the natural and anthropogenic carbon cycle is integral to predicting the future response of the ocean to increasing levels of CO_2 and to informing policy (*Fox-Kemper et al.*, 2021). The first global climatology of air-sea CO_2 flux based on ship measurements was compiled by *Takahashi et al.* (1997), in which polar oceans, and in particular the Southern Ocean was highlighted as an important sink of CO_2. Since, the development of

machine learning techniques (*Gregor et al.*, 2018; *Landschützer et al.*, 2014) and the addition of SOCCOM floats (*Bushinsky et al.*, 2019; *Gray et al.*, 2018) has provided further nuance to these estimates. Nevertheless, Southern Ocean air-sea CO_2 fluxes remain uncertain - largely a result of sparse observations regionally and temporally over the winter months (*Buckingham et al.*, 2016). In addition, attributing drivers of the observed CO_2 fluxes continues as an area of active research. While the physical solubility pump is the primary mechanism by which carbon in cycled in the oceans, not accounting for biology (that sets the vertical gradient of CO_2 in the ocean), would increase CO_2 levels in the atmosphere two-fold (*Maier-Reimer et al.*, 1996).

Biological carbon export in the Weddell Sea has been shown to contribute disproportionately to the global carbon cycle (*Hoppema*, 2004; *MacGilchrist et al.*, 2019). In *Paper IV*, we show that deeper winter mixing supports higher amplitude blooms and high export flux in the Weddell Sea. We link deeper winter mixing with increased sea ice formation. Sea ice is likely to decrease in the future (*Roach et al.*, 2020), expanding the area available for primary production. Together with enhanced nutrient supply from low-latitudes (*Tagliabue et al.*, 2021), this would also lead to increased primary production. However, the trade-off between the stabilising effects of sea ice meltwater and the mixing effects of summer winds (*Fitch and Moore*, 2007) will require further inquiry. In concert, CMIP6 models further predict that export flux in the Southern Ocean will increase under future climate change (Shared Socioeconomic Pathways 5-8.5 *Henson et al.*, 2022). Observations already suggest that primary production is increasing in much of the Southern Ocean, although there is uncertainty in trends between primary production models (*Pinkerton et al.*, 2021). The uncertainty in model predictions stems from the complexity of processes that drive both primary production, carbon export flux and export efficiency. Notably, in *Paper IV*, we find that while increased primary production results in increased export flux beyond the mixed layer, it does not necessarily result in increased export flux beyond the deepest winter mixed layer. That is, we find contrasting signs between export efficiency and transfer efficiency. The available evidence suggests that the main difference between the two blooms is their community composition. This implies differences in particle size, with links to sinking speed, bacterial load, grazers and rates of remineralization. A number of other factors could also be at play that were not considered (e.g. fragmentation, zooplankton and fish vertical migration, particle stickiness). While this work does not provide conclusive process understanding to the biological carbon pump in the Weddell Sea, the results show that phytoplankton respond to sea ice-driven changes in nutrient and light availability, which has impacts on the transfer efficiency of carbon to depth and therefore carbon sequestration. Finally, the preceding chapters of this thesis focused on small-scale processes which are known to influence nutrient supply, phytoplankton community composition, and export in the world's oceans (*Lévy et al.*, 2018; *Mahadevan*, 2016). These questions were not addressed in this thesis, but are put forward as a future avenue to research that can build on the larger scale view that was provided by this work. The analyses we put forward suggests enhanced bloom magnitudes following deeper winter mixing in some regions of the sea-ice impacted Southern Ocean. We did not consider the net impact on the carbon cycle of this proposed mechanism, and whether enhancing primary production via deeper winter mixing outweighs the simultaneous enhancement of carbon outgassing by the self-same process (the underlying UCDW is rich in iron and carbon) is another important consideration (*de Boer et al.*, 2010; *Toggweiler et al.*, 2006).

8.3 Limitations and future directions

The limitations of various aspects of this work pave the way forward for future work. In the following section, we suggest avenues of research that build upon the findings of this thesis. An overall limitation is the need to simultaneously observe small and large scale processes. An understanding of the mesoscale fields in which the gliders are sampling would provide insight into the scales of interacting processes. These details could be provided by, for example, the upcoming Surface Water and Ocean Topography (SWOT) mission, which will observe changes in sea surface height at high resolution ($\sim$4 km). It would be interesting to link satellite observations to the turbulent processes that we observe with gliders, expanding the reach of these types of analyses.

Spectral Analysis methods on moving platforms

The application of spectral analysis methods in order to assess and analyze the nature and variability of geophysical fluid flow is widely in use (as discussed in section 3.3, *Paper II*). In particular, a number of studies have used horizontal spectra to approximate the presence of submesoscale flows (e.g. *Callies and Ferrari*, 2013; *Jaeger et al.*, 2020; *Timmermans and Winsor*, 2013). In *Papers I and II*, we similarly compute the spectra of the horizontal density. We do this for each transect completed by the Sailbuoy and gliders to compare the observed spectra to theoretical spectra of interior and surface quasi-geostrophic and ageostrophic turbulence (*Blumen*, 1978; *Boyd*, 1992; *Capet et al.*, 2008; *Charney*, 1971). The most robust result was the seasonal reduction in Potential Energy (represented by the integral of the density variance spectra). This was supported by the glider mesoscale transects that showed a decrease in mesoscale gradients later in the summer. The analysis of the slope of the density spectra retains some uncertainty, even though we found a degree of agreement with the predicted slopes (with k ranging between -2 and -4). Spectral methods have three challenges: 1) aliasing due to discrete sampling intervals, 2) spectral blurring, due to the truncation of a continuous process to a finite duration, and 3) variance, due to stochastic variability. I will address each in turn with reference to the glider observations.

Aliasing The internal Rossby radius of deformation, L_r, during the observational period ranged from $\sim$0.5-3 km, depending on the vertical stratification. Submesoscale flows can develop only at scales below L_r. To fully resolve submesoscale flows, it would be required to measure with a horizontal frequency of half the L_r. The glider, however, has a horizontal sampling resolution that ranged from 0.3-4 km, which we interpolated to a uniform grid of 1 km. Hence, it is likely that the effects of aliasing, which introduces increased potential energy that is not physical, contaminate the data. This could be improved by increasing the horizontal resolution of sampling, but would mean that the glider would be limited to dive to shallower depths and thus increasing its power consumption.

Spectral Blurring Spectral blurring occurs as an outcome of sub-sampling a continuous process in the time-domain. This blurring smooths the physical process by a box-car window resulting in a convolution in the frequency domain which introduces broadband bias (error) at low wavenumbers (high frequencies). These effects cannot be avoided but can be reduced by multiplying the data set with optimised tapering windows (the most common being the Hanning window). A result of tapering is the loss of information at the edges of the time series, thereby increasing variance. Therefore, a short timeseries (with a low number of samples, N) will have larger variance than longer timeseries.

Variance Variance occurs as a result of stochastic variability under the assumption of sta-

tionarity. There are two approaches to dealing with variance. The first is to average over multiple orthogonal tapers (referred to as the multi-taper method). The second, is to have multiple samples of the same process (repeat transects). However, by reducing variance, the data is smoothed which increased spectral blurring. The trade-offs between the two approaches need to be balanced. Variance could be reduced in Figure 3b of *Paper I* by averaging over the individual Sailbuoy transects. In *Paper II*, we applied multitaper windows and averaged over the shorter $\sim$20 km transects (*Paper II*, Figure 8). These shorter transects were associated with steeper spectral slopes than the mesoscale transects and theoretical predictions. On reflection, it is likely that the observed variance was artificially reduced through tapering and averaging over timeseries with a low number of samples, resulting in steeper than expected slopes.

In addition to these well known challenges of spectral analysis, we necessarily assume that spatial scales are evolving slower than temporal scales and thus interpret the data as a timeseries (assuming a "frozen field"). This is complicated when considering a moving platform that samples in both space and time at non-equal sampling intervals. The more consistent and surface-only sampling of the Sailbuoy has a lower probability of propagating sampling bias, but nevertheless it is not certain what information is lost on either the Sailbuoy or gliders by this assumption. This could be tested using a model that reproduces the same environment that the autonomous vehicle is sampling in. A model analysis would also inform the optimum sampling intervals required to resolve the submesoscale ocean in this region. A mooring could further provide a valuable comparison in a Eulerian field.

The role of mixing in Southern Ocean warming

The Southern Ocean is warming (*Auger et al.*, 2021). The results of this thesis show that in the sea ice impacted Southern Ocean, strong stratification limits the exchange of heat between the interior and surface ocean at submesoscales (*Paper II*), while wind-driven shear production of turbulence can transport heat from the surface to subsurface in the summertime (*Paper III*). These results contribute to the growing understanding of the drivers of surface boundary layer turbulence in the Southern Ocean, emphasising the latitudinal variation in dominant processes, also highlighted in the recent regional mixed layer budget analysis by *du Plessis et al.* (2022). Because of uncertainties in mixing estimates at the base of the mixed layer, *du Plessis et al.* (2022) neglected the vertical mixing term in their analysis. *Sallée et al.* (2021) use 20 years of observational evidence to show that stratification is increasing in the summertime globally, while simultaneously mixed layers are deepening. They attribute this to increased wind-driven shear production of turbulence, but do not have estimates of mixing to support the postulation. In *Paper III*, I posit that surface-boundary layer turbulence is driven by winds by applying the Law of the Wall surface scaling. To a good approximation, our assumption holds. In addition, the role of Langmuir turbulence in driving boundary-layer turbulence is known to be important in the Southern Ocean in all seasons and especially in the summertime (*Belcher et al.*, 2012; *Li et al.*, 2019). In our results we find an offset between predicted dissipation and measured dissipation. An offset is also identified in independent estimates of dissipation near the Antarctic Polar Front by *Nicholson et al.* (2022). Given the likely important, and increasingly so, role of winds and waves in driving upper ocean mixing (*Young and Ribal*, 2019), these findings warrant a re-evaluation of the surface ocean boundary layer, scaling with a Southern Ocean focus, especially since most of the observations have been made under destabilizing buoyancy conditions and in the Northern Hemisphere (*Esters et al.*, 2018; *Li et al.*, 2019).

In *Paper III*, we approximate heat flux from observed dissipation rates using the *Osborn* (1980) model. In this model, we approximate the mixing efficiency coefficient, Γ, for

mechanically-driven turbulence depending on the rate of dissipation and level of stratification as in (*Bouffard and Boegman*, 2013). However, the mixing efficiency varies depending on the turbulent regime within the mixed boundary layer. In order to improve the estimates of heat flux across this layer, which may be more important for water mass transformation than previously understood (e.g. *Abernathey et al.*, 2016, does not include this as an important factor in water mass transformation), an avenue of future research lies in the use of Large Eddy Simulations to directly determine the mixing efficiency under varying forcing and when submesoscale front-wind interactions are active (e.g. *Whitt and Taylor*, 2017; *Whitt et al.*, 2019). One recent analysis by *Chor et al.* (2022) based on LES shows a range of mixing efficiencies between 0.05 and 0.3, significantly departing from the canonical $\Gamma = 0.17$ *Gregg et al.* (2018).

An important result of *Paper III* was the identification of a region preconditioned for strong double diffusive convection (DDC) at the base of the winter water layer. In the case of double diffusion, mixing efficiency is close to 1 (*St. Laurent and Schmitt*, 1999), therefore increasing the rate of eddy diffusivity. Through analysis of the winter water temperature budget, we found a substantial contribution to up-gradient vertical heat flux via double diffusion. However, global estimates of diffusivity in the stratified ocean do not take this process into account (mixing efficiency is largely taken to be 0.2, under the assumption of shear-driven stratified turbulence). While *van der Boog et al.* (2021) make an argument for its irrelevance to the global energy budget, their study is based on course-resolution quantification of thermohaline staircases, which is sure to underestimate the prevalence of DDC. Quantifying the contribution of DDC to ocean mixing in the changing subpolar Southern Ocean via new methods (e.g. *Middleton et al.*, 2021) and the incorporation of DDC to mixing parameterizations in ocean models seems imperative.

In the Southern Ocean, including the sea ice impacted Southern Ocean, wind-driven upper ocean mixing is important for the distribution of heat between the ocean interior and surface, as suggested by the results of *Papers II and III*. However, in both these works, our conclusions are based on only one season of observations. Recent developments in dissipation parameterizations allow for the estimation of dissipation from high resolution glider observations of temperature and salinity (*Evans et al.*, 2018b; *Middleton et al.*, 2021). With the growing archive of glider observations in the Southern Ocean, applying these methods to gliders will allow for a statistical and regional analysis of the contribution of winds to heat fluxes and thus the sensitivity of Southern Ocean heat distribution to changes in wind forcing.

Double Diffusive Convection

In their recent global analysis of thermohaline staircases, *van der Boog et al.* (2021), conclude that DDC has a negligible contribution to global energetics. In *Paper III*, we find that DDC is likely an important driver of subsurface heat flux into the winter water, contributing to its seasonal warming. Winter water is a circumpolar feature in the subpolar Southern Ocean and therefore DDC is expected to be spatially widespread. *Evans et al.* (2018a) show that winter water acts as a conduit for the transformation of Upper Circumpolar Deep Water to Antarctic Intermediate Water and therefore in controlling the upper limb of the Meridional Overturning Circulation (MOC). Given that DDC is an important process in setting the properties of winter water, which directly feeds into AAIW and the upper MOC, DDC is likely more important than currently understood. In *Paper III*, we demonstrate the contribution of DDC heat fluxes in one case study. This contribution could be better constrained if a similar analysis is applied to more sample locations, or perhaps to the Southern Ocean Argo array. Adapting the method proposed by (*Middleton et al.*, 2021) for use with gliders and in regions that are sensitive to the non-

linearities of the equation of state, could provide further insights to the contribution of DDC to dissipation rates in the subpolar Southern Ocean. Analyses of water mass transformation rate with DCC, and without DDC, may constrain its role in the ocean overturning circulation.

An ecosystem approach to understanding carbon export

In *Paper IV*, we found preliminary evidence that increased winter mixing induced by sea ice formation supports higher amplitude phytoplankton blooms the following summer. This results in increased short-term carbon export but not necessarily increased long-term carbon export. We suggest a number of possibilities for the disconnect between short-term and long-term carbon export, but are unable to definitively come to a conclusion. The limiting factor in this study is the lack of biological metrics. Simultaneous knowledge of the phytoplankton community composition, zooplankton activity and bacterial and viral load and their interactions would enable more robust conclusions. Observations of these metrics at the same spatio-temporal resolution as the glider observations of chlorophyll *a* and optical backscatter are at the frontier of current observational capabilities. The incorporation of imaging platforms on underwater gliders is under development but are currently limited by payload size and power constraints (*Lopez et al.*, 2015). Acoustic Doppler Profilers are however able to estimate zooplankton biomass (*Powell and Ohman*, 2012), although power consumption limits deployment time. A mooring, which could support cytometers and ADCPs in the region deployed simultaneously with underwater glider could elucidate much of the unknowns in such a study. This would further allow for the deployment of sediment traps (*Trull et al.*, 2001) to provide an independent estimate of carbon export, together with the backscatter spike method (*Briggs et al.*, 2011) that was used in *Paper IV*. Finally, we did not measure trace minerals. We attribute the changes in chlorophyll *a* biomass, primary production and phytoplankton community structure to differing supplies of the trace mineral, Iron, mixed into the surface waters during winter. Whether this is the driving process, whether the rate of primary production is Iron-limited, or perhaps Manganese-limited (*Browning et al.*, 2021) can currently only be constrained with direct experimentation using ship-based studies.

Frontiers of glider observations

Observing the ocean with gliders, which can sample the ocean for many months, has become a key platform in advancing our understanding of small scale ocean processes over sustained periods of time and in challenging conditions. If these observations are to become legacy datasets with which we are able to monitor long term change as imagined by Henry Stommel (*Stommel*, 1989), a community approach to the processing and quality control of essential ocean variables is needed. Dynamical errors in salinity arise partly as a result of thermal-inertia, and can become a substantial source of uncertainty when deriving the mixed layer depth or buoyancy gradients, particularly in oceans where the density is set by salinity and in oceans characterized by large thermal gradients. These should be corrected for as discussed in *Paper II*, but more importantly, community collaboration and agreement in the methods for correction are needed in order for cross-platform comparisons. Such standards are being developed by Ocean Gliders and should continue to advance. For initiatives such as these to be sustainable, additional recognition of work towards open-source community software and the allocation of funding and time to their continuous development, is required.

8.4 Closing remarks

The interdisciplinary scope of this thesis has advanced our understanding of the role of sea ice in modulating multi-scale turbulent processes and the biological carbon pump in the subpolar Southern Ocean. First, lateral density gradients at submesoscales O(0.1-10) km are active following the melt of sea ice in the subpolar Southern Ocean. While these fronts persist through the austral summer season, they are modified by wind interactions. Second, melt water stirring of submesoscale flows sustains lateral variability in the mixed layer, such that the mixed layer heat fluxes cannot be explained by vertical processes alone. However, melt water simultaneously sustains strong stratification at the base of the mixed layer, such that the subduction of surface transformed waters must occur remotely to where they are formed (*Paper II*). Third, beneath the mixed layer, winter water heat variability is well explained by surface and subsurface vertical processes. Variations in temperature are attributable to entrainment and detrainment while the seasonal summertime warming is attributable to diapycnal mixing from wind driven eddy diffusivity at the base of the mixed layer and double diffusive convection at the base of the winter water layer (*Paper III*). Fourth, primary production responds positively following winters with high sea ice volume (enhancing winter mixing and summer stratification), which may result in increased short term carbon export supporting mesopelagic ecosystems. However, we were not able to link long term carbon export to an intrinsic physical process. We hypothesize that long term carbon export is explained by non-linear biologically forced interactions involving rates of bacterial remineralization and phytoplankton community composition (*Paper IV*). The insights gained motivate for urgent focus on this rapidly changing and climatically important oceanic system, with a plethora of open and exciting questions still to be explored.

> "We have found, over the years, that the payoff in increase of knowledge often is greatest the more unconventional the idea, especially when it conflicts with collective wisdom"
>
> *Henry Stommel, 1989*

Bibliography

Abernathey, R. P., I. Cerovecki, P. R. Holland, E. Newsom, M. Mazloff, and L. D. Talley (2016), Water-mass transformation by sea ice in the upper branch of the Southern Ocean overturning, *Nature Geoscience*, *9*(8), 596–601, doi:10.1038/ngeo2749. 2.1, 2.2, 8.1, 8.2, 8.3

Ansorge, I. J., S. Speich, J. R. E. Lutjeharms, G. J. Goni, C. J. d. W. Rautenbach, P. W. Froneman, M. Rouault, and S. Garzoli (2005), Monitoring the oceanic flow between Africa and Antarctica : report of the first GoodHope cruise : research in action, *South African Journal of Science*, *101*(1), 29–35, doi:10.10520/EJC96351, _eprint: https://journals.co.za-/doi/pdf/10.10520/EJC96351. (document)

Appen, W.-J., C. Wekerle, L. Hehemann, V. Schourup-Kristensen, C. Konrad, and M. Iversen (2018), Observations of a Submesoscale Cyclonic Filament in the Marginal Ice Zone, *Geophys. Res. Lett*, doi:10.1029/2018GL077897. 8.2

Ardyna, M., H. Claustre, J.-B. Sallée, F. D'Ovidio, B. Gentili, G. van Dijken, F. D'Ortenzio, and K. R. Arrigo (2017), Delineating environmental control of phytoplankton biomass and phenology in the Southern Ocean: Phytoplankton Dynamics in the SO, *Geophysical Research Letters*, *44*(10), 5016–5024, doi:10.1002/2016GL072428. 2.4, 2.4, 8.1

Arrigo, K. R., G. L. van Dijken, and S. Bushinsky (2008), Primary production in the Southern Ocean, 19972006, *Journal of Geophysical Research*, *113*(C8), C08,004, doi:10.1029/2007JC004551. 2.1, 2.4

Arteaga, L. (2021), artlionel/SOCCOM_bgc_float_data_public:v1.0, doi:https://doi.org/10.5281/zenodo.4770029. 7.2

Arteaga, L., E. Boss, M. J. Behrenfeld, T. K. Westberry, and J. L. Sarmiento (2020), Seasonal modulation of phytoplankton biomass in the Southern Ocean, *Nature Communications*, *11*(1), 5364, doi:10.1038/s41467-020-19157-2. 2.4, 7.1

Auger, M., R. Morrow, E. Kestenare, J.-B. Sallée, and R. Cowley (2021), Southern Ocean in-situ temperature trends over 25 years emerge from interannual variability, *Nature Communications*, *12*(1), 514, doi:10.1038/s41467-020-20781-1. 8.3

Baldry, K., P. G. Strutton, N. A. Hill, and P. W. Boyd (2020), Subsurface Chlorophyll-a Maxima in the Southern Ocean, *Frontiers in Marine Science*, *7*, 671, doi:10.3389/fmars.2020.00671. 7.2

Barnes, D. (2015), Antarctic sea ice losses drive gains in benthic carbon drawdown, *Current Biology*, *25*(18), R789–R790, doi:10.1016/j.cub.2015.07.042. 2.1

Bebieva, Y., and K. Speer (2019), The Regulation of Sea Ice Thickness by DoubleDiffusive Processes in the Ross Gyre, *Journal of Geophysical Research: Oceans*, *124*(10), 7068–7081, doi:10.1029/2019JC015247. 2.3.2

Behrenfeld, M. J., and P. G. Falkowski (1997), Photosynthetic rates derived from satellite-based chlorophyll concentration, *Limnology and Oceanography*, *42*(1), 1–20, doi:10.4319/lo.1997.42.1.0001. 7.2

Behrenfeld, M. J., E. Boss, D. A. Siegel, and D. M. Shea (2005), Carbon-based ocean productivity and phytoplankton physiology from space: Phytoplankton growth rates and ocean productivity, *Global Biogeochemical Cycles*, *19*(1), doi:10.1029/2004GB002299. 7.2

Belcher, S. E., A. L. M. Grant, K. E. Hanley, B. Fox-Kemper, L. Van Roekel, P. P. Sullivan, W. G. Large, A. Brown, A. Hines, D. Calvert, A. Rutgersson, H. Pettersson, J.-R. Bidlot, P. A. E. M. Janssen, and J. A. Polton (2012), A global perspective on Langmuir turbulence in the ocean surface boundary layer, *Geophysical Research Letters*, *39*(18), doi:10.1029/2012GL052932. 2.3.2, 8.2, 8.3

Biddle, L. C., and S. Swart (2020), The Observed Seasonal Cycle of Submesoscale Processes in the Antarctic Marginal Ice Zone, *Journal of Geophysical Research: Oceans*, *125*(6), doi:10.1029/2019JC015587. 2.1, 2.2, 2.3.1, 5.1

Blumen, W. (1978), Uniform Potential Vorticity Flow: Part I. Theory of Wave Interactions and Two-Dimensional Turbulence, *Journal of Atmospheric Sciences*, *35*(5), 774 – 783, doi:10.1175/1520-0469(1978)035<0774:UPVFPI>2.0.CO;2. 8.3

Boccaletti, G., R. Ferrari, and B. Fox-Kemper (2007), Mixed Layer Instabilities and Restratification, *Journal of Physical Oceanography*, *37*(9), 2228–2250, doi:10.1175/JPO3101.1. 2.3.1

Bodner, A. S., B. Fox-Kemper, L. Johnson, L. P. Van Roekel, J. C. McWilliams, P. P. Sullivan, P. S. Hall, and J. Dong (2022), Modifying the Mixed Layer Eddy Parameterization to Include Frontogenesis Arrest by Boundary Layer Turbulence, *Journal of Physical Oceanography*, doi:10.1175/JPO-D-21-0297.1. 5.2

Bouffard, D., and L. Boegman (2013), A diapycnal diffusivity model for stratified environmental flows, *Dynamics of Atmospheres and Oceans*, *61-62*, 14–34, doi:10.1016/j.dynatmoce.2013.02.002. 8.3

Boyd, J. P. (1992), The Energy Spectrum of Fronts: Time Evolution of Shocks in Burgers Equation, *Journal of Atmospheric Sciences*, *49*(2), 128 – 139, doi:10.1175/1520-0469(1992)049<0128:TESOFT>2.0.CO;2. 8.3

Boyd, P. W., H. Claustre, M. Levy, D. A. Siegel, and T. Weber (2019), Multi-faceted particle pumps drive carbon sequestration in the ocean, *Nature*, *568*(7752), 327–335, doi:10.1038/s41586-019-1098-2. 2.4

Brenner, S., L. Rainville, J. Thomson, and C. Lee (2020), The evolution of a shallow front in the Arctic marginal ice zone, *Elem Sci Anth*, *8*(1), 17, doi:10.1525/elementa.413. 5.1, 8.2

Briggs, N., M. J. Perry, I. Cetini, C. Lee, E. D'Asaro, A. M. Gray, and E. Rehm (2011), High-resolution observations of aggregate flux during a sub-polar North Atlantic spring

bloom, *Deep Sea Research Part I: Oceanographic Research Papers*, *58*(10), 1031–1039, doi:10.1016/j.dsr.2011.07.007. 7.2, 8.3

Browning, T. J., E. P. Achterberg, A. Engel, and E. Mawji (2021), Manganese co-limitation of phytoplankton growth and major nutrient drawdown in the Southern Ocean, *Nature Communications*, *12*(1), 884, doi:10.1038/s41467-021-21122-6. 8.3

Buckingham, C. E., A. C. Naveira Garabato, A. F. Thompson, L. Brannigan, A. Lazar, D. P. Marshall, A. J. George Nurser, G. Damerell, K. J. Heywood, and S. E. Belcher (2016), Seasonality of submesoscale flows in the ocean surface boundary layer, *Geophysical Research Letters*, *43*(5), 2118–2126, doi:10.1002/2016GL068009. 8.2

Buesseler, K. O. (1998), The decoupling of production and particulate export in the surface ocean, *Global Biogeochemical Cycles*, *12*(2), 297–310, doi:10.1029/97GB03366. 7.2

Bushinsky, S. M., P. Landschützer, C. Rödenbeck, A. R. Gray, D. Baker, M. R. Mazloff, L. Resplandy, K. S. Johnson, and J. L. Sarmiento (2019), Reassessing Southern Ocean AirSea CO $_2$ Flux Estimates With the Addition of Biogeochemical Float Observations, *Global Biogeochemical Cycles*, *33*(11), 1370–1388, doi:10.1029/2019GB006176. 8.2

Callies, J., and R. Ferrari (2013), Interpreting Energy and Tracer Spectra of Upper-Ocean Turbulence in the Submesoscale Range (1200 km), *Journal of Physical Oceanography*, *43*(11), 2456–2474, doi:10.1175/JPO-D-13-063.1. 8.3

Capet, X., J. C. McWilliams, M. J. Molemaker, and A. F. Shchepetkin (2008), Mesoscale to Submesoscale Transition in the California Current System. Part II: Frontal Processes, *Journal of Physical Oceanography*, *38*(1), 44–64, doi:10.1175/2007JPO3672.1. 8.3

Cavan, E. L., F. A. C. Le Moigne, A. J. Poulton, G. A. Tarling, P. Ward, C. J. Daniels, G. M. Fragoso, and R. J. Sanders (2015), Attenuation of particulate organic carbon flux in the Scotia Sea, Southern Ocean, is controlled by zooplankton fecal pellets, *Geophysical Research Letters*, *42*(3), 821–830, doi:10.1002/2014GL062744. 7.3

Cavan, E. L., S. L. C. Giering, G. A. Wolff, M. Trimmer, and R. Sanders (2018), Alternative Particle Formation Pathways in the Eastern Tropical North Pacific's Biological Carbon Pump, *Journal of Geophysical Research: Biogeosciences*, *123*(7), 2198–2211, doi:10.1029/2018JG004392. 7.3

Cetini, I., M. J. Perry, E. D'Asaro, N. Briggs, N. Poulton, M. E. Sieracki, and C. M. Lee (2015), A simple optical index shows spatial and temporal heterogeneity in phytoplankton community composition during the 2008 North Atlantic Bloom Experiment, *Biogeosciences*, *12*(7), 2179–2194, doi:10.5194/bg-12-2179-2015. 7.3

Charney, J. G. (1971), Geostrophic Turbulence, *Journal of the Atmospheric Sciences*, *28*(6), 1087–1095, doi:10.1175/1520-0469(1971)028<1087:GT>2.0.CO;2. 2.3, 8.3

Chassignet, E. P., S. G. Yeager, B. Fox-Kemper, A. Bozec, F. Castruccio, G. Danabasoglu, C. Horvat, W. M. Kim, N. Koldunov, Y. Li, P. Lin, H. Liu, D. V. Sein, D. Sidorenko, Q. Wang, and X. Xu (2020), Impact of horizontal resolution on global oceansea ice model simulations based on the experimental protocols of the Ocean Model Intercomparison Project phase 2 (OMIP-2), *Geoscientific Model Development*, *13*(9), 4595–4637, doi:10.5194/gmd-13-4595-2020. 8.2

Chelton, D. B., R. A. deSzoeke, M. G. Schlax, K. El Naggar, and N. Siwertz (1998), Geographical Variability of the First Baroclinic Rossby Radius of Deformation, *Journal of Physical Oceanography*, *28*(3), 433–460, doi:10.1175/1520-0485(1998)028<0433:GVOTFB>2.0.CO;2. 5.1

Chor, T., J. O. Wenegrat, and J. Taylor (2022), Insights into the Mixing Efficiency of Submesoscale CentrifugalSymmetric Instabilities, *Journal of Physical Oceanography*, *52*(10), 2273–2287, doi:10.1175/JPO-D-21-0259.1. 8.3

Collen, L. (2005), *Boy*, Bloomsbury., London.

Comiso, J. C., R. A. Gersten, L. V. Stock, J. Turner, G. J. Perez, and K. Cho (2017), Positive Trend in the Antarctic Sea Ice Cover and Associated Changes in Surface Temperature, *Journal of Climate*, *30*(6), 2251–2267, doi:10.1175/JCLI-D-16-0408.1. 2.1

D'Asaro, E., C. Lee, L. Rainville, R. Harcourt, and L. Thomas (2011), Enhanced Turbulence and Energy Dissipation at Ocean Fronts, *Science*, *332*(6027), 318, doi:10.1126/science.1201515. 2.3.1

de Boer, A. M., A. J. Watson, N. R. Edwards, and K. I. C. Oliver (2010), A multi-variable box model approach to the soft tissue carbon pump, *Climate of the Past*, *6*(6), 827–841, doi:10.5194/cp-6-827-2010. 8.2

De Vries, T., and F. Primeau (2011), Dynamically and Observationally Constrained Estimates of Water-Mass Distributions and Ages in the Global Ocean, *Journal of Physical Oceanography*, *41*(12), 2381–2401, doi:10.1175/JPO-D-10-05011.1. (document)

De Vries, T., M. Holzer, and F. Primeau (2017), Recent increase in oceanic carbon uptake driven by weaker upper-ocean overturning, *Nature*, *542*(7640), 215–218, doi:10.1038/nature21068. 1

Deppeler, S. L., and A. T. Davidson (2017), Southern Ocean Phytoplankton in a Changing Climate, *Frontiers in Marine Science*, *4*, doi:10.3389/fmars.2017.00040. 2.4, 7.1

Dove, L. A., A. F. Thompson, D. Balwada, and A. R. Gray (2021), Observational Evidence of Ventilation Hotspots in the Southern Ocean, *Journal of Geophysical Research: Oceans*, *126*(7), doi:10.1029/2021JC017178. 5.2

du Plessis, M., S. Swart, I. J. Ansorge, A. Mahadevan, and A. F. Thompson (2019), Southern Ocean Seasonal Restratification Delayed by Submesoscale WindFront Interactions, *Journal of Physical Oceanography*, *49*(4), 1035–1053, doi:10.1175/JPO-D-18-0136.1. 2.3.1

du Plessis, M. D., S. Swart, L. C. Biddle, I. S. Giddy, P. M. S. Monteiro, C. J. C. Reason, A. F. Thompson, and S. Nicholson (2022), The DailyResolved Southern Ocean Mixed Layer: Regional Contrasts Assessed Using Glider Observations, *Journal of Geophysical Research: Oceans*, *127*(4), doi:10.1029/2021JC017760. 2.1, 5.2, 6.1, 6.2, 8.2, 8.3

Eayrs, C., D. Holland, D. Francis, T. Wagner, R. Kumar, and X. Li (2019), Understanding the Seasonal Cycle of Antarctic Sea Ice Extent in the Context of Longer-Term Variability, *Reviews of Geophysics*, *57*(3), 1037–1064, doi:10.1029/2018RG000631. 2.1

Esters, L., O. Breivik, S. Landwehr, A. ten Doeschate, G. Sutherland, K. H. Christensen, J.-R. Bidlot, and B. Ward (2018), Turbulence Scaling Comparisons in the Ocean Surface Boundary Layer, *Journal of Geophysical Research: Oceans*, *123*(3), 2172–2191, doi:10.1002/2017JC013525. 8.3

Evans, D. G., J. D. Zika, A. C. Naveira Garabato, and A. J. G. Nurser (2018a), The Cold Transit of Southern Ocean Upwelling, *Geophysical Research Letters*, *45*(24), doi:10.1029/2018GL079986. 2.2, 2.3.2, 6.1, 8.3

Evans, D. G., N. S. Lucas, V. Hemsley, E. FrajkaWilliams, A. C. Naveira Garabato, A. Martin, S. C. Painter, M. E. Inall, and M. R. Palmer (2018b), Annual Cycle of Turbulent Dissipation Estimated from Seagliders, *Geophysical Research Letters*, *45*(19), 10,560–10,569, doi:10.1029/2018GL079966. 8.3

Fer, I., A. K. Peterson, and J. E. Ullgren (2014), Microstructure Measurements from an Underwater Glider in the Turbulent Faroe Bank Channel Overflow, *Journal of Atmospheric and Oceanic Technology*, *31*(5), 1128–1150, doi:10.1175/JTECH-D-13-00221.1. 4.2, 4.4

Fitch, D. T., and J. K. Moore (2007), Wind speed influence on phytoplankton bloom dynamics in the Southern Ocean Marginal Ice Zone, *Journal of Geophysical Research*, *112*(C8), C08,006, doi:10.1029/2006JC004061. 8.2

Fox-Kemper, B., R. Ferrari, and R. Hallberg (2008), Parameterization of Mixed Layer Eddies. Part I: Theory and Diagnosis, *Journal of Physical Oceanography*, *38*(6), 1145–1165, doi:10.1175/2007JPO3792.1. 2.3.1, 5.2, 5.2

Fox-Kemper, B., G. Danabasoglu, R. Ferrari, S. Griffies, R. Hallberg, M. Holland, M. Maltrud, S. Peacock, and B. Samuels (2011), Parameterization of mixed layer eddies. III: Implementation and impact in global ocean climate simulations, *Ocean Modelling*, *39*(1-2), 61–78, doi:10.1016/j.ocemod.2010.09.002. 5.2

Fox-Kemper, B., A. Adcroft, C. W. Böning, E. P. Chassignet, E. Curchitser, G. Danabasoglu, C. Eden, M. H. England, R. Gerdes, R. J. Greatbatch, S. M. Griffies, R. W. Hallberg, E. Hanert, P. Heimbach, H. T. Hewitt, C. N. Hill, Y. Komuro, S. Legg, J. Le Sommer, S. Masina, S. J. Marsland, S. G. Penny, F. Qiao, T. D. Ringler, A. M. Treguier, H. Tsujino, P. Uotila, and S. G. Yeager (2019), Challenges and Prospects in Ocean Circulation Models, *Frontiers in Marine Science*, *6*, 65, doi:10.3389/fmars.2019.00065. 1, 5.2

Fox-Kemper, B., H. Hewitt, C. Xiao, G. Aðalgeirsdóttir, S. Drijfhout, T. Edwards, N. Golledge, M. Hemer, R. Kopp, G. Krinner, A. Mix, D. Notz, S. Nowicki, I. Nurhati, L. Ruiz, J.-B. Sallée, A. Slangen, and Y. Yu (2021), Ocean, Cryosphere and Sea Level Change., in *Climate Change 2021: The Physical Science Basis. Contribution of Working Group I to the Sixth Assessment Report of the Intergovernmental Panel on Climate Change*, pp. 1211–1362, Cambridge University Press, Cambridge, United Kingdom and New York, NY, USA, masson-Delmotte, V., P. Zhai, A. Pirani, S.L.ăConnors, C. Péan, S. Berger, N. Caud, Y. Chen, L. Goldfarb, M.I. Gomis, M. Huang, K. Leitzell, E. Lonnoy, J.B.R.ăMatthews, T.K. Maycock, T. Waterfield, O. Yelekçi, R. Yu, and B. Zhou (eds.). 5.2, 8.2

Freilich, M., and A. Mahadevan (2021), Coherent Pathways for Subduction From the Surface Mixed Layer at Ocean Fronts, *Journal of Geophysical Research: Oceans*, *126*(5), doi:10.1029/2020JC017042. 2.3.1, 2.4

Frölicher, T., J. Sarmiento, D. Paynter, J. Dunne, J. Krasting, and M. Winton (2015), Dominance of the Southern Ocean in Anthropogenic Carbon and Heat Uptake in CMIP5 Models, *Journal of Climate*, *28*, 862–886,, doi:10.1175/JCLI-D-14-00117.1. 1

Gordon, A. L. (2012), Circumpolar View of the Southern Ocean from 1962 to 1992, *Oceanography*, *25*(3), 18–23. (document)

Gray, A. R., K. S. Johnson, S. M. Bushinsky, S. C. Riser, J. L. Russell, L. D. Talley, R. Wanninkhof, N. L. Williams, and J. L. Sarmiento (2018), Autonomous Biogeochemical Floats Detect Significant Carbon Dioxide Outgassing in the HighLatitude Southern Ocean, *Geophysical Research Letters*, *45*(17), 9049–9057, doi:10.1029/2018GL078013. 8.2

Gregg, M., E. D'Asaro, J. Riley, and E. Kunze (2018), Mixing Efficiency in the Ocean, *Annual Review of Marine Science*, *10*(1), 443–473, doi:10.1146/annurev-marine-121916-063643. 8.3

Gregor, L., S. Kok, and P. M. S. Monteiro (2018), Interannual drivers of the seasonal cycle of CO₂ in the Southern Ocean, *Biogeosciences*, *15*(8), 2361–2378, doi:10.5194/bg-15-2361-2018. 8.2

Gregor, L., T. J. Ryan-Keogh, S.-A. Nicholson, M. du Plessis, I. Giddy, and S. Swart (2019), GliderTools: A Python Toolbox for Processing Underwater Glider Data, *Frontiers in Marine Science*, *6*, 738, doi:10.3389/fmars.2019.00738. 4.2.2

Gruber, N., M. Gloor, S. E. Mikaloff Fletcher, S. C. Doney, S. Dutkiewicz, M. J. Follows, M. Gerber, A. R. Jacobson, F. Joos, K. Lindsay, D. Menemenlis, A. Mouchet, S. A. Müller, J. L. Sarmiento, and T. Takahashi (2009), Oceanic sources, sinks, and transport of atmospheric CO2, *Global Biogeochemical Cycles*, *23*(1), doi:https://doi.org/10.1029/2008GB003349. 1

Haumann, F. A., N. Gruber, and M. Münnich (2020), SeaIce Induced Southern Ocean Subsurface Warming and Surface Cooling in a Warming Climate, *AGU Advances*, *1*(2), doi:10.1029/2019AV000132. 2.1, 8.1

Hemsley, V. S., T. J. Smyth, A. P. Martin, E. Frajka-Williams, A. F. Thompson, G. Damerell, and S. C. Painter (2015), Estimating Oceanic Primary Production Using Vertical Irradiance and Chlorophyll Profiles from Ocean Gliders in the North Atlantic, *Environmental Science & Technology*, *49*(19), 11,612–11,621, doi:10.1021/acs.est.5b00608. 7.2

Henson, S., F. Le Moigne, and S. Giering (2019), Drivers of Carbon Export Efficiency in the Global Ocean, *Global Biogeochemical Cycles*, *33*(7), 891–903, doi:https://doi.org/10.1029/2018GB006158, _eprint: https://agupubs.onlinelibrary.wiley.com/-doi/pdf/10.1029/2018GB006158. 2.4, 7.1, 7.2

Henson, S. A., C. Laufkötter, S. Leung, S. L. C. Giering, H. I. Palevsky, and E. L. Cavan (2022), Uncertain response of ocean biological carbon export in a changing world, *Nature Geoscience*, doi:10.1038/s41561-022-00927-0. 2.1, 2.4, 7.1, 7.2, 8.2

Hersbach, H., B. Bell, P. Berrisford, G. Biavati, A. Horányi, J. Muñoz Sabater, J. Nicolas, C. Peubey, R. Rozum, A. Simmons, C. Soci, D. Dee, and J.-N. Thépaut (2018), ERA5 hourly data on single levels from 1979 to present. 4.6

Hewitt, H., B. Fox-Kemper, B. Pearson, M. Roberts, and D. Klocke (2022), The small scales of the ocean may hold the key to surprises, *Nature Climate Change*, *12*(6), 496–499, doi: 10.1038/s41558-022-01386-6. 5.2, 8.2

Hofman, R. J. (2017), Sealing, whaling and krill fishing in the Southern Ocean: past and possible future effects on catch regulations, *Polar Record*, *53*(1), 88–99, doi:10.1017/ S0032247416000644. (document)

Holland, P. R., and R. Kwok (2012), Wind-driven trends in Antarctic sea-ice drift, *Nature Geoscience*, *5*(12), 872–875, doi:10.1038/ngeo1627. 2.1

Hoppema, M. (2004), Weddell Sea is a globally significant contributor to deep-sea sequestration of natural carbon dioxide, *Deep Sea Research Part I: Oceanographic Research Papers*, *51*(9), 1169 – 1177, doi:https://doi.org/10.1016/j.dsr.2004.02.011. 2.2, 2.4, 7.1, 8.2

Horvat, C., E. Tziperman, and J.-M. Campin (2016), Interaction of sea ice floe size, ocean eddies, and sea ice melting, *Geophysical Research Letters*, *43*(15), 8083–8090, doi:10.1002/ 2016GL069742. 5.1

Huntemann, M., G. Heygster, L. Kaleschke, T. Krumpen, M. Mäkynen, and M. Drusch (2014), Empirical sea ice thickness retrieval during the freeze-up period from SMOS high incident angle observations, *The Cryosphere*, *8*(2), 439–451, doi:10.5194/tc-8-439-2014. 4.6

Iudicone, D., G. Madec, B. Blanke, and S. Speich (2008), The Role of Southern Ocean Surface Forcings and Mixing in the Global Conveyor, *Journal of Physical Oceanography*, *38*(7), 1377–1400, doi:10.1175/2008JPO3519.1. 2.2

Jaeger, G. S., J. A. MacKinnon, A. J. Lucas, E. Shroyer, J. Nash, A. Tandon, J. T. Farrar, and A. Mahadevan (2020), How Spice is Stirred in the Bay of Bengal, *Journal of Physical Oceanography*, *50*(9), 2669–2688, doi:10.1175/JPO-D-19-0077.1. 8.3

Jenkins, W. J. (1982), Oxygen utilization rates in North Atlantic subtropical gyre and primary production in oligotrophic systems, *Nature*, *300*(5889), 246–248, doi:10.1038/300246a0. 7.2

Kelley, D. E. (1990), Fluxes through diffusive staircases: A new formulation, *Journal of Geophysical Research*, *95*(C3), 3365, doi:10.1029/JC095iC03p03365. 6.2

Kheireddine, M., G. Dall'Olmo, M. Ouhssain, G. Krokos, H. Claustre, C. Schmechtig, A. Poteau, P. Zhan, I. Hoteit, and B. H. Jones (2020), Organic Carbon Export and Loss Rates in the Red Sea, *Global Biogeochemical Cycles*, *34*(10), doi:10.1029/2020GB006650. 7.2

Koenig, Z., I. Fer, E. Kolås, T. O. Fossum, P. Norgren, and M. Ludvigsen (2020), Observations of Turbulence at a NearSurface Temperature Front in the Arctic Ocean, *Journal of Geophysical Research: Oceans*, *125*(4), doi:10.1029/2019JC015526. 5.1

Kolmogorov, A. N. (1941), Dissipation of Energy in Locally Isotropic Turbulence, *Akademiia Nauk SSSR Doklady*, *32*, 16. 2.3

Kraichnan, R. H. (1967), Inertial Ranges in Two-Dimensional Turbulence, *Physics of Fluids*, *10*(7), 1417, doi:10.1063/1.1762301. 2.3

Lampitt, R., B. Boorman, L. Brown, M. Lucas, I. Salter, R. Sanders, K. Saw, S. Seeyave, S. Thomalla, and R. Turnewitsch (2008), Particle export from the euphotic zone: Estimates using a novel drifting sediment trap, 234Th and new production, *Deep Sea Research Part I: Oceanographic Research Papers*, *55*(11), 1484–1502, doi:10.1016/j.dsr.2008.07.002. 7.2

Landschützer, P., N. Gruber, D. C. E. Bakker, and U. Schuster (2014), Recent variability of the global ocean carbon sink, *Global Biogeochemical Cycles*, *28*(9), 927–949, doi:10.1002/2014GB004853. 8.2

Lavergne, T., A. M. Sørensen, S. Kern, R. Tonboe, D. Notz, S. Aaboe, L. Bell, G. Dybkjær, S. Eastwood, C. Gabarro, G. Heygster, M. A. Killie, M. Brandt Kreiner, J. Lavelle, R. Saldo, S. Sandven, and L. T. Pedersen (2019), Version 2 of the EUMETSAT OSI SAF and ESA CCI sea-ice concentration climate data records, *The Cryosphere*, *13*(1), 49–78, doi:10.5194/tc-13-49-2019. 4.6

Lavery, C. (2019), Antarctica and Africa: Narrating alternate futures, *Polar Record*, *55*(5), 347–350, doi:10.1017/S0032247419000743. (document)

Le Moigne, F. A. C., S. A. Henson, R. J. Sanders, and E. Madsen (2013), Global database of surface ocean particulate organic carbon export fluxes diagnosed from the ²³⁴Th technique, *Earth System Science Data*, *5*(2), 295–304, doi:10.5194/essd-5-295-2013. 7.2

Lenton, A., B. Tilbrook, R. M. Law, D. Bakker, S. C. Doney, N. Gruber, M. Ishii, M. Hoppema, N. S. Lovenduski, R. J. Matear, B. I. McNeil, N. Metzl, S. E. Mikaloff Fletcher, P. M. S. Monteiro, C. Rödenbeck, C. Sweeney, and T. Takahashi (2013), Seaair CO₂ fluxes in the Southern Ocean for the period 19902009, *Biogeosciences*, *10*(6), 4037–4054, doi:10.5194/bg-10-4037-2013. 1

Li, Q., B. G. Reichl, B. FoxKemper, A. J. Adcroft, S. E. Belcher, G. Danabasoglu, A. L. M. Grant, S. M. Griffies, R. Hallberg, T. Hara, R. R. Harcourt, T. Kukulka, W. G. Large, J. C. McWilliams, B. Pearson, P. P. Sullivan, L. Van Roekel, P. Wang, and Z. Zheng (2019), Comparing Ocean Surface Boundary Vertical Mixing Schemes Including Langmuir Turbulence, *Journal of Advances in Modeling Earth Systems*, *11*(11), 3545–3592, doi:10.1029/2019MS001810. 8.3

Li, X., D. M. Holland, E. P. Gerber, and C. Yoo (2014), Impacts of the north and tropical Atlantic Ocean on the Antarctic Peninsula and sea ice, *Nature*, *505*(7484), 538–542, doi:10.1038/nature12945. 2.1

Lopez, P., T. C. O'Reilly, and D. Klimov (2015), Cytometers Set Sail With Sea-Going Mobile Robots, *Marine Technology Society Journal*, *49*(3), 17–26, doi:10.4031/MTSJ.49.3.9. 8.3

Lévy, M., P. J. S. Franks, and K. S. Smith (2018), The role of submesoscale currents in structuring marine ecosystems, *Nature Communications*, *9*(1), 4758, doi:10.1038/s41467-018-07059-3. 2.3.1, 8.2

MacGilchrist, G. A., A. C. Naveira Garabato, P. J. Brown, L. Jullion, S. Bacon, D. C. E. Bakker, M. Hoppema, M. P. Meredith, and S. Torres-Valdés (2019), Reframing the carbon cycle of the subpolar Southern Ocean, *Science Advances*, *5*(8), eaav6410, doi:10.1126/sciadv.aav6410. 2.2, 2.4, 7.1, 8.2

Mahadevan, A. (2016), The Impact of Submesoscale Physics on Primary Productivity of Plankton, *Annual Review of Marine Science*, *8*(1), 161–184, doi:10.1146/annurev-marine-010814-015912. 2.3, 8.2

Mahadevan, A., E. DAsaro, C. Lee, and M. J. Perry (2012), Eddy-Driven Stratification Initiates North Atlantic Spring Phytoplankton Blooms, *Science*, *337*(6090), 54–58, doi:10.1126/science.1218740. 2.3.1

Maier-Reimer, E., U. Mikolajewicz, and A. Winguth (1996), Future ocean uptake of CO2: interaction between ocean circulation and biology:, *Climate Dynamics*, *12*(10), 711–722, doi:10.1007/s003820050138. 2.4, 8.2

Manucharyan, G. E., and A. F. Thompson (2017), Submesoscale Sea Ice-Ocean Interactions in Marginal Ice Zones, *Journal of Geophysical Research: Oceans*, *122*(12), 9455–9475, doi:10.1002/2017JC012895. 2.2, 2.3.1, 5.1

Marshall, J., and K. Speer (2012), Closure of the meridional overturning circulation through Southern Ocean upwelling, *Nature Geoscience*, *5*(3), 171–180, doi:10.1038/ngeo1391. 2.2

Martin, J. H., G. A. Knauer, D. M. Karl, and W. W. Broenkow (1987), VERTEX: carbon cycling in the northeast Pacific, *Deep Sea Research Part A. Oceanographic Research Papers*, *34*(2), 267–285, doi:10.1016/0198-0149(87)90086-0. 2.4

Massom, R. A., and S. E. Stammerjohn (2010), Antarctic sea ice change and variability Physical and ecological implications, *Polar Science*, *4*(2), 149 – 186, doi:https://doi.org/10.1016/j.polar.2010.05.001. 2.1, 2.4

McDougall, T. J., and P. M. Barker (2011), *Getting started with TEOS-10 and the Gibbs Seawater (GSW) Oceanographic Toolbox*, Trevor J McDougall, Battery Point, Tas. 4.5

McPhee, M., and J. Morison (2001), Under-ice Boundary Layer, in *Encyclopedia of Ocean Sciences*, pp. 3071–3078, Elsevier, doi:10.1006/rwos.2001.0146. 2.3.2

McWilliams, J. C. (2016), Submesoscale currents in the ocean, *Proceedings of the Royal Society A: Mathematical, Physical and Engineering Sciences*, *472*(2189), 20160,117, doi:10.1098/rspa.2016.0117. 2.3, 2.3.1

Meehl, G. A., J. M. Arblaster, C. T. Y. Chung, M. M. Holland, A. DuVivier, L. Thompson, D. Yang, and C. M. Bitz (2019), Sustained ocean changes contributed to sudden Antarctic sea ice retreat in late 2016, *Nature Communications*, *10*(1), 14, doi:10.1038/s41467-018-07865-9. 2.1

Meredith, M., M. Sommerkorn, S. Cassotta, C. Derksen, A. Ekaykin, A. Hollowed, G. Kofinas, A. Mackintosh, J. Melbourne-Thomas, M. Muelbert, G. Ottersen, H. Pritchard, and E. Schuur (2019), Polar Regions, in *IPCC Special Report on the Ocean and Cryosphere in a Changing Climate*, pp. 203–320, Cambridge University Press, Cambridge, UK and New York, NY, USA. (document), 1, 1.1

Middleton, L., E. C. Fine, J. A. MacKinnon, M. H. Alford, and J. R. Taylor (2021), Estimating Dissipation Rates Associated With Double Diffusion, *Geophysical Research Letters*, *48*(15), doi:10.1029/2021GL092779. 6.2, 8.3

Moore, J. K., W. Fu, F. Primeau, G. L. Britten, K. Lindsay, M. Long, S. C. Doney, N. Mahowald, F. Hoffman, and J. T. Randerson (2018), Sustained climate warming drives declining marine biological productivity, *Science*, *359*(6380), 1139–1143, doi:10.1126/science.aao6379. (document)

Moreau, S., P. W. Boyd, and P. G. Strutton (2020), Remote assessment of the fate of phytoplankton in the Southern Ocean sea-ice zone, *Nature Communications*, *11*(1), 3108, doi:10.1038/s41467-020-16931-0. 7.2

Muench, R. D., H. J. S. Fernando, and G. R. Stegen (1990), Temperature and Salinity Staircases in the Northwestern Weddell Sea, *Journal of Physical Oceanography*, *20*(2), 295–306, doi:10.1175/1520-0485(1990)020<0295:TASSIT>2.0.CO;2. 2.3.2

Nasmyth, P. W. (1970), *Oceanic turbulence*, University of British Columbia, publisher:. 4.4

Naveira Garabato, A. C., G. A. MacGilchrist, P. J. Brown, D. G. Evans, A. J. S. Meijers, and J. D. Zika (2017), High-latitude ocean ventilation and its role in Earth's climate transitions, *Philosophical Transactions of the Royal Society A: Mathematical, Physical and Engineering Sciences*, *375*(2102), 20160,324, doi:10.1098/rsta.2016.0324. 2.4

Nicholson, S.-A., M. Lévy, J. Jouanno, X. Capet, S. Swart, and P. M. S. Monteiro (2019), Iron Supply Pathways Between the Surface and Subsurface Waters of the Southern Ocean: From Winter Entrainment to Summer Storms, *Geophysical Research Letters*, *46*(24), 14,567–14,575, doi:10.1029/2019GL084657. 2.3.2

Nicholson, S.-A., D. B. Whitt, I. Fer, M. D. du Plessis, A. D. Lebéhot, S. Swart, A. J. Sutton, and P. M. S. Monteiro (2022), Storms drive outgassing of CO2 in the subpolar Southern Ocean, *Nature Communications*, *13*(1), 158, doi:10.1038/s41467-021-27780-w. 2.3.2, 8.3

Omand, M. M., E. A. DAsaro, C. M. Lee, M. J. Perry, N. Briggs, I. Cetini, and A. Mahadevan (2015), Eddy-driven subduction exports particulate organic carbon from the spring bloom, *Science*, *348*(6231), 222, doi:10.1126/science.1260062. 2.4

Orozco-Muñiz, J. P., T. Salgado-Jimenez, and N. A. Rodriguez-Olivares (2020), Underwater Glider Propulsion Systems VBS Part 1: VBS Sizing and Glider Performance Analysis, *Journal of Marine Science and Engineering*, *8*(11), 919, doi:10.3390/jmse8110919. 4.2

Osborn, T. R. (1980), Estimates of the Local Rate of Vertical Diffusion from Dissipation Measurements, *Journal of Physical Oceanography*, *10*(1), 83–89, doi:10.1175/1520-0485(1980)010<0083:EOTLRO>2.0.CO;2. 2.3.2, 8.3

OSI-430-b (2019), Global sea-ice concentration interim climate data record 2016 onwards (v2.0), [Online]. 4.6

OSI-450. (2017), Global sea-ice concentration climate data record 1979-2015 (v2.0), [Online]. 4.6

Parkinson, C. L. (2019), A 40-y record reveals gradual Antarctic sea ice increases followed by decreases at rates far exceeding the rates seen in the Arctic, *Proceedings of the National Academy of Sciences*, *116*(29), 14,414–14,423, doi:10.1073/pnas.1906556116. 2.1, 8.1

Pellichero, V., J.-B. Sallée, S. Schmidtko, F. Roquet, and J.-B. Charrassin (2017), The ocean mixed layer under Southern Ocean sea-ice: Seasonal cycle and forcing, *Journal of Geophysical Research: Oceans*, *122*(2), 1608–1633, doi:10.1002/2016JC011970. 2.2, 8.2

Pellichero, V., J.-B. Sallée, C. C. Chapman, and S. M. Downes (2018), The southern ocean meridional overturning in the sea-ice sector is driven by freshwater fluxes, *Nature Communications*, *9*(1), 1789, doi:10.1038/s41467-018-04101-2. 2.1, 2.2, 8.1, 8.2

Pinkerton, M. H., P. W. Boyd, S. Deppeler, A. Hayward, J. Höfer, and S. Moreau (2021), Evidence for the Impact of Climate Change on Primary Producers in the Southern Ocean, *Frontiers in Ecology and Evolution*, *9*, 592,027, doi:10.3389/fevo.2021.592027. 2.4, 7.1, 7.2, 8.2

Platt, T., and S. Sathyendranath (1993), Estimators of primary production for interpretation of remotely sensed data on ocean color, *Journal of Geophysical Research*, *98*(C8), 14,561, doi:10.1029/93JC01001. 7.2

Powell, J. R., and M. D. Ohman (2012), Use of glider-class acoustic Doppler profilers for estimating zooplankton biomass, *Journal of Plankton Research*, *34*(6), 563–568, doi:10.1093/plankt/fbs023. 8.3

Riihelä, A., R. M. Bright, and K. Anttila (2021), Recent strengthening of snow and ice albedo feedback driven by Antarctic sea-ice loss, *Nature Geoscience*, *14*(11), 832–836, doi:10.1038/s41561-021-00841-x. 2.1

Roach, L. A., J. Dörr, C. R. Holmes, F. Massonnet, E. W. Blockley, D. Notz, T. Rackow, M. N. Raphael, S. P. O'Farrell, D. A. Bailey, and C. M. Bitz (2020), Antarctic Sea Ice Area in CMIP6, *Geophysical Research Letters*, *47*(9), doi:10.1029/2019GL086729. 2.1, 8.2

Roden, N. P., B. Tilbrook, T. W. Trull, P. Virtue, and G. D. Williams (2016), Carbon cycling dynamics in the seasonal sea-ice zone of East Antarctica, *Journal of Geophysical Research: Oceans*, *121*(12), 8749–8769, doi:10.1002/2016JC012008. 1

Rudnick, D. L. (2016), Ocean Research Enabled by Underwater Gliders, *Annual Review of Marine Science*, *8*(1), 519–541, doi:10.1146/annurev-marine-122414-033913. (document)

Sallée, J.-B., E. Shuckburgh, N. Bruneau, A. J. S. Meijers, T. J. Bracegirdle, and Z. Wang (2013), Assessment of Southern Ocean mixed-layer depths in CMIP5 models: Historical bias and forcing response: MIXED-LAYER DEPTHS IN CMIP5 MODELS, *Journal of Geophysical Research: Oceans*, *118*(4), 1845–1862, doi:10.1002/jgrc.20157. 1

Sallée, J.-B., V. Pellichero, C. Akhoudas, E. Pauthenet, L. Vignes, S. Schmidtko, A. N. Garabato, P. Sutherland, and M. Kuusela (2021), Summertime increases in upper-ocean stratification and mixed-layer depth, *Nature*, *591*(7851), 592–598, doi:10.1038/s41586-021-03303-x. 8.3

Sanders, R., L. Brown, S. Henson, and M. Lucas (2005), New production in the Irminger Basin during 2002, *Journal of Marine Systems*, *55*(3-4), 291–310, doi:10.1016/j.jmarsys.2004.09.002. 7.2

Sarmiento, J. L., and N. Gruber (2006), *Ocean biogeochemical dynamics*, Princeton University Press. 2.4

Sarmiento, J. L., N. Gruber, M. A. Brzezinski, and J. P. Dunne (2004), High-latitude controls of thermocline nutrients and low latitude biological productivity, *Nature*, *427*(6969), 56–60, doi:10.1038/nature02127. (document)

Sathyendranath, S., R. Brewin, C. Brockmann, V. Brotas, B. Calton, A. Chuprin, P. Cipollini, A. Couto, J. Dingle, R. Doerffer, C. Donlon, M. Dowell, A. Farman, M. Grant, S. Groom, A. Horseman, T. Jackson, H. Krasemann, S. Lavender, V. Martinez-Vicente, C. Mazeran, F. Mélin, T. Moore, D. Müller, P. Regner, S. Roy, C. Steele, F. Steinmetz, J. Swinton, M. Taberner, A. Thompson, A. Valente, M. Zühlke, V. Brando, H. Feng, G. Feldman, B. Franz, R. Frouin, R. Gould, S. Hooker, M. Kahru, S. Kratzer, B. Mitchell, F. Muller-Karger, H. Sosik, K. Voss, J. Werdell, and T. Platt (2019), An Ocean-Colour Time Series for Use in Climate Studies: The Experience of the Ocean-Colour Climate Change Initiative (OC-CCI), *Sensors*, *19*(19), 4285, doi:10.3390/s19194285. 4.6

Scheifele, B., S. Waterman, and J. R. Carpenter (2021), Turbulence and Mixing in the Arctic Oceans Amundsen Gulf, *Journal of Physical Oceanography*, *51*(1), 169–186, doi:10.1175/JPO-D-20-0057.1. 8.2

Scher, H. D., and E. E. Martin (2006), Timing and Climatic Consequences of the Opening of Drake Passage, *Science*, *312*(5772), 428–430, doi:10.1126/science.1120044. (document)

Shaw, W. J., and T. P. Stanton (2014), Dynamic and Double-Diffusive Instabilities in a Weak Pycnocline. Part I: Observations of Heat Flux and Diffusivity in the Vicinity of Maud Rise, Weddell Sea, *Journal of Physical Oceanography*, *44*(8), 1973–1991, doi:10.1175/JPO-D-13-042.1. 2.3.2

Siegelman, L., P. Klein, P. Rivière, A. F. Thompson, H. S. Torres, M. Flexas, and D. Menemenlis (2020), Enhanced upward heat transport at deep submesoscale ocean fronts, *Nature Geoscience*, *13*(1), 50–55, doi:10.1038/s41561-019-0489-1. 2.4

Small, R. J., A. K. DuVivier, D. B. Whitt, M. C. Long, I. Grooms, and W. G. Large (2021), On the control of subantarctic stratification by the ocean circulation, *Climate Dynamics*, *56*(1-2), 299–327, doi:10.1007/s00382-020-05473-2. 1

Speer, K., S. R. Rintoul, and B. Sloyan (2000), The Diabatic Deacon Cell*, *Journal of Physical Oceanography*, *30*(12), 3212–3222, doi:10.1175/1520-0485(2000)030<3212:TDDC>2.0.CO;2. 2.2

Spreen, G., L. Kaleschke, and G. Heygster (2008), Sea ice remote sensing using AMSR-E 89-GHz channels, *Journal of Geophysical Research: Oceans*, *113*, doi:10.1029/2005JC003384. 4.1

St. Laurent, L., and R. W. Schmitt (1999), The Contribution of Salt Fingers to Vertical Mixing in the North Atlantic Tracer Release Experiment*, *Journal of Physical Oceanography*, *29*(7), 1404–1424, doi:10.1175/1520-0485(1999)029<1404:TCOSFT>2.0.CO;2. 8.3

Stommel, H. (1989), The Slocum Mission, *Oceanography*, *2*(1), 22–25, publisher: Oceanography Society. 4.2.2, 8.3

Su, Z., J. Wang, P. Klein, A. F. Thompson, and D. Menemenlis (2018), Ocean submesoscales as a key component of the global heat budget, *Nature Communications*, *9*(1), 775, doi:10.1038/s41467-018-02983-w. 2.3.1

Swart, S., S. T. Gille, B. Delille, S. Josey, M. Mazloff, L. Newman, A. F. Thompson, J. Thomson, B. Ward, M. D. du Plessis, E. C. Kent, J. Girton, L. Gregor, P. Heil, P. Hyder, L. P. Pezzi, R. B. de Souza, V. Tamsitt, R. A. Weller, and C. J. Zappa (2019), Constraining Southern Ocean Air-Sea-Ice Fluxes Through Enhanced Observations, *Frontiers in Marine Science*, *6*, 421, doi:10.3389/fmars.2019.00421. 1

Swart, S., M. D. Plessis, A. F. Thompson, L. C. Biddle, I. Giddy, T. Linders, M. Mohrmann, and S. Nicholson (2020), Submesoscale Fronts in the Antarctic Marginal Ice Zone and Their Response to Wind Forcing, *Geophysical Research Letters*, *47*(6), doi:10.1029/2019GL086649. 2.2

Tagliabue, A., J.-B. Sallée, A. R. Bowie, M. Lévy, S. Swart, and P. W. Boyd (2014), Surface-water iron supplies in the Southern Ocean sustained by deep winter mixing, *Nature Geoscience*, *7*(4), 314–320, doi:10.1038/ngeo2101. 2.4

Tagliabue, A., L. Kwiatkowski, L. Bopp, M. Butenschön, W. Cheung, M. Lengaigne, and J. Vialard (2021), Persistent Uncertainties in Ocean Net Primary Production Climate Change Projections at Regional Scales Raise Challenges for Assessing Impacts on Ecosystem Services, *Frontiers in Climate*, *3*, 738,224, doi:10.3389/fclim.2021.738224. 2.1, 2.4, 8.2

Takahashi, T., R. A. Feely, R. F. Weiss, R. H. Wanninkhof, D. W. Chipman, S. C. Sutherland, and T. T. Takahashi (1997), Global air-sea flux of CO_2 : An estimate based on measurements of seaair pCO_2 difference, *Proceedings of the National Academy of Sciences*, *94*(16), 8292–8299, doi:10.1073/pnas.94.16.8292. 8.2

Tamsitt, V., R. P. Abernathey, M. R. Mazloff, J. Wang, and L. D. Talley (2018), Transformation of Deep Water Masses Along Lagrangian Upwelling Pathways in the Southern Ocean, *Journal of Geophysical Research: Oceans*, *123*(3), 1994–2017, doi:10.1002/2017JC013409. 2.2

Thomalla, S. J., N. Fauchereau, S. Swart, and P. M. S. Monteiro (2011), Regional scale characteristics of the seasonal cycle of chlorophyll in the Southern Ocean, *Biogeosciences*, *8*(10), 2849–2866, doi:10.5194/bg-8-2849-2011. 2.4, 7.1

Thomas, L. N., A. Tandon, and A. Mahadevan (2008), Submesoscale processes and dynamics, in *Geophysical Monograph Series*, vol. 177, edited by M. W. Hecht and H. Hasumi, pp. 17–38, American Geophysical Union, Washington, D. C., doi:10.1029/177GM04. 2.2, 2.3.1

Thompson, A. F., A. Lazar, C. Buckingham, A. C. Naveira Garabato, G. M. Damerell, and K. J. Heywood (2016), Open-Ocean Submesoscale Motions: A Full Seasonal Cycle of Mixed Layer Instabilities from Gliders, *Journal of Physical Oceanography*, *46*(4), 1285–1307, doi:10.1175/JPO-D-15-0170.1. 4.2.2

Timmermans, M.-L., and S. R. Jayne (2016), The Arctic Ocean Spices Up, *Journal of Physical Oceanography*, *46*(4), 1277–1284, doi:10.1175/JPO-D-16-0027.1. 8.2

Timmermans, M.-L., and P. Winsor (2013), Scales of horizontal density structure in the Chukchi Sea surface layer, *Continental Shelf Research*, *52*, 39 – 45, doi:https://doi.org/10.1016/j.csr.2012.10.015. 5.1, 8.2, 8.3

Timmermans, M.-L., S. Cole, and J. Toole (2012), Horizontal Density Structure and Restratification of the Arctic Ocean Surface Layer, *Journal of Physical Oceanography*, *42*(4), 659–668, doi:10.1175/JPO-D-11-0125.1. 8.2

Toggweiler, J. R., J. L. Russell, and S. R. Carson (2006), Midlatitude westerlies, atmospheric CO2 , and climate change during the ice ages: westerlies and CO2 during the ice ages, *Paleoceanography*, *21*(2), n/a–n/a, doi:10.1029/2005PA001154. 8.2

Trull, T. W., S. G. Bray, S. J. Manganini, S. Honjo, and R. François (2001), Moored sediment trap measurements of carbon export in the Subantarctic and Polar Frontal zones of the Southern Ocean, south of Australia, *Journal of Geophysical Research: Oceans*, *106*(C12), 31,489–31,509, doi:10.1029/2000JC000308. 8.3

Tréguer, P., C. Bowler, B. Moriceau, S. Dutkiewicz, M. Gehlen, O. Aumont, L. Bittner, R. Dugdale, Z. Finkel, D. Iudicone, O. Jahn, L. Guidi, M. Lasbleiz, K. Leblanc, M. Levy, and P. Pondaven (2018), Influence of diatom diversity on the ocean biological carbon pump, *Nature Geoscience*, *11*(1), 27–37, doi:10.1038/s41561-017-0028-x. 7.3

van der Boog, C. G., H. A. Dijkstra, J. D. Pietrzak, and C. A. Katsman (2021), Double-diffusive mixing makes a small contribution to the global ocean circulation, *Communications Earth & Environment*, *2*(1), 46, doi:10.1038/s43247-021-00113-x. 2.3.2, 8.3

van der Loeff, M. R., P. H. Cai, I. Stimac, A. Bracher, R. Middag, M. B. Klunder, and S. M. van Heuven (2011), 234Th in surface waters: Distribution of particle export flux across the Antarctic Circumpolar Current and in the Weddell Sea during the GEOTRACES expedition ZERO and DRAKE, *Deep Sea Research Part II: Topical Studies in Oceanography*, *58*(25-26), 2749–2766, doi:10.1016/j.dsr2.2011.02.004. 7.2

von Appen, W.-J., C. Wekerle, L. Hehemann, V. Schourup-Kristensen, C. Konrad, and M. H. Iversen (2018), Observations of a Submesoscale Cyclonic Filament in the Marginal Ice Zone, *Geophysical Research Letters*, doi:10.1029/2018GL077897. 5.1

von Berg, L., C. J. Prend, E. C. Campbell, M. R. Mazloff, L. D. Talley, and S. T. Gille (2020), Weddell Sea Phytoplankton Blooms Modulated by Sea Ice Variability and Polynya Formation, *Geophysical Research Letters*, *47*(11), doi:10.1029/2020GL087954. 8.1

Wenegrat, J. O., L. N. Thomas, M. A. Sundermeyer, J. R. Taylor, E. A. DAsaro, J. M. Klymak, R. K. Shearman, and C. M. Lee (2020), Enhanced mixing across the gyre boundary at the Gulf Stream front, *Proceedings of the National Academy of Sciences*, *117*(30), 17,607–17,614, doi:10.1073/pnas.2005558117. 5.2

Westberry, T., M. J. Behrenfeld, D. A. Siegel, and E. Boss (2008), Carbon-based primary productivity modeling with vertically resolved photoacclimation:Carbon-based Porduction Model, *Global Biogeochemical Cycles*, *22*(2), doi:10.1029/2007GB003078. 7.2

Whitt, D. B., and J. R. Taylor (2017), Energetic Submesoscales Maintain Strong Mixed Layer Stratification during an Autumn Storm, *Journal of Physical Oceanography*, *47*(10), 2419–2427, doi:10.1175/JPO-D-17-0130.1. 8.3

Whitt, D. B., M. Lévy, and J. R. Taylor (2019), Submesoscales Enhance StormDriven Vertical Mixing of Nutrients: Insights From a Biogeochemical Large Eddy Simulation, *Journal of Geophysical Research: Oceans*, *124*(11), 8140–8165, doi:10.1029/2019JC015370. 8.3

Wilson, E. A., S. C. Riser, E. C. Campbell, and A. P. S. Wong (2019), Winter Upper-Ocean Stability and IceOcean Feedbacks in the Sea IceCovered Southern Ocean, *Journal of Physical Oceanography*, *49*(4), 1099–1117, doi:10.1175/JPO-D-18-0184.1. 2.1, 2.3.2

Young, I. R., and A. Ribal (2019), Multiplatform evaluation of global trends in wind speed and wave height, *Science*, *364*(6440), 548–552, doi:10.1126/science.aav9527. 8.2, 8.3

Chapter 9

Scientific papers

Paper I

Submesoscale Fronts in the Antarctic Marginal Ice Zone and Their Response to Wind Forcing.

Swart, S., M. du Plessis, A.F. Thompson, L. Biddle, **I. Giddy**, T. Linders, M. Mohrmann, S-A. Nicholson
Geophysical Research Letters, **47 (6), e2019GL086649** (2020)

AGU ADVANCING EARTH AND SPACE SCIENCE

Geophysical Research Letters

RESEARCH LETTER
10.1029/2019GL086649

Submesoscale Fronts in the Antarctic Marginal Ice Zone and Their Response to Wind Forcing

Sebastiaan Swart[1,2], Marcel D. du Plessis[2,3], Andrew F. Thompson[4], Louise C. Biddle[1], Isabelle Giddy[1,2], Torsten Linders[1], Martin Mohrmann[1], and Sarah-Anne Nicholson[3]

[1]Department of Marine Sciences, University of Gothenburg, Gothenburg, Sweden, [2]Department of Oceanography, University of Cape Town, Rondebosch, South Africa, [3]Southern Ocean Carbon-Climate Observatory (SOCCO), CSIR, Cape Town, South Africa, [4]Environmental Science and Engineering, California Institute of Technology, Pasadena, CA, USA

Abstract Submesoscale flows in the ocean are energetic motions, O(1–10 km), that influence stratification and the distributions of properties, such as heat and carbon. They are believed to play an important role in sea-ice-impacted oceans by modulating air-sea-ice fluxes and sea-ice extent. The intensity of these flows and their response to wind forcing are unobserved in the sea-ice regions of the Southern Ocean. We present the first submesoscale-resolving observations in the Antarctic marginal ice zone (MIZ) collected by surface and underwater autonomous vehicles, for >3 months in austral summer. We observe salinity-dominated lateral density fronts occurring at sub-kilometer scales. Surface winds are shown to modify the magnitude of the mixed-layer density fronts, revealing strongly coupled atmosphere-ocean processes. We posture that these wind-front interactions occur as a continuous interplay between front slumping and vertical mixing, which leads to the dispersion of submesoscale fronts. Such processes are expected to be ubiquitous in the Southern Ocean MIZ.

Plain Language Summary Satellite radar imagery shows evidence of 1–10 km eddies and jets in the ocean adjacent to the sea-ice edge around Antarctica. We use field observations of temperature, salinity, and wind speed from autonomous robotic platforms deployed in the sea-ice zone for >3 months. These measurements provide estimates of the surface ocean density fronts which are controlled primarily by lateral variations in salinity. We show that, during high wind speeds, these surface fronts temporarily dissipate, indicating an atmosphere-ocean coupling occurring at the submesoscale. The fronts strengthen again during low wind speed, which is thought to be because the stirring of the fresher surface layer by mesoscale eddies leads to the generation of the submesoscale fronts. Providing in situ observations of such features improves our understanding of the small-scale ocean and climate processes at play, such as how heat and carbon may exchange between the atmosphere and the ocean.

Key Points:
- Using combined surface and underwater robotic observations, we observe haline-dominated submesoscale fronts in the Antarctic MIZ
- Enhanced wind speeds reduce the magnitude of lateral submesoscale fronts within the surface mixed layer
- Submesoscale wind-front interactions cause a continuous interplay between front slumping and vertical mixing, arresting lateral shear

Supporting Information:
- Supporting Information SI

Correspondence to:
S. Swart,
sebastiaan.swart@marine.gu.se

Citation:
Swart, S., du Plessis, M. D., Thompson, A. F., Biddle, L. C., Giddy, I., Linders, T., et al. (2020). Submesoscale fronts in the Antarctic marginal ice zone and their response to wind forcing. *Geophysical Research Letters*, *47*, e2019GL086649. https://doi.org/10.1029/2019GL086649

Received 13 DEC 2019
Accepted 2 MAR 2020
Accepted article online 4 MAR 2020

1. Introduction

The sea-ice-impacted ocean around Antarctica is vast, with annual sea-ice growth and melt occurring over approximately 18 $\times 10^6$ km^2—equivalent to the surface area of South America. Southern Ocean air-sea-ice fluxes impact the ocean heat and carbon budget (e.g., Marshall & Zanna, 2014), water mass transformation (Walin, 1982), the global overturning circulation (Abernathey et al., 2016), sea-ice distribution, and numerous biogeochemical processes. Despite this, atmosphere-ocean physical processes within the Marginal Ice Zone (MIZ) are poorly understood due to the paucity of *in situ* observations brought about by its seasonal ice cap and remoteness. Ongoing efforts (e.g., under-ice profiling floats and seal tag data) are helping to address this data gap, albeit at relatively coarse temporal and spatial resolution (e.g., Campbell et al., 2019; Pellichero et al., 2017). Current observational efforts remain unable to resolve the rapidly evolving dynamics of the surface layer ocean in the MIZ. This contributes to both a poor mechanistic understanding and to uncertainty in modeling the impact of ocean-ice-atmosphere processes on larger-scale climate.

In addition to surface mechanical and buoyancy forcing, the formation and evolution of lateral density gradients, or fronts, may also significantly impact upper ocean stratification. These fronts can become unstable to instabilities that form mixed layer eddies (Boccaletti et al., 2007; Thomas & Ferrari, 2008), which evolve rapidly (in the order of hours – days and at small lateral scales, O(1 km); Thomas et al., 2008), otherwise known as submesoscale flows (Rossby numbers of O(1)). When these flows become baroclinically

unstable, they slump and can generate rapid restratification in the mixed layer (Hosegood et al., 2006). Winds blowing over mixed-layer fronts can aid and destroy vertical stratification, depending on their orientation (du Plessis et al., 2019; Mahadevan et al., 2010; Thomas & Lee, 2005). In the MIZ, the surface layer is expected to contain energetic submesoscale processes given the potential for strong lateral gradients fed by seasonal sea-ice-induced freshwater fluxes (sea-ice melt and formation, such as those observed in the Arctic; Timmermans et al., 2008), while the presence of a freshwater lens will act to suppress submesoscale flows from forming in shallow mixed layers (reduction in the frontal potential energy). Alternatively, submesoscale flows, whether intermittent or quasi-permanent, are likely to generate vertical fluxes of heat and salt (Thomas et al., 2008) that will alter the buoyancy and heat budget of the upper ocean, further adjusting sea-ice melt and formation rates. This is especially relevant in the Antarctic MIZ, where warm and salty Circumpolar Deep Water (CDW) lies closely under the surface mixed layer.

Although submesoscale fronts are considered to be ubiquitous in the surface ocean (e.g., Adams et al., 2019; Johnson et al., 2016; Ramachandran et al., 2018; Thomas et al., 2013), until now, we have no observations at the required scale to assess their prevalence and strength in the Antarctic MIZ. This is especially true at seasonal scales that capture sea-ice formation or melting processes and their associated impact on the upper ocean physics and biogeochemistry. Most of our understanding of submesoscale processes in the sea-ice polar regions exists from theoretical estimates and modeling simulations (Horvat et al., 2016; Lu et al., 2015; Manucharyan & Thompson, 2017) and a handful of observational efforts limited to the Arctic (Lu et al., 2015; Timmermans et al., 2008, Timmermans & Winsor, 2013; Toole et al., 2010; von Appen et al., 2018). In the Antarctic, sea-ice extends to considerably lower latitudes (55°S) compared with the Arctic and is exposed to stronger surface forcing, related to storms located in the westerly wind belt, as well as a more energetic surface circulation, associated with the Antarctic Circumpolar Current and northern limbs of the polar gyres. This means that lessons learned from the Arctic may not immediately translate to Southern Ocean conditions. To our knowledge, multiscale (fine spatial scale to multi-month temporal scale) observations have not previously been reported from the Southern Ocean MIZ.

The field site of the Robotic Observations and Modeling of the MIZ (ROAM-MIZ) project represents a nexus for active surface wind forcing and enhanced vertical and lateral property gradients in the upper ocean brought on primarily by sea-ice formation and melt processes (e.g., Pellichero et al., 2017), which gives rise to lateral gradients in density. Strong time-mean wind stress, where a band of maximum wind force (Lin et al., 2018) induced by transient storms (> 20 m s^{-1}; Yuan, 2004), characterizes our study region. These storms add a time-varying and rotational component to the background wind forcing, which interacts directly with lateral density ocean gradients (du Plessis et al., 2019) driven mostly by seasonal freshwater fluxes (varying buoyancy flux; e.g., Massom & Stammerjohn, 2010). We see evidence for these density gradients and associated instabilities occurring in the MIZ from high-resolution Sentinel-SAR imagery (Figure 1a), where signatures of 5- to 10-km-scale ocean eddies and filaments are apparent in the sea ice (Manucharyan & Thompson, 2017). We hypothesize that following the sea-ice melt, freshwater anomalies are stirred by mesoscale motions that generate haline-dominated fronts through frontogenesis. These fronts store potential energy that can promote submesoscale flows. Furthermore, the intense surface winds of the Southern Ocean interact with these fine-scale fronts at synoptic time scales, providing vertical shear that can destroy vertical stratification and impact the intensity of submesoscale fronts.

We present high-resolution in situ observations (0.2- to 120-km resolution between December 2018 and March 2019) obtained in the Southern Ocean MIZ from an autonomous surface vehicle, a Sailbuoy, paired with a profiling Seaglider. With these observations, we show that submesoscale fronts persist into late summer, but their intensity responds rapidly to intermittent wind forcing. We expect such atmosphere-ocean interactions to be ubiquitous in both the Southern Ocean and Arctic MIZs.

2. Data and Methods

Robotic surveys were conducted in recently formed open waters, approximately 100 km from the rapidly retreating sea-ice edge (Figure 1b) at 60°S, 0°E. At the experiment location, satellite data depict the sea-ice present ~4 days before deployment (Figure 1c) and then rapidly retreating ~700 km southwards in a week. An autonomous surface vehicle, the Offshore Sensing Sailbuoy (2-m length, 60-kg displacement), collected surface temperature (T), salinity (S), and meteorological measurements. The Sailbuoy is wind propelled,

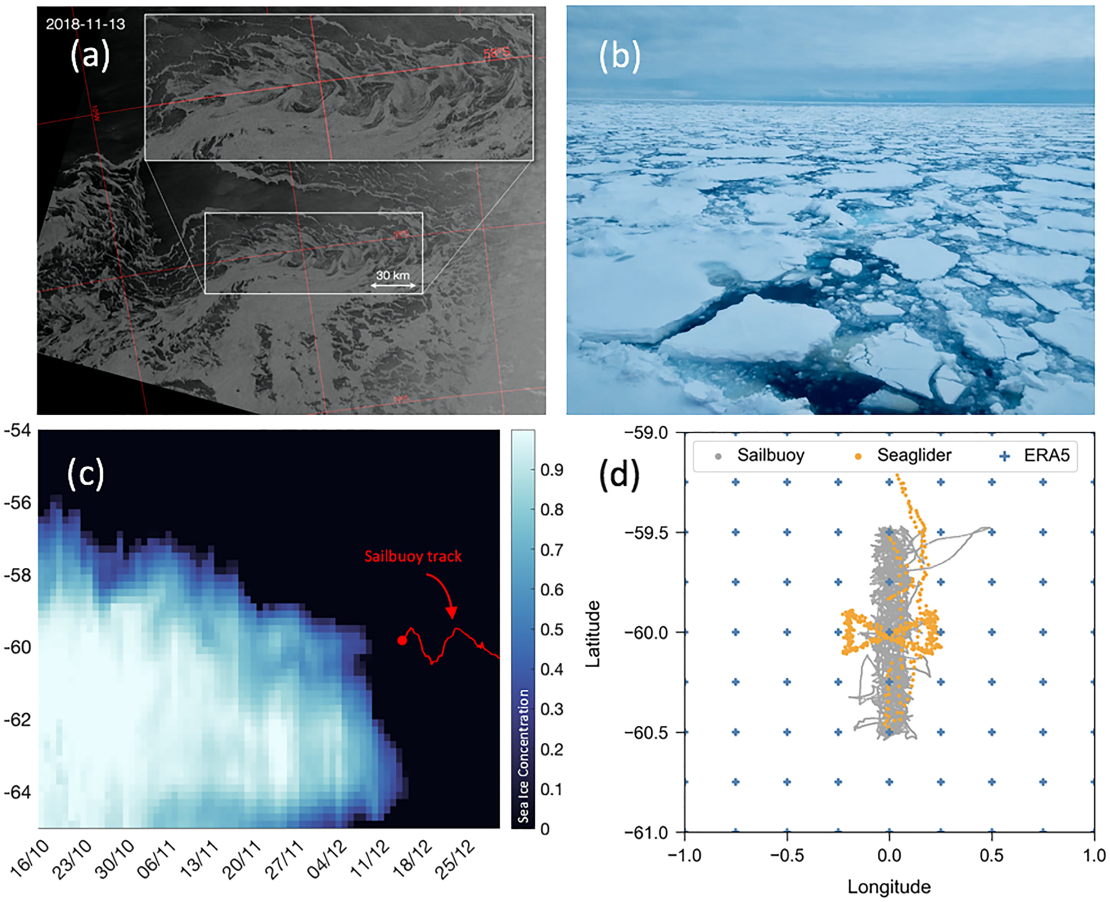

Figure 1. (a) Sentinel-1 synthetic aperture radar image from 13 November 2018 (1 month prior to robotic deployments) suggesting ocean submesoscale features present at the sea-ice margins of O(5–10 km). (b) Photo taken from the SA Agulhas II (15 December 2018; 61.07°S, 0.05°E) showing sea-ice conditions ~100 km south of the study location. (c) Hövmöller of the sea-ice concentration from combined AMSR2 and SSMI data centered on 0°E (the red dot and line shows the deployment and initial track of the Sailbuoy). (d) Seaglider and Sailbuoy locations during the study. Crosses denote the ERA5 reanalysis winds grid, as in Figure S1.

with solar panels powering scientific sensors and navigation systems, enabling it to remain at sea for months (Ghani et al., 2014). During the deployment, between 15 December 2018 and 1 March 2019, the Sailbuoy maintained a north-south transect of 112 km in length (Figure 1d), achieving 17 (O(100 km)) transects repeated every 4.1 ± 1.8 days. An Aanderaa 4319 conductivity and temperature sensor was installed at 0.5-m depth in a flow through keel-bulb that sampled every 30 s. Data were averaged in 10-min bins and transmitted back to shore. Future observational efforts should seek even higher sampling frequency to account for rapidly changing properties over space and time. Antifouling coating was applied to the platform and bulb with no biofouling evident on recovery and no sensor drift recorded when compared to conductivity-temperature-depth (CTD) measurements from collocated glider and ship thermosalinograph measurements.

An Airmar WX-200 Ultrasonic Weather Station was mounted on a mast 0.7 m above sea level measuring true wind speed, wind gust (maximum wind speed every 10 min) and direction, barometric pressure, and air temperature. The instrument is designed for moving platforms, with the ability to dynamically correct winds using an internal compass and correct up to a 30° pitch in rough seas. The sensor sampled at 1 Hz and then averaged the data in 10-min bins, before transmitting data back to shore. Details on sensor accuracy and behavior in variable weather conditions, as well as referencing the surface winds to 10 m above sea level, can be found in Schmidt et al. (2017). On 8 February 2019, we lost functionality of the Airmar sensor due to unknown damage (suspected iceberg collision) to the vehicle during the mission. To extend the wind speed time series and collocate wind observations with the glider data, we use gridded wind reanalysis

products. ERA5, NCEP, and CFS reanalysis winds are compared to in situ Sailbuoy winds, which shows that CSF and ERA5 are comparable and better than NCEP. We thus use ERA5 winds in this study ($r = 0.75$; RMSE = 2.09 m s^{-1}; Figure S1 of the supporting information). This result is supported by Schmidt et al. (2017) using wind speed measurements from multiple Wave Gliders in the Southern Ocean.

Hydrographic data were collected by a Seaglider, profiling to 1,000 m, over the central domain of the Sailbuoy transect from 15 December 2018 and 26 March 2019 (101 days). The glider was placed in a repeat "bow-tie" sampling pattern with lateral length-scale transects of 22 km (Figure 1d) and on two occasions completed a 100-km north-south transect to resolve the local mesoscale (O(100 km)) gradient. The CTD sampled nominally at 0.2 Hz and the data were quality controlled against ship CTD profiles (as in Swart et al., 2015), as well as applying the most up-to-date conductively thermal lag corrections based on the glider flight model to estimate conductivity cell flow through rates (C. Eriksen, unpublished). Only observations between the surface and until 15 m above the mixed layer depth (MLD) are used to compute mixed layer gradients in order to avoid internal wave processes or larger conductivity thermal lag errors nearer the pycnocline. By utilizing the upper part of the glider "saw-tooth" pattern (successive climb and dive profiles; Figure S2a), we are able to resolve surface-layer lateral density gradients at resolutions of between 10 and 200 m and ~20 min, (median lateral spacing ~120 m between 0- and 50-m depth; Figures S2b and S2c). This high-resolution "snapshot" sampling of the lateral density gradient is repeated at each glider dive interval, which is approximately 4 hourly. ERA5 wind speed data are collocated at the location and time of the glider throughout the deployment.

3. Results and Discussion

3.1. Surface-Layer Gradients and Their Scale Sensitivity

Sailbuoy surface T and S sampling obtained an average resolution of 0.49 ± 0.23 km, thus resolving length scales of O(1 km), enabling observations of submesoscale lateral fronts and features. An internal Rossby radius, (Lr = NH/f, where N is the buoyancy frequency in the mixed layer, H is the MLD, which was 41 ± 8.6 m during the survey, as determined using the density criteria, $\rho = 0.03$ kg m^{-3}, and $f \approx 1.2 \times 10^{-4}$ s^{-1} is the Coriolis frequency) provides the length scale for submesoscale flows to develop in the surface layer (Boccaletti et al., 2007). During our survey period, Lr = 2.0 ± 0.5 km was obtained from the glider survey, suggesting the applicability of the autonomous platforms to sample at scales smaller than Lr.

We find lateral density gradients existing at all observed scales (sub-kilometer to 100 km scales; Figures 2a and 3; note that in Figure 2, T and S are scaled according to their respective contributions to changes in density). Lateral changes in density are dominated by S variations, compared with only minor contributions from changes in T. The relative contribution of T and S gradients to lateral density fronts is further estimated using the lateral density ratio, $R = \alpha\Delta T/\Delta S$, where α and β are the thermal expansion and haline contraction coefficients, respectively, and ΔT and ΔS are the lateral temperature and salinity gradients, respectively. $R = 1$ would infer full compensation, while deviations from 1 represent uncompensated fronts by either temperature ($R > 1$) or salinity ($0 < R < 1$) (Rudnick & Ferrari, 1999). $R < 0$ indicates conditions where fronts are reinforced by temperature gradients working in concert with salinity gradients. The high-resolution data show that lateral T and S gradients are noncompensating and S variations dominate the density gradients ($R < 1$) with the histogram peaking at $R \sim 0$ (Figure 2c). This contrasts the midlatitude regions, where T dominates uncompensated density fronts (Hosegood et al., 2006; Johnson et al., 2012). Separating the analysis between early summer and late summer shows a flattening and small deviation in the distribution of R towards −1, over the 3-month time series (Figure 2c). This indicates an increasing role of T towards reinforcing density fronts due to seasonal warming and a reduction in the strength of the S contribution to the density gradient of the fronts, potentially by slow mixing processes or entrainment (the low saline mixed-layer waters from the early summer sea-ice melt are mixed with saltier CDW from below). However, the solar heating of the mixed layer in summer (0–190 W m^{-2} during this study) is not enough to significantly adjust R towards T control of the surface density gradients. Nonetheless, strong salinity-driven fronts continue to occur with time (Figure 2a), indicating that mixing processes do not significantly reduce surface ocean density gradients (similar to Chukchi Sea observations by Timmermans & Winsor, 2013) and that the stirring of waters with varying salinity continue long after the sea ice has retreated. We speculate that a supply of

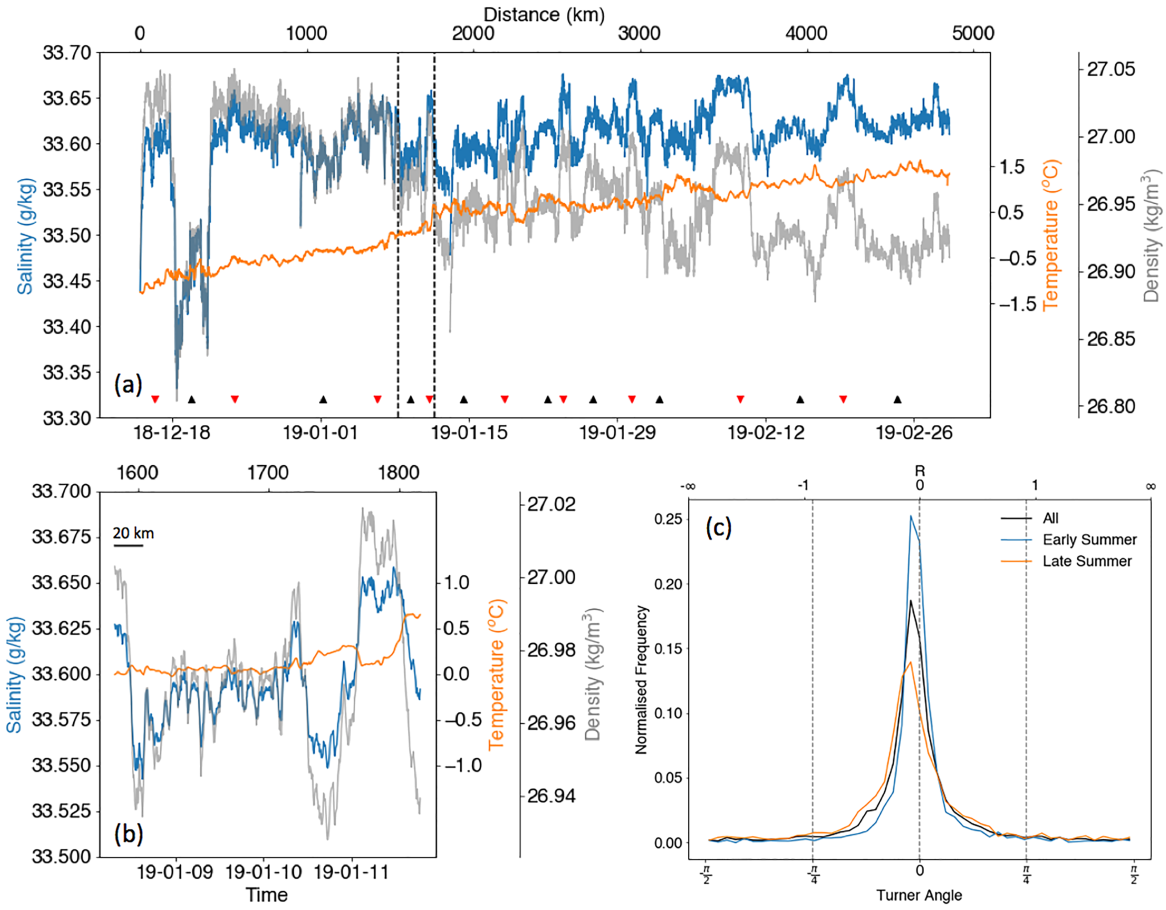

Figure 2. (a) Continuous surface temperature (T), salinity (S), and density measurements by the Sailbuoy over ~2.5 months. Red (black) triangle markers represent the start of Sailbuoy transects heading southward (northward). The dashed lines indicate an expanded view in (b) of T, S and density gradients at ~200-km scale. T and S ranges are proportionally scaled by the thermal expansion (α) and haline contraction (β) coefficients, so that equal displacements have equal effect on density. (c) Distributions of the density ratio, R, and Turner angle calculated from the Sailbuoy surface data for early summer (blue), late summer (orange), and the entire deployment (black).

freshwater is advected from more southern latitudes over time, where sea-ice melt extends further into the summer season.

The variations in the haline fronts (<1 km) observed by the Sailbuoy can exceed 0.5 g kg^{-1} km^{-1} with the 50th percentile = 0.03 g kg^{-1} km^{-1} and 95th percentile = 0.141 g kg^{-1} km^{-1} (Figure 2b). The lateral salinity gradients obtained only between consecutive glider up-cast and down-cast data (see section 2; Figure S2) indicate comparable, strong salinity fronts within the mixed layer (50th percentile = 0.025 g kg^{-1} km^{-1} and 95th percentile = 0.241 g kg^{-1} km^{-1}). The small, yet potentially important remains of thermal lag error in the salinity data within the mixed layer, between successive Seaglider climb and dive profiles (0.01 ± 0.02 g kg^{-1} km^{-1}), can lead to lateral salinity gradients being overestimated by ~15 ± 31%. This is an upper bound overestimate given that the salinity differences between profiles include actual lateral salinity fronts too.

Furthermore, wavenumber spectra are used to show the variance in the lateral density measured by the Sailbuoy over wavelengths of 1–50 km (Figure 3b). The surface density was first linearly interpolated to 400 m, the average distance between sampling, detrended, and smoothed with a 2 km Gaussian window before the power density spectra was computed. The best-fit wavenumber (k) slope for the surface density is $k \sim -2.4$ (Figure 3b). The fairly less steep wavenumber spectra found in this study indicate somewhat more energetic small-scale structures compared with those observed in the Arctic at 70°N ($k = -2.8$ from Timmermans & Winsor, 2013) and under Arctic sea ice (Timmermans et al., 2012) where spectra slopes

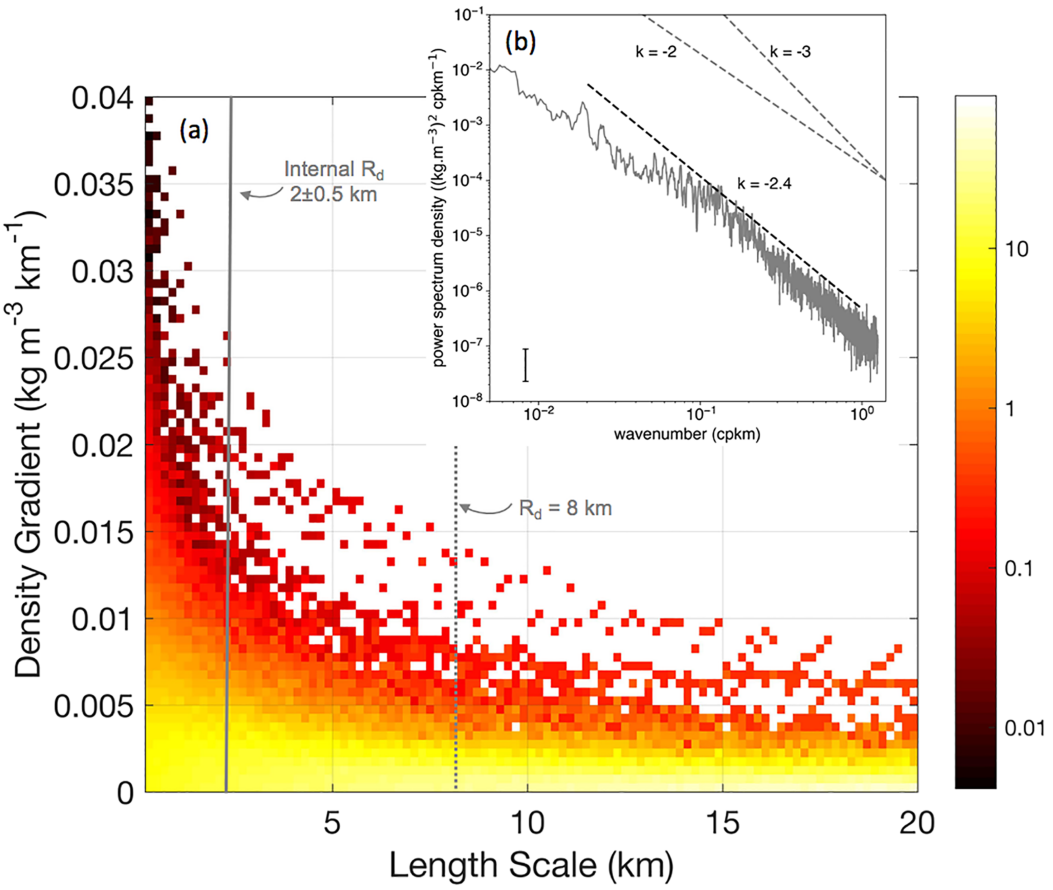

Figure 3. (a) Distribution of surface density gradients (kg m^{-3} km^{-1}) as sampled by different horizontal length scales (0.2 to 20 km). The log color scale represents the percentage count of the gradients at various scales. The internal and full-depth Rossby deformation radius for the study region are indicated. (b) Horizontal wavenumber spectra of the surface density variance from the Sailbuoy dataset. Dashed black line is the best-fit slope of −2.4 between 1 and 50 km. For reference, k^{-2} and k^{-3} slopes are indicated with gray dashed lines. The 95% confidence interval is shown.

were closer to k^{-3}. Overall, the in situ observations confirm the evidence of these active submesoscale flows seen in the SAR imagery (Figure 1a) adjacent to and extending ~100 km into the sea ice.

To assess the scale sensitivity of the fronts, continuous time series of surface density are subsampled between 0.2 and 30 km (Figure 3). The highest-resolution sampling (mean = 0.46 ± 0.23 km) reveals a spread of density gradients reaching up to 0.06 kg m^{-3} km^{-1} (equivalent lateral buoyancy gradient = 6×10^{-7} s^{-2}, hereafter reported as a lateral density gradient). These density gradients are lower bound estimates given that the surface fronts were unlikely to have been sampled perpendicularly by the Sailbuoy. By assessing the difference between the glider dive direction and the estimated front direction, we estimate that the glider (and comparatively for the Sailbuoy) underestimate the true lateral buoyancy gradient by 51% on average (similarly, this is computed to be 64% and 71% for glider observations by du Plessis et al., 2019, and Thompson et al., 2016, respectively). Once the sampling length scale is increased incrementally, there is a sharp drop off in density gradients, which converge between the internal and full-depth Rossby radius of deformation at this latitude ($R_{d\_internal}$ = 2 km, R_d = 8 km; Figure 2c). As a case in point, if one were to measure the surface thermohaline gradients in this region at length scales greater than 8 km, one would only observe density gradients of less than 0.01 kg m^{-3} km^{-1}, with the vast majority (63%) sampled at <0.005 kg m^{-3} km^{-1}. This emphasizes the need to sample at high spatial resolutions (<1 km) to capture the full surface variance in density at high latitudes, particularly in relatively shallow mixed layer environments (leading to smaller $R_{d\_internal}$) where sea-ice-induced freshwater layers can prevail (e.g., in the Arctic—Wulff et al., 2016).

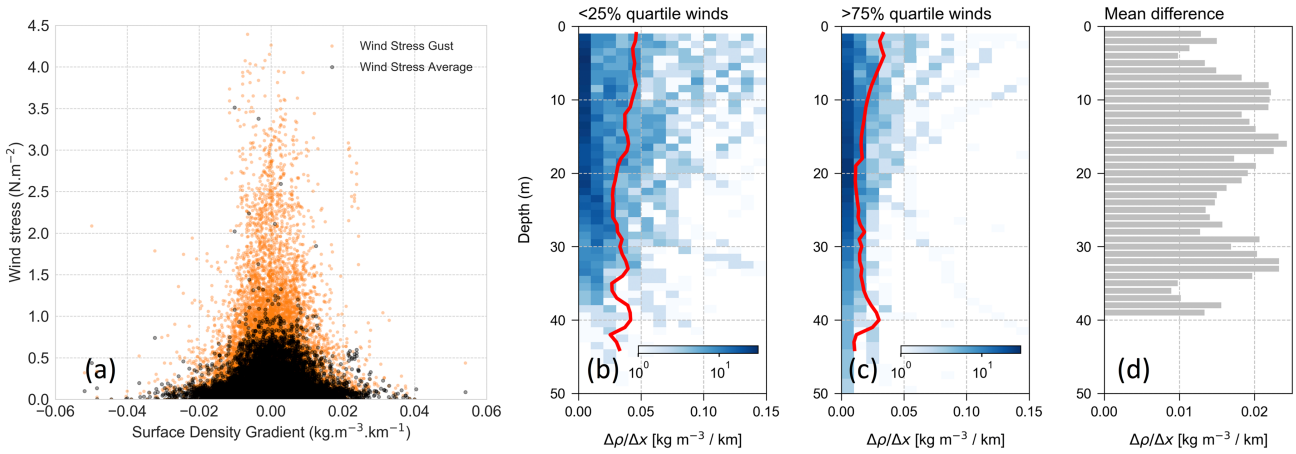

Figure 4. (a) Relation between surface lateral density gradients and wind stress (?) during the 2.5-month Sailbuoy deployment. Instantaneous 10-min wind gust stress is shown using gray dots. Seaglider measured lateral density gradients with depth at (b) low wind speeds (lower quartile) and (c) high wind speeds (upper quartile). The mean distribution of the gradients with depth are depicted by the red lines for each quartile. (d) The difference between the mean lateral density gradients for the high and low wind speed quartiles.

The heterogeneity in surface salinity ~4 days after the sea ice has melted from this location (Figure 1c) suggests that the open ocean near the sea-ice edge is almost immediately susceptible to lateral density gradients. These fronts have the potential to tilt from the vertical to the lateral and provide a restratifying buoyancy flux to the upper ocean over and above the existing buoyant freshwater layers associated with the recent sea-ice melt. Calculations of the vertical buoyancy flux associated with submesoscale mixed layer eddies (Boccaletti et al., 2007) from the glider data in this study show intermittent (weekly) periods of equivalent heat fluxes reaching up to 200 W m^{-2} (lower bound estimates given nonperpendicular transect of the buoyancy fronts by the glider). These equivalent heat fluxes, albeit intermittent, are of similar magnitude or larger than the solar heat flux received in this region during summer.

3.2. Surface-Layer Density Fronts Modified by Surface Winds

The paired Sailbuoy and Seaglider platforms provide high-resolution T and S data and concomitant wind speed measurements that allow us to assess the relationship between the fine-scale lateral gradients and wind. Interestingly, we observe a strong wind-front relationship in the study region, with higher wind stress resulting in a suppression of the stronger density gradients (Figure 4a). Sailbuoy data show that the largest density gradients (0.02–0.04 kg m^{-3} km^{-1}) decrease sharply at wind stress greater than ~0.3 N m^{-2}. Binning the data in 0.05 N m^{-2} intervals of wind stress reveals a sharp decrease in the density gradients at wind stress >0.4 N m^{-2}, while a Pearson correlation of $r = -0.77$ ($p \ll 0.01$) between the wind stress and density gradients underpins this as evidence for a coupled wind-front relationship.

A similar relationship is apparent from glider observations (upper 50 m; Figure S2), where the magnitude of submesoscale fronts separate out between the upper and lower quartiles of collocated ERA5 wind speeds (Figures 4b and 4c). High wind events (>75th percentile; 12.7 ± 2.6 m s^{-1}) are able to reduce lateral density gradients throughout the mixed layer by an average of 0.01 kg m^{-3} km^{-1} or reduce the median lateral fronts by 47 ± 12% compared with the quiescent wind phases (<25th percentile; 4.4 ± 1.2 m s^{-1}). This apparent wind-front interaction is consistent in the upper 40 m of the ocean with a slight decrease in the difference in the lateral gradients with depth (Figure 4d).

A plausible mechanism for these wind-front interactions, at the submesoscale, is termed thermohaline shear dispersion (first introduced in atmospheric studies by Moran & Pielke, 1994; and in high-resolution ocean simulations by Ferrari et al., 2001). To explain this mechanism, we pose that, in the Antarctic MIZ, energetic lateral density fronts dominated by salinity gradients slump under the action of baroclinic instability (e.g., Boccaletti et al., 2007; Fox-Kemper et al., 2008). Passing storms, and their associated higher wind forcing, enhance vertical shear stresses between the recently slumped surface layer and the layer below, driving shear-driven mixing by inertial oscillations that weaken the lateral density gradients in the upper ocean.

At these latitudes, inertial oscillations have a period of ~13 hr and a width of O(1 km), depending on the current velocity. In fairly shallow MIZ mixed layers (~40 m), the inertial oscillations will generate strong lateral currents and shear that can dissipate the lateral density fronts. Following the storm events, submesoscale fronts are thought to regenerate by the stirring of the fresher surface layer by mesoscale eddies. The modification of these fronts by stronger wind stress suggests that storm-driven mixing ultimately diffuses the submesoscale fronts by dispersion.

Our study region, and more broadly the Antarctic MIZ, is likely prone to such processes given that seasonal freshwater inputs by melting sea-ice result in strongly uncompensated fronts (Figure 2c), particularly given that the shear dispersion strength increases as the lateral buoyancy gradient squared (compensated fronts are balanced and thereby do not experience shear dispersion; Ferrari et al., 2001) and because of the strong wind forcing occurring in the Southern Ocean. How these processes are moderated in ice-covered oceans is yet to be observed and understood. However, the literature shows that lateral buoyancy gradients (and associated submesoscale fluxes) are present under Arctic sea ice (Timmermans et al., 2012) and so ice-induced shear stresses to the surface layer are likely to result in shear dispersion being active in ice-covered oceans.

4. Discussion and Summary

Following the rapid retreat of the Antarctic sea ice in early summer, in situ observations reveal lateral density fronts characterized by submesoscale salinity variations persisting to late summer. Resolving these surface-layer submesoscale fronts require sampling at sub-kilometer lateral scales and sub-daily temporal scales accounting for the rapidly-evolving effects of surface forcing (synoptic to seasonal variations in wind stress). Despite the suppression of submesoscale fronts by winds, they are not dissipated over the 3 months. This contrasts to the Bay of Bengal, where strong atmospheric forcing can adjust the basin-wide submesoscale gradients (Shroyer et al., 2019).

We expect these wind-front interactions to be ubiquitous over regions of large surface seasonal freshwater fluxes and strong surface winds such as the Southern Ocean MIZ. Resolving such fine-scale processes and associated submesoscale-induced vertical velocities (Klein & Lapeyre, 2009) are likely to have implications for accurately determining air-sea and air-sea-ice physical and biogeochemical fluxes (Swart et al., 2019). Current global climate model simulations show a large sensitivity to the magnitude and variability of vertical biophysical fluxes in the Southern Ocean (IPCC AR5). Therefore, subgrid scale processes are required to be parameterized correctly (Fox-Kemper et al., 2008) or otherwise represented directly in numerical simulations (Gruber et al., 2019). Future projections of the intensified and southward shifting westerly winds (positive Southern Annular Mode phase; Marshal, 2003) may have implications for submesoscale processes in the MIZ. This work suggests intensified winds are likely to reduce the lateral gradients associated with submesoscales. This may impact various important climate processes, such as air-sea-ice fluxes of heat and carbon and rates of biological production, due to modifications in upper ocean stratification and circulation.

Our results have implications for understanding sea-ice formation, melt, and extent in the Southern Ocean. Numerical studies or observations in the Arctic (e.g., Lu et al., 2015) suggest that submesoscale processes enhance both the lateral and vertical heat transport by ~100 W m^{-2} each, which can buffer heat loss to the atmosphere and delay sea-ice onset (Su et al., 2018). Lateral freshwater transport can directly impact timing and magnitude of sea-ice formation or melting, while lateral stirring can impact sea-ice distribution (e.g., widening of the MIZ - Manucharyan & Thompson, 2017). Our observations show for the first time in the Southern Ocean the persistence (over several months) of lateral density gradients in the MIZ. This provides a continuous potential for submesoscale restratification (e.g., du Plessis et al., 2017), reducing the potential for mixing and thus ventilation of warm and carbon rich Circumpolar Deep Waters beneath the stratified winter water layer. We suggest future observational efforts (e.g., glider surveys, towed instruments), sampling at the appropriate time and space scales, should focus on the transition zone between open water and sea ice to further unravel the magnitude and scales of atmosphere-ocean processes at the edge of and under sea ice.

Acknowledgments
This work was supported by the following grants: Wallenberg Academy Fellowship (WAF 2015.0186), Swedish Research Council (VR 2019-04400), STINT-NRF Mobility Grant and NRF-SANAP (SNA170522231782), and AFT was supported by the Terrestrial Hazard Observations and Reporting (THOR) and ONR (N00014-19-1-2421). We thank Sea Technology Services (STS), SANAP, the captain and crew of the S.A. Agulhas II for their field-work/technical assistance. We thank David Peddie of Offshore Sensing AS for assistance with the Sailbuoy. S.S. is grateful to Geoff Shilling and Craig Lee (APL, University of Washington) for hosting the gliders on IOP and the technical advice provided. ERA5 data are generated using Copernicus Climate Change Service Information, available online (www.ecmwf.int/en/forecasts/datasets/archive-datasets/reanalysis-datasets/era5). Data are available online (ftp://roammiz.com via anonymous login).

References

Abernathey, R., Cerovecki, I., Holland, P., Newsom, E., Mazloff, M., & Talley, L. D. (2016). Water-mass transformation by sea ice in the upper branch of the Southern Ocean overturning. *Nature Geoscience*, *9*(8), 596–601. https://doi.org/10.1038/ngeo2749

Adams, K., MacKinnon, J., Lucas, A. J., Nash, J., Shroyer, E., & Farrar, J. T. (2019). Multi-platform observations of small-scale lateral mixed layer variability in the northern Bay of Bengal. *Deep Sea Research Part II*, *168*. https://doi.org/10.1016/j.dsr2.2019.07.017

Boccaletti, G., Ferrari, R., & Fox-Kemper, B. (2007). Mixed layer instabilities and restratification. *Journal of Physical Oceanography*, *37*, 2228–2250. https://doi.org/10.1175/JPO3101.1

Campbell, E. C., Wilson, E. A., Moore, G. W. K., Riser, S. C., Brayton, C. E., Mazloff, M. R., & Talley, L. D. (2019). Antarctic offshore polynyas linked to Southern Hemisphere climate anomalies. *Nature*, *570*(7761), 319–325. https://doi.org/10.1038/s41586-019-1294-0

du Plessis, M., Swart, S., Ansorge, I. J., & Mahadevan, A. (2017). Submesoscale processes accelerate seasonal restratification in the Subantarctic Ocean. *Journal of Geophysical Research*, *122*, 2960–2975. https://doi.org/10.1002/2016JC012494

du Plessis, M. D., Swart, S., Ansorge, I. J., Mahadevan, A., & Thompson, A. F. (2019). Southern Ocean seasonal restratification delayed by submesoscale wind-front interactions. *Journal of Physical Oceanography*, *49*(4), 1035–1053. https://doi.org/10.1175/JPO-D-18-0136.1

Ferrari, R., Paparella, F., Rudnick, D. L., & Young, W. R. (2001). The temperature-salinity relationship of themixed layer. In P. Müller & D. Henderson (Eds.), *Proceedings of the 12th 'Aha Huliko' a Hawaiian Winter Workshop* (pp. 95–104). Department of Oceanography, University of Hawaii (*From Stirring to Mixing in a Stratified Ocean*).

Fox-Kemper, B., Ferrari, R., & Hallberg, R. (2008). Parameterization of mixed layer Eddies. Part I: Theory and diagnosis. *Journal of Physical Oceanography*, *38*, 1145–1165. https://doi.org/10.1175/2007JPO3792.1

Ghani, M. H., Hole, L. R., Fer, I., Kourafalou, V. H., Wienders, N., Kang, H., et al. (2014). The Sailbuoy remotely-controlled unmanned vessel: Measurements of near surface temperature, salinity and oxygen concentration in the northern Gulf of Mexico. *Methods in Oceanography*, *10*, 104–121. https://doi.org/10.1016/j.mio.2014.08.001

Gruber, N., Landschützer, P., & Lovenduski, N. S. (2019). The variable Southern Ocean carbon sink. *Annual Review of Marine Science*, *11*(1), 159–186. https://doi.org/10.1146/annurev-marine-121916-063407

Horvat, C., Tziperman, E., & Campin, J.-M. (2016). Interaction of sea ice floe size, ocean eddies, and sea ice melting. *Geophysical Research Letters*, *43*, 8083–8090. https://doi.org/10.1002/2016GL069742

Hosegood, P., Gregg, M. C., & Alford, M. H. (2006). Sub-mesoscale lateral density structure in the oceanic surface mixed layer. *Geophysical Research Letters*, *33*, L22604. https://doi.org/10.1029/2006GL026797

Johnson, G. C., Schmidtko, S., & Lyman, J. M. (2012). Relative contributions of temperature and salinity to seasonal mixed layer density changes and horizontal density gradients. *Journal of Geophysical Research*, *117*, C04015. https://doi.org/10.1029/2011JC007651

Johnson, L., Lee, C. M., & D'Asaro, E. A. (2016). Global Estimates of Lateral Springtime Restratification. *Journal of Physical Oceanography*, *46*, 1555–1573. https://doi.org/10.1175/JPO-D-15-0163.1

Klein, P., & Lapeyre, G. (2009). The oceanic vertical pump induced by mesoscale and submesoscale turbulence. *Annual Review of Marine Science*, *1*(1), 351–375. https://doi.org/10.1146/annurev.marine.010908.163704

Lin, X., Zhai, X., Wang, Z., & Munday, D. R. (2018). Mean, variability, and trend of Southern Ocean wind stress: Role of wind fluctuations. *Journal of Climate*, *31*, 3557–3573. https://doi.org/10.1175/JCLI-D-17-0481.1

Lu, K., Weingartner, T., Danielson, S., Winsor, P., Dobbins, E., Martini, K., & Statscewich, H. (2015). Lateral mixing across ice meltwater fronts of the Chukchi Sea shelf. *Geophysical Research Letters*, *42*, 6754–6761. https://doi.org/10.1002/2015GL064967

Mahadevan, A., Tandon, A., & Ferrari, R. (2010). Rapid changes in mixed layer stratification driven by submesoscale instabilities and winds. *Journal of Geophysical Research*, *115*, C03017. https://doi.org/10.1029/2008JC005203

Manucharyan, G. E., & Thompson, A. F. (2017). Submesoscale Sea ice-ocean interactions in marginal ice zones. *Journal of Geophysical Research: Oceans*, *122*, 9455–9475. https://doi.org/10.1002/2017JC012895

Marshall, D. P., & Zanna, L. (2014). A conceptual model of ocean heat uptake under climate change. *Journal of Climate*, *27*(22), 8,444–8,465. https://doi.org/10.1175/JCLI-D-13-00344.1

Marshall, G. J. (2003). Trends in the Southern Annular Mode from observations and reanalyses. *Journal of Climate*, *16*, 4134–4143.

Massom, R. A., & Stammerjohn, S. E. (2010). Antarctic Sea ice change and variability—Physical and ecological implications. *Polar Science*, *4*(2), 149–186. https://doi.org/10.1016/j.polar.2010.05.001

Moran, M. D., & Pielke, R. A. (1994). Delayed shear enhancement in mesoscale atmospheric dispersion. United States. American Meteorological Society annual meeting, Nashville, TN (United States), 23-28 Jan 1994.

Pellichero, V., Sallée, J.-B., Schmidtko, S., Roquet, F., & Charrassin, J.-B. (2017). The ocean mixed layer under Southern Ocean sea-ice: Seasonal cycle and forcing. *Journal of Geophysical Research: Oceans*, *122*, 1608–1633. https://doi.org/10.1002/2016JC011970

Ramachandran, S., Tandon, A., Mackinnon, J., Lucas, A. J., Pinkel, R., Waterhouse, A. F., et al. (2018). Submesoscale processes at shallow salinity fronts in the Bay of Bengal: Observations during the winter monsoon. *Journal of Physical Oceanography*, *48*, 479–509. https://doi.org/10.1175/JPO-D-16-0283.1

Rudnick, D. L., & Ferrari, R. (1999). Compensation of horizontal temperature and salinity gradients in the ocean mixed layer. *Science*, *283*(5401), 526–529. https://doi.org/10.1126/science.283.5401.526

Schmidt, K. M., Swart, S., Reason, C., & Nicholson, S. -A. (2017). Evaluation of satellite and reanalysis wind products with in situ Wave Glider wind observations in the Southern Ocean. *Journal of Atmospheric and Oceanic Technology*, *34*(12), 2551–2568. https://doi.org/10.1175/JTECH-D-17-0079.1

Shroyer, E. L., Gordon, A. L., Jaeger, G. S., Freilich, M., Waterhouse, A. F., & Farrar, J. T. (2019). Upper layer thermohaline structure of the Bay of Bengal during the 2013 northeast monsoon. *Deep Sea Research Part II: Topical Studies in Oceanography*, 104630. https://doi.org/10.1016/j.dsr2.2019.07.018

Su, Z., Wang, J., Klein, P., Thompson, A. F., & Menemenlis, D. (2018). Ocean submesoscales as a key component of the global heat budget. *Nature Communications*, *9*(1), 775. https://doi.org/10.1038/s41467-018-02983-w

Swart, S., Gille, S. T., Delille, B., Josey, S., Mazloff, M., Newman, L., et al. (2019). Constraining Southern Ocean air-sea-ice fluxes through enhanced observations. *Frontiers in Marine Science*, *6*, 421. https://doi.org/10.3389/fmars.2019.00421

Swart, S., Thomalla, S. J., & Monteiro, P. M. S. (2015). The seasonal cycle of mixed layer characteristics and phytoplankton biomass in the Sub-Antarctic Zone: A high-resolution glider experiment. *Journal of Marine Systems*. https://doi.org/10.1016/j.jmarsys.2014.06.002

Thomas, L. N., & Ferrari, R. (2008). Friction, frontogenesis, and the stratification of the surface mixed layer. *Journal of Physical Oceanography*, *38*, 2501–2518.

Thomas, L. N., & Lee, C. M. (2005). Intensification of ocean fronts by down-front winds. *Journal of Physical Oceanography*, *35*, 1086–1102.

Thomas, L. N., Tandon, A., & Mahadevan, A. (2008). Submesoscale processes and dynamics. In *Ocean Modeling in an Eddying Regime*, *Geophys. Monogr.* (Vol. 177, pp. 17–38). Washington, DC: American Geophysical Union. https://doi.org/10.1029/177GM04

Thomas, L. N., Taylor, J. R., Ferrari, R., & Joyce, T. M. (2013). Symmetric instability in the Gulf Stream. *Deep Sea Research, Part II*, *91*, 96–110.

Thompson, A. F., Lazar, A., Buckingham, C., Naveira Garabato, A. C., Damerell, G. M., & Heywood, K. J. (2016). Open-ocean submesoscale motions: A full seasonal cycle of mixed layer instabilities from gliders. *Journal of Physical Oceanography*, *46*, 1285–1307. https://doi.org/10.1175/JPO-D-15-0170.1

Timmermans, M.-L., Cole, S., & Toole, J. (2012). Horizontal density structure and restratification of the Arctic Ocean surface layer. *Journal of Physical Oceanography*, *42*, 659–668.

Timmermans, M.-L., Toole, J., Proshutinsky, A., Krishfield, R., & Plueddemann, A. (2008). Eddies in the Canada Basin, Arctic Ocean, observed from ice-tethered profilers. *Journal of Physical Oceanography*, *38*, 133–145. https://doi.org/10.1175/2007JPO3782.1

Timmermans, M.-L., & Winsor, P. (2013). Scales of horizontal density structure in the Chukchi Sea surface layer. *Continental Shelf Research*, *52*, 39–45. https://doi.org/10.1016/j.csr.2012.10.015

Toole, J. M., Timmermans, M.-L., Perovich, D. K., Krisheld, R. A., Proshutinsky, A., & Richter-Menge, J. A. (2010). Influences of the ocean surface mixed layer and thermohaline stratification on Arctic Sea ice in the central Canada Basin. *Journal of Geophysical Research*, *115*, C10018. https://doi.org/10.1029/2009JC005660

von Appen, W.-J., Wekerle, C., Hehemann, L., Schourup-Kristensen, V., Konrad, C., & Iversen, M. H. (2018). Observations of a submesoscale cyclonic filament in the marginal ice zone. *Geophysical Research Letters*, *45*, 6141–6149. https://doi.org/10.1029/2018GL077897

Walin, G. (1982). On the relation between sea-surface heat flow and thermal circulation in the ocean. *Tellus*, *34*, 187–195. https://doi.org/10.1111/j.2153-3490.1982.tb01806.x

Wulff, T., Bauerfeind, E., & von Appen, W.-J. (2016). Physical and ecological processes at a moving ice edge in the Fram Strait as observed with an AUV. *Deep Sea Research*, *115*, 253–264. https://doi.org/10.1016/j.dsr.2016.07.001

Yuan, X. (2004). High-wind-speed evaluation in the Southern Ocean. *Journal of Geophysical Research*, *109*, D13101. https://doi.org/10.1029/2003JD004179

Geophysical Research Letters

Supporting Information for

Submesoscale fronts in the Antarctic marginal ice zone and their response to wind forcing

Sebastiaan Swart[1, 2], Marcel D. du Plessis[2, 3], Andrew F. Thompson[4], Louise C. Biddle[1], Isabelle Giddy[1, 2], Torsten Linders[1], Martin Mohrmann[1], Sarah-Anne Nicholson[3]

[1] Department of Marine Sciences, University of Gothenburg, Gothenburg, Sweden
[2] Department of Oceanography, University of Cape Town, Rondebosch, South Africa
[3] Southern Ocean Carbon-Climate Observatory (SOCCO), CSIR, Cape Town, South Africa
[4] Environmental Science and Engineering, California Institute of Technology, Pasadena, USA

Contents of this file

Introduction

This supporting information provides additional information and data pertaining to the choice of reanalysis wind products used in this study and methodology used to estimate observed lateral property gradients in the upper mixed layer of the ocean.

Three gridded reanalysis wind products are compared with *in situ* measured wind speed data (Figure S1a) observed by the autonomous Sailbuoy platform (Figure S1c). The Sailbuoy winds are averaged 6-hourly to directly compare with the reanalysis winds (Figure S1b) and it is shown that CFS and ERA5 wind products compare better than NCEP with the Sailbuoy observations. Thus we use ERA5 winds in this study.

Only the upper portion of successive climb and dive profiles from a Seaglider are used to resolve surface layer lateral temperature, salinity and density gradients in the upper mixed layer of the ocean (Figure S2a). We report here the distributions of horizontal distance and time between the sequential climb-dive glider profiles (Figure S2b & c) to illustrate the time-space scales at which we resolve the mixed layer gradients. This approach allows us to obtain high-resolution 'snapshot' sampling of mixed layer lateral gradients at each glider dive interval, which is approximately every 4 hours.

The field data presented here originates from the deployment of a Sailbuoy and Seaglider between December 2018 and March 2019 as part of the Robotic Observations and Modelling of the Marginal Ice Zone (ROAM-MIZ) project.

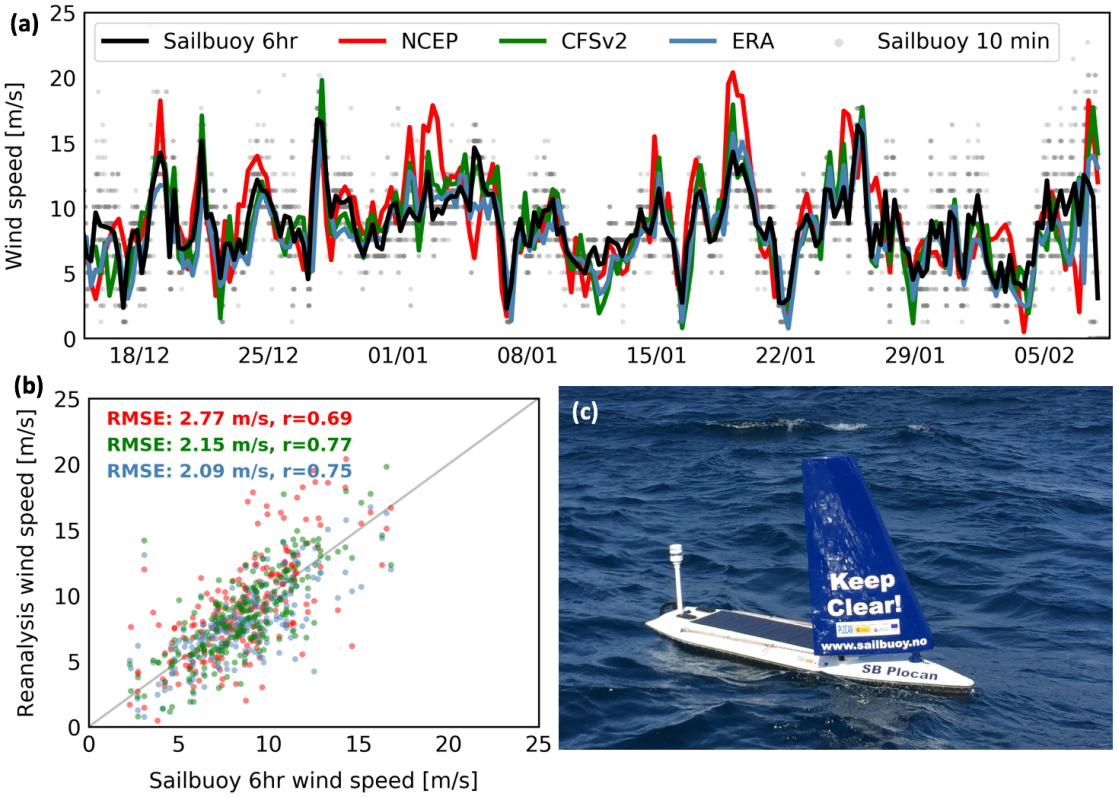

Figure S1. (a) Comparison of *in situ* Sailbuoy wind speed (6 hourly averages, black line) with reanalysis wind products (ERA5, NCEP, CFSv2). The 10-minute Sailbuoy wind speeds are shown in grey dots. **(b)** Correlation analysis between *in situ* and reanalysis wind speeds with RMSE and correlation coefficients reported. **(c)** The Sailbuoy platform with the Airmar 200WX sensor on the stern.

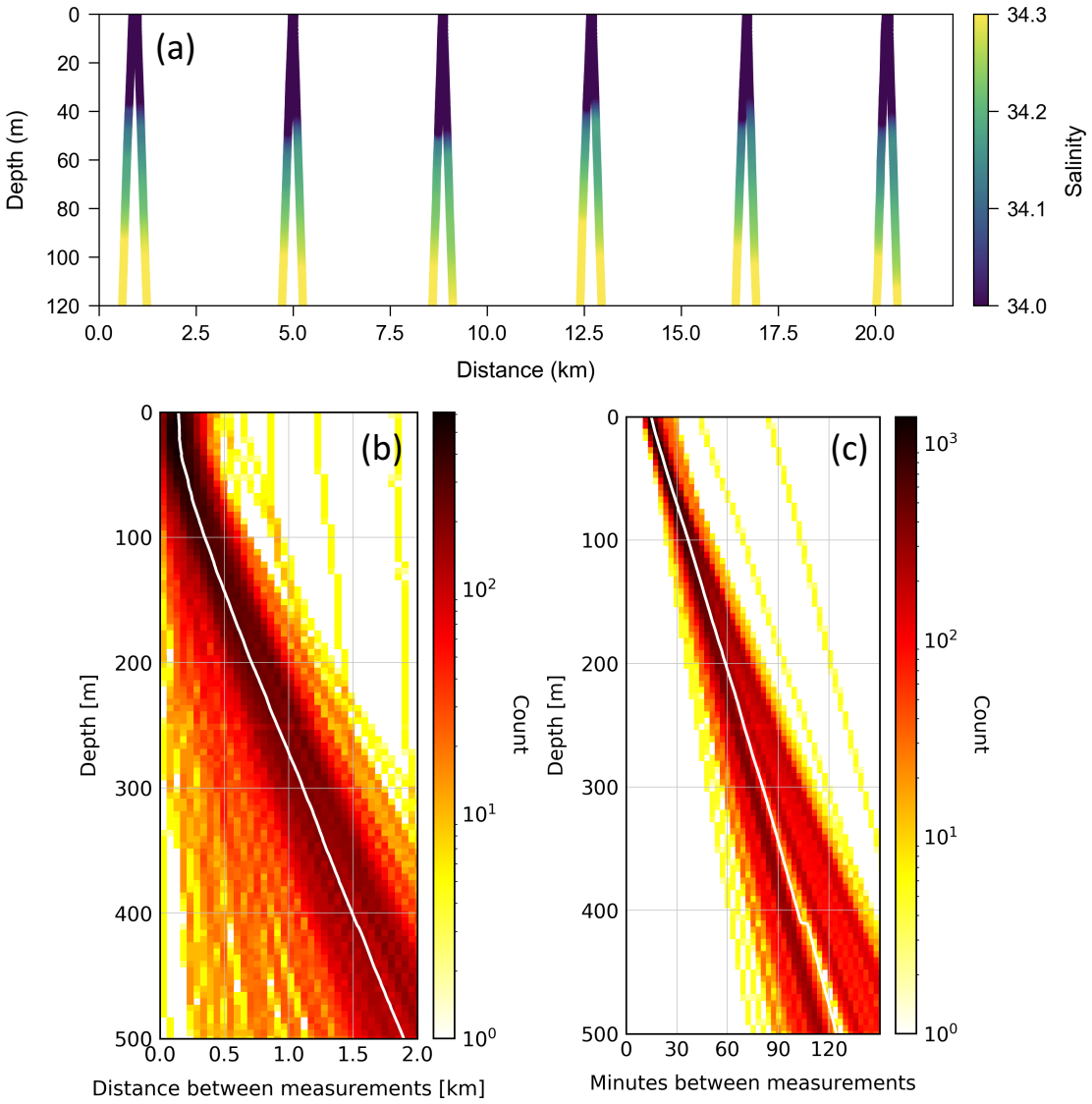

Figure S2. (a) The Seaglider climb-dive sequence showing salinity data in the upper ocean. Distribution of the **(b)** horizontal distance (km) and **(c)** time (minutes) between sequential glider climb and dive profiles. The median is shown in the white line.

Paper II

Stirring of Sea-Ice Meltwater Enhances Submesoscale Fronts in the Southern Ocean

I. Giddy, S. Swart, M. du Plessis, A.F. Thompson, S-A Nicholson
Journal of Geophysical Research: Oceans, **126(4), e2020JC016814** (2021)

JGR Oceans

RESEARCH ARTICLE
10.1029/2020JC016814

Stirring of Sea-Ice Meltwater Enhances Submesoscale Fronts in the Southern Ocean

I. Giddy[1,2,3], S. Swart[1,2], M. du Plessis[2,3], A. F. Thompson[4], and S.-A. Nicholson[3]

[1]Department of Oceanography, University of Cape Town, Rondebosch, South Africa, [2]Department of Marine Sciences, University of Gothenburg, Gothenburg, Sweden, [3]Southern Ocean Carbon-Climate Observatory, CSIR, Cape Town, South Africa, [4]Environmental Science and Engineering, California Institute of Technology, Pasadena, CA, USA

Key Points:

- Sea-ice meltwater controls the buoyancy of the mixed layer during early summer
- Mixed layer eddies grow from mesoscale meltwater lateral gradients but are confined to the surface boundary layer
- Observations suggest that mixed layer variability at submesoscales is dominated by wind-front interactions

Supporting Information:

Supporting Information may be found in the online version of this article.

Correspondence to:

I. Giddy,
isgiddy@gmail.com

Citation:

Giddy, I., Swart, S., du Plessis, M., Thompson, A. F., & Nicholson, S.-A. (2021). Stirring of sea-ice meltwater enhances submesoscale fronts in the Southern Ocean. *Journal of Geophysical Research: Oceans*, *126*, e2020JC016814. https://doi.org/10.1029/2020JC016814

Received 22 SEP 2020
Accepted 2 MAR 2021

Abstract In the sea-ice-impacted Southern Ocean, the spring sea-ice melt and its impact on physical processes set the rate of surface water mass modification. These modified waters will eventually subduct near the polar front and enter the global overturning circulation. Submesoscale processes modulate the stratification of the mixed layer (ML) and ML properties. Sparse observations in polar regions mean that the role of submesoscale motions in the exchange of properties across the base of the ML is not well understood. The goal of this study is to determine the interplay between sea-ice melt, surface boundary layer forcing, and submesoscale flows in setting properties of the surface ML in the Antarctic marginal ice zone. High-resolution observations suggest that fine-scale lateral fronts arise from either/both mesoscale and submesoscale stirring of sea-ice meltwater anomalies. The strong salinity-driven stratification at the base of the ML confines these fronts to the upper ocean, limiting submesoscale vertical fluxes across the ML base. This strong stratification prevents the local subduction of modified waters by submesoscale flows, suggesting that the subduction site that links to the global overturning circulation does not correspond with the location of sea-ice melt. However, surface-enhanced fronts increase the potential for Ekman-driven cross-frontal flow to modulate the stability of the ML and ML properties. The parameterization of submesoscale processes in coupled-climate models, particularly those contributing to the Ekman buoyancy flux, may improve the representation of ML heat and freshwater transport in the ice-impacted Southern Ocean during summer.

Plain Language Summary Sea-ice melt around Antarctica is an annual event in which the state of the surface ocean is transformed, during which over 15 trillion liters of freshwater enter the upper ocean. This fresh layer separates the upper ocean from the deep ocean and suppresses the exchange of heat and gases—like carbon dioxide—between the deep ocean and the atmosphere, with important implications for the climate system. Using state-of-the-art autonomous underwater gliders, we observed key physical properties of the surface ocean following the melt of sea-ice. The presence of fine-scale fronts (sharp changes in density), of less than 10 km at horizontal scales, revealed that sea-ice melt not only stabilizes the upper ocean, but also provides additional energy for small eddies and filaments to form. While the eddies are unable to extend deeper than the fresher surface layer, they enhance the ocean response to winds. These findings may contribute to the improvement of global climate models and our understanding of how the ocean will react to changes in sea-ice under a warmer climate.

1. Introduction

Around Antarctica, sea-ice forms a relatively thin (~1 m) insulative layer over the ocean's surface, covering an area of ~19 million km^2 (roughly equivalent in size to the Antarctic continent itself) and retreating to an area of ~3 million km^2 in summer (Parkinson, 2014). The expansion and contraction of sea-ice is important for Southern Ocean heat uptake since it modulates the transfer of heat between the atmosphere and deep waters through its influence on the salinity and density of the surface waters (Bitz et al., 2006; Kirkman & Bitz, 2011). However, climate models continue to diverge in their representation of heat and carbon exchange in the Southern Ocean (Frölicher et al., 2015). With the paucity of observations south of 50°S (Newman et al., 2019; Swart et al., 2019), some of the model uncertainties can likely be attributed to misrepresented atmosphere-ocean processes associated with the sea-ice-impacted Southern Ocean (Chemke & Polvani, 2020).

The seasonal melt of Antarctic sea-ice is the primary source of freshwater in the Southern Ocean south of 50°S (Abernathey et al., 2016). When the melting of sea-ice occurs in the spring, freshwater (more than 15 trillion liters) is reintroduced into the surface waters and advected by Ekman processes (Speer et al., 2000) northwards. This phenomenon is associated with net freshening and lightening of the mixed layer (ML) (Pellichero et al., 2017). Through the resultant impact on water mass transformation (Abernathey et al., 2016), the ice-impacted ML acts as a conduit between sea-ice dynamics and the global ocean circulation (e.g., Haumann et al., 2016; Pellichero et al., 2018).

At the northern edge of the sea-ice, a dynamic band of low concentration sea-ice defines the marginal ice zone (MIZ), separating the open ocean from the ice pack. One-dimensional mixing processes associated with local sea-ice melt and vertical mixing have been shown to dominate upper ocean physics in MIZs (Dewey et al., 2017; Smith et al., 2018). However, it has been demonstrated by theory and models that submesoscale flows in MIZs interact with horizontal gradients in density to modify ML structure (Horvat et al., 2016; Lu et al., 2015; Manucharyan & Thompson, 2017), and by observations in the Arctic (Brenner et al., 2020; Koenig et al., 2020; Timmermans & Winsor, 2013) and more recently in the Antarctic (e.g., Biddle & Swart, 2020; Swart et al., 2020).

ML baroclinic instabilities (MLIs, Fox-Kemper et al., 2008), a class of submesoscale flows, are characterized dynamically by order one Richardson and Rossby numbers (McWilliams, 2016; Thomas et al., 2008). MLIs give rise to mixed layer eddies (MLEs), which can increase surface stratification through an eddy overturning and induce large vertical velocities and fluxes. In this way, surface stratification is influenced both diabatically through heat gain and loss to the atmosphere, and adiabatically, through dynamical restratification by frontal slumping. While a range of submesoscale flows can impact surface boundary layer variability, MLEs, associated with baroclinic instabilities, are ubiquitous in the surface ocean.

MLI has the potential to structure the upper ocean in sea-ice-impacted regions. A combination of simulations and observations by Horvat et al. (2016) and Lu et al. (2015) show MLI can be formed from freshwater fronts by melted sea-ice and result in the horizontal mixing of heat, enhancing the melt of nearby ice floes. Similarly, Manucharyan and Thompson (2017) model MLI which feed off existing frontal structures in a MIZ. The submesoscale structuring of fronts and filaments leads to intermittent fluxes of heat and sea-ice which can contribute to the structuring of the upper ocean in MIZs. MLEs, which grow from the MLI, may contribute to the flux of underlying warmer water to the surface. Adding a layer of complexity, von Appen et al. (2018) propose that subduction associated with baroclinic instabilities and ML fronts is enhanced due to increased mixing from cabbeling—when two water masses of the same density mix and the resultant water mass is denser. MLEs tend to give rise to increased stratification; however, Brenner et al. (2020) could not conclusively show that eddies formed from baroclinic instabilities were a leading factor in setting the ML stratification. Their study suggests that MLEs may not be sufficiently strong in MIZs to impact upper-ocean stratification. The results from ice-covered (Timmermans et al., 2012) and ice-free (Timmermans & Winsor, 2013) Arctic MIZ observational campaigns provide evidence for submesoscale restratification, albeit with potential density spectral slopes steeper (k^{-3}) than the upper ocean boundary layer in the open ocean mid-latitudes (k^{-2}), suggesting that different physical mechanisms are controlling the horizontal structure of the upper ocean compared to mid-latitudes. In the Antarctic, evidence of active MLI has been observed (Biddle & Swart, 2020), even under suppressed surface forcing (reduced wind and solar heat loss from sea-ice cover), emphasizing the role of sea-ice fronts in the production of submesoscale instabilities. While it has been shown that MLI is actively structuring the ML in MIZs—through restratification or lateral and vertical mixing—it remains uncertain in observations whether MLI is strong enough to result in significant vertical fluxes across the base of the ML in the strongly stratified MIZs.

Observations of wind-front interactions in ice-free MIZs yield contrasting results between the studies. Under winter conditions near the Arctic MIZ, Koenig et al. (2020) provide evidence of sustained turbulence by forced symmetric instabilities associated with downfront winds and heat loss from the surface layer, which extract potential vorticity from the water column at submesoscale fronts. Conversely, Brenner et al. (2020) found that upfront winds lead to frontogenesis on time scales shorter than Ekman dynamics. The Antarctic MIZ differs from the Arctic in that the Antarctic sea-ice sector experiences strong, event-scale storms (Patoux et al., 2009; Vichi et al., 2019). Swart et al. (2020) suggest that in the stormy conditions of the Antarctic MIZ, wind forced thermohaline shear dispersion, in combination with slumping by MLEs, act to reduce the

strength of freshwater surface layer fronts. When the winds subside, fronts are able to reform by the stirring of the fresher surface layer by mesoscale eddies and therefore persist well into the summer.

Submesoscale motions and instabilities are seasonal across the world's oceans, with stronger flows under winter/low ML stratification conditions (Callies et al., 2015). In the Antarctic MIZ during summer, solar heating and freshwater input from bulk sea-ice melt both act to stratify the surface layer (Swart et al., 2020), similar to other freshwater-driven systems (e.g., Gulf of Mexico; Luo et al., 2016). However, while the freshwater influx stratifies the ML, the dispersing freshwater, originating from sea-ice melt, also introduces mesoscale fronts from which submesoscale instabilities can form. The dynamic nature of the Southern Ocean surface layer, influenced by strong winds and passing storms, maintains stratification weaker than otherwise. This sets up a unique interplay between submesoscale ML fronts, stratifying 1D ocean-atmosphere buoyancy fluxes and destratifying mechanical mixing by winds. Dissecting these interactions and their seasonal evolution is the topic of this study.

The preceding research suggests that the properties of the surface layer in polar MIZs are not driven purely by one-dimensional processes. Here, we hypothesize that the persistence of submesoscale activity in the ice-free Antarctic MIZ is associated with northwards advecting freshwater from sea-ice melt. We use high resolution in situ data in combination with satellite and reanalysis products to interrogate the evolution of the ML in the Antarctic MIZ, from immediately after sea-ice melt to the end of summer.

2. Data and Methods

2.1. Study Region

The Robotic Observations and Modeling of the Marginal Ice Zone (ROAM-MIZ) project (2019–2023) involves a field campaign set in the Antarctic MIZ, south of the southern boundary of the Antarctic circumpolar current (ACC) (Figure 1a), with a key objective of characterizing the role of submesoscale flows on stratification, air-sea fluxes and mixed-layer-interior exchange in the sea-ice-impacted Southern Ocean. Satellite color imagery (from 7 January, at a nominal spatial resolution of ∼0.3 km, Figure 1b) reveal surface chlorophyll concentrations that suggest the presence of both mesoscale and submesoscale variability. The study region is covered entirely by sea-ice during the winter (Figure 1d).

The maximum and minimum sea-ice extent for the 2018–2019 season occurred on September 3, 2018 and February 23, 2019, respectively (computed as the maximum integral of pixels with a sea-ice concentration >0.15 from AMSR2; Figures 1a and 1d). The surface ocean is impacted by ocean-atmosphere buoyancy fluxes (here confined to surface heating defined as the sum of shortwave, longwave, latent and sensible heat, plus evaporation-precipitation (E-P); refer to Section 2.4 for a more detailed explanation of the data used). At the ROAM-MIZ site, ocean-atmosphere buoyancy fluxes peak on 25 December at 256 W m^{-2}, largely attributable to incoming solar heat (Figures 2a and 2b). Precipitation events occurred throughout the summer season (Figure 2b). The mean wind stress is 0.09 $\pm$ 0.08 N m^{-2} with three wind events (storms) reaching 0.4–0.6 N m^{-2} (Figure 2c). Wind direction was variable, but predominantly westerly.

2.2. Seaglider Mission and Data Processing

A Seaglider was deployed at 60°S, 0°E, 445 km south of the southern boundary of the ACC, estimated using the criteria of Swart et al. (2010), based on contours of SSH (Figure 1b). The deployment commenced in early summer (December 14, 2018), just four days after the melt of sea-ice when the surface heat flux into the ocean was almost at its maximum (Figure 1d), and continued for 102 days, until 26 March. The Seaglider was piloted in a “bow-tie” sampling pattern completing repeat transects of approximately 20 km in length. The bow-tie sampling strategy was adopted as there is no preferred orientation of lateral gradients at submesoscales. Thus the bow-tie pattern provides a statistical representation of the lateral gradients in the region (see Section 2.5). To assess the background mesoscale field, at the start and middle of the mission, two north-south mesoscale transects (185 and 120 km, respectively) were completed. In total, the Seaglider covered a distance of 2,074 km, collecting 974 profiles, 1,000 m in depth. Noting that Seagliders sample in both time and space, for the analysis, we interpret the data in an Eulerian sense, similar to the approach used by du Plessis et al. (2019).

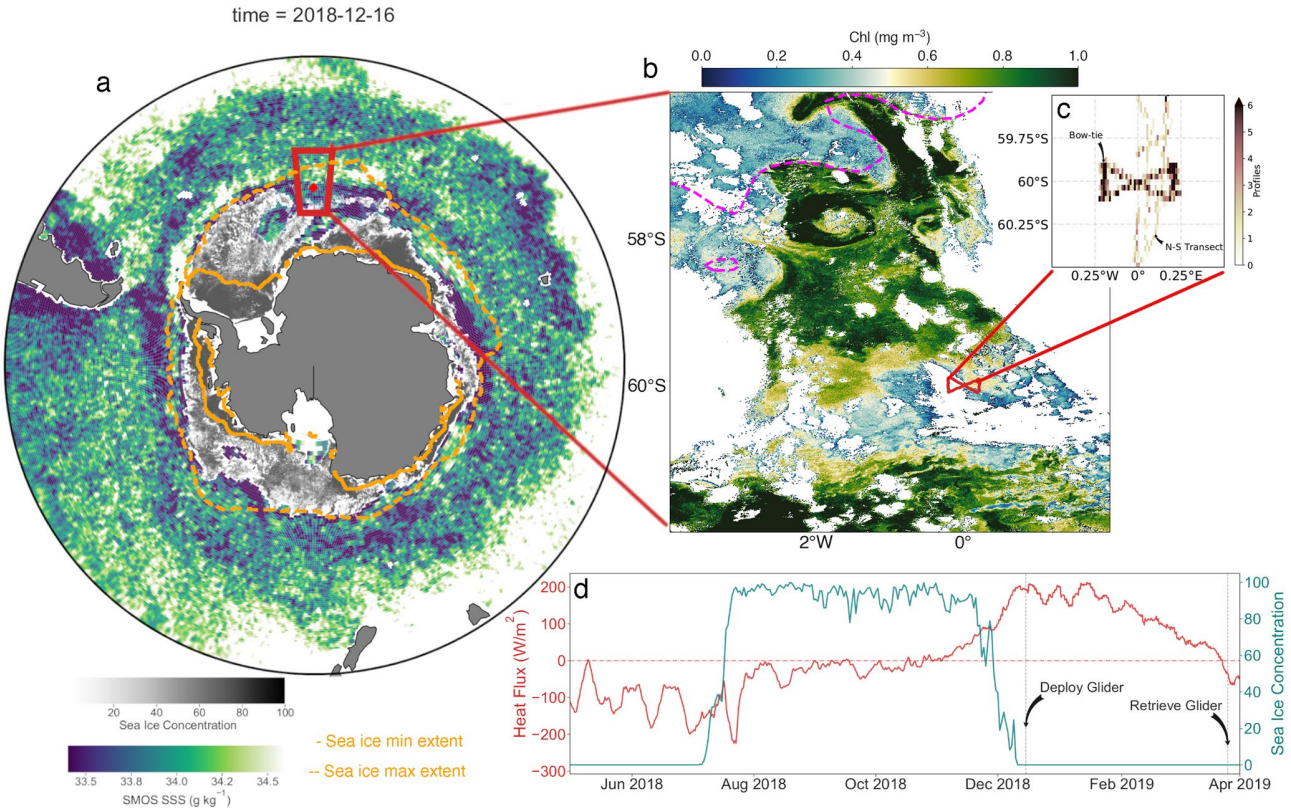

Figure 1. (a) Regional view of the ROAM-MIZ study site, showing SMOS salinity on December 16, 2018, and the sea-ice concentration at the time of deployment (December 14, 2018). Maximum and minimum sea-ice extent for the year 2018–2019 are contoured in dotted and solid orange lines, respectively. (b) A snapshot of Sentinal-3A OCLI Chlorophyll Ocean Color in cloud-free conditions on January 6, 2020, during the deployment. The southern boundary of the ACC is demarcated by the dashed magenta line. The deployment is marked by the red bow-tie, reflecting the sampling pattern that was maintained for the duration of the deployment. (c) Heat map showing the spatial distribution of profiles captured by the Seaglider. (d) Annual time series of net downward heat flux and sea-ice concentration at 60°S, 0°E. Zero heat flux is marked with a dash-dot red line. The time of deployment and retrieval of the Seaglider is indicated by the black arrows. SMOS, Soil Moisture Ocean Salinity.

The Seaglider sampled temperature and conductivity (salinity) nominally at 0.2 Hz, equating to a vertical resolution of 0.2–1.5 m, with an average resolution of 0.5 m in the upper 400 m. The Seaglider data were prepared for analysis using GliderTools (Gregor et al., 2019). Salinity and temperature were converted to absolute salinity and conservative temperature, respectively, using the Gibbs Seawater toolbox (McDougall & Barker, 2011). Finally, the Seaglider conductivity and temperature data were corrected against the calibrated shipborne data from conductivity-temperature-depth (CTD) casts at the deployment and retrieval of the Seaglider (as per Swart et al., 2015). The mixed layer depth (MLD) is calculated from the Seaglider data using the density difference criteria of 0.03 kg m^{-3} from a reference depth of 10 m (de Boyer Montgut et al., 2004).

2.3. Thermal Lag Correction of Salinity

Small errors in profile-to-profile temperature and salinity estimates can artificially enhance estimates of lateral buoyancy gradients. The accurate estimation of submesoscale fluxes, which are a function of lateral buoyancy gradients, demands minimizing instrumental error.

Salinity is inferred from measured conductivity and temperature. A temperature sensor measures seawater temperature outside of the conductivity cell, while a conductivity sensor measures seawater conductivity inside of the conductivity cell. This spatiotemporal mismatch introduces an offset in the temperature of the water that the conductivity sensor actually measures, resulting in thermal lag that needs to be corrected to

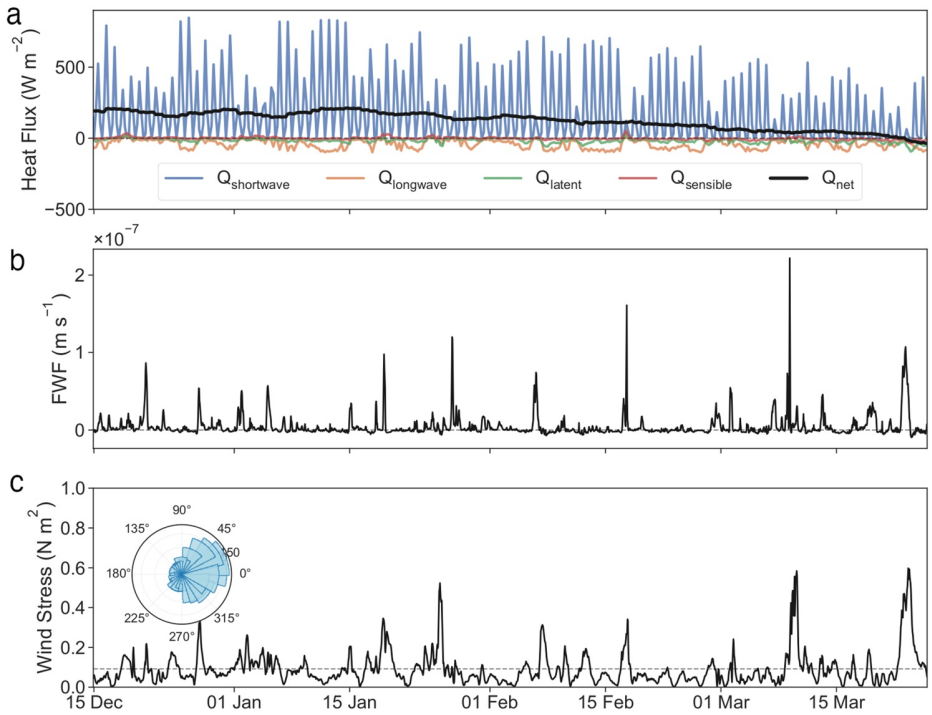

Figure 2. Summer time series of surface forcing from ERA5 reanalysis at the ROAM-MIZ site between December 2018 and March 2019. (a) Surface heat flux decomposed into its components: shortwave, longwave, sensible, and latent heat flux with the sum of components, the net surface heat flux plotted in black. A running mean of 24 h is applied to the net surface heat flux, (b) surface freshwater flux (E–P), and (c) wind stress with the distribution of the wind direction inset. The average wind stress is marked with a gray dashed line.

obtain accurate salinity measurements. The presence of thermal lag in data results in errors in salinity and density, especially at the thermocline where there are sharp gradients in temperature and salinity.

In the case of unpumped CTDs, the vehicle propulsion is what induces flow through the sensor. Thermal-lag effects change as the speed of the vehicle fluctuates, especially across the thermocline and when the vehicle is at apogee. A correction, as described by Lueck and Picklo (1990) and more recently Garau et al. (2011), is applied to the conductivity and temperature sensor in the initial processing. The effectiveness of this correction depends on knowing the speed of the vehicle and, therefore, the speed of the flow of water through the conductivity sensor, which is reliant on determining a good flight model. Two models are derived: (1) from the change in pressure observed by the vehicle (glider-slope model) and (2) from the change in buoyancy (hydrodynamic model) of the vehicle (Frajka-Williams et al., 2011), which rely on good estimations of the gliders lift, drag, induced drag coefficients, volumes, glider absolute compressibility, and glider volumetric thermal expansion. The accuracy of these variables relies first on pre-deployment measurements and initial piloting procedures, and second by minimizing error in the flight model (e.g., regressing the glider-slope model with the hydrodynamic model, as implemented in the UEA-GliderToolbox [http://www.byqueste.com/toolbox.html]).

Error induced in the data by thermal lag is particularly pertinent in waters where the density is set by salinity; this is because salinity is most affected by thermal lag, with the correction resulting in a root mean square error of 4×10^{-3} g kg^{-1}. An analysis of the offset between climb (when the glider is ascending through the water column) and dive (when the glider is descending), that is, profiles which are close to each other in space, "∧" shape, and separately, dive and climb profiles during the deployment (profiles with a "∨" shape), highlights the regions where thermal lag most affects the data (Figure 3).

To constrain the error in our analysis of submesoscale fluxes, we quantify the error contribution to ML lateral density gradients by thermal lag. We compute the horizontal difference in density, averaged vertically

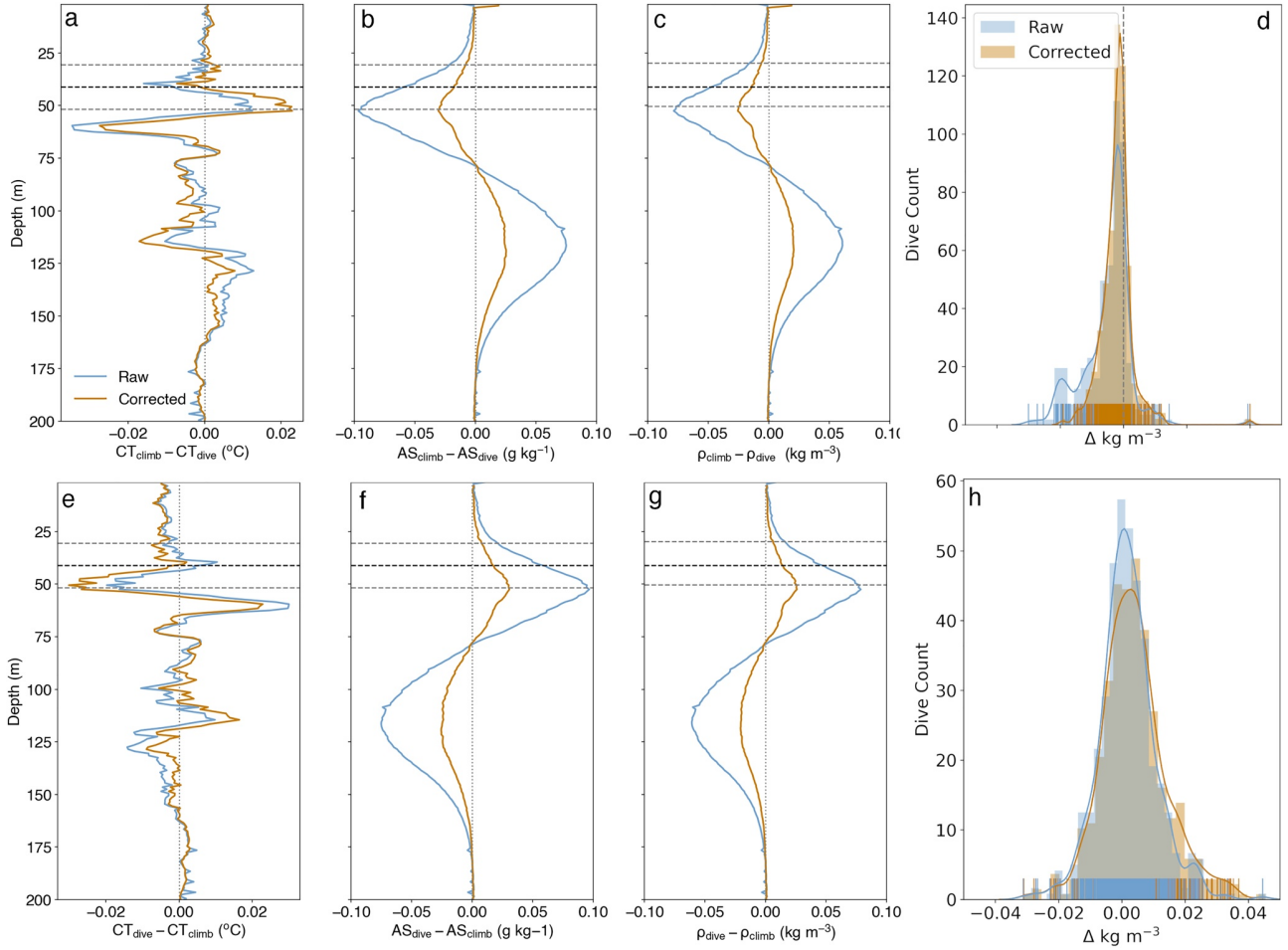

Figure 3. Seaglider uncorrected and thermal lag corrected (a and e) conservative temperature (CT), (b and f) absolute salinity (AS) and (c and g) density (ρ). The mean and standard deviation of the ML depth is indicated by dashed lines. (d and h) Distribution of the horizontal density differences, where density is vertically averaged between the surface and 15 m above the MLD, between all climb and dive Seaglider profiles. (a–c) Average of horizontal density differences between climb minus dive profiles("∧") (e–g) average of horizontal density differences between dive minus climb profiles ("∨").

between the surface and 15 m above the MLD (the average MLD is 40 m), between dive-climb (climb-dive) profiles (Figures 3d and 3h). The distribution plots show a 50th percentile residual error of -1×10^{-3} kg m^{-3} in the dive-climb profiles and 0.001 kg m^{-3} in the climb-dive profiles. This skewness toward underestimating (overestimating) the density differences is consistent with the Seaglider transiting from a warmer surface layer to a cooler winter water (WW) on the dive, or from a cooler WW to a warmer surface layer on the climb.

Lateral density gradients (change in density per km) of up to 0.015 kg m^{-3} km^{-1} are captured by the Seaglider. Considering the 50th percentile residual error after correcting for thermal lag quoted above, we compute this contribution to the magnitude of lateral gradients. We estimate an overestimation of lateral density gradients per km by 6% on the climb/dive pairs and a negligible error on the dive/climb pairs (much reduced because the distance between these dive pairs is larger). The overestimation of lateral gradients due to thermal lag is likely balanced by the underestimation of these gradients caused by the Seaglider not sampling fronts perpendicularly (see Section 4.5.1).

2.4. Atmospheric Reanalysis and Satellite Data

Surface forcing was obtained from ECMWFs (European Center for Medium-Range Weather Forecasts) ERA5 reanalysis. Wind stress ($\tau = \rho_a C_D U_{10}^2$) was computed from the density of air, the drag coefficient over the ocean surface (Large & Pond, 1981) and the meridional and zonal winds at 10 m height. Net surface heat fluxes (Q_{net}) were computed from shortwave and longwave contributions, as well as latent and sensible heat fluxes. Net freshwater fluxes (FWFs) were computed as evaporation-precipitation (E-P). Sea-ice fluxes are not included because the region was sampled after the sea-ice had melted. For comparison to Q_{net}, FWF is first converted to a surface buoyancy flux and then to an equivalent heat flux with the following equation as in (Pellichero et al., 2018):

$$Q_{FWF} = \rho_0 C_p \frac{\beta}{\alpha} S_{surf}\left(E - P\right), \tag{1}$$

where $\rho_0 = 1{,}027$ kg m^{-3} is a reference density, $C_p = 4{,}000$ J K^{-1} kg^{-1} is the heat capacity of water, $\alpha = 5.7$ K^{-1} is the thermal expansion coefficient of water and $\beta = 7.8 \times 10^{-4}$ kg g^{-1}, is the haline contraction coefficient. S_{surf} is the surface salinity (taken at 15 m), and (E-P) is evaporation-precipitation.

The sea surface height fields used to determine the location of the southern boundary of the ACC are based on SSALTO/Duacs Maps of Absolute Dynamic Height (MADT), following the method of Swart et al. (2010). Daily sea-ice concentration from AMSR2 (Spreen et al., 2008), with a 6.25 km lateral resolution, was used in this study. The sea-ice sector of the Southern Ocean was defined by the winter maximum of sea-ice, with sea-ice concentration greater than 15%. The regional maps of salinity are produced from ESA's Soil Moisture Ocean Salinity (SMOS) Earth Explorer mission using de-biased sea surface salinity L3 v4 maps that were generated by LOCEAN/ACRI-ST Expertise Center (Boutin et al., 2018). The global standard deviation of SMOS is 0.20 psu in the open ocean, compared to 100-km averaged ship SSS, but in polar seas, this is increased. Acknowledging this, we use SMOS only to characterize the regional impact of sea-ice on salinity, rather than relying on the actual magnitude in salinity. The surface chlorophyll map was produced with Level 2 data from the Copernicus Sentinel-3 Ocean and Land Color Instrument.

2.5. Buoyancy Gradients

Along-track (as measured by the Seaglider) time series of buoyancy were calculated as

$$b = g(1 - \rho \,/\, \rho_o). \tag{2}$$

where g is gravity and ρ_o is as defined in Equation 1. The contribution of temperature and salinity to the magnitude of lateral (along-track) density gradients was computed as:

$$b_x = g\alpha \frac{\partial T}{\partial x} - g\beta \frac{\partial S}{\partial x}. \tag{3}$$

By design, Seagliders sample in a "saw tooth" pattern as they propel themselves through adjusting their buoyancy. This results in ML (z ~ 10–40 m) profiles which are captured at high resolution ($x \sim 300$ m) between a climb profile and a dive profile, and profiles that are further apart ($x \sim 4$ km) between a dive profile and a climb profile. An in-depth analysis of the implications of this sampling pattern in capturing lateral gradients in the ML is provided by (Swart et al., 2020) (see Figure S2).

The calculation of lateral buoyancy gradients $\frac{\partial b}{\partial x}$ and associated submesoscale fluxes necessitated interpolation onto a uniform grid. For this analysis, along-track measurements of temperature and salinity, after binning to 1 m vertical bins, were linearly interpolated onto a uniform grid of $\partial x = 1$ km, from which density and buoyancy were computed. The ML lateral buoyancy gradient is computed as the along-track buoyancy in the middle of the ML. Errors may be introduced as a result of thermal lag (as discussed in Section 2.3)

as well as through interpolating across non-uniform distances. Errors in buoyancy are expected to lead to amplified errors in buoyancy gradients when the measurements are closer together.

2.6. Stratification and Turner Angle Analysis

The Brunt-Väisälä frequency is computed and decomposed into contributions from temperature and salinity using the following formulation:

$$N_{ts}^2 = \frac{\partial b}{\partial z} = g\alpha\frac{\partial T}{\partial z} - g\beta\frac{\partial S}{\partial z}. \tag{4}$$

The relative influence of temperature and salinity on vertical density stratification (N^2) is quantified with the Turner angle, which is defined as $\mathrm{Tu} = \arctan(R_p)$, using the density ratio $R_p \equiv \alpha\frac{\partial T}{\partial z}\left(\beta\frac{\partial S}{\partial z}\right)^{-1}$ (Turner, 1973). $\frac{\partial T}{\partial z}$ and $\frac{\partial S}{\partial z}$ are the vertical derivatives of temperature and salinity. The Turner angle is positive when temperature and salinity have competing effects on density stratification. For $Tu = \pi/4$, temperature stratification is fully compensated by salinity stratification. For $Tu = -\pi/4$, salinity and temperature contribute equally to the density stratification. Salinity stratification exceeds the contribution from temperature stratification when $-\pi/4 < Tu < \pi/4$, and temperature stratification dominates when $|Tu| > \pi/4$.

Similarly, a horizontal Turner angle can be defined by replacing the vertical gradient in temperature with a horizontal gradient. In this way the temperature and salinity contribution to lateral fronts can be decomposed. Fronts in which the Turner angle is positive are at least partially compensated, with $Tu > \pi/4$ indicating that temperature has a stronger impact on density than salinity. Fronts where $Tu < 0$ are anti-compensated in which salinity and temperature are acting constructively to create differences in density. These situations have the potential to produce strong density fronts; however, horizontal density gradients can slump due to gravity and may not persist (Rudnick & Cole, 2011). The horizontal Turner angle is computed using a length scale of 1 km.

To test whether the distribution in the vertical and horizontal Turner angles changes over the course of the summer season, the data is split into the first quartile (early summer) and last quartile (late summer) of the full data set until the atmospheric heat flux becomes zero. Each quartile consists of 500 data points, equivalent to 22 and 25 days in early and late summer, respectively, a temporal resolution of roughly 1 h.

2.7. Submesoscale Equivalent Heat Fluxes

The non-dimensional Richardson number $\left(Ri = \frac{N^2}{(\partial u\,/\,\partial z)^2} = \frac{f^2}{N^2}\left(\frac{\partial x}{\partial z}\right)^2\right)$, which provides a ratio between vertical stratification and geostrophic shear, characterizes the dynamic regime where large values, $Ri \gg 1$, represent quasi-geostrophic flow and small values, $Ri \approx 1$, an ageostrophic regime where submesoscale flows may be active. Using Seaglider observations, we apply the thermal wind assumption such that geostrophic shear is given by the squared along-track lateral gradient normalised by the Coriolis acceleration to give the bulk Richardson number, $Ri_b = \frac{f^2N^2}{b_x^2}$.

MLIs develop through cross-frontal motion that results in the stretching or compression of fluid parcels. Because vorticity is conserved during this process, there is an inverse cascade of energy and eddies are formed (referred to as MLEs), that typically manifest at horizontal scales O (0.1–10 km) and can induce vertical velocities of O(100) m day^{-1} (Boccaletti et al., 2007) by converting horizontal buoyancy gradients into vertical gradients. This overturning of density surfaces restratifies the water column and can be expressed in terms of a vertical stream function (Fox-Kemper et al., 2008):

$$\psi_{MLI} = 0.06\frac{\mu(z)b_xH^2}{|f|}, \tag{5}$$

where μ, represents the vertical structure and is set to unity for simplicity and H is the depth of the ML. The vertical buoyancy flux associated with the MLI stream function can be represented as an equivalent heat flux (Mahadevan et al., 2012):

$$Q_{MLE} = 0.06 \frac{b_x^2 H^2}{|f|} \frac{C_p \rho_0}{\alpha g}, \quad (6)$$

where 0.06 is an empirically defined coefficient determined by numerical models (Fox-Kemper et al., 2008) and b_x is the along-track buoyancy gradient. Because the MLI parameterization by Fox-Kemper et al. (2008) is based on the assumption that MLI grow from the potential energy stored in mesoscale lateral gradients, we applied a rolling window of 8 km (~4 times the ML Rossby radius of deformation) such that the Q_{MLE} values estimated here are based on the mesoscale field.

While Q_{MLE} is always positive and acts to restratify the ML, cross-frontal Ekman-driven flow by overlying wind fields results in lateral density advection. In particular, surface wind stress oriented downfront, or in the direction of the geostrophic shear, produces an Ekman transport that advects less buoyant over more buoyant water, a condition that is gravitationally unstable and induces turbulent mixing, arresting restratification. This mechanical surface forcing can, similarly to MLI, be expressed as an equivalent heat flux, referred to as Ekman buoyancy flux (EBF), which involves the component of the wind stress aligned with the submesoscale front (D'Asaro et al., 2011; Thomas & Lee, 2005):

$$Q_{EBF} = -\frac{b_x \tau^y}{f} \frac{C_p}{\alpha g}. \quad (7)$$

In calculating the along-front (across-track) wind stress, the wind will not always be aligned with the surface fronts. Following Viglione et al. (2018), the winds were rotated relative to the Seaglider orientation to determine the wind stress component perpendicular to the Seaglider's trajectory (τ^Y). Negative values of Q_{EBF} correspond to destabilizing, down-front conditions.

For this analysis, we assume the Ekman layer is equivalent to the MLD. This assumption simplifies the vertical structure of the upper ocean. While we acknowledge this is a non-trivial assumption, the equivalence of the MLD and the Ekman layer is perhaps reasonable under these summer conditions, when the ML is shallow and the winds are strong. A scaling analysis of the Ekman depth based on a κ_d, the turbulent diffusivity, ~ 0.1 $m^2 s^{-1}$, gives an Ekman depth ($H_E = \sqrt{2\kappa_d / f}$) of about 40 m, which is the average MLD of the upper ocean in these observations.

A case study is presented to contextualize the results described later in this study. A subset of the Seaglider observations (with the Seaglider moving both in the southward direction and the northward direction; horizontal distance covered by glider in the case study is 30.5 km) and winds from which the submesoscale processes of MLI and EBF are computed is shown in Figure 4. EBF is positive (restratifying) under conditions where the across-track winds are oriented upfront. Upfront winds are defined when the across-track winds and along-track b_x observed by the Seaglider have the same sign. For example, during the northward transect, negative b_x and negative τ^Y indicate lighter, more buoyant water to the south in combination with westerly winds. In the southern hemisphere, westerly winds result in Ekman transport to the north, pushing lighter water over denser water and restratification.

3. Results

3.1. Mixed Layer Properties

The ML properties evolve over summer from cold and fresh (34 g kg^{-1}, −1.2°C), to warmer and saltier (1.5°C, 34.2 g kg^{-1}, Figure 5). A cold, relatively salty WW layer, defined as the temperature minimum layer below the 1,027.5 kg m^{-3} isopycnal, separates the ML from the warm and salty upper Circumpolar Deep Water (uCDW) at the 1,027.7 kg m^{-3} isopycnal (see Figure S1). Four days after the complete melt of sea-ice, the surface layer had shoaled from ~100 m (observed by a nearby SOCCOM float, see Figure S2) to 41.0 m, gradually deepening to 80 m over the 3-month glider deployment.

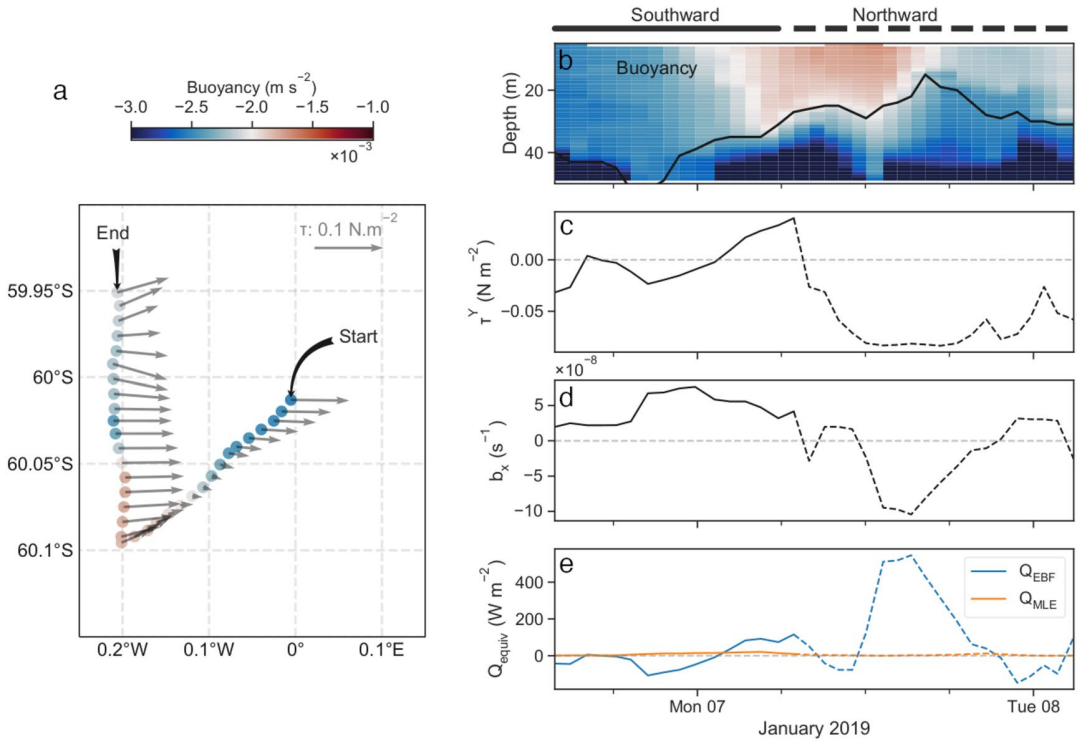

Figure 4. Case study of Seaglider observations during which a strong lateral gradient was sampled. (a) Glider trajectory, colored by the buoyancy at 15 m. Black arrows indicate the start and end of the subsample. Wind stress vectors are overlaid in gray. (b) Section of buoyancy with the mixed layer depth overlaid in black. (c) Wind stress oriented perpendicular to the Seaglider track (positive to the left of the glider orientation). (d) Along-track buoyancy gradient as observed by the Seaglider. (e) Estimated submesoscale equivalent heat fluxes (Q_{equiv}): Q_{MLE}, Q_{EBF}. The solid lines indicate when the Seaglider was moving southwards, while the dashed lines indicate when the Seaglider was moving northwards. The entire distance covered by the glider in this case study is 30.5 km.

ML buoyancy increases from -3×10^{-3} m s^{-2} in December to -1.5×10^{-3} m s^{-2} by late February, before decreasing again. Buoyancy gradients of up to 1.5×10^{-7} s^{-2} are observed, equivalent to density fronts of 0.015 kg m^{-3} km^{-1}, and salinity fronts of 0.02 g kg^{-1} km^{-1}. The largest lateral buoyancy gradients (those greater than 5×10^{-8} s^{-2}, Figure 5d) are observed until mid-February. Early summer is characterized by N^2 values at the base of the ML of $1.1 \times 10^{-4} \pm 4.6 \times 10^{-5}$ s^{-2}, which decrease in late summer to $6.7 \times 10^{-5} \pm 3.9 \times 10^{-5}$ s^{-2}. Toward the end of summer, from ~ 8 March, the ML deepens to 80 m, WW isopycnals move closer together, and stratification at the base of the ML increases again to $1.4 \times 10^{-4} \pm 6.6 \times 10^{-5}$ s^{-1} in March.

Seaglider observed conditions in the upper ocean are embedded within a larger mesoscale field. In this region, and during the sea-ice melt season, the mesoscale field is predominantly structured by northwards advecting freshwater from sea-ice melt. The freshwater signal emanating from the melting sea-ice, observed in SMOS sea surface salinity (Figure 1a), is mirrored in the Seaglider profiles (Figure 5a) and specifically in the first mesoscale transect (Figure 6a). Low saline water is advected northwards by the predominantly westerly winds. We confirm this by estimating the Ekman component of the salinity tendency budget from lateral salinity gradients observed during the mesoscale transects.

$$\frac{\partial S_{Ekman}}{\partial t} = -U_e.\nabla S_m, \tag{8}$$

where

$$U_e = \frac{1}{\rho_o f H}\begin{pmatrix} \tau^y \\ -\tau^x \end{pmatrix} \tag{9}$$

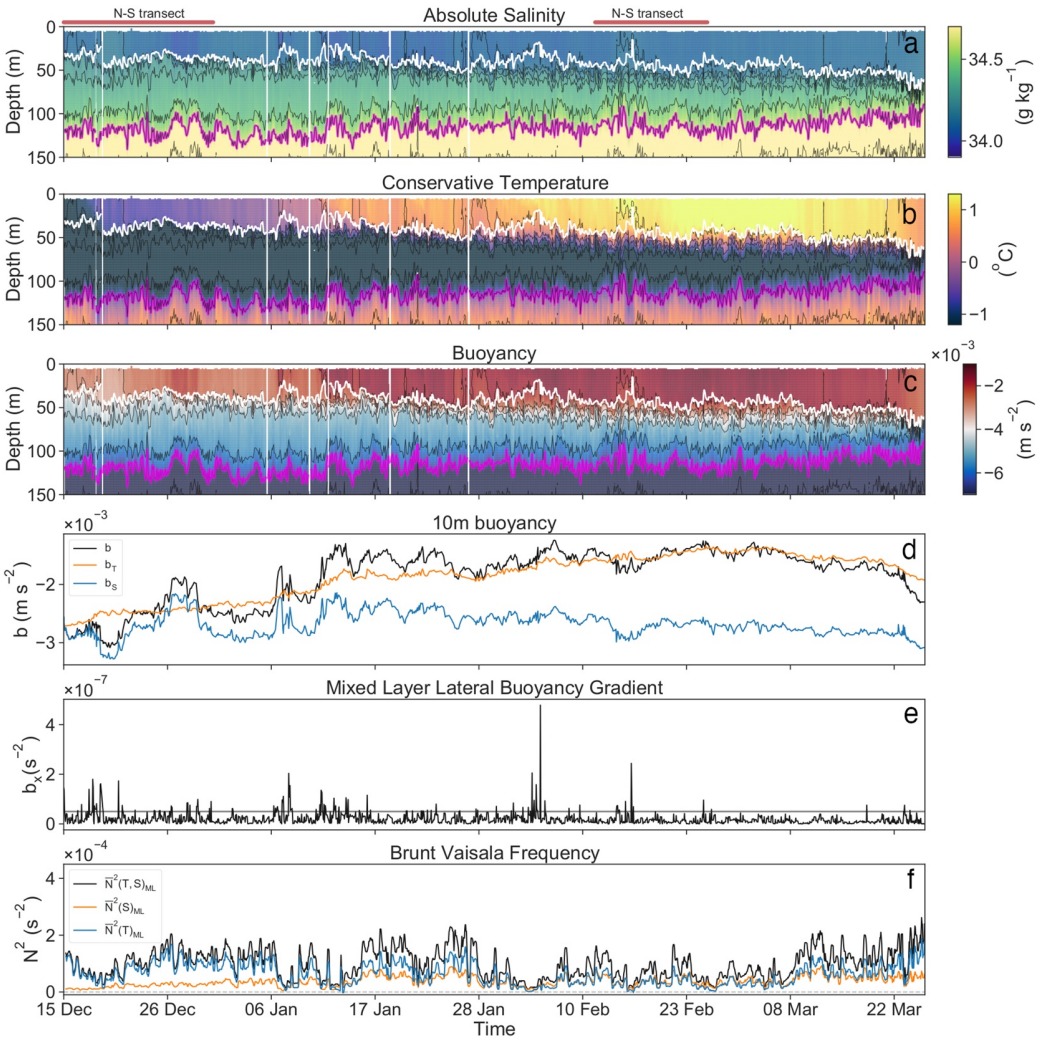

Figure 5. Time series of the summer season 2018-2019: (a) Seaglider sampled absolute salinity. Thin black lines denote density isopycnals with an interval of 0.01 kg m^{-3}. The mixed layer depth is shown in white. The lower bound of winter water is marked with magenta lines, identified by the density isopycnal = 1,027.7 kg m^{-3}, the temperature maximum beneath the mixed layer. (b) The same as (a) but for conservative temperature; (c) The same as (a) but for buoyancy. (d) Temperature and salinity contribution to ML buoyancy (at 10 m depth). (e) The average mixed layer buoyancy gradients and (f) Temperature and salinity contribution to vertical stratification at the base of the mixed layer. The solid red lines above the plot indicate when the Seaglider was completing mesoscale transects.

$\frac{\partial S_{Ekman}}{\partial t}$ is computed by taking an average across-track wind stress of 0.09 N m^{-2} to the east (note that the wind stress varies synoptically and not seasonally), and the large scale gradient across the two mesoscale transects shown in Figure 6. The Ekman contribution to the upper ocean salinity tendency is larger than or comparable to the salinity tendency attributable to FWF by evaporation and precipitation ($\frac{\partial S_{Ekman}}{\partial t} \sim 2.1 \times 10^{-8}$ g kg^{-1} s^{-1} and $\frac{\partial S_{FWF}}{\partial t} \sim 4.8 \times 10^{-9}$ g kg^{-1} s^{-1}). The contribution of S_{ekman} decreases in the second mesoscale transect as the mesoscale lateral salinity gradient decreases (Figure 6b), potentially indicating a decrease in freshwater advection northwards.

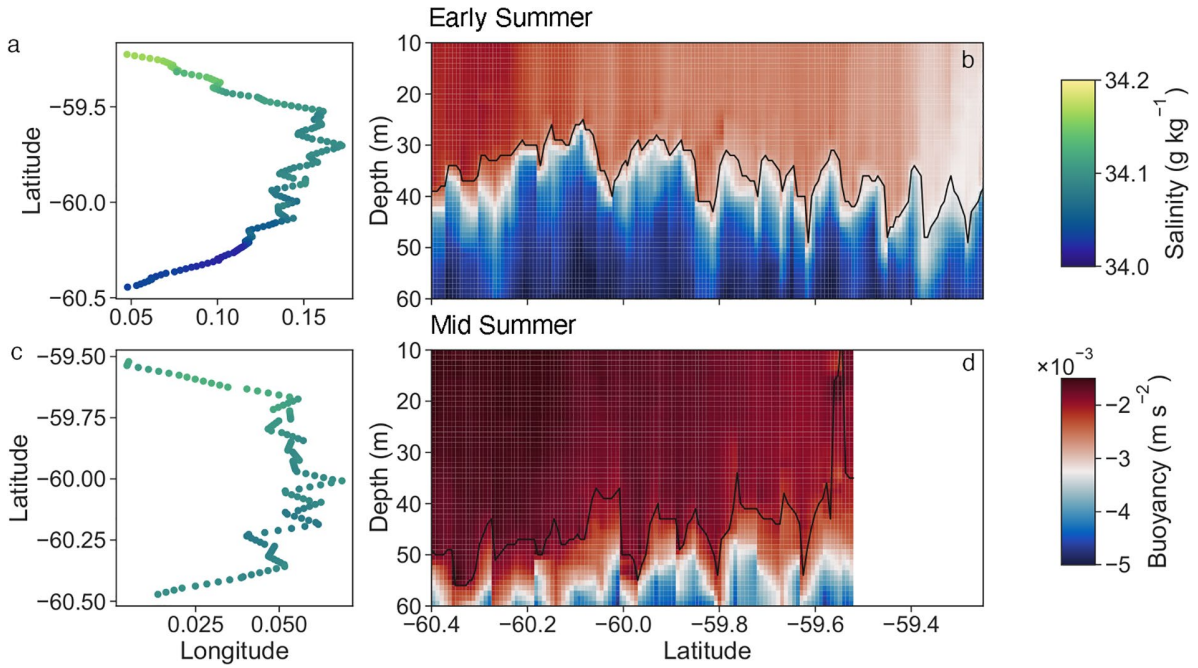

Figure 6. Subset of the Seaglider data showing the mesoscale transects at the beginning (a and b) and middle of the deployment (c and d). Panels (a and c) show the Seaglider trajectory with salinity overlaid. Panels (c and d) are sections of the glider-observed buoyancy. Black lines in (c and d) are the mixed layer depth.

3.2. Vertical and Lateral Stratification

To quantify the contribution of salinity and temperature to ML density, the vertical and horizontal Turner angles were computed. In both cases, the haline contribution to density decreases as the season progresses (Figure 7).

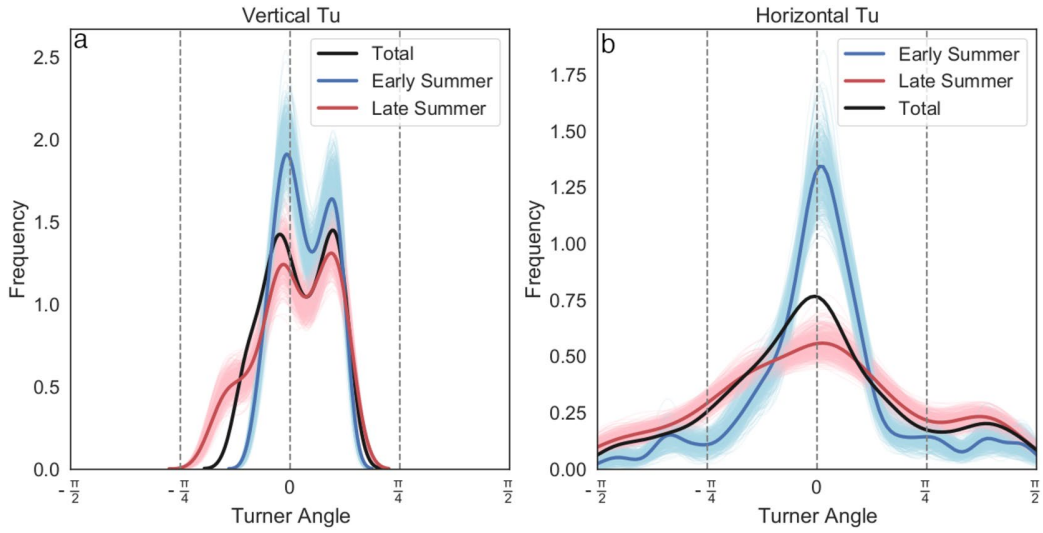

Figure 7. Distribution of the Turner angle in the upper ocean at 60°S, 0°E during summer (black line), decomposed into early summer (blue line) and late summer (red line). (a) Histogram of the vertical Turner angle averaged in the upper 200 m. (b) Histogram of the horizontal Turner angle. Bootstrapping was applied to the early summer and later summer subsets to give the confidence intervals marked in light blue and pink shading, respectively.

In the vertical, the average Turner angle of the upper 200 m reveals a bimodal structure representing the interface between the surface water and WW, and the interface between uCDW and WW (shown in the time series, Figures 5a and 5b). In late summer, the distribution of the vertical Turner angle shifts toward $\frac{-\pi}{4}$, representing the increased role of temperature in setting vertical stratification.

Similar to the vertical stratification, lateral density variations in the ML are determined by salinity anomalies during early summer (Turner angle distribution centered at zero, Figure 7b), moving toward mixed salinity and temperature compensated fronts in late summer (distribution broadens).

3.3. Submesoscale Instabilities and Fluxes

Wavenumber spectra are used to describe the horizontal density variance in the ML and analyze the seasonal timescale of active scales of energy variance. There is a growing body of literature to describe submesoscale turbulence based on the spectral slopes of energy and tracer variance, assuming constant stratification (see review by Jaeger et al., 2020). While constant stratification is rare in the world's ocean, and theoretical power laws in question are based on the assumptions of an inertial subrange and of statistical homogeneity of the flow field, the spectra nevertheless provide a useful metric with which to assess scales of variance in the ocean.

Interior quasi-geostrophic (IQG) turbulence theory, which typically scales with variance slopes of $\sim k^{-3}$ (Charney, 1971) describes turbulence that originates from deep baroclinic instabilities and is applicable away from surface boundaries because it assumes no ML and constant density at the boundary. Surface quasi-geostrophic (SQG) theory (Blumen, 1978), assumes a buoyancy gradient which, through stirring of this gradient, results in frontogenesis and a cascade of eddies to give an inertial subrange of $k^{-5/3}$. Both these scaling laws describe flows that are in geostrophic balance, and need to be adjusted for an ageostrophic component of the flow, which tends to steepen SQG energy and tracer slopes to k^{-2} (Boyd, 1992; Capet et al., 2008). Considering the assumptions behind these power laws and the errors that propagate in observations, observations have not always confirmed these predictions. Jaeger et al. (2020) review the existing observational literature of spectral analysis with a focus on tracer analysis, finding that in most cases, the power laws are inconsistent with both IQG and SQG and being more consistent with ageostrophic frontogenesis theory which predicts power laws of k^{-2}.

In this study, both meso- (~100 km) and submeso- (<10 km) scales were resolved. After separating the glider transects into these two scales (Figure 1c), the wavenumber power spectrum of density (potential energy) variance is computed for both the mesoscale (Figure 8a, $N = 2$) and submesoscale (Figures 8b and 8c, $N = 36$) glider transects in the ML (10 m). In the following analysis, we assume that density spectra are a proxy for potential energy spectra. By taking the spectra of density, we measure the variance of density at different wavenumbers. The integral over all the wavenumbers gives the total density variance, which can be converted to potential energy by dividing by N^2 and multiplying by relevant constants. Typically, N^2 is assumed to be constant, leaving density variance an appropriate measure of potential energy variance. A multi-taper method with adaptive weighting and five smoothing windows is applied. Discrete prolate spheroidal sequences (DPSSs) are used as data windowing functions. Confidence intervals are determined from a X^2distribution for which the degrees of freedom are computed as a function of the number of windowed segments and the length of the spectra. The instrument noise is determined to be 3 km and marked on the plots. Inertial subrange slopes are then computed for the mesoscale transects between 50 and 3 km and for the submesoscale transects between 8 km (the full depth Rossby radius of deformation) and 3 km.

While the mesoscale transects are more informative as they capture a larger range of scales, the submesoscale transects are additionally taken into account, the averages of which allow for the assumption of statistical stationarity. There is a trade-off with this assumption because of a level of uncertainty in the shorter transects due to the inertial subrange being computed over only one order of magnitude.

The mesoscale snapshots display spectra with inertial subrange slopes of $k^{-2.16 \pm 0.2}$ and $k^{-2.2 \pm 0.3}$ in early summer and late summer, respectively-essentially remaining constant over the season. The submesoscale

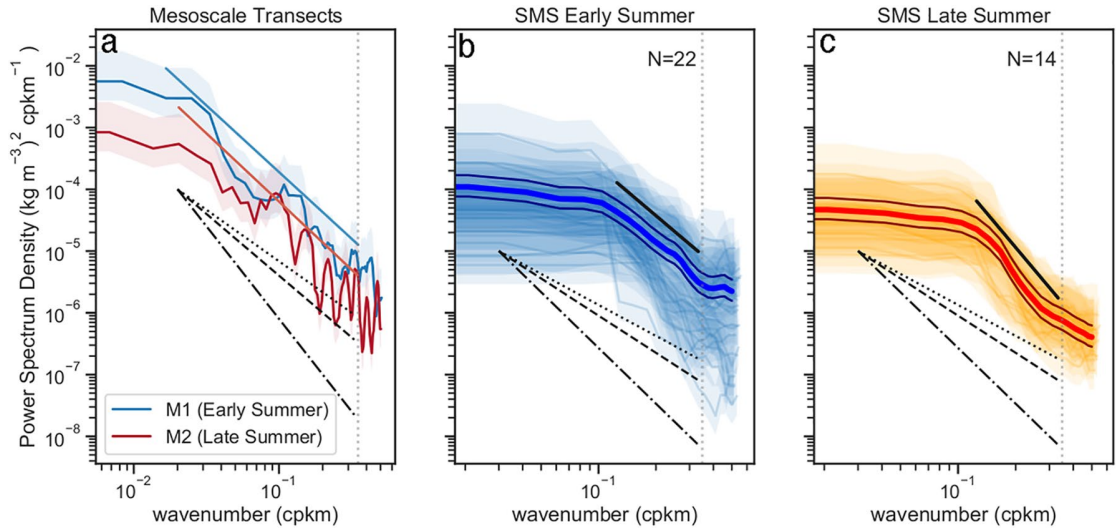

Figure 8. Power spectra of density at 10 m for (a) the glider mesoscale transects and (b) submesoscale transects during early summer (December to January, $N = 22$ transects) and (c) submesoscale transects during late summer (February to March, $N = 14$ transects). The 95% confidence interval (CI) of the spectra is shaded, the 95% CI for the average spectra is indicated by solid lines adjacent to the average spectra in (b) and (c). The noise cutoff wavenumber (3 km), is marked by the gray dotted line. Inertial subrange slopes are calculated for the mesoscale transects between 50 and 3 km. The slope in the first mesoscale transect (M1) is $k^{-2.16 \pm 0.2}$ and $k^{-2.2 \pm 0.3}$ in the later transect (M2). Inertial subrange slopes for the submesoscale transects in (b and c) are computed over the range 8–3 km to give average slopes of $k^{-2.6 \pm 0.2}$ and $k^{-3.6 \pm 0.3}$, respectively. Reference slopes of $k^{-5/3}$ (dotted line), k^{-2} (dashed line), and k^{-3} (dash-dot line) are indicated in the figure.

slopes have an average slope of $k^{-2.6 \pm 0.2}$ and $k^{-3.6 \pm 0.3}$ in early and late summer, respectively. The individual submesoscale transects are noisy, ranging from k^{-1} to k^{-4}. The total potential energy in the system (integration under the spectra, assuming constant N^2) is reduced toward late summer.

We focus our analysis on the potential for MLI to form the submesoscale structure suggested in Figure 8. Conditions where lateral gradients have scales of O(1) km and stratification is weak (Richardson numbers ~ O(1)), indicate when the water column is predisposed for submesoscale overturning to occur. We assess the wavelength and growth rate of the fastest growing MLI, defined as (Fox-Kemper et al., 2008; Stone, 1970):

$$l_{max} = \frac{2\pi U}{f}\sqrt{\frac{1+Ri}{5/2}}, \tag{10}$$

$$\tau_{max} = \sqrt{\frac{54}{5}}\frac{\sqrt{1+Ri}}{f}, \tag{11}$$

U, is the geostrophic velocity in the ML, determined by multiplying H by the geostrophic shear, calculated from the Seaglider derived lateral buoyancy gradient, as $|b_x|/f$, under the assumption of thermal wind balance:

$$U \equiv \frac{|b_x|}{f}H.$$

For the ice-free Antarctic MIZ during summer, taking $Ri = 1$, a typical maximum growth rate is 10 h, using $f \sim 1.26 \times 10^{-4}$ s^{-1}, the local inertial frequency, with a typical length scale of 1.4 km (using a MLD of 40 m and lateral buoyancy gradient of 1×10^{-7} s^{-1}). These scales are comparable to simulations by Fox-Kemper et al. (2008), in which a MLD of 100 m and $b_x^2 = 2f^2$, results in $\tau_{max} \sim 16.8$ h and $l \sim 3.9$ km.

Using the Seaglider measured lateral buoyancy gradient, MLD and Richardson number, we extend the analysis of the MLI growth rate and wavelength to the full-time series (Figure 9). Within the ML, the

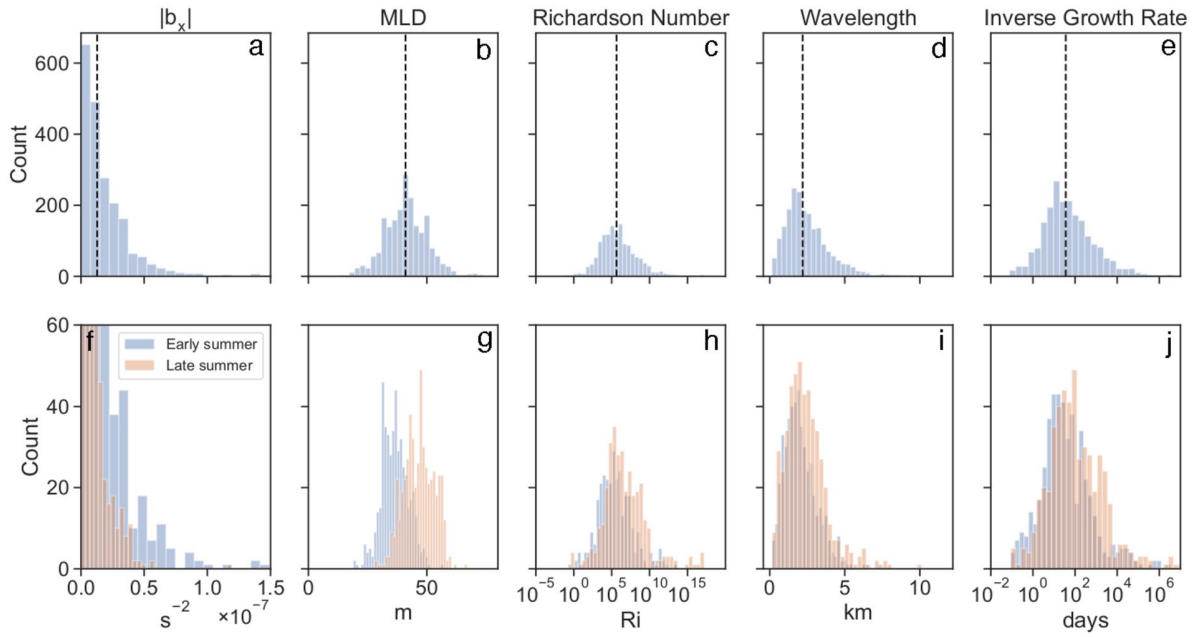

Figure 9. Histograms of: (a) magnitude of along-track buoyancy gradient, (b) MLD, (c) Richardson number, (d) MLI wavelength, (e) MLI inverse growth rate. Median values are indicated by the black dashed lines. Panels (f and j) show the seasonal shift in distributions of (a–e) from early summer to late summer using the same definitions as in Figure 5. MLD, mixed layer depth; MLI, mixed layer instability.

Richardson number varied over several orders of magnitude (Figure 9c), a function of stratification at the base of the ML and the strength of the lateral buoyancy gradients. During the summer season, most of the ML flows are characterized by Ri $\gg$ 1, influenced by the strong stratification resulting from the recent sea-ice melt, $Ri_{ML} \sim 1 \times 10^5$. Very intermittently, a combination of weaker stratification and strong lateral buoyancy gradients brings the system toward an ageostrophic regime where $Ri_{ML} < 4$ in 2% of profiles (Figure 9c). The distribution of the magnitude of lateral buoyancy gradients is skewed to the left, with the majority of lateral gradients being weak (Figure 9a). In early summer, the occurrence of strong lateral buoyancy gradients is more frequent than during later summer (Figure 9f). For the same time period, the distribution of MLD is centered around a mean value of $\sim$ 40 m, with 98% of the observations found between 15 and 75 m (Figure 9b), shifting to a deeper average during late summer (Figure 9g). The majority of the distribution of the wavelength of the fastest growing MLI is typically less than 5 km (Figure 9d), similar to the ML Rossby radius of deformation, $Lr = \mathrm{NH}/f = 2 \pm 0.6$ km. The inverse growth rate of MLI is a function of the Richardson number and follows a similar distribution to that of the Richardson number (Figure 9e). The Richardson number, wavelength, and growth rate of MLI display a tendency toward higher magnitudes during late summer (Figures 9h and 9j). Together, these results suggest that the upper ocean undergoes a shift from early summer to late summer in the scales that describe the instabilities and eddies.

Similarly, MLE fluxes and EBF, which both depend on lateral buoyancy gradients, weaken as the summer season progresses and the strength of lateral buoyancy gradients decreases (Figure 10). When MLIs are active, their stratifying potential is weak (<50 W m^{-2}). Conversely, wind interactions with ML fronts have the potential to impact stratification in the ML, with the observed submesoscale fronts ($b_x \sim$ (O) 5×10^{-8} s^{-2}), sufficient to induce EBF fluxes greater than 200 W m^{-2}. Together, EBF and MLE increase the variability of the total equivalent heat flux in the ML during early summer by 55% (from a standard deviation of 35.9 W m^{-2} to 80.5 W m^{-2}), compared to late summer when the influence of submesoscale fluxes is almost negligible (standard deviation increases from 32.4 to 34.4 W m^{-2} with the inclusion of submesoscale fluxes) (Figure 10c).

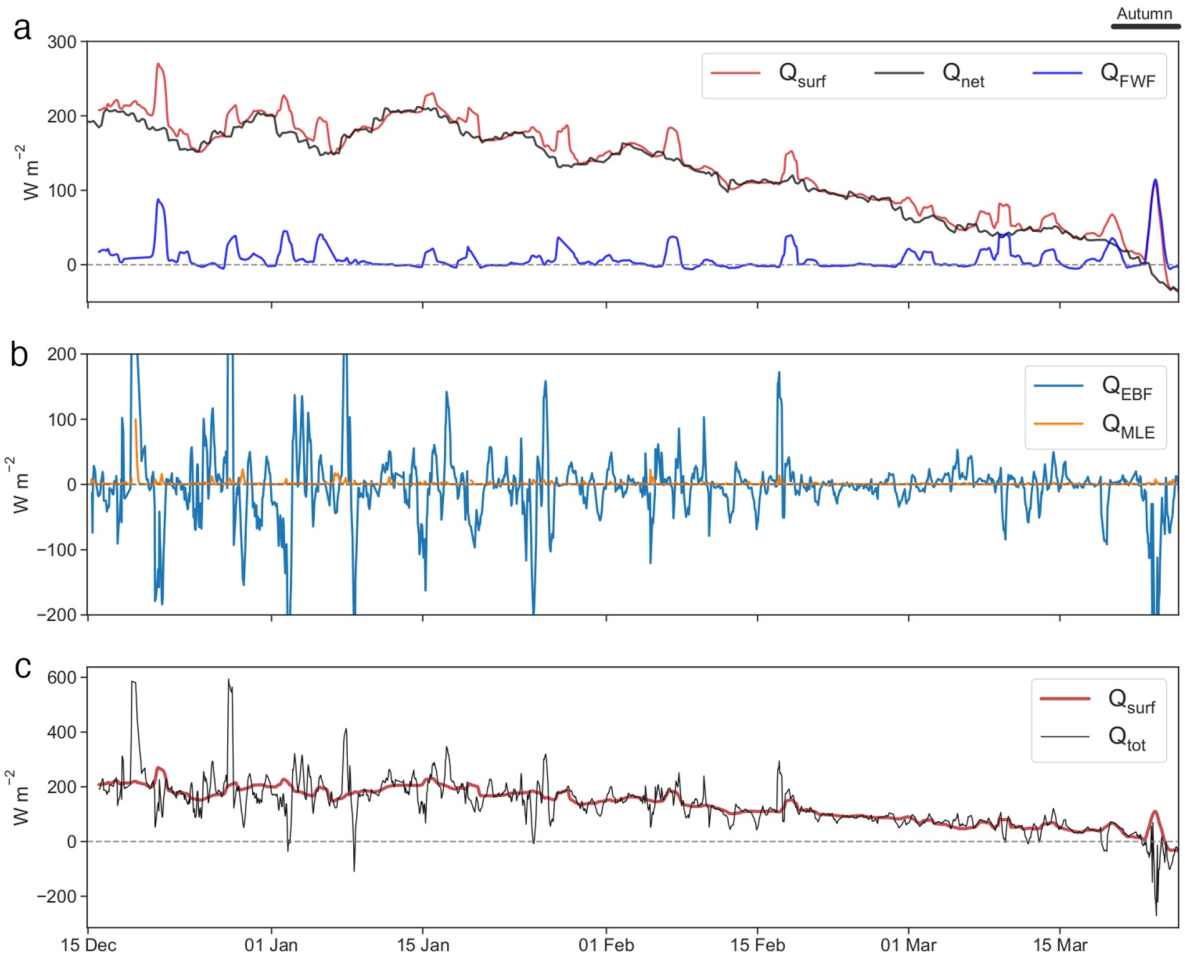

Figure 10. Timeseries of the summer season 2018–2019: (a) Surface heat flux (Q_{net}, black) and equivalent freshwater flux ($Q_{freshwater}$, blue) are expressed as an equivalent heat flux from ERA5 reanalysis and the sum of the two (Q_{surf}, red). Rolling means of 24 h are applied. (b) Equivalent heat flux by submesoscale overturning due to mixed layer baroclinic instability (Q_{MLE}, orange) and Ekman Buoyancy Flux (Q_{EBF}, blue). A rolling mean of the inertial period (10 h) was applied to Q_{EBF} to reduce the emphasis on sporadic events. (c) Sum of the total surface buoyancy forcing, restratification due to MLEs, and wind-driven submesoscale Ekman transport ($Q_{tot} = Q_{surf} + Q_{MLE} + Q_{EBF}$) expressed as an equivalent heat flux. The red curve shows Q_{surf} as in (a) for reference. The onset of autumn is indicated by the black line above the plot, defined by a shift from positive to negative heat flux into the ocean. *Note*. The change in scale on the *y*-axis.

4. Discussion

This study investigates ML dynamics over a summer season in the Antarctic MIZ, in which our three main aims are addressed. First, we investigate whether ML fronts, formed by recent sea-ice meltwater, remain prevalent during the early summer in the ice-free MIZ. Second, we characterize submesoscale flows as the summer season progresses, and third, we evaluate their impact on the structure of the ML, such as its depth and stratification.

4.1. A Salinity-Driven System

We find a shift from salinity-dominated to mixed salinity/temperature-controlled buoyancy variability through the progression of the summer season. Salinity-driven buoyancy variability is expected in the ice-impacted Southern Ocean, where sea-ice-derived waters drive the seasonal ML salinity budget (Pellichero et al., 2017). Similar occurrences are observed in the Arctic MIZ, with salinity driving ML density variability during ice-free conditions (Timmermans & Winsor, 2013).

Initially, cold, low saline water is advected through the sample region, and positive buoyancy anomalies, driven by salinity, are observed (Figure 5). ML buoyancy becomes more sensitive to temperature fluctuations as the summer season progresses, with temperature exerting a stronger influence on density. This is also reflected in the flattening of the horizontal turner angle distribution (Figure 7). In early summer, the water temperatures are cold (<1°C), and thus temperature has a small impact on buoyancy because of nonlinearities in the equation of state. As the water temperatures increase, so too does the thermal expansion coefficient and, correspondingly, the temperature contribution to buoyancy. In this region, the largest contributor to positive surface buoyancy flux is solar heating. Increased buoyancy associated with a warmer ML increases the stability of the ML, with the potential to suppress MLI.

Temperature determines the seasonal trend in ML buoyancy (Figure 5c), but variations in salinity that continue throughout the season give rise to lateral density gradients. Salinity contribution to buoyancy varies around a stationary mean, reflecting swirling horizontal gradients likely characteristic of submesoscale eddies (McWilliams, 2016), and providing evidence that MLEs may be contributing to the observed lateral buoyancy gradients.

The time series we present here extends beyond that of Swart et al. (2020), in which they show that submesoscale fronts persist into summer in an interplay between thermohaline slumping by winds and frontogenesis. Corresponding with their observations, lateral buoyancy gradients observed here persist from December to February, but eventually reduce in magnitude from mid-February until the end of March when the surface heat flux turns negative (Figure 2) and the supply of freshwater from the south decreases (Figure 6). While the strength of the overlying westerlies does not noticeably diminish, the amount of freshwater available to advect northwards decreases as the sea-ice reaches its minimum extent, ~1,000 km south of the study site (Figure 1a). The dampening of surface lateral buoyancy gradients in late summer may reflect this loss of a source of positive buoyancy anomalies. In summary, our observations support the hypothesis that sharp (e.g., $b_x > 5 \times 10^{-8}$ s^{-2}, Figure 5c) sea-ice meltwater fronts persist in the ice-impacted Southern Ocean after the sea-ice has melted.

4.2. Summer Submesoscale Processes

We observed salinity-driven lateral fronts at submesoscales during summer in the ice-free Antarctic MIZ, with increased prevalence occurring with close proximity to the sea-ice melt out (occurring at this study site on December 10, 2018, Figure 1d). This frontal structure agrees with concurrent surface observations described by Swart et al. (2020) (Figure 3, density spectral slopes scaling at $k^{-2.4}$), revealing an active submesoscale regime during early summer. The mesoscale and submesoscale density spectral slopes observed by the Seaglider in this study range from k^{-2} to steeper than k^{-3} (Figure 8). In this study, while the mesoscale slopes converge at $k^{-2.2}$ (Figure 8a); the submesoscale slopes show more variability (Figures 8b and 8c). It remains challenging to distinguish the contributions of different physical mechanisms from spectral slopes (Erickson et al., 2020). Nevertheless, below, we present potential explanations for the change in density spectra slopes from that predicted by theory.

The physical interpretation of the potential energy inertial subrange in the upper ocean is best described by SQG which predicts a slope of $k^{-5/3}$, while observations and models which include an ageostrophic component steepen the SQG predicted slope to $k^{-2.2}$. For SQG in the ML, the tracer spectra and potential energy spectra follow the same power law (Callies & Ferrari, 2013). Global observations of tracer spectral slopes are mostly steeper than $k^{-5/3}$ (Jaeger et al., 2020). In the observations presented in Figure 8, $k^{-5/3}$ and k^{-2} are not robustly distinguishable given the noise across the individual transects, and we continue the discussion with reference to k^{-2}. IQG, which predicts steeper slopes of k^{-3}, represents the energy cascade in the interior ocean and is thus not applicable for the surface ocean. In the literature, the steeper density slopes have been interpreted to describe an upper ocean in which eddy kinetic energy is small; therefore, the majority of the energy is injected at larger mesoscales with a tendency for an inverse cascade of energy (e.g., in the Arctic and in the North Pacific; Callies & Ferrari, 2013; Timmermans et al., 2012; Timmermans & Winsor, 2013). The mesoscale slopes presented in Figure 8a present an energy cascade for this region which follows a power law steeper than predicted by SQG but not as steep as that predicted by IQG.

We hypothesize that submesoscale fronts in this region are formed from stirring of MLEs, which grow from ML instabilities. These submesoscale instabilities themselves draw energy from the larger scale mesoscale fronts that potentially stir freshwater anomalies by sea-ice melt (see Swart et al., 2020). The large inter-transect slope variability (in Figures 8b and 8c, ranging from $\sim k^{-1}$ to k^{-4}) may reflect the intermittent nature of surface turbulent motion in the region. That this variability decreases over the summer season and the slope steepens (Figure 8c), is suggestive that the tight interplay between strong stratifying forcing and turbulent motion decreases later in summer, to give way to a generally quiescent ocean. As the summer season progresses and the sea-ice meltwater fronts are mixed and/or advected out of the region, the available potential energy for MLIs decreases (the magnitude of the integration of the density spectra decreases, which is directly related to APE through the QG approximation of constant N^2, Figure 8a). At the same time, the frequency of strong submesoscale fronts in this region decreases toward the late summer (Figure 5e).

While there is a possibility that the steeper slopes observed in the later part of the summer season in Figure 8c are revealing a more quiescent ocean at the submesoscale, this is not reflected in the mesoscale transect (M2, Figure 8a), and it is acknowledged that there is a large amount of uncertainty in the data and methods to robustly come to this conclusion.

Uncertainties may arise from the high sensitivity of the slope to the wavenumber band chosen as well as the range over which the slope is calculated, with increased uncertainty when computed over a single order of magnitude (as in the submesoscale transects presented). A further source of error may be linked to the glider being unable to capture all the energy at large wavenumbers (small-scale structure) and artificially steepening the spectral slopes (the glider horizontal sampling resolution is limited to ~300 m to 3 km). In the latter half of the observations, the slope steepens to $k^{-3.6}$. With a weaker background gradient, it is possible that the glider observations are not high resolution enough to capture the fine-scale energy during this time and so the slope appears steeper. Further errors may be introduced into these spectra as a result of the necessary linear interpolation (Callies & Ferrari, 2013; Klymak et al., 2015).

Even though a submesoscale regime is evident (Figure 10), we found that if the fine-scale fronts observed reflect stirring of MLEs, their impact on surface stratification is weak (Q_{MLE} = 5–20 W m^{-2}). With an average surface heat flux of 200 W m^{-2}, restratification by MLEs is not large enough to compete. Winds oriented up or down front have impacts on the lifetime of the fronts with implications to mixing and the persistence of fronts. EBF varies between 100 and 1,000 W m^{-2}, up to two orders of magnitude greater than Q_{MLE}, and often larger than the ambient surface heat flux. EBF acts to intermittently increase stratification or increase mixing. The effect of winds interacting with ML fronts, decreases later in summer. These results indicate that mechanical wind-forced interactions with the observed fine-scale fronts can be important to the ML structure. Estimates of MLI and EBF are slightly larger than that estimated by Swart et al. (2020) for the same region during summer ($Q_{MLE} \sim$ O(10) W m^{-2}, $Q_{EBF} \sim$ O(100) W m^{-2}), likely linked to their data record only beginning during late summer conditions and the higher resolution of our sampling (0.3–4 km vs. ~ 9 km in Biddle & Swart, 2020).

North of the southern boundary of the ACC, similar submesoscale fluxes have been observed in the regions between the ACC jets. EKE is relatively weak and MLD is <100 m resulting in similar MLE fluxes to this study (du Plessis et al., 2019), but in the energetic Drake Passage, MLs are deeper (MLD > 100 m) and lateral gradients are stronger (up to 3×10^{-7} s^{-2}), providing MLE fluxes that can reach up to 4,000 W m^{-2} (Viglione et al., 2018). By definition, MLEs draw more APE from deeper MLDs (Fox-Kemper et al., 2008). The potential for MLE fluxes in our data is thus limited by the relatively shallow summer MLDs. A secondary peak in MLE potential during early autumn in the Antarctic MIZ, concurrent with ML deepening, is shown by Biddle and Swart (2020). Similarly, at the end of this data set, with the onset of autumn and a deepening ML, MLEs begin to increase in magnitude again.

An alternative mechanism, that accounts for the large MLI wavelength and growth rates predicted by linear instability theory (Figure 9), and perhaps contributes to the steepening of the spectral slopes (Figure 8) is that the small scale lateral buoyancy gradients are evidence that there is a tendency for weak frontogenesis in the upper ocean due to the strong lateral density gradient imposed by sea-ice melt. The seasonal decrease in the total magnitude of density variability in the upper ocean (Figure 8), together with the small (~2 km) ML Rossby radius of deformation, allows for balanced fronts and filaments that have been drawn out by

mesoscale stirring to persist at small-scales in this region. These surface anomalies would have a signature in the power spectra at the submesoscale, but not generate mixed-layer eddies or increased vertical velocities. Nevertheless, these weak fronts would likely be surface confined due to the strong stratification imposed by sea-ice meltwater.

In the Southern Ocean, denser waters are generally located to the south, with lighter waters to the north. The predominantly westerly winds over this meridional gradient in density create a large-scale destratifying EBF over the region. Within the ACC, similar observations of EBF to the present study support this mechanism at the submesoscale as well (du Plessis et al., 2019). Conversely, at the MIZ, after sea-ice melt, the meridional gradient is variable as lighter fresher water advects northwards intermittently, resulting in both stratifying and destratifying EBF under similar wind forcing (Figures 10 and S3).

These results show that while submesoscale front generation is likely due to mesoscale stirring of freshwater, stratification may be more strongly influenced by wind-front interactions, represented here by EBF. These findings are in line with previous observations in the Weddell Sea (Biddle & Swart, 2020), suggesting that these dynamics are not limited to the year of this study.

4.3. Mixed Layer Response to Submesoscale Flow

It is challenging to infer the impact of submesoscale flow on the ML structure empirically due to the ephemeral nature of submesoscales together with the multiple processes that impact the variability of the MLD. Yet, our summer data provides evidence that submesoscale processes actively modify the ML, but likely do not penetrate below the ML.

The sea-ice impacted ML reflects the influence of atmosphere-ocean fluxes, sea-ice, and internal ocean variability. Here, we have focused on the relative contribution and interactions of atmospheric forcing, sea-ice, and submesoscale flows to the ML structure. Heat flux into the ocean is the dominant process in setting the ML stratification over the summer season, with a relatively small contribution from evaporation and precipitation (Figure 10a). Nevertheless, ML buoyancy anomalies are driven by salinity changes, even well into the summer season (although the magnitude of the anomalies decreases).

In our study, MLEs have weak stratifying potential over the summer season (Figure 10b). Under summer conditions, when the ML is shallow, there is less available potential energy for MLEs to restratify the upper ocean. Nevertheless, model studies (Callies & Ferrari, 2018) show that MLIs are unlikely to be damped out in shallow summer MLs, even if mixing time scales are short. One possibility is that MLIs do grow and lead to restratification of the ML in summer after sea-ice melt but quickly exhaust the energy fueling their growth.

The significant contribution of EBF to the upper ocean surface equivalent heat flux was observed, particularly in early summer following sea-ice melt (Figure 10). In some studies, submesoscale activity under shallow ML conditions has resulted in deepening MLs (Luo et al., 2016; Lévy et al., 2010) due to the increased vertical mixing induced by the fronts that erode the shallow base of the ML. In this study, while we do not test the evolution of the ML structure with and without the inclusion of submesoscale activity, we speculate that the Antarctic MIZ could be responding similarly and observe a gradual deepening of the ML over the summer season. The presence of fine-scale fronts as a result of swirling MLEs may enhance upper ocean mixing through interactions with surface wind stress. Evidence that this may be the case is presented at the end of the observational time series (~ March 20, 2018, Figure 10). A strong wind and precipitation event (Figures 3b and 3c) occur over a strong lateral buoyancy gradient ($>1 \times 10^{-7}$ s^{-2}), inducing very strong submesoscale EBF (>500 W m^{-2}), with the potential to erode the base of the ML and mix the underlying waters into the ML. Similar strength wind events occurred before in the time series (January 18, 2018 and ~ March 10, 2018), but during those times, the lateral buoyancy gradients were weak, and thus EBF was not significant. Because of the intermittency of both the passing wind events and the submesoscale MLEs, it is probable that similar events were missed by the observational platform. It could be speculated, that in nearby regions unobserved by the Seaglider, these wind events, in combination with the lateral buoyancy gradients, may be driving local mixing more than if the submesoscale flows were not active (i.e., when the upper ocean is more homogeneous, winds may not have a large impact).

Here, we argue that the fine-scale lateral gradients observed are representative of MLEs. Mesoscale eddies are present in the region, as evidenced by surface chlorophyll-a (map in Figure 1); however, these are likely concentrated further north near the Southern Boundary of the ACC. If mesoscale stirring is important for frontogenesis (Manucharyan & Thompson, 2017), these fronts, similar to those associated with MLEs in the region, would not penetrate deep into the water column, as sea-ice melt maintains strong vertical stratification. This emphasizes two points: (1) that most of the buoyancy anomalies observed in the ML were confined to the ML, and (2) the confinement of surface fronts in the ML suggests that there is a limited exchange with the interior as a result of sea-ice melt that increases upper ocean stratification and prevents strong cross-isopycnal transport.

Combined, these results support the hypothesis that sea-ice melt enhances the generation of surface fronts. These fronts can potentially allow for large EBF, which impacts the ML structure during early summer in the Antarctic MIZ. In particular, our evidence highlights the role of submesoscale wind-front interactions to maintain weaker early summer stratification at the base of the ML under otherwise highly stratifying conditions in a relatively quiescent ocean.

4.4. Implications

As per Swart et al. (2020), we have shown that submesoscale flow is more active during early summer after sea-ice has melted, most likely energized by the regional impact of meltwater fronts, than later in the summer season. Meltwater is an important driver of water mass transformation in the Southern Ocean (Abernathey et al., 2016; Pellichero et al., 2018). In the summer, the shallow ML of the ice-impacted Southern Ocean is subject to transformation through the influx of fresher meltwater, solar heating, stirring by both mesoscale and submesoscale flows, and the passage of strong wind events. We find that MLI has a low potential to restratify the ML and subduct water to depth. This confirms the necessary advection of these modified waters northward, or potentially downstream in the ACC, before subducting as Antarctic intermediate water (AAIW) and connecting with the global circulation system (e.g., Figure 1; Pellichero et al., 2018). The substantial increase in the impact of winds on the ML when strong lateral buoyancy gradients or fronts are present, provides a secondary mechanism for eroding the base of the ML and mixing with the underlying warmer and saltier waters. It is interesting to consider whether wind interactions with submesoscale flow play an important role in mixing the uCDW waters into the ML. uCDW waters are warm, salty, and high in nutrients; thus, the upwards mixing of these waters will act to support primary production as well as modify the properties of the ML. The implications for ML interior exchange in this region under weak MLEs but stronger EBF when submesoscale fronts are active or reduced is an avenue for future research.

Current models and observations indicate that the Southern Ocean is freshening (Haumann et al., 2016, 2020). Even though the ML may become shallower as it becomes fresher, it is likely that MLI will persist (Callies & Ferrari, 2018), and the dynamics described here will continue to be relevant. It has been suggested that the predicted shallower MLs of a warming climate will suppress submesoscale activity (Richards et al., 2020). Here, we show an Antarctic example with evidence of submesoscale activity when the ML is shallow.

4.5. Caveats

4.5.1. Frontal Processes Observed by Gliders

ML lateral buoyancy gradients are a central parameter in much of the analysis presented in this study. The interpretation of ML fronts observed by profiling gliders is not trivial, and a number of assumptions were made in the presentation of the results.

In this field campaign, the Seaglider was piloted to complete repeat bow-tie patterns over a single geographical area. A complete bow-tie took, on average, 7 days to complete. Sampling fronts in this way means that the Seaglider may sample a single front multiple times. Given the transient nature of surface submesoscale fronts and an ML eddy growth rate of ~10 h, it is unlikely that the same front is indeed sampled multiple times by the Seaglider. Moreover, the background mean flow was ~8 cm s^{-1}, compared to the velocity of the Seaglider ~23 cm s^{-1}. Nevertheless, the data is analyzed such that the results do not rely on repeat sampling

of a front, or the sampling of many fronts, but provides a basis by which to statistically estimate the average presence and strength of these fine-scale fronts and associated impact on the ML, acknowledging that individual features can be very different.

We assume the Seaglider samples fronts perpendicularly. Acknowledging this is not the case, a statistical analysis shows that the lateral gradients are underestimated by a factor of 0.64. Compared to the lateral gradients captured by a Sailbuoy (measuring values of b_x up to 0.06 kg m^{-3} km^{-1}, Swart et al., 2020), which was sampling the study site concurrently, the lateral gradients observed by the Seaglider are small (b_x up to 0.015 kg m^{-3} km^{-1}), but nevertheless comparable to those observed in the Arctic MIZ by Seagliders (~ 0.03 kg m^{-3} km^{-1}, Timmermans & Winsor, 2013).

Additionally, synoptic winds are not always oriented directly downstream or upstream of the fronts. The Seaglider interpretation of the EBF can be analyzed by computing the observed EBF (EBF$_{obs}$) to the actual EBF (EBF$_{actual}$), estimated from all the observed Seaglider angles and wind angles with respect to a fixed buoyancy gradient (following Thompson et al., 2016). The Seaglider tends to capture either all or little of the EBF; however, this method can also overestimate EBF under conditions where the glider perpendicularly crosses the lateral buoyancy gradient while the wind is aligned perpendicular to the front, when, our definition would interpret the wind as aligned parallel to the front and thus overestimate EBF. On average, the ratio of the root mean square of EBF$_{obs}$ to EBF$_{actual}$ is 0.71, suggesting that the EBF values presented here are underestimated.

4.5.2. Regionality

We present the results with reference to Antarctic MIZs, but our conclusions are drawn from a subset of high-resolution data within a 1° × 1° degree box at the northern edge of the Weddell Sea MIZ. We focus on the interactions of processes that are likely prevalent throughout the ice-impacted Southern Ocean. However, we acknowledge that the Antarctic MIZ varies regionally in terms of atmospheric forcing. For example, the Amundsen Sea Low (ASL) controls winds near West Antarctica. If the zonal winds are intensified because of a deeper ASL, the melt of sea-ice occurs earlier in the spring season and solar warming over summer is enhanced (Holland et al., 2017). In such a case, it is likely that submesoscale processes will be more suppressed during summer. In this way, different regions may experience different leading order forcing mechanisms (like the ASL), which may alter the conclusions drawn from these results.

5. Conclusion

Throughout this study, we have demonstrated the influence of sea-ice-derived freshwater on the vertical and lateral structure of the ML. Predominantly northwards, Ekman transport of sea-ice meltwater stratifies the ML in the Antarctic MIZ. However, at the same time, the strong north-south mesoscale gradients that stir early summer sea-ice meltwater create conditions for the formation of fine-scale fronts. We show that while these fronts are confined to the surface boundary layer because of the strong stratification, wind interactions with the resultant fine-scale fronts enhance ML variability and thus the rate of upper ocean modification. The winds interact with the fine-scale fronts, increasing variability within the ML through both stratifying and destratifying buoyancy fluxes induced by cross-front Ekman-driven transport. When the freshwater source decreases later in summer, the magnitude of lateral buoyancy gradients, as well as the submesoscale EBF also decrease. These results show that sea-ice impacted MLs, while predominantly forced by the 1D influx of meltwater during summer, cannot be solely treated as 1D systems. Submesoscale fronts are enhanced by the meltwater mesoscale gradients, modulating the influence of winds on the ML. It, therefore, becomes possible that the ML response to wind forcing and, subsequently, heat and freshwater transport, may be misrepresented in coupled-climate models if the submesoscale is not resolved or accurately parameterized.

Data Availability Statement

ERA5 data are generated using Copernicus Climate Change Service Information, available online (www.ecmwf.int/en/forecasts/datasets/archive-datasets/reanalysis-datasets/era5). All the data used for this analysis can be accessed online (ftp://ssh.roammiz.com) via anonymous login and navigate to giddy_2020. The code used to produce this analysis is available at http://doi.org/10.5281/zenodo.4043036.

Acknowledgments
This work was supported by the following grants of S. Swart: Wallenberg Academy Fellowship (WAF 2015.0186), Swedish Research Council (VR 2019-04400), STINT-NRF Mobility Grant (STNT180910357293). S. A. Nicholson and S. Swart: NRF-SANAP (SNA170522231782, SANAP200324510487) and S. A. Nicholson, the Young Researchers Establishment Fund (YREF 2019 0000007361). S. Swart and M. du Plessis have received funding from the European Union's Horizon 2020 research and innovation program under Grant agreement no. 821001 (SO-CHIC). A. F. Thompson is supported by ONR (N00014-19-1-2421), NSF (1756956, 1829969), and a Linde Center Discovery Fund grant. The authors thank Sea Technology Services (STS), SANAP, the captain, and crew of the S.A. Agulhas II for their field-work/technical assistance. Zach Erickson, Mar Flexas, and Giuliana Viglione (Caltech) contributed to glider piloting throughout the deployment. S. Swart is grateful to Geoff Shilling and Craig Lee (APL, University of Washington) for hosting gliders on IOP. B. Queste is thanked for insightful discussions on glider processing and thermal lag corrections, which was made possible through the UCT-UEA Newton Fund. Special thanks is extended to Isabelle Ansorge for the generous support of I. Giddy in her doctoral studies and training, from which this paper is derived (SANAP 110733 SAMOC-SA). I. Giddy is further supported by the Oppenheimer Memorial Trust. The authors are grateful to the insightful and constructive reviews of Dr. Balwada and one anonymous reviewer, which greatly improved this manuscript.

References

Abernathey, R. P., Cerovecki, I., Holland, P. R., Newsom, E., Mazloff, M., & Talley, L. D. (2016). Water-mass transformation by sea ice in the upper branch of the Southern Ocean overturning. *Nature Geoscience*, *9*(8), 596–601. https://doi.org/10.1038/ngeo2749

Biddle, L. C., & Swart, S. (2020). The observed seasonal cycle of submesoscale processes in the Antarctic marginal ice zone. *Journal of Geophysical Research: Oceans*, *125*(6). https://doi.org/10.1029/2019JC015587

Bitz, C. M., Gent, P. R., Woodgate, R. A., Holland, M. M., & Lindsay, R. (2006). The influence of sea ice on ocean heat uptake in response to increasing CO_2. *Journal of Climate*, *19*(11), 2437–2450. https://doi.org/10.1175/JCLI3756.1

Blumen, W. (1978). Uniform potential vorticity flow: Part I. Theory of wave interactions and two-dimensional turbulence. *Journal of the Atmospheric Sciences*, *35*(5), 774–783. https://doi.org/10.1175/1520-0469(1978)035⟨0774:UPVFPI⟩2.0.CO;2

Boccaletti, G., Ferrari, R., & Fox-Kemper, B. (2007). Mixed layer instabilities and restratification. *Journal of Physical Oceanography*, *37*(9), 2228–2250. https://doi.org/10.1175/JPO3101.1

Boutin, J., Vergely, J. L., Marchand, S., D'Amico, F., Hasson, A., Kolodziejczyk, N., & Vialard, J. (2018). New SMOS sea surface salinity with reduced systematic errors and improved variability. *Remote Sensing of Environment*, *214*, 115–134. https://doi.org/10.1016/j.rse.2018.05.022

Boyd, J. P. (1992). The energy spectrum of fronts: Time evolution of shocks in Burgers equation. *Journal of the Atmospheric Sciences*, *49*(2), 128–139. https://doi.org/10.1175/1520-0469(1992)049⟨0128:TESOFT⟩2.0.CO;2

Brenner, S., Rainville, L., Thomson, J., & Lee, C. (2020). The evolution of a shallow front in the Arctic marginal ice zone. *Elementa: Science of the Anthropocene*, *8*(1), 17. https://doi.org/10.1525/elementa.413

Callies, J., & Ferrari, R. (2013). Interpreting energy and tracer spectra of upper-ocean turbulence in the submesoscale range (1200 km). *Journal of Physical Oceanography*, *43*(11), 2456–2474. https://doi.org/10.1175/JPO-D-13-063.1

Callies, J., & Ferrari, R. (2018). Baroclinic instability in the presence of convection. *Journal of Physical Oceanography*, *48*(1), 45–60. https://doi.org/10.1175/JPO-D-17-0028.1

Callies, J., Ferrari, R., Klymak, J. M., & Gula, J. (2015). Seasonality in submesoscale turbulence. *Nature Communications*, *6*(1), 6862. https://doi.org/10.1038/ncomms7862

Capet, X., McWilliams, J. C., Molemaker, M. J., & Shchepetkin, A. F. (2008). Mesoscale to submesoscale transition in the California current system. Part II: Frontal processes. *Journal of Physical Oceanography*, *38*(1), 44–64. https://doi.org/10.1175/2007JPO3672.1

Charney, J. G. (1971). Geostrophic turbulence. *Journal of the Atmospheric Sciences*, *28*(6), 1087–1095. https://doi.org/10.1175/1520-0469(1971)028⟨1087:GT⟩2.0.CO;2

Chemke, R., & Polvani, L. M. (2020). Using multiple large ensembles to elucidate the discrepancy between the 1979–2019 modeled and observed Antarctic sea ice trends. *Geophysical Research Letters*. *47*(15), e2020GL088339. https://doi.org/10.1029/2020GL088339

D'Asaro, E., Lee, C., Rainville, L., Harcourt, R., & Thomas, L. (2011). Enhanced turbulence and energy dissipation at ocean fronts. *Science*, *332*(6027), 318. https://doi.org/10.1126/science.1201515

de Boyer Montgut, C., Madec, G., Fischer, A. S., Lazar, A., & Iudicone, D. (2004). Mixed layer depth over the global ocean: An examination of profile data and a profile-based climatology. *Journal of Geophysical Research*, *109*(C12). https://doi.org/10.1029/2004JC002378

Dewey, S. R., Morison, J. H., & Zhang, J. (2017). An edge-referenced surface fresh layer in the Beaufort Sea seasonal ice zone. *Journal of Physical Oceanography*, *47*(5), 1125–1144. https://doi.org/10.1175/JPO-D-16-0158.1

du Plessis, M., Swart, S., Ansorge, I. J., Mahadevan, A., & Thompson, A. F. (2019). Southern ocean seasonal restratification delayed by submesoscale wind–front interactions. *Journal of Physical Oceanography*, *49*(4), 1035–1053. https://doi.org/10.1175/JPO-D-18-0136.1

Erickson, Z. K., Thompson, A. F., Callies, J., Yu, X., Garabato, A. N., & Klein, P. (2020). The vertical structure of open-ocean submesoscale variability during a full seasonal cycle. *Journal of Physical Oceanography*, *50*(1), 145–160. https://doi.org/10.1175/JPO-D-19-0030.1

Fox-Kemper, B., Ferrari, R., & Hallberg, R. (2008). Parameterization of mixed layer eddies. Part I: Theory and diagnosis. *Journal of Physical Oceanography*, *38*(6), 1145–1165. https://doi.org/10.1175/2007JPO3792.1

Frajka-Williams, E., Eriksen, C. C., Rhines, P. B., & Harcourt, R. R. (2011). Determining vertical water velocities from seaglider. *Journal of Atmospheric and Oceanic Technology*, *28*(12), 1641–1656. https://doi.org/10.1175/2011JTECHO830.1

Frölicher, T., Sarmiento, J., Paynter, D., Dunne, J., Krasting, J., & Winton, M. (2015). Dominance of the Southern Ocean in anthropogenic carbon and heat uptake in CMIP5 models. *Journal of Climate*, *28*, 862–886. https://doi.org/10.1175/JCLI-D-14-00117.1

Garau, B., Ruiz, S., Zhang, W. G., Pascual, A., Heslop, E., Kerfoot, J., & Tintor, J. (2011). Thermal lag correction on Slocum CTD glider data. *Journal of Atmospheric and Oceanic Technology*, *28*(9), 1065–1071. https://doi.org/10.1175/JTECH-D-10-05030.1

Gregor, L., Ryan-Keogh, T. J., Nicholson, S.-A., du Plessis, M., Giddy, I., & Swart, S. (2019). GliderTools: A Python toolbox for processing underwater glider data. *Frontiers in Marine Science*, *6*, 738. https://doi.org/10.3389/fmars.2019.00738

Haumann, F. A., Gruber, N., & Mnnich, M. (2020). Sea-ice induced Southern Ocean subsurface warming and surface cooling in a warming climate. *AGU Advances*, *1*(2). https://doi.org/10.1029/2019AV000132

Haumann, F. A., Gruber, N., Mnnich, M., Frenger, I., & Kern, S. (2016). Sea-ice transport driving Southern Ocean salinity and its recent trends. *Nature*, *537*(7618), 89–92. https://doi.org/10.1038/nature19101

Holland, M. M., Landrum, L., Raphael, M., & Stammerjohn, S. (2017). Springtime winds drive Ross Sea ice variability and change in the following autumn. *Nature Communications*, *8*(1), 731. https://doi.org/10.1038/s41467-017-00820-0

Horvat, C., Tziperman, E., & Campin, J.-M. (2016). Interaction of sea ice floe size, ocean eddies, and sea ice melting. *Geophysical Research Letters*, *43*(15), 8083–8090. https://doi.org/10.1002/2016GL069742

Jaeger, G. S., MacKinnon, J. A., Lucas, A. J., Shroyer, E., Nash, J., Tandon, A., & Mahadevan, A. (2020). How spice is stirred in the Bay of Bengal. *Journal of Physical Oceanography*, *50*(9), 2669–2688. https://doi.org/10.1175/JPO-D-19-0077.1

Kirkman, C. H., & Bitz, C. M. (2011). The effect of the sea ice freshwater flux on Southern Ocean temperatures in CCSM3: Deep-ocean warming and delayed surface warming. *Journal of Climate*, *24*(9), 2224–2237. https://doi.org/10.1175/2010JCLI3625.1

Klymak, J. M., Crawford, W., Alford, M. H., MacKinnon, J. A., & Pinkel, R. (2015). Along-isopycnal variability of spice in the North Pacific. *Journal of Geophysical Research: Oceans*, *120*(3), 2287–2307. https://doi.org/10.1002/2013JC009421

Koenig, Z., Fer, I., Kols, E., Fossum, T. O., Norgren, P., & Ludvigsen, M. (2020). Observations of turbulence at a near surface temperature front in the Arctic Ocean. *Journal of Geophysical Research: Oceans*, *125*(4). https://doi.org/10.1029/2019JC015526

Large, W. G., & Pond, S. (1981). Open ocean momentum flux measurements in moderate to strong winds. *Journal of Physical Oceanography*, *11*(3), 324–336. https://doi.org/10.1175/1520-0485(1981)011⟨0324:OOMFMI⟩2.0.CO;2

Lévy, M., Klein, P., Tréguier, A.-M., Iovino, D., Madec, G., Masson, S., & Takahashi, K. (2010). Modifications of gyre circulation by sub-mesoscale physics. *Ocean Modelling*, *34*(1–2), 1–15. https://doi.org/10.1016/j.ocemod.2010.04.001

Lu, K., Weingartner, T., Danielson, S., Winsor, P., Dobbins, E., Martini, K., & Statscewich, H. (2015). Lateral mixing across ice meltwater fronts of the Chukchi Sea shelf. *Geophysical Research Letters*, *42*(16), 6754–6761. https://doi.org/10.1002/2015GL064967

Lueck, R. G., & Picklo, J. J. (1990). Thermal inertia of conductivity cells: Observations with a sea-bird cell. *Journal of Atmospheric and Oceanic Technology*, *7*(5), 756–768. https://doi.org/10.1175/1520-0426(1990)007⟨0756:TIOCCO⟩2.0.CO;2

Luo, H., Bracco, A., Cardona, Y., & McWilliams, J. C. (2016). Submesoscale circulation in the northern Gulf of Mexico: Surface processes and the impact of the freshwater river input. *Ocean Modelling*, *101*, 68–82. https://doi.org/10.1016/j.ocemod.2016.03.003

Mahadevan, A., D'Asaro, E., Lee, C., & Perry, M. J. (2012). Eddy-driven stratification initiates North Atlantic spring phytoplankton blooms. *Science*, *337*(6090), 54–58. https://doi.org/10.1126/science.1218740

Manucharyan, G. E., & Thompson, A. F. (2017). Submesoscale sea ice-ocean interactions in marginal ice zones. *Journal of Geophysical Research: Oceans*, *122*(12), 9455–9475. https://doi.org/10.1002/2017JC012895

McDougall, T. J., & Barker, P. M. (2011). *Getting started with TEOS-10 and the Gibbs seawater (GSW) oceanographic toolbox*. (pp. 28).

McWilliams, J. C. (2016). Submesoscale currents in the ocean. *Proceedings of the Royal Society A: Mathematical, Physical & Engineering Sciences*, *472*(2189), 20160117. https://doi.org/10.1098/rspa.2016.0117

Newman, L., Heil, P., Trebilco, R., Katsumata, K., Constable, A., van Wijk, E., & Spreen, G. (2019). Delivering sustained, coordinated, and integrated observations of the Southern Ocean for global impact. *Frontiers in Marine Science*, *6*, 433. https://doi.org/10.3389/fmars.2019.00433

Parkinson, C. L. (2014). Global sea ice coverage from satellite data: Annual cycle and 35-Yr trends. *Journal of Climate*, *27*(24), 9377–9382. https://doi.org/10.1175/JCLI-D-14-00605.1

Patoux, J., Yuan, X., & Li, C. (2009). Satellite-based midlatitude cyclone statistics over the Southern Ocean: 1. Scatterometer-derived pressure fields and storm tracking. *Journal of Geophysical Research*, *114*(D4). https://doi.org/10.1029/2008JD010873

Pellichero, V., Salle, J.-B., Chapman, C. C., & Downes, S. M. (2018). The southern ocean meridional overturning in the sea-ice sector is driven by freshwater fluxes. *Nature Communications*, *9*(1), 1789. https://doi.org/10.1038/s41467-018-04101-2

Pellichero, V., Salle, J.-B., Schmidtko, S., Roquet, F., & Charrassin, J.-B. (2017). The ocean mixed layer under Southern Ocean sea-ice: Seasonal cycle and forcing. *Journal of Geophysical Research: Oceans*, *122*(2), 1608–1633. https://doi.org/10.1002/2016JC011970

Richards, K. J., Whitt, D. B., Brett, G., Bryan, F. O., Feloy, K., & Long, M. C. (2020). The impact of climate change on ocean submesoscale activity. *Oceanography*. https://doi.org/10.1002/essoar.10503524.1

Rudnick, D. L., & Cole, S. T. (2011). On sampling the ocean using underwater gliders. *Journal of Geophysical Research*, *116*(C8). https://doi.org/10.1029/2010JC006849

Smith, M., Stammerjohn, S., Persson, O., Rainville, L., Liu, G., Perrie, W., & Thomson, J. (2018). Episodic reversal of autumn ice advance caused by release of ocean heat in the Beaufort Sea. *Journal of Geophysical Research: Oceans*, *123*(5), 3164–3185. https://doi.org/10.1002/2018JC013764

Speer, K., Rintoul, S. R., & Sloyan, B. (2000). The diabatic Deacon cell. *Journal of Physical Oceanography*, *30*(12), 3212–3222. https://doi.org/10.1175/1520-0485(2000)030⟨3212:TDDC⟩2.0.CO;2

Spreen, G., Kaleschke, L., & Heygster, G. (2008). Sea ice remote sensing using AMSR-E 89-GHz channels. *Journal of Geophysical Research*, *113*. https://doi.org/10.1029/2005JC003384

Stone, P. H. (1970). On non-geostrophic baroclinic stability: Part II. *Journal of the Atmospheric Sciences*, *27*(5), 721–726. https://doi.org/10.1175/1520-0469(1970)027⟨0721:ONGBSP⟩2.0.CO;2

Swart, S., du Plessis, M. D., Thompson, A. F., Biddle, L. C., Giddy, I., Linders, T., & Nicholson, S.-A. (2020). Submesoscale fronts in the Antarctic marginal ice zone and their response to wind forcing. *Geophysical Research Letters*, *47*(6), e2019GL086649. https://doi.org/10.1029/2019GL086649

Swart, S., Gille, S. T., Delille, B., Josey, S., Mazloff, M., Newman, L., & Zappa, C. J. (2019). Constraining Southern Ocean air-sea-ice fluxes through enhanced observations. *Frontiers in Marine Science*, *6*, 421. https://doi.org/10.3389/fmars.2019.00421

Swart, S., Speich, S., Ansorge, I. J., & Lutjeharms, J. R. E. (2010). An altimetry-based gravest empirical mode south of Africa: 1. Development and validation. *Journal of Geophysical Research*, *115*(C3), C03002. https://doi.org/10.1029/2009JC005299

Swart, S., Thomalla, S. J., & Monteiro, P. M. S. (2015). The seasonal cycle of mixed layer dynamics and phytoplankton biomass in the Sub-Antarctic Zone: A high-resolution glider experiment. *Journal of Marine Systems*, *147*, 103–115. https://doi.org/10.1016/j.jmarsys.2014.06.002

Thomas, L. N., & Lee, C. M. (2005). Intensification of ocean fronts by down-front winds. *Journal of Physical Oceanography*, *35*(6), 1086–1102. https://doi.org/10.1175/JPO2737.1

Thomas, L. N., Tandon, A., & Mahadevan, A. (2008). Submesoscale processes and dynamics. In M. W. Hecht & H. Hasumi (Eds.), *Ocean modeling in an eddying regime*. https://doi.org/10.1029/177GM04

Thompson, A. F., Lazar, A., Buckingham, C., Naveira Garabato, A. C., Damerell, G. M., & Heywood, K. J. (2016). Open-ocean submesoscale motions: A full seasonal cycle of mixed layer instabilities from gliders. *Journal of Physical Oceanography*, *46*(4), 1285–1307. https://doi.org/10.1175/JPO-D-15-0170.1

Timmermans, M.-L., Cole, S., & Toole, J. (2012). Horizontal density structure and restratification of the Arctic Ocean surface layer. *Journal of Physical Oceanography*, *42*(4), 659–668. https://doi.org/10.1175/JPO-D-11-0125.1

Timmermans, M.-L., & Winsor, P. (2013). Scales of horizontal density structure in the Chukchi Sea surface layer. *Continental Shelf Research*, *52*, 39–45. https://doi.org/10.1016/j.csr.2012.10.015

Turner, J. (1973). *Buoyancy effects in fluids*. (pp. 367). Cambridge, UK: Cambridge University Press.

Vichi, M., Eayrs, C., Alberello, A., Bekker, A., Bennetts, L., Holland, D., & Toffoli, A. (2019). Effects of an explosive polar cyclone crossing the Antarctic marginal ice zone. *Geophysical Research Letters*, *46*(11), 5948–5958. https://doi.org/10.1029/2019GL082457

Viglione, G. A., Thompson, A. F., Flexas, M. M., Sprintall, J., & Swart, S. (2018). Abrupt transitions in submesoscale structure in Southern Drake Passage: Glider observations and model results. *Journal of Physical Oceanography*, *48*(9), 2011–2027. https://doi.org/10.1175/JPO-D-17-0192.1

von Appen, W.-J., Wekerle, C., Hehemann, L., Schourup-Kristensen, V., Konrad, C., & Iversen, M. H. (2018). Observations of a submesoscale cyclonic filament in the marginal ice zone. *Geophysical Research Letters*, *45*(12), 6141–6149. https://doi.org/10.1029/2018GL077897

Supporting Information for "Stirring of sea ice meltwater enhances submesoscale fronts in the Southern Ocean"

I. Giddy[1,2,3], S. Swart[1,2], M. du Plessis[2,3], A. F. Thompson[4]

, S.A. Nicholson[3]

[1]Department of Oceanography, University of Cape Town, Rondebosch, South Africa

[2]Department of Marine Sciences, University of Gothenburg, Gothenburg, Sweden

[3]Southern Ocean Carbon-Climate Observatory (SOCCO), CSIR, Cape Town, South Africa

[4]Environmental Science and Engineering, California Institute of Technology, Pasadena, CA,USA

Contents of this file

1. Figures S1 to S3

Introduction

The supporting information contains four additional figures.

The first figure is used to define the water masses referred to in the main text.

The second places the Seaglider deployment into a seasonal context by comparison with a co-located SOCCOM float (5904397). Specifically, this was used in the main text to

---

Corresponding author: I. Giddy, Department of Oceanography, University of Cape Town, Rondebosch, South Africa (isgiddy@gmail.com)

determine when the mixed layer summer shoaling event occured and from what depth. The SOCCOM data is freely available via `soccom.princeton.edu`

The final figure gives the cumulative sum of local submesoscale Ekman Buoyancy Fluxes highlighting the increased variability during early summer.

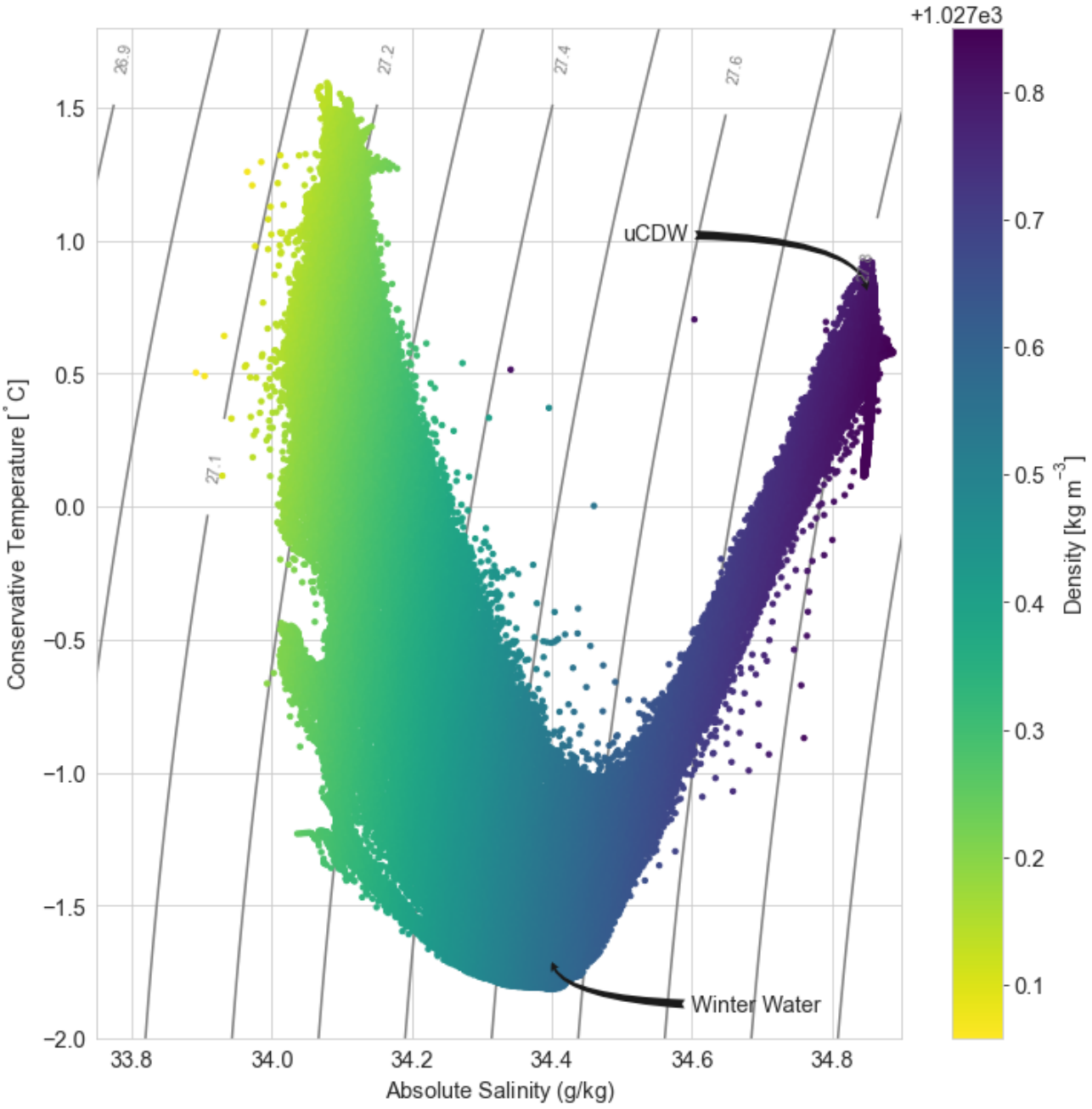

Figure S1. TS diagram for the full deployment. The definitions of Winter Water and upper Circumpolar Water are indicated with the arrows.

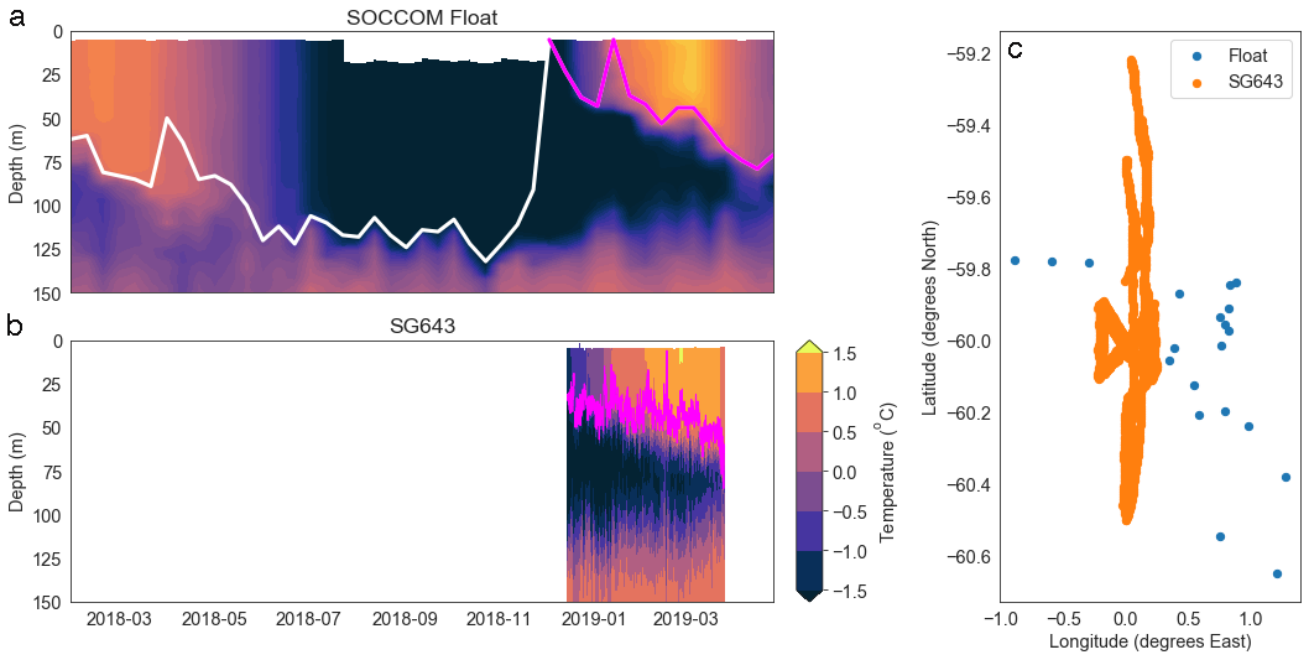

Figure S2. Colocated SOCCOM float (id: 5904397) compared with the Seaglider. a) Temperature section observed by the SOCCOM float. The white and magenta line is the mixed layer depth. The magenta line corresponds to the blue points in c). b) Temperature section observed by the Seaglider. The magenta line indicates the mixed layer depth. c) Location of the Seaglider (orange points) and SOCCOM float (blue points).

Figure S3. Time cumulative sum of submesoscale Ekman Buoyancy Flux.

Paper III

Vertical convergence of turbulent and double diffusive heat flux drives warming and erosion of Antarctic Winter Water in summer

I. Giddy, I. Fer, S. Swart, S-A. Nicholson
Journal of Physical Oceanography, **manuscript**

Vertical convergence of turbulent and double diffusive heat flux drives warming and erosion of Antarctic Winter Water in summer

in prep for submission to the Journal of Physical Oceanography

I.S. Giddy,[a,b,c] I. Fer,[d] S. Swart,[a, b] S-A. Nicholson,[c]

[a] *Department of Marine Sciences, University of Gothenburg*

[b] *Department of Oceanography, University of Cape Town*

[c] *Southern Ocean Carbon-Climate Observatory, CSIR, South Africa*

[d] *Geophysical Institute, University of Bergen and Bjerknes Center for Climate Research, Bergen, Norway*

Corresponding author: I.S. Giddy, isgiddy@gmail.com

ABSTRACT: The seasonal warming of Antarctic winter waters is a key process along the pathway of deep water transformation to intermediate waters entering the upper branch of the circumpolar overturning circulation. However, the driving mechanisms that mediate the warming of Antarctic winter water have not been quantified. Using 38 days of glider measurements of microstructure shear, we characterize the rate of turbulent dissipation and its drivers over a summer season in the northern Weddell Sea. Observed dissipation rates in the surface layer are mainly forced by winds, and explained by the stress scaling (r^2=0.84). However, mixing to the base of the mixed layer during strong wind events is suppressed by vertical stratification from sea ice melt. Between the winter water layer and the warm and saline circumpolar deep water, a subsurface layer of enhanced dissipation is maintained by double-diffusive convection (DDC). We develop a winter water layer temperature budget and show that a warming trend (0.2°C over 28 days) is driven by a convergence of heat flux through mechanically-driven mixing at the base of the mixed layer and DDC at the base of the winter water layer. Notably, excluding the contribution from DDC results in an underestimation of winter water warming by 23%, highlighting the importance of adequately representing DDC in ocean models. These results further suggest that an increase in storm intensity and frequency during summer could increase the rate of warming of the winter water layer with implications for rates of upper ocean water mass transformation.

SIGNIFICANCE STATEMENT: Around Antarctica, the summer warming of the subsurface cold Antarctic winter water feeds the upper layer of the overturning circulation. This study aims to quantify the mechanisms that mediate the warming of Antarctic winter water. Our results reveal that the observed warming of this layer can be explained by both surface wind-driven mixing processes as well as double-diffusive convection occurring beneath the winter water layer. Understanding the role of these mechanisms is important for understanding the regions upper ocean heat distribution, the rates of water mass transformation and how they might respond to changes in sea ice, stratification and the overlying large-scale winds.

1. Introduction

A unique characteristic of polar ocean regions is the formation of winter waters through intense heat loss to the atmosphere and sea ice freezing. In summer, the subsurface winter waters act as a barrier between the atmosphere and deep water sources of heat and carbon, thereby modulating the direct exchange of heat and carbon between the atmosphere and ocean interior. South of the Antarctic Polar Front (APF), cold Antarctic winter waters form an inversion separating the warm surface waters from the warm, CO_2-rich upper Circumpolar Deep Water (UCDW). Here UCDW upwells towards the surface, where it is transformed by air-sea-ice buoyancy fluxes, thereafter subducting as part of the upper branch of the meridional overturning circulation (Abernathey et al. 2016; Pellichero et al. 2018). The along-isopycnal link between the deep ocean and the surface in this region means that changes in the physical drivers of upper ocean properties, and therefore the rate of water mass transformation, can have global implications. The rate of water mass transformation in the upper-ocean has been linked to the transport and melt of sea ice (Abernathey et al. 2016), which increases the buoyancy of surface waters before they enter the upper branch of the overturning circulation. Below the mixed layer, the exchange of water properties between the mixed layer and UCDW, across the Antarctic winter water layer plays an important part in the transformation of UCDW to Antarctic Intermediate Water (AAIW) during summer (Evans et al. 2018). Thus, understanding the processes that form and modify winter water is of global climatic relevance.

Winter water is formed during cold winter months under destabilizing buoyancy forcing through cooling and sea ice growth. During these months, the surface mixed layer cools and deepens, en-

training underlying deep waters (UCDW, Foster and Carmack 1976; Hoppema 2004) and resulting in vertical fluxes of heat and salt (Gordon and Huber 1984; Martinson 1990; Evans et al. 2018). If the mixed layer cools sufficiently for sea ice formation, subsequent brine rejection during sea ice growth will increase the density of the mixed layer and entrain more heat from below, which will in turn warm the mixed layer further. This balance limits the volume of sea ice that can form, maintaining a relatively thin layer (~0.5 m) of sea ice across the subpolar Southern Ocean (Gordon and Huber 1990; Shaw and Stanton 2014). The interplay between surface cooling and sea ice formation with the resultant upwards heat fluxes also limits the depth of surface mixing, confining the mixed layer to the upper 200 m (Gordon and Huber 1990; Pellichero et al. 2017; Wilson et al. 2019). Regional heterogeneity in the thermodynamic coupling between winter sea ice and upper ocean stratification, highlighted by Wilson et al. (2019), showed that stronger pycnoclines require far greater winter sea ice growth to erode the pycnocline in regions of the Pacific Ocean whereas, in the Atlantic sector, typically weaker pycnoclines precondition the region for deeper convection. Weak stratification coupled with a sharp thermocline that is characteristic in the Weddell Sea, favors a high rate of wintertime heat ventilation and a strong negative feedback to ice growth, as observed by Shaw and Stanton (2014).

In the winter, mixing across the mixed layer/UCDW interface cools UCDW, priming it for transformation to intermediate waters in the summer (Evans et al. 2018). During austral-summer, winter water is identified as a local subsurface temperature minimum, capped between the warm, fresh surface waters and the underlying warm and salty UCDW (Toole 1981; Gordon and Huber 1990; Evans et al. 2018; Sabu et al. 2020). The depth of temperature minimum ranges from ~300 m near the Polar Front to shallower depths (~50 m) with proximity to the Antarctic continent, where sea ice melt additionally stratifies the upper ocean (Toole 1981). As summer progresses, the subsurface winter water layer warms and erodes. Evans et al. (2018) show that these two aforementioned seasonal transitions of winter water formation and progression, and its role in UCDW transformation, i.e, via cooling and freshening of UCDW as winter water is formed, followed by summertime warming and freshening of UCDW, is driven both by air-ice-sea buoyancy fluxes at the surface and mixing at the subsurface. They attribute the wintertime transformation of dense water into lighter upper-ocean mixed layer water to the action of cabbeling (in which two water parcels mix to form a denser water parcel), at the subsurface between salty, cold mixed layer

waters and the warm and salty UCDW water. The summertime transformation is attributed to heat exchange with the atmosphere and sea ice melt. While Evans et al. (2018) addressed the processes driving the transformation of UCDW to AAIW at basin scales, the surface and subsurface mixing processes were not explicitly observed. Ultimately, water properties are irreversibly mixed at the scale of dissipation. Here, we use direct observations of dissipation to attribute the drivers of and quantify the rate of surface and subsurface mixing processes that control the transformation of winter water to AAIW during austral summer.

The main sources of turbulence production in the surface ocean are convection, winds and waves. In the summer, the surface buoyancy fluxes are typically stabilizing (positive into the ocean) through surface warming and sea ice melt (Pellichero et al. 2017; Giddy et al. 2021). Thus, the remaining sources of turbulence production at the surface are primarily from winds and waves (Belcher et al. 2012). Wind and wave-driven shear production is prevalent in the Southern Ocean in all seasons (Belcher et al. 2012). Mixing due to wind-driven shear production in the surface mixed layer is important in driving fluxes of carbon between UCDW and the mixed layer (e.g. Song et al. 2019; Nicholson et al. 2022). Processes that drive enhanced wind-driven shear above the cold winter water may result in substantial heat exchange, increasing the rate of warming and erosion of the winter water. Indeed, winter water properties in the Southern Ocean vary zonally over summer in both temperature and thickness (Figure 1; Sabu et al. 2020), responding to changes in wind forcing (Anilkumar et al. 2006) and large scale atmospheric variability (e.g. Southern Annular Mode, SAM). Stronger winds and a positive SAM promote enhanced warming of winter water, likely through shear-driven mixing in the mixed layer (Sabu et al. 2020).

The possible subsurface mixing processes are shear instabilities from background shear, and breaking internal waves. Additionally, in polar oceans, the vertical thermohaline structure preconditions the ocean to double-diffusive convection (DDC, van der Boog et al. 2021). DDC was shown to be present at the base of the winter water where warm, salty water underlies cooler, fresher water (Shaw and Stanton 2014; Bebieva and Speer 2019). However, its contribution to the warming of the winter water layer is not known in summer. DDC can occur when gravitationally stable colder, and fresher water, overlies warmer, saltier water. At a molecular level, heat diffuses approximately 100 times faster than salt in sea water. Thus, if a parcel of fluid is displaced downwards, it will quickly absorb heat by diffusion from its surroundings and ”overshoot” when rising back through

the medium. This leads to an oscillation of growing amplitude and convecting cells, ultimately forming well-mixed layers separated by thin interfaces with temperature and salinity steps. The vertical structure is visible as characteristic layering or staircases in the temperature and salinity profiles when background turbulent mixing is sufficiently weak to allow the formation of the layer (Bebieva and Timmermans 2016; Shaw and Stanton 2014; Shibley et al. 2017). The resultant convection can lead to elevated rates of dissipation. Notably, the convecting cells can effectively exchange heat and salt across the interface because all potential energy (PE) is used to produce Turbulent Kinetic Energy (TKE, St. Laurent and Schmitt 1999; Inoue et al. 2007). This differs from shear-driven turbulence production wherein a proportion of TKE (~0.2; Osborn 1980) is expended in raising the PE of the water parcel and driving a buoyancy flux under stable stratification. An outstanding question pertains to the role of DDC in ice free summertime conditions and its contribution to the observed thinning and warming of winter water.

The aforementioned mixing processes may drive modifications to winter water through the summer via turbulence production in the surface and subsurface. The primary goal of this study is to investigate the role of turbulent mixing in the transformation of winter water during summer using 38 days of direct observations of turbulent dissipation in the Weddell Sea. We (1) present a detailed characterisation of turbulent dissipation, (2) confirm the likely sources of turbulence, (3) quantify mean vertical heat fluxes and (4) determine the contribution of diapycnal heat fluxes to the seasonal warming of the winter water and therefore the processes that may increase or reduce the rate of transformation of winter water.

2. Data and Methods

a. Slocum

A 1000-m-rated Teledyne Webb Research (TWR) Slocum G2 electric glider, referred through text as “glider”, was deployed from the *RV SA Agulhas II* at 58°S, 0°E on the 17 December 2019. The glider then transited directly south for 10 days, completing a ”mesoscale transect” (~224 km), until it reached 60°S on 25 December 2019. Thereafter, the glider completed a bow-tie pattern of shorter ”submesoscale transects” (~20-60 km) until it was retrieved on 18 February 2020 (see inset on Fig. 1a). The bow-tie sampling pattern is chosen to increase the range of angles that the glider crosses lateral gradients within the mixed layer (Thompson et al. 2016). The glider was fitted with

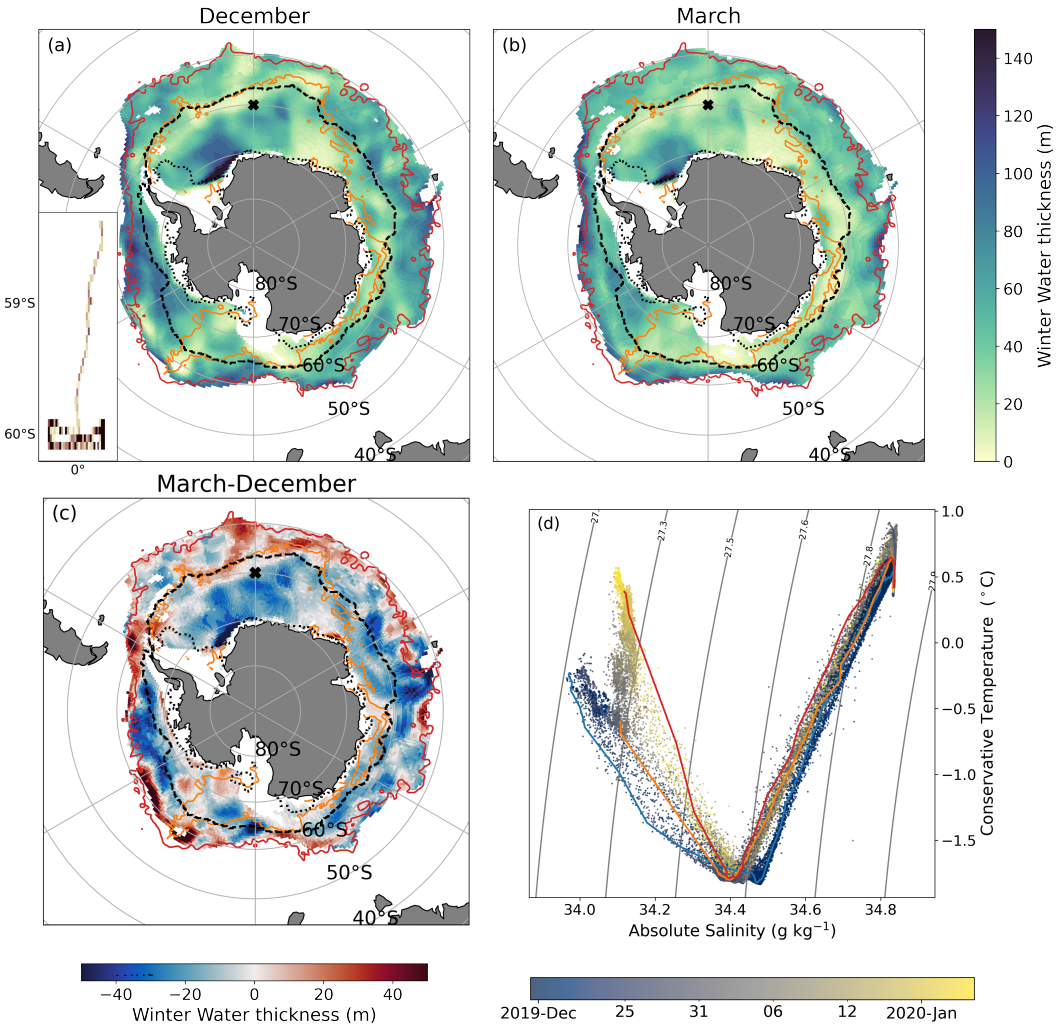

FIG. 1. Study location where Antarctic winter water is present and the location of the glider (black X at 0°E 60°S) deployed from December 2019 to February 2020. The inset on (a) shows the glider sampling pattern. The average winter water thickness and its spatial extent are shown in (a) and (b), which is derived from Monthly Isopycnal and Mixed Layer Climatology (MIMOC; Schmidtko et al. 2013) data for December and March respectively. The seasonal progression of the thickness of the winter water (e.g. the difference between March and December climatologies) is shown in (c). Contours on (a-c) indicate Antarctic Polar Front (red), Southern Boundary of the Antarctic Circumpolar Current (orange), and the maximum (black dashed) and minimum (black dotted) extent of sea ice (National Snow and Ice Data Center). (d) Temperature and salinity plot colored by time based on measurements from the glider highlighting the summer seasonal progression of thermohaline properties of the Mixed Layer, Winter water and Upper Circumpolar Deep Water (UCDW). Three example profiles of the progression in TS properties during the observational period (deployment, start of submesoscale transects and retrieval) are plotted in blue, orange and red, respectively.

a Sea-Bird Slocum Glider Pumped Conductivity, Temperature and Depth sensor (GPCTD). On 24 January 2020 the CT-pump failed because of a blockage, rendering the salinity data thereafter unusable until it unblocked on 10 February 2020. For the purposes of this study we elected to truncate the data at this point, and only included data until 24 January 2020, resulting in 38 days of continuous 1-second resolution temperature, salinity and pressure observations. The glider data were processed and corrected for thermal inertia of the conductivity cell using the software kindly provided by Dr. Gerd Krahmann (GEOMAR, Germany). This includes a hydrodynamic model from which the angle of attack and flow rate past the sensor are computed. Temperature and salinity measurements were compared with in situ CTD casts during deployment and retrieval of the glider. No correction was applied to temperature, but salinity was corrected for an initial offset of +0.0125 g kg^{-1} and a linear drift of -3.8×10^{-4} g kg^{-1} day-1 over the full deployment.

b. Microstructure

The glider was fitted with a neutrally buoyant, low-power, self-contained turbulence instrument package MicroRider-1000LP (MR), manufactured by Rockland Scientific International, Canada. The MR was equipped with two orthogonal airfoil velocity shear probes (SPM-38), a pressure transducer, a two-axis vibration sensor (a pair of piezo-accelerometers), and a high-accuracy dual-axis inclinometer (ADIS 16209, pitch and roll angles accurate to 0.18°). Shear microstructure measurements were made to 500 m on both up and down casts throughout the deployment. The sampling frequency is 512 Hz on all turbulence channels (vibration, shear) and 64 Hz for the other channels (pitch, roll, and pressure).

The viscous dissipation rate of TKE per unit mass (dissipation hereafter) is derived from the shear microstructure following Fer et al. (2014) using an adaption of the Rockland Scientific ODAS v4.4.04 software. The record from each shear probe is segmented into half-overlapping 30 second long portions for spectral analysis. A fast Fourier transform (FFT) length corresponding to 5 seconds is chosen, and each 5 second segment is detrended and Hanning windowed before calculating the spectra. The average speed through the water, or equivalently, the flow past the MR sensor, U_P, was 0.37 m s^{-1} during the deployment. We use this value, together with the size of the glider (~2 m) to determine the time interval over which to calculate the rate of dissipation, noting that the FFT length should not be greater than the length of the platform. For statistical reliability

the ratio of dissipation length to FFT length should never be less than 2. We elected to use the 30 second interval, with a 5 second FFT length and 50% overlap (15 seconds), which gives a degrees of freedom of 5. This selection is equivalent to 1.8 m along path length and resolves the low wavenumber part of the spectrum that is crucial for the roll off for low dissipation rates. The shear probe signal coherent with the accelerometer data (from the two-axis vibration sensor) is removed using the method outlined in (Goodman et al. 2006). The frequency spectra are converted into along-path wavenumber, k, spectra using Taylor's frozen field turbulence hypothesis and U_P. The dissipation rate for each segment is then calculated, assuming isotropic turbulence, by integrating the wavenumber spectrum as:

$$\varepsilon_j = \frac{15}{2}\nu\overline{(\frac{\partial u_j}{\partial x})^2} \approx \frac{15}{2}\nu\int_{k_l}^{k_u}\Psi(k)dk, \tag{1}$$

where $\frac{\partial u_j}{\partial x}$ is the turbulent scale shear component measured along the glider's along-path coordinate x, j identifies the shear probe number oriented orthogonal to measure the transverse and vertical components of the along-path shear, ν is the kinematic viscosity of seawater, that is a function of the local water temperature, and the overbar denotes averaging. The shear wavenumber spectrum is integrated between k_l, set by the window length and k_u, the minimum in a curve fit to the shear spectrum, that is unaffected by noise. The empirical model for the turbulence spectrum, determined by Nasmyth (1970), is used to correct for unresolved variance.

Following the initial estimation of dissipation a number of quality control steps were applied, detailed in Appendix A.1. The noise floor for ε is determined to be 10^{-12} W kg^{-1}.

c. Ancillary Data

Additional data products are used together with the glider data to estimate and characterize the surface forcing and ocean dynamics for the region. Co-located zonal and meridional wind stress as well as sensible, latent, shortwave and long wave heat fluxes together with evaporation and precipitation, were retrieved from ERA5 reanalysis at hourly intervals, with a 0.25° x 0.25° resolution (Hersbach et al. 2018). The sea surface height fields used to determine the location of the Antarctic Polar Front and the Southern Boundary of the Antarctic Circumpolar Current (ACC) are based on SSALTO/Duacs Maps of Absolute Dynamic Height (MADT). Monthly Isopycnal and

Mixed-layer Ocean Climatology (MIMOC; Schmidtko et al. 2013) is used to produce the winter water thickness maps shown in Fig 11.

d. Surface Buoyancy and Momentum Fluxes

Net buoyancy into the ocean is defined as:

$$Bo = -g[\frac{\alpha Q_{net}}{\rho c_p} + \beta S(E-P)], \tag{2}$$

where g = 9.8 m s^{-2} is gravitational acceleration, α is the thermal expansion coefficient computed from Absolute Salinity and Conservative Temperature using the Gibbs Sea Water Toolbox (McDougall and Barker 2011)], Q_{net} is the net heat flux into the ocean (shortwave + longwave + latent + sensible), c_p is the heat capacity of water = 4000 J K^{-1} kg^{-1}, ρ_0=1027 kg m^{-3} is a reference density, β is the saline contraction coefficient, E, evaporation, P, precipitation, and S is surface salinity measured by the glider.

e. Water Mass Definitions

The water mass layers are defined as follows. The mixing layer depth is derived from estimates of turbulent dissipation following (Brainerd and Gregg 1995) where active mixing occurs above a threshold of $\varepsilon = 10^{-8}$ W kg^{-1}. The mixed layer depth is defined based on a change in density of 0.03 kg m^{-3} from a reference depth of 10 m (Boyer Montégut et al. 2004). The base of the winter water is identified as the isopycnal of the maximum winter mixed layer depth measured by a BGC-Argo float (WMO ID: 5094397, Talley et al. 2019), that was circulating in close proximity to the glider. In the case of the MIMOC data, the base of the winter water is similarly computed using the seawater density in the mixed layer in September when the mixed layer is, on average, deepest. A transition layer between the winter water and UCDW is defined as the region of high stratification below the winter water (as in Dohan and Davis 2011). To remove the effects of internal waves, the transition layer was smoothed by the inertial period (13 hours). Beneath the transition layer lies the UCDW.

f. Derivation of turbulence parameters

The turbulent buoyancy or heat flux can be expressed as a down-gradient mixing of density at a rate given by a diapycnal eddy diffusivity, K. Diapycnal diffusivity is estimated from measurements of turbulent viscous dissipation following the Osborn (1980) model for mixing in a stratified ocean and assuming isotropy.

$$K = \Gamma \frac{\varepsilon}{N^2}, \tag{3}$$

where Γ is the mixing efficiency coefficient, ε is viscous dissipation and N is the Brunt-Vaïsala frequency, calculated using the Gibbs Seawater TEOS-10 Toolbox (McDougall and Barker 2011).

In this model, a parameterization of mixing efficiency, the mixing efficiency coefficient, Γ , is applied. The mixing efficiency coefficient indicates the conversion efficiency of TKE into PE and is assumed, at its upper limit, to be a constant, 0.2. However, the mixing efficiency varies depending on the intensity of mixing. Turbulence intensity is measured using the Reynolds buoyancy number (Re) which quantifies the energetic capacity of the stratified flow to develop vertical overturns that lead to diapycnal mixing.

$$\mathrm{Re} = \frac{\epsilon}{\nu N^2}, \tag{4}$$

where $\nu = 1.8 \times 10^{-6}$ m^2 s^{-1} is the kinematic viscosity.

At high or low mixing intensities the mixing efficiency decreases (Gregg et al. 2018). Bouffard and Boegman (2013) developed four regimes based on the Reynolds buoyancy number to modulate diapycnal diffusivity depending on the ratio of turbulent mixing to stratification. These regimes are marked in Figure 3. The above holds for conditions where shear is the source of turbulent production, however because double diffusive convection is driven by the release of PE, the production term of the TKE budget becomes negligible such that the efficiency coefficient can be assumed to be close to 1 (St. Laurent and Schmitt 1999).

Further assuming the eddy diffusivity of density is equivalent to the eddy diffusivity of temperature, the vertical flux of heat (positive upward) can be defined as:

$$F_H = -\rho_0 c_p K \frac{\partial T}{\partial z}, \tag{5}$$

where K is the diapycnal eddy diffusivity and $\partial T/\partial z$ is the vertical gradient in temperature with depth. We use the gradient in temperature and density computed over 3 meters.

g. Double Diffusive Convection

Double Diffusive Convection (DDC) is an efficient mechanism for heat and salt transport in the ocean. The potential for DDC to occur is assessed using the density ratio (R_ρ) defined here as:

$$R_\rho \equiv \frac{\alpha \Delta T}{\beta \Delta S}, \tag{6}$$

in which ΔT /ΔS is the ratio of the bulk vertical gradients of temperature and salinity, estimated as the difference in temperature and salinity between the adjacent layers.

The density ratio can be mapped onto polar coordinates to give the Turner Angle (Turner 1973):

$$\mathrm{Tu} = \tan^{-1}(\alpha \frac{\partial T}{\partial z} - \beta \frac{\partial S}{\partial z}, \alpha \frac{\partial T}{\partial z} + \beta \frac{\partial S}{\partial z}. \tag{7}$$

When Tu is less than $\frac{-\pi}{4}$ and greater than $\frac{-\pi}{2}$, the water column is susceptible to DDC, with values closer to $\frac{-\pi}{4}$ experiencing stronger DDC.

h. Geometric and Arithmetic Means

Turbulent dissipation spans many orders of magnitude, is intermittent and patchy in space and time. These characteristics mean that dissipation has a log-normal distribution (Baker and Gibson 1987). Therefore, we elect to calculate the geometric mean instead of the arithmetic mean as a measure of the mixing rate over the course of the deployment. Using the arithmetic mean, which, in a log-normal distribution, is generally biased to a small number of large values on the right-hand side of the distribution, rather characterizes the integrated effect of the distribution (see discussion by Scheifele et al. 2021). For the estimation of eddy diffusivity, we use the geometric mean, but both values are reported. For clarity, when we apply the geometric mean, it is stated, and always plotted in grey, otherwise the arithmetic mean is assumed.

3. Results

a. Observations of summertime warming and erosion of Antarctic Winter Water

During austral summer, the subpolar Southern Ocean (south of the Antarctic Polar Front) is characterized by the widespread presence of subsurface winter water (Figure 1a-b). The thickness of the winter water (49 ± 28 m), which is ultimately an indication of the extent of the barrier between the surface mixed layer and the deeper interior heat and carbon reservoirs, is spatially heterogeneous. In December, the thickest winter water layers are located in the southern Weddell Sea (~250 m), with a band of thinner winter water at the Southern Boundary of the ACC (~10 m; Figure 1a). The rate of erosion or thinning of the winter water layer over the summer season is also widespread but heterogeneous (Figure 1c). Notably, winter water in the Ross Sea and in regions further to the north is observed to spread vertically (become thicker instead of thinner).

In situ glider observations, which are carried out in a region where on average winter water thickness erodes in summer (by ~ 20 m, Figure 1c), provide a high-resolution perspective of the seasonal evolution of the vertical structure of the upper ocean in this region. The water column at the glider location in the north east Weddell Sea is composed of three distinct water masses identified in temperature and salinity space (Figure 1d): the surface mixed layer (ML), the winter water characterized by the temperature minimum and the deep warm and saline UCDW. The surface waters and winter waters increase in temperature, seen as an upwards shift in the T/S plot at densities below the 27.6 kg m^{-3} isopycnal (Figure 1d). Three profiles are identified (also shown in Figure 2a) from the start of the observation period (blue), near the start of the submesoscale transects (orange) and towards the end of the deployment (red) to highlight the seasonal warming of the winter water.

The subsurface temperature minimum that identifies the winter water is again evident in the time-averaged vertical profile of temperature (Figure 2a). Recent sea ice melt caps the cold, salty surface water that formed during winter with a shallow, fresh layer that rapidly warms under positive heat fluxes from the atmosphere (Figure 4a). The combination of these stabilizing buoyancy fluxes results in a strongly stratified mixed layer (Figure 2b-d). Strong, but intermittent mixing in the surface mixed layer is evident from the high values of dissipation ($O(10^{-6})$ W kg^{-1}). A secondary layer of stratification lies at the base of the winter water, where warm and salty UCDW comes

into contact with the overlying cold and less saline waters. Coincident at the interface between the winter water and UCDW, is a band of enhanced turbulent dissipation (Figure 2e-f). This region is hereon referred to as the transition layer (TL).

b. Rates of turbulent dissipation

The distribution of turbulent dissipation values are skewed to the right (Figure 3a), spanning several orders of magnitude from 10^{-12} to 10^{-6} W kg^{-1}, with 63% of the observations measured in quiescent conditions ($\varepsilon < 10^{-10}$ W kg^{-1}) and only 3% greater than 10^{-7} W kg^{-1}.

Rates of dissipation also vary with depth (Figure 2b, Figure 3a, Table 1). The highest rates (2×10^{-8} W kg^{-1}, geometric mean) of dissipation occur at the surface, where the ocean is in direct contact with the atmosphere and subject to mechanical forcing by winds. There is a secondary region of enhanced dissipation rates at the base of the subsurface winter water, centered around the transition layer (3.8×10^{-10} W kg^{-1}, geometric mean). Below this layer the geometric mean dissipation rate is 3.3×10^{-11} W kg^{-1}.

The buoyancy Reynolds number (Figure 3b) quantifies the energetic capacity of the stratified flow to develop vertical overturns that lead to diapycnal mixing. It is defined as the ratio of turbulent kinetic energy, given by dissipation, that would lead to vertical overturns, to the potential energy stored in stratification, which tends to inhibit overturns. Typically, a critical value of Re $\sim$ 10 is assumed, below which diapycnal turbulent mixing is unlikely (Shih et al. 2005; Bouffard and Boegman 2013). While a large number of measurements recorded low values of dissipation, 83% of the measurements occurred under conditions where Re $\geq$ 10, suggesting that in most cases, stratification was not sufficiently strong to inhibit even weak vertical overturns. This shows that vertical fluxes of properties such as heat and carbon are largely set by turbulent mixing rather than molecular diffusion. This is different than the more quiescent Arctic marginal ice zone, which is also impacted by positive buoyancy during ice melt but does not experience the strong wind forcing that is characteristic of the Southern Ocean (Scheifele et al. 2021; Young and Ribal 2019).

c. Mixing processes

Here we present evidence for the primary drivers of turbulent dissipation in the upper subpolar Southern Ocean. The motivation for this is two-fold. Firstly, different turbulent regimes (e.g.

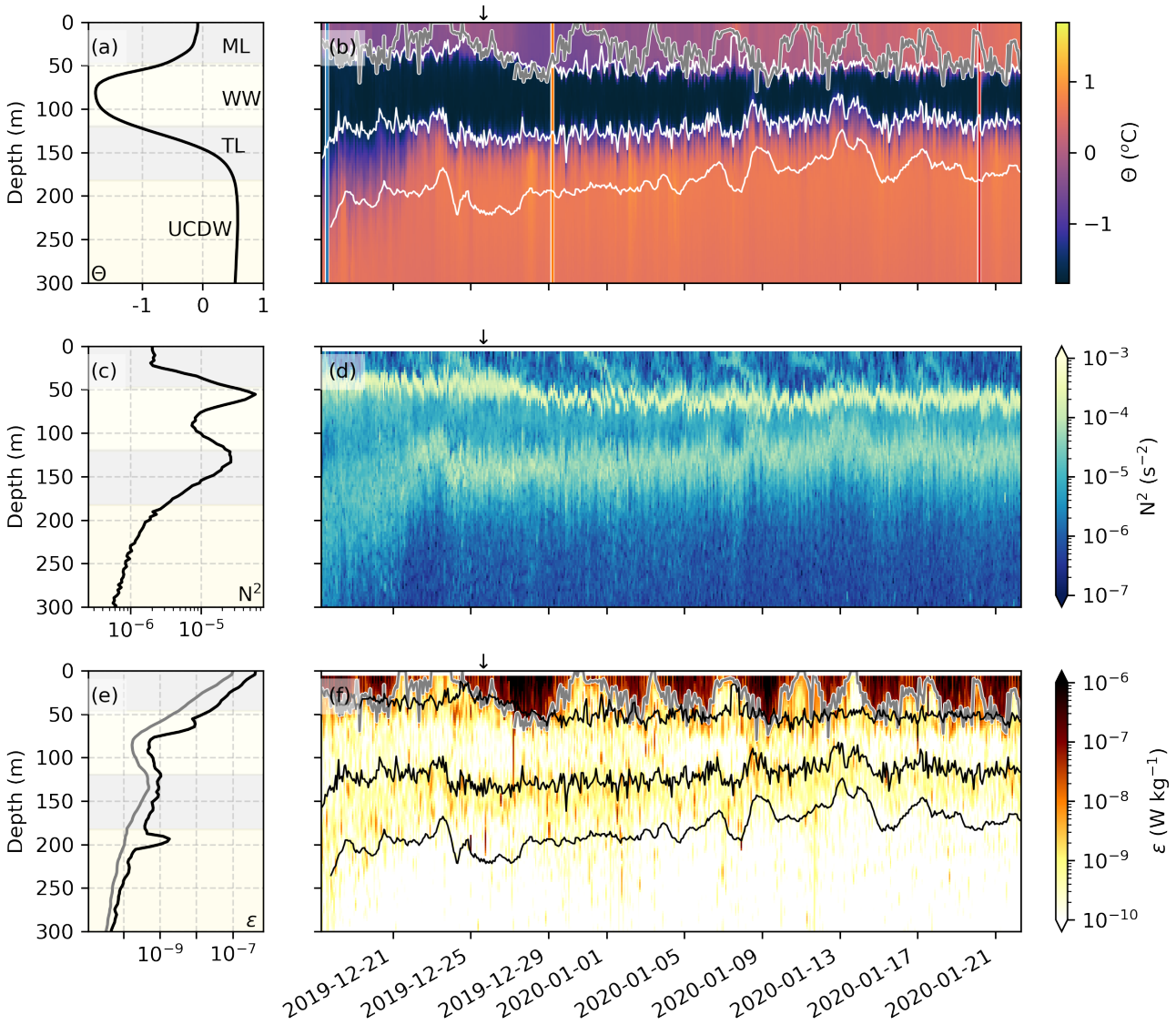

318 FIG. 2. Mean (a,c,e) and temporal evolution (b,d,f) of Conservative Temperature (Θ), stratification (N^2) and
319 turbulent dissipation (ε). From the surface to depth the extent of the mixing layer (grey line) and the mixed layer
320 (ML), the winter water layer (WW) and the transition layer (TL, below the WW although typically thought of as
321 beneath the MLD) are shown. The grey and yellow shading in the left hand column indicates the time-averaged
322 vertical extents of the ML, the WW, the TL and the Upper Circumpolar Deep Water (UCDW). The arrow in
323 (b,d,f,) indicate when the bowtie sampling pattern begins. In (a), vertical lines correspond to the profiles shown
324 in Fig 1d.

355 shear production versus DDC) are associated with different mixing efficiencies which will impact

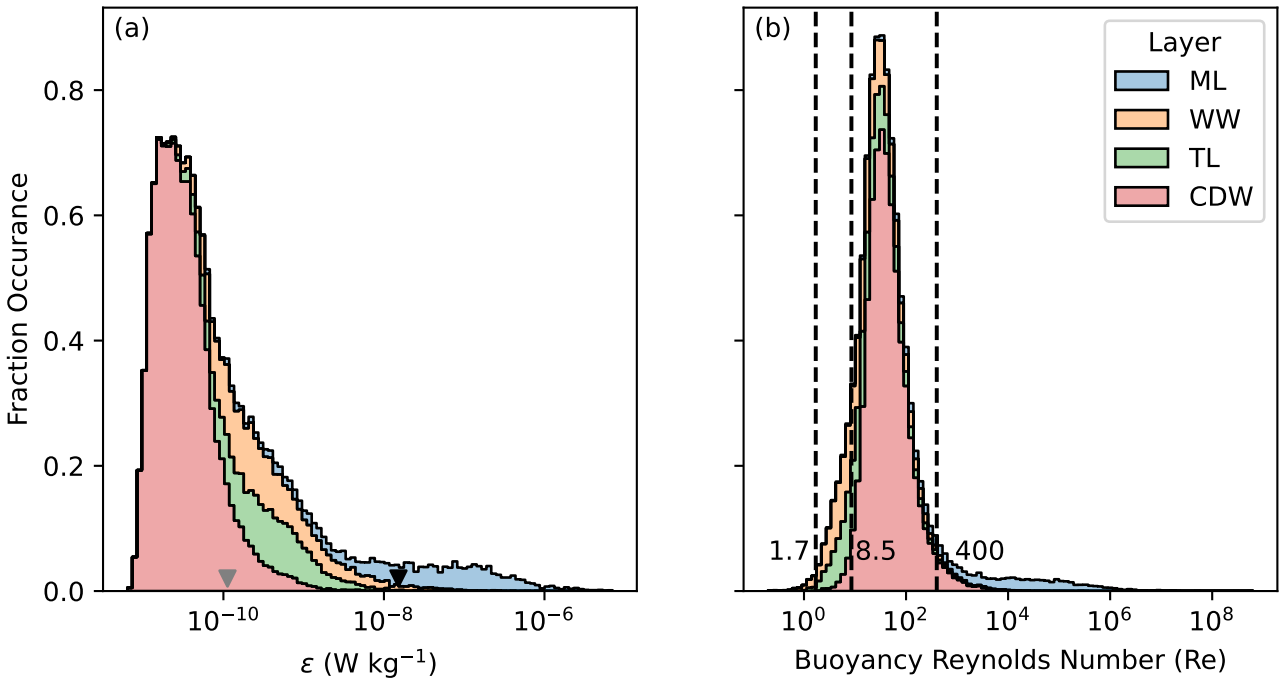

FIG. 3. (a) Stacked histogram of turbulent dissipation, ε, separated into upper-ocean layers: Mixed Layer (ML), Winter Water (WW), Transitional Layer (TL) and Upper Circumpolar Deep Water (UCDW). Inverted triangles identify the geometric mean (grey) and arithmetic mean (black) of the complete dataset. (b) Distribution of the Buoyancy Reynolds number, Re, also separated by layers. Vertical lines identify the thresholds used to derive diapycnal diffusivity, K (Bouffard and Boegman 2013).

approximations of vertical heat fluxes. Secondly, an understanding of the drivers of turbulent mixing is essential for the interpretation of the variability in the mixing itself.

Buoyancy forcing is largely stabilizing (negative out of the ocean), except during night (Figure 4a), such that wind becomes a major source of turbulence in the surface ocean. The Monin-Obukhov length scale is used to determine the relative importance of wind forcing to buoyancy forcing and defined as:

$$\mathrm{L_{MO}} = \frac{-u_*^3}{\kappa B_o}, \tag{8}$$

where u_* is the friction velocity defined as $\sqrt{\frac{\tau}{\rho_o}}$, κ is the von Kármán constant and B_o is the surface buoyancy flux. During the period of observation, buoyancy forces are predominantly stabilizing

TABLE 1. Statistics of turbulent parameters (all quantities are binned to 3 m in the vertical).

		ε (W kg^{-1})	Re	K (m^2 s^{-1})	Count
All	AM	1.5×10^{-8}	6207	1×10^{-4}	80355
	GM	1.1×10^{-10}	-	9.4×10^{-6}	
	Median	5.3×10^{-11}	32	9.6×10^{-6}	
Mixed Layer	AM	1.6×10^{-7}	73765	-	7582
	GM	2.0×10^{-8}	-	-	-
	Median	2.7×10^{-8}	1443	-	
Winter water	AM	3.2×10^{-9}	64	1.3×10^{-5}	11754
	GM	3.6×10^{-10}	-	3.6×10^{-6}	
	Median	2.6×10^{-10}	13	4×10^{-6}	
Transition Layer	AM	9.7×10^{-10}	105	1.2×10^{-5}	10225
	GM	3.8×10^{-10}	-	4.1×10^{-6}	
	Median	3.0×10^{-10}	14	4×10^{-6}	
Upper Circumpolar Deep Water	AM	7.1×10^{-11}	126	2.3×10^{-5}	50794
	GM	3.3×10^{-11}	-	1.1×10^{-5}	
	Median	2.8×10^{-11}	38	1×10^{-5}	

(Fig 4a). Nevertheless, —L_{MO}— has a large dynamic range (>1000 m under strong winds and < 1 m under weak winds and stabilizing buoyancy forcing with negative B_o) (Fig 4b,c).

MECHANICALLY-DRIVEN MIXING

The possible sources of shear in the surface layer and immediately below the mixed layer are shear resulting from geostrophic current, and winds and inertial shear. Deeper below the base of the mixed layer, possible sources are geostrophic currents and internal waves.

We assess the potential importance of geostrophic shear in producing turbulence by estimating the thermal wind shear, $\frac{\partial u_g}{\partial z} = g\frac{\partial \rho}{\partial y}/f$, from temperature and salinity measured by the glider. We assume that the glider is mostly measuring the meridional density gradient (see glider sampling pattern in Fig 1a). While some shear due to geostrophic currents was present, shear was low compared to local stratification and therefore geostrophic shear production of turbulence between the layer interfaces was likely negligible ($\left(\frac{\partial u_g}{\partial z}\right)^2 \sim O(10^{-7}\ \mathrm{s}^{-2})$; $N^2 \sim O(10^{-5}\ \mathrm{s}^{-2})$). This is unsurprising given the region is relatively quiescent in terms of larger-scale currents (du Plessis et al. 2022, their Figure 1a).

We estimate dissipation attributed to internal waves in the ocean interior using the strain-based fine scale parameterization for dissipation (Polzin et al. 1995; Whalen et al. 2015), over 64 m

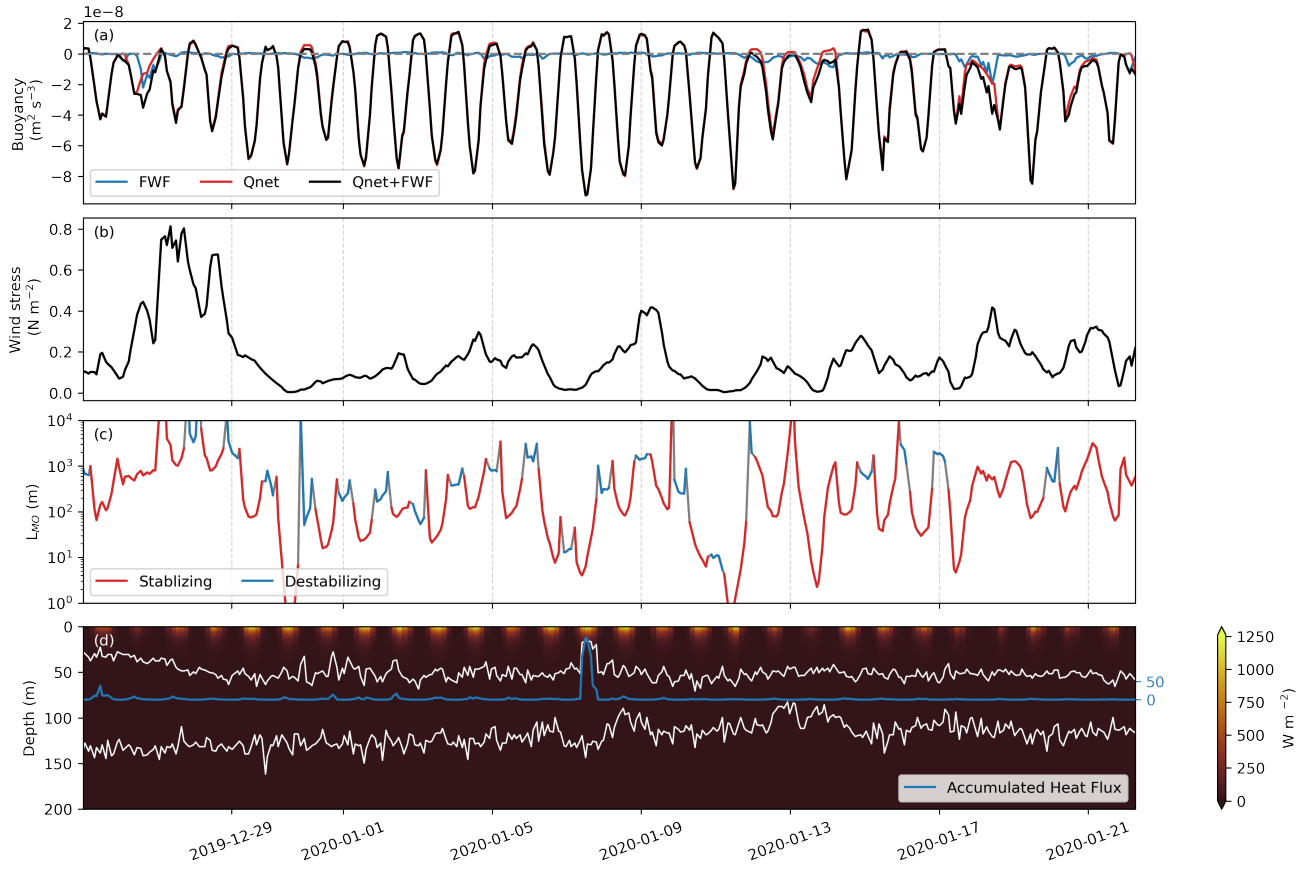

FIG. 4. Timeseries (25 Dec 2019 to 22 Jan 2020) of surface fluxes at 60°S; 0°E. (a) Net buoyancy (black, positive upwards), decomposed into freshwater (blue) and heat (red) components; (b) wind stress; (c) Monin-Obukhov lengthscale, L_{MO}, plotted on log-scale. Colors identify stabilizing and destabilizing regimes at z =5; and (d) decay with depth of incoming shortwave radiation. The accumulated shortwave flux into the winter water is overlain in blue. White contours show the mixed layer and the base of the winter water layer

half-overlapping vertical bins. The time-averaged geometric mean dissipation below in the UCDW layer is 4.9×10^{-11} W kg^{-1}, which is similar to that observed, suggesting that internal waves account for the background dissipation in the ocean interior. The time-averaged strain-based dissipation estimate between the mixed layer and UCDW is 4.0×10^{-10} W kg^{-1}, also comparable to the observations (Table 1), however, this method does not hold in regions susceptible to DDC, considered in the following section.

We use similarity scaling to assess the role of wind stress in shear production of turbulence. To a first approximation, the surface of the ocean can be seen as a flat, rigid wall, beneath which a

purely shear-driven boundary layer evolves, given by the boundary layer similarity scaling, Law of the Wall, which describes viscous dissipation as decaying with distance from the surface.

$$\varepsilon_{\mathrm{LOW}}(z) = \frac{u_*^3}{\kappa|z|}, \tag{9}$$

where z is the distance from the surface. We reconstruct vertical profiles of turbulent dissipation using the LOW relation. The theoretical dissipation rates predict 84% (Fig 5a) of the variability in glider observed dissipation rates (averaged between 5-15 m and smoothed over ~4-hours), indicating that shear-driven turbulence production in this region is largely driven by wind forcing. Outliers at low values of dissipation, marked on Fig 5a in red, are associated with measurements that were taken when $\mathrm{XLD}/|L_{MO}| > 1$ (when buoyancy forcing is strong relative to wind forcing). The markers in blue define where wind forcing is dominant (here defined as $\mathrm{XLD}/|L_{MO}| < 0.3$). The threshold of L_{MO} that defines where overturns are driven solely by wind was selected based on the best fit in Fig 5b, wherein the mixing layer depth deepens under increasing friction velocity ($r^2 = 0.61$). Mixing layer depth is normalized by the mixed layer depth to identify where the mixing layer deepens below the mixed layer and entrainment can occur. The outliers at high wind stress show that the mixing layer is deepening less than expected (this coincides with the strong wind event centered around 28 December 2019, Fig 4b). In this case, we see that mixing depth is deeper than the mixed layer (XLD/MLD >1), suggesting entrainment. The vertical extent of mixing is shallower than predicted by LOW alone, because turbulence is suppressed by the stratification at the base of the mixed layer.

Double diffusive convection

Double diffusive convection conditions are often found in high latitudes and are characteristic of waters in the Weddell Sea, where the cold, fresh winter water overlies warm and salty UCDW (Muench et al. 1990; Shaw and Stanton 2014). A band of DDC conducive conditions was identified where $-\pi/2 < \mathrm{Tu} < -\pi/4$ (equation 7). The average depth range of the DDC band was between 60 and 230 m, at the interface between the base of the winter water and UCDW (Fig 6c). DDC often appear as staircases in the temperature profiles (see example profile in Fig 6b). Not every profile was characterized by thermohaline staircases, even if the Turner angle indicated that conditions were favourable for DDC to occur and Re is, on average, lower in the winter water and transition

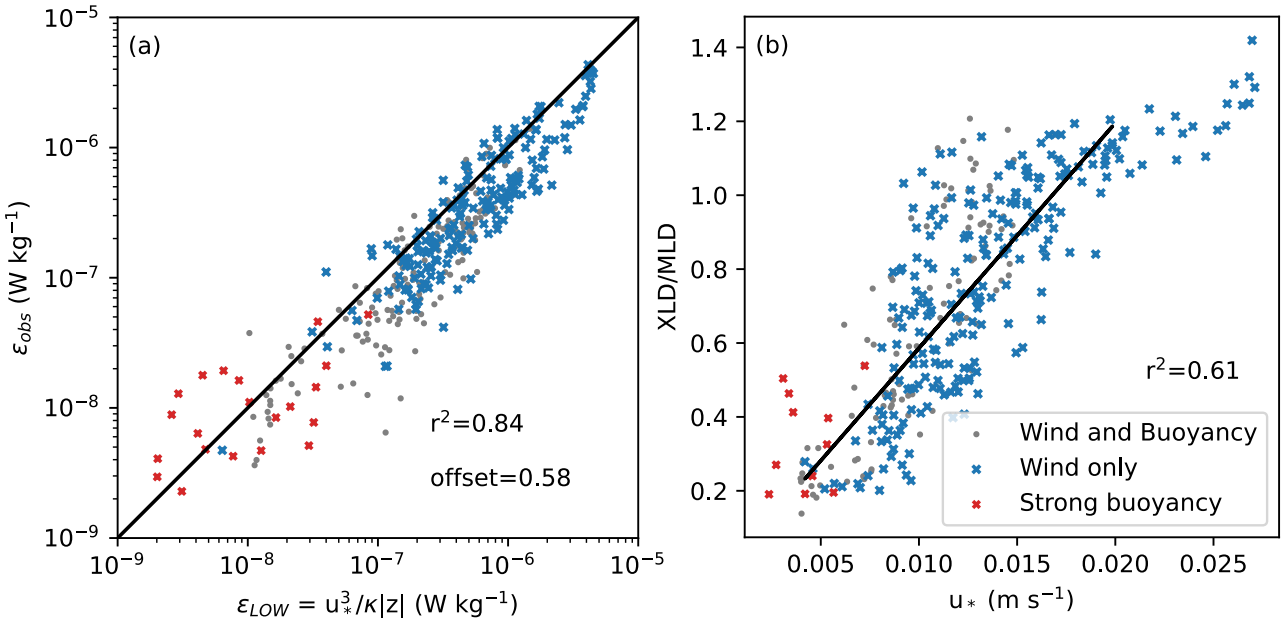

FIG. 5. (a) Relationship between theoretical dissipation rates (ε_{LOW}) and glider observed dissipation rates (ε_{obs}) averaged over 5-15 m depth (on logarithmic scales) during the submesocale transects of the deployment (25 December 2019 - 22 January 2020), corrected for an offset of 0.58. The 1:1 line is plotted for reference in black. (b) Relationship between mixing layer depth (XLD, defined as in Brainerd and Gregg 1995) normalized by the mixed layer depth, MLD, and the friction velocity, u_*. The markers are colored according to the dominant forcing, given by the ratio of XLD to the Monin Obhukov lengthscale, L_{MO}. Wind forcing (XLD/L_{MO} < 0.3) in blue, strong buoyancy forcing (XLD/L_{MO} > 1 in red, and the remainder in grey dots). A rolling mean over 3 profiles (~4-hours) was applied. The black line is the linear regression (with r^2=0.61) computed for XLD/L_{MO} < 0.3, but excluding the points when the friction velocity is greater than 0.02 m s^{-1}.

layers (Table 1). Nevertheless, in these cases, it is possible that intermittent energetic turbulent mixing (e.g. from enhanced shear driven by internal waves) prevents the staircase structures from persisting even under DDC conducive conditions (e.g., Guthrie et al. 2017; Shibley and Timmermans 2019). But, considering that the distribution of buoyancy Reynolds number in the winter water and transition layer is skewed to the left (Fig 3b), shear-driven turbulence in these layers is likely not dominant. Additionally, the glider's average sampling vertical resolution of 0.2 m (1 Hz sampling frequency) limits the ability to resolve temperature staircases to scales larger than 40 cm, missing finer-scale staircases.

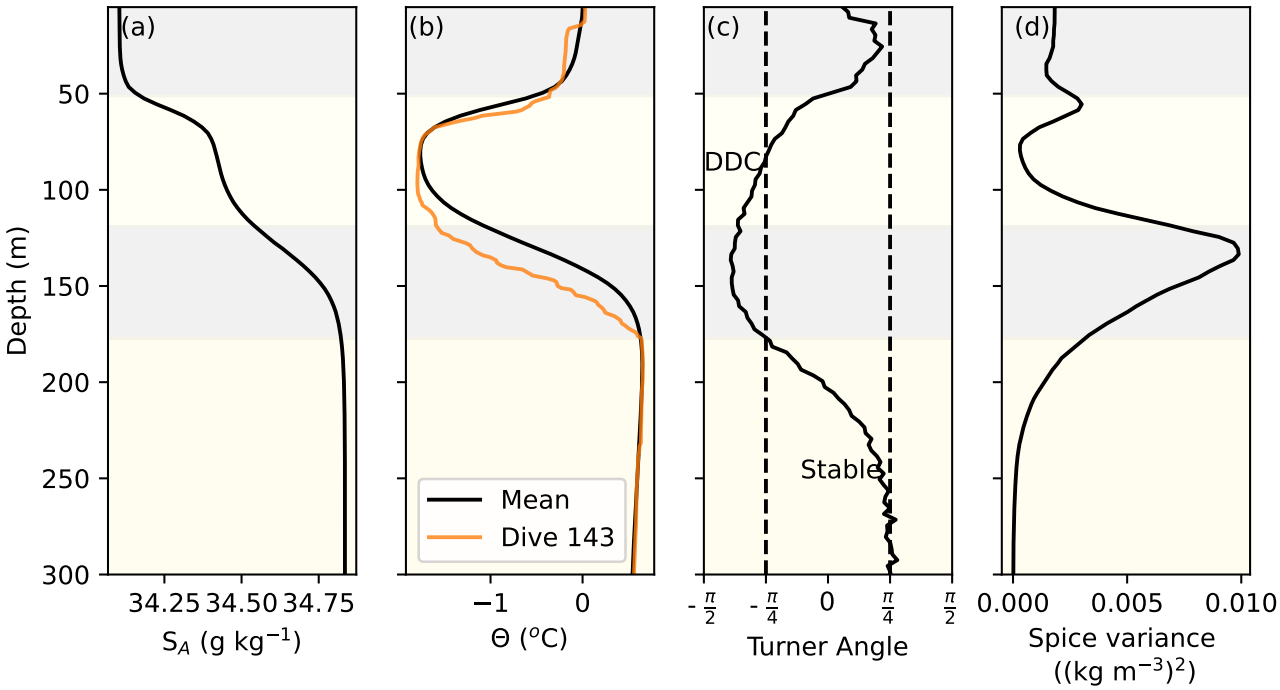

FIG. 6. Mean vertical profiles (during the submesoscale transects) of (a) Absolute Salinity, S_A, (b) Conservative Temperature, Θ (c) Turner angle and (d) spice variance. Temperature staircases of a characteristic profile of temperature is shown in (b). Regions that are susceptible to double diffusive convection are labelled in (c). The shading indicates the mean extent of the ML, WW, TL and UCDW as in Fig 2

A further line of evidence for the presence of DDC is given in the recent work by Middleton et al. (2021) in which they propose that temperature and salinity compensated (spice) gradients generated by along-isopycnal stirring drive double-diffusive motions. It is thus predicted that DDC will be active where there is high spice variance (given negligible shear). We observe that the region of highest time-averaged spice variance (computed from the Gibbs Sea Water TEOS-10 Toolbox, McDougall and Barker 2011) coincides with the region susceptible to DDC in terms of the Turner Angle (Fig 6). From this, Middleton et al. (2021) developed a method by which dissipation rates can be estimated. This will be considered in future work.

d. Vertical turbulent heat fluxes into the winter water

Turbulent eddies can effectively transport heat across a temperature gradient. The resulting heat flux is approximated based on the rate of turbulent eddy diffusivity and the strength of the vertical

gradient (refer to methods section 2f). Because of the characteristic temperature minimum at the core of the subsurface winter water layer, the temperature gradient peaks both at the base of the mixed layer and the base of the winter water layer (Fig 2a). At these interfaces, there are also enhanced vertical overturns (high rates of dissipation), which, together with the strong vertical gradient in temperature (~0.05 °C m^{-1}), result in the vertical transport of heat. An average heat flux of 18 W m^{-2} from the mixed layer into the winter water layer, together with an average of 4 W m^{-2} upwards from the underlying UCDW result in a convergence of heat in the subsurface layer (Fig 7).

Diffusivity by DDC is almost an order of magnitude greater than that resulting from shear production of turbulence. The average diffusivity by DDC where $\frac{-\pi}{2} < Tu < \frac{-\pi}{4}$ is $(2.5 \pm 0.9) \times 10^{-5}$ m^2 s^{-1}, whereas the average turbulent diffusivity over the same depth range is $(4.5 \pm 1) \times 10^{-6}$ m^2 s^{-1}. We additionally estimate the double diffusive contribution to heat flux following the four-thirds flux law (Kelley 1990) that allows for estimates of heat flux without microstructure measurements. We compare DDC heat fluxes based on observations of dissipation to estimates based on the empirical flux law, in the case where double-diffusive convection drives turbulent heat fluxes. For this we hand selected a number of profiles where thermohaline staircases were well-defined and applied the four-thirds flux law (Kelley 1990; Guthrie et al. 2015).

$$F_{4/3} = 0.0032 \exp\left(\frac{4.8}{R_\rho^{0.72}}\right) \rho c_p \left(\frac{\alpha g \kappa}{P_r}\right)^{1/3} \Delta T^{4/3}, \tag{10}$$

where R_ρ is the density ratio, κ is the molecular diffusivity of heat for seawater, 1.4×10^{-7} m^2 s^{-1}, P_r is the Prandtl number = $\frac{\nu}{\kappa}$. ΔT is the temperature difference between adjacent layers. Ungridded 1-second resolution temperature profiles were used for these calculations. The non-dimensional density ratio is a bulk value and was computed from the 3 m gridded data to represent a background average.

The mean density ratio (equation 6) for all profiles over the deployment was 2.9 ± 0.3. For each selected profile, the most defined interface was selected. From this, the mean density ratio and the maximum gradient in temperature were used to compute an upper limit estimate for the flux law, giving an average over 33 selected profiles of 4.7 ± 1.5 W m^{-2}, which is comparable to the average heat flux computed from direct measurements of dissipation (4.5 ± 1.8 W m^{-2}). As such, $F_{4/3}$ can approximate the vertical heat fluxes by DDC in this region.

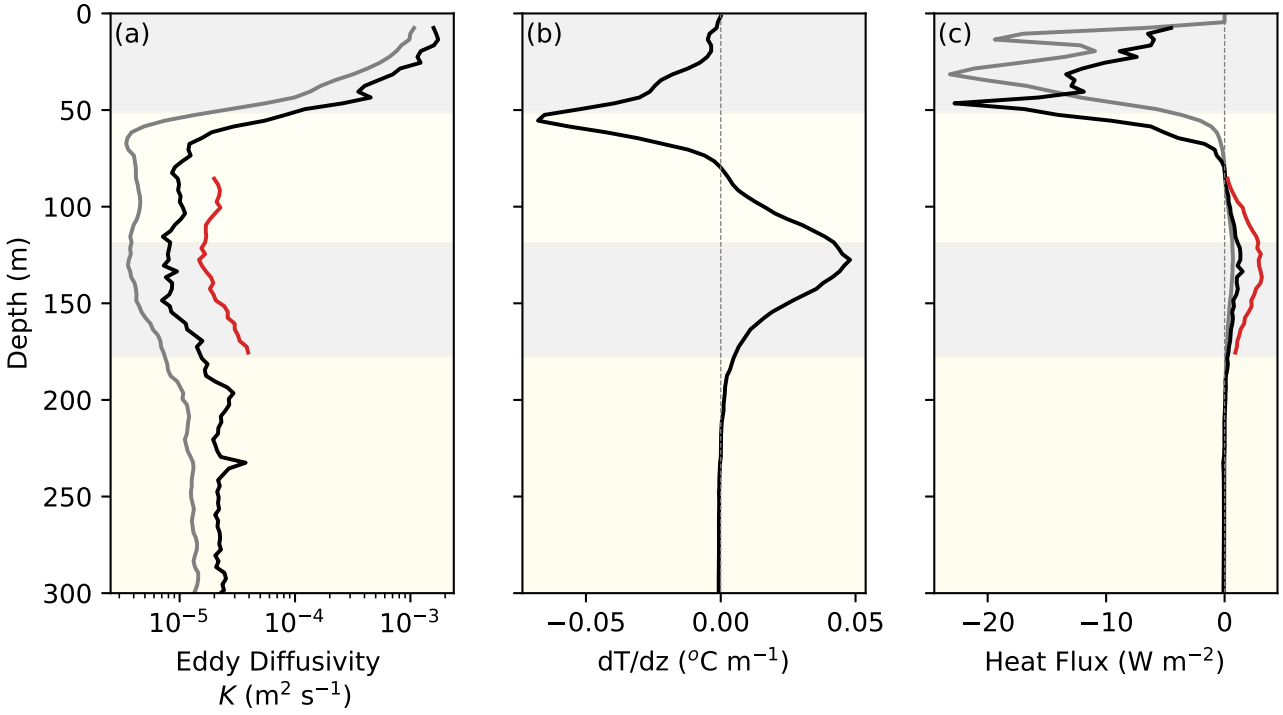

FIG. 7. Mean profiles of eddy diffusivity, vertical temperature gradient and heat flux. The black lines are the arithmetic means, the grey lines, the geometric means and the red line, the geometric mean for the double-diffusive case. Grey and yellow shading is as defined in Fig 2

Over the summer season, we observe a warming and thinning trend in the winter water layer (Fig 8) and hypothesize that this warming is driven primarily by turbulent heat fluxes. To test this hypothesis we develop a winter water temperature budget, described in the following section.

e. Drivers of seasonal warming of Antarctic Winter Water

A winter water temperature budget is developed to investigate the drivers of the seasonal warming of the winter water layer. The mean temperature in this layer increases by 0.2°C over 28 days (Fig 1d, 2b, 8a), even though the incoming solar radiation decreases later in the time series (Fig 4a). Concurrently, the thickness of the layer reduces by 36 m over the same time period (Fig 2a, 8c). No significant trend in salinity is observed (Fig 8b), suggesting that the trend in the thickness of the layer is likely driven by the trend in temperature. Similar warming and thinning trends are observed across the Southern Ocean where winter water is present. For example, in the MIMOC climatology (Fig 1), on average, winter water thins by 20 m at 60°S, 0°E between

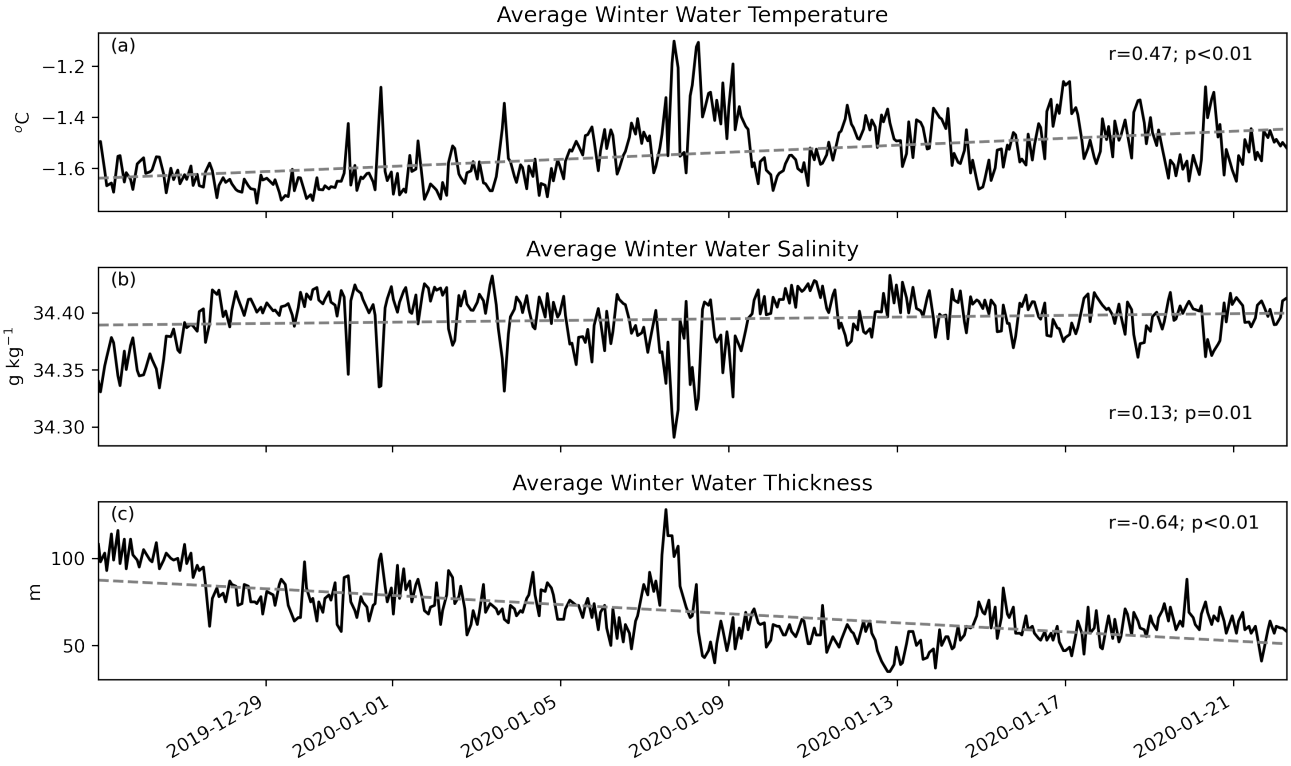

490 FIG. 8. Temporal evolution of averaged properties within the winter water layer are provided for (a) Conservative
491 Temperature, Θ and (b) Absolute Salinity, S_A. The Winter Water Layer thickness (defined as difference between
492 the base of the mixed layer and the deepest mixed layer isopycnal during winter) is provided in (c). Marked on
493 (a-c) are the trends estimated over the observational period (grey dashed-line). r is the correlation coefficient
494 and $p < 0.01$ shows a significant trend.

503 December and March. And, in glider observations during the preceding year (2018-19 summer
504 season), the winter water is observed to warm by 1.1 °C over three months (du Plessis et al. 2022).
505
506 Heat into the winter water layer originates from both lateral and vertical sources. Because we
507 do not have in situ parallel observations of horizontal flow, the temperature budget is simplified
508 to neglect the lateral components contributing to winter water layer variability. Within the sea
509 ice impacted Southern ocean surface mixed layer, the lateral transport component has been shown
510 to be considerable (Giddy et al. 2021; du Plessis et al. 2022); however, because of the strong
511 stratification at the base of the mixed layer, we make the assumption that the processes driving the
512 lateral transport (Ekman transport, mixed layer eddy stirring) are confined to the mixed layer and

can reasonably be neglected in the subsurface layer. Vertical sources considered are entrainment through variation in the depth of the mixed layer and the base of the winter water layer (defined as the isopycnal of the the deepest winter mixed layer), turbulent heat fluxes and incoming solar radiation.

$$\underbrace{(\frac{\partial T}{\partial t})_{WW}}_{\text{Temperature tendency}} = \underbrace{+\frac{1}{h_{WW} c_p \rho_o}(Q_{SW(ML)} - Q_{SW(WW)})}_{\text{I: Shortwave radiation}} \underbrace{-\frac{1}{h_{WW}}([-K\frac{\partial T}{\partial z}]_{-hML} - [-K_{DDC}\frac{\partial T}{\partial z}]_{-hWW})}_{\text{II: Vertical mixing}} \underbrace{-\frac{1}{h_{WW}}[H(W_{eML})(T_{ML} - T_{WW}) + H(W_{eWW}(T_{WW} - T_{WW+5}))]}_{\text{III: Vertical entrainment}}. \quad (11)$$

Depth is positive upwards. T_{ML} is the mean temperature in the mixed layer, T_{WW} is the mean temperature in the winter water layer. h_{WW} is the thickness of the winter water layer.

The first term on the right hand side (I) is the accumulation of shortwave heat flux (Q_{SW}) in the winter water layer (Fig 4d). This term is approximated by exponentially decaying the incoming shortwave with depth following Wijesekera (2005), using the a double exponential formulation for the decay of penetrative solar radiation for Jerlov Type II waters, applicable for the open ocean where chl $a > 0.01$ mg m^{-3} (Paulson and Simpson 1977).

$$R_s(z) = R_s(0)[0.77\exp(-|z|/1.4) + 0.23\exp(-|z|/14)], \quad (12)$$

where $R_s(0)$ is the net shortwave radiative flux at the surface and z is depth. The difference in Q_{SW} at the base of the mixed layer and the base of the winter water is taken as the accumulated Q_{SW}.

The second term (II) is the vertical mixing term, decomposed into shear-driven mixing at the base of the mixed layer and double-diffusive mixing at the base of the winter water layer. K is the eddy diffusivity at the mixed layer base and K_{DDC} is the eddy diffusivity where DDC is assumed. $\frac{\partial T}{\partial z}]_{-hML}$ and $\frac{\partial T}{\partial z}]_{-hWW}$ are the vertical temperature gradients across the mixed layer and winter water interface respectively. The last term (III) is the entrainment into or detrainment

out of the winter water layer from above and below. The vertical velocity across the upper and lower boundaries is computed as $W_e \approx \frac{dh}{dt}$ at each boundary respectively, assuming negligible Ekman pumping velocities (average $W_{ekman} = (\frac{d\tau_y}{dx} - \frac{d\tau_x}{dy})/\rho_o f \sim 10^{-7}$ m s^{-1}, two orders of magnitude smaller than the average entrainment velocity at the base of the mixed layer). H is the Heaviside function, where $W_{eML} < 0$ and $W_{eWW} > 0$ is entrainment and $W_{eML} > 0$ and $W_{eWW} < 0$ is detrainment. T_{ML}-T_{WW} is the difference in mean temperature within the mixed layer and the winter water and T_{WW} - T_{WW+5} is the difference in temperature between the average winter water temperature and 5 m below the winter water base. Vertical entrainment estimates are sensitive to the choice of smoothing for the vertical velocity calculation dh/dt. In this study we selected a 13 hour smoothing (the inertial period at this latitude).

The temperature fluctuations in the winter water are resolved by entrainment and detrainment from above and below the mixed layer (e.g., compare Fig 9a,d), however the warming trend (Fig 8a) is explained primarily by the convergence of turbulent heat fluxes (average 22 W m^{-2} into the winter water, increasing the temperature by 0.18°C; Fig 9c), similar to the warming trend observed in the data (0.2°C; Fig 8a). The accumulation of shortwave radiation results in a small additional temperature increase of 0.02°C (3.1 W m^{-2}; 9b). The contribution from the shortwave component increases when the mixed layer shoals (Fig 4). It is also likely to increase further during low concentration phytoplankton blooms or when the bloom terminates (thus changing the exponential decay of shortwave heat flux). The observed winter water temperature trend agrees well with that modelled in the budget (Fig 9a). Episodic offsets (particularly evident between 13 - 20 January 2020), are likely attributable to some contribution from the lateral components which were not included in the budget.

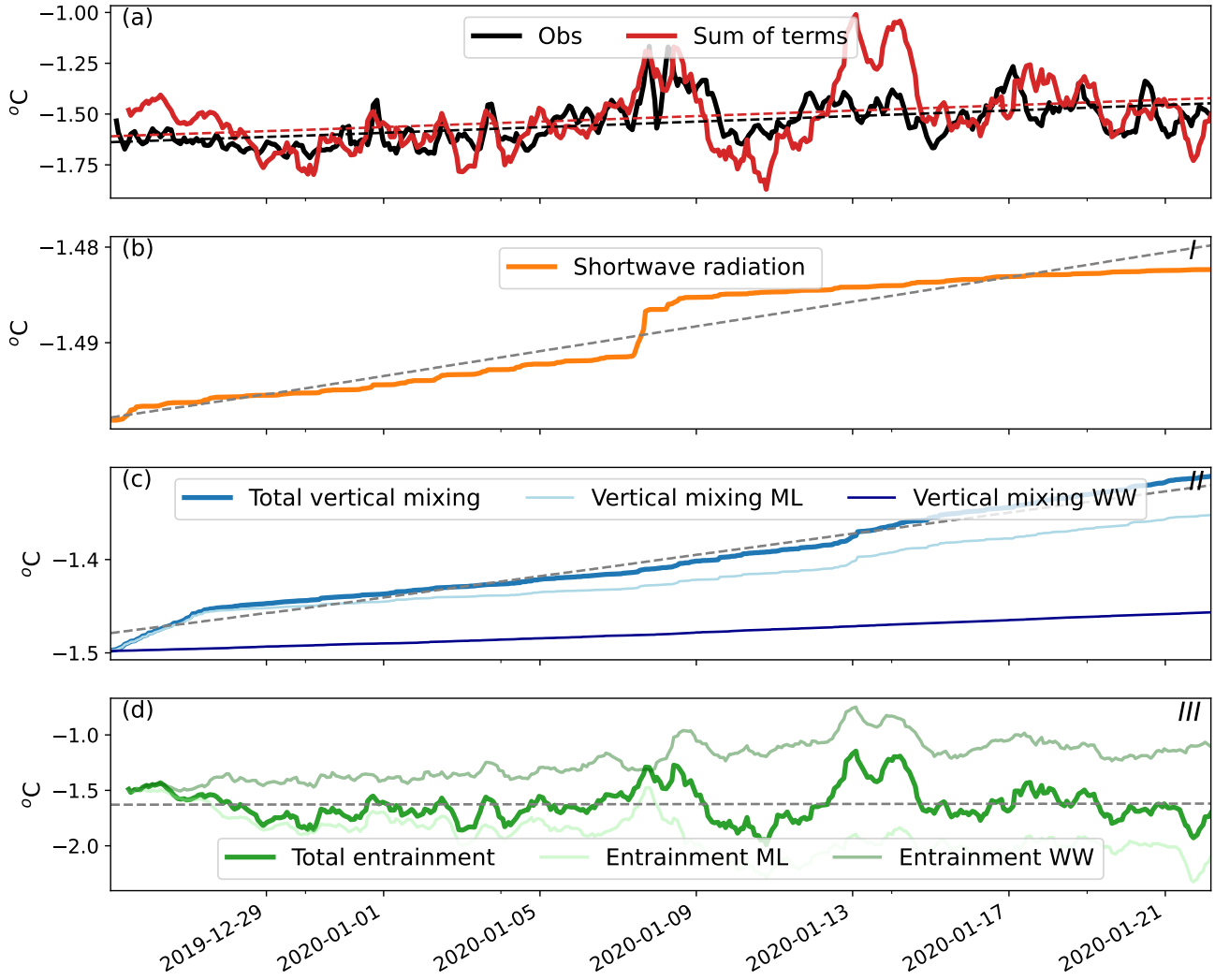

543 FIG. 9. (a) Observed (black) and modeled (red) winter water temperature tendency and the associated
544 components: (b) shortwave radiation; (c) total turbulent vertical mixing (blue), down-gradient vertical mixing
545 across the base of the mixed layer (light blue), up-gradient vertical mixing across the base of the winter water layer
546 (dark blue) and (d) total vertical entrainment (dark green), entrainment across the base of the mixed layer (green),
547 entrainment across the base of the winter water layer (light green). Trends are indicated by the grey dashed lines
548 on a-d. Note the different scales on the y-axes. The roman numerals on top right of (b,c,d) correspond with the
549 terms in equation (11).

562 ## 4. Discussion and Conclusions

563 This study provides a detailed characterization of the observed turbulent mixing processes in the
564 sea-ice impacted Southern Ocean during austral summer. During the period of observation at our

study site, recent sea ice melt had stratified the surface layer, capping the cold winter water layer between the warm surface waters and the underlying warm UCDW (Fig 2). Subsequently, the layer of winter water gradually warms and reduces in thickness over the summer season (Fig 2,8a,c). The subsurface temperature inversion preconditioned, through the setup of a down-gradient of heat from the surface mixed layer to the winter water and an up-gradient of heat from UCDW to the winter water (Fig 2a,b), a convergence of heat flux into the winter water that explains the warming of the layer over the season (Fig 7, 8).

Overall, mechanically-driven turbulent mixing accounts for an average of 18 W m^{-2} of heat flux into the winter water layer. Assuming DDC drives all the turbulent dissipation at the base of the winter water, DDC accounts for a heat flux from the underlying UCDW into the winter water layer of ~ 4 W m^{-2}. While this is an upper estimate, it provides evidence that DDC is likely the primary driver of the upwards transfer of heat from the UCDW into the surface layer during austral summer. If DDC is not taken into account (i.e. a mixing efficiency coefficient of 0.2 is used) the upwards heat flux would be < 1 W m^{-2}, and result in an underestimation of this term.

These results suggest that it is the accumulation of heat fluxes into the winter water layer via vertical turbulent mixing and DDC that accounts for the seasonal warming trend in the observations (Fig 9). While the strong wind event on 28 December 2019 is limited by stratification effects, the rate of dissipation, and therefore eddy diffusivity, is higher and supports enhanced vertical fluxes of heat, temporarily increasing the rate of warming of the winter water. This observation indicates that increased frequency of such events will result in a faster transformation rate of the winter water. This corroborates with longer term observations in which variations in Southern Annular Mode are linked to variations in the winter water (e.g., Sabu et al. 2020).

Uncertainties

Outstanding uncertainties pertain to two aspects of this study. First, eddy diffusivity is approximated based on a constant mixing efficiency (Osborn 1980; Bouffard and Boegman 2013). This approximation is not always appropriate near the base of the mixed layer as it was developed under the assumption of a stratified ocean (Gregg et al. 2018). Secondly, the winter water layer temperature budget does not account for lateral processes (geostrophic and ageostrophic advection, lateral eddy diffusivity) which may remove or add heat to the budget. Uncertainties in the estimation

of heat fluxes associated with mixing efficiencies as well as lateral processes could be further constrained with velocity measurements. The addition of such observations would improve our understanding of the relative importance of processes in the evolution of the winter water layer in this climatically important region, and should be integrated to future field campaigns.

Spatial variability in the seasonal erosion of winter water

While the observations presented here are based in a single location, these findings are discussed in the broader spatial context of the winter water forming regions of the Southern Ocean (Fig 1). Fig 1c demonstrates that the erosion of winter water is not consistent across the subpolar Southern Ocean with the Weddell Sea showing some of the most extensive winter water erosion. Here, regionally weaker stratification predisposes the region to enhanced vertical fluxes (Wilson et al. 2019). The heat fluxes into the winter water that were quantified in the Weddell Sea in this study therefore likely approximate an upper limit for the subpolar Southern Ocean. Conversely, the region that is not directly influenced by sea ice (north of the maximum sea ice extent) increases in thickness during the summer season. This water is warmer and fresher (not transformed by brine rejection during winter, Toole 1981). As such the vertical temperature gradients are expected to be weaker, reducing the potential for enhanced heat fluxes. On average, the core of the winter water is also deeper in these regions, requiring more energy to drive vertical heat fluxes.

The Ross Sea is also subject to a broadening of the winter water vertical extent. Notably, this region has already been identified as one where DDC heat fluxes are weak (Bebieva and Speer 2019) and strong stratification between temperature staircases can act as a thermal barrier (Martinson 1990). Further research into the drivers of an expanding winter water is needed to fully understand these patterns, but the observation of regional variability in the summer evolution of the winter water layer suggests that there will be a spatially heterogeneous response of the subpolar Southern Ocean to changing wind and sea ice patterns in the future (Young and Ribal 2019; Roach et al. 2020).

Southern Ocean significance

Winter water is a widespread feature of the sea-ice impacted Southern Ocean (Fig 1). Heat and carbon exchange between the UCDW and surface ocean is modulated by the winter water layer,

which slows (or mediates) the exchange of water properties between these two water masses during austral summer. As winter water warms through the season, it reduces in thickness and erodes, bringing the underlying UCDW into closer contact with the surface mixed layer. The processes that drive the erosion of this layer therefore play an important role in mediating the amount of heat and carbon that is absorbed in the ocean or lost to the atmosphere. These observations demonstrate that mixing across the winter water layer (and therefore warming of the winter water) is driven both by top-down and bottom-up processes. The winter water layer warms by 0.2°C in one month (Fig 8), following a similar trend observed in previous years (e.g., total of 1 °C over three months, du Plessis et al. 2022). As discussed, the convergence of heat into the winter water is predominantly attributed to wind-driven shear production at the base of the mixed layer (Fig 5) that mixes warm surface water into the colder winter water layer and DDC (Fig 6) at the base of the winter water layer that mixes warm UCDW water upwards into the winter water. Thus, changes to the rate of mixing has the potential to impact both sea ice formation and water mass transformation. Firstly, strong wind events, through increased turbulent mixing, will act to increase the rate of heat transfer into the winter water layer, warm the winter water and increase the rate of its erosion. This may imply, with the observed increase in storm frequency (Young and Ribal 2019), the winter water layer may become thinner over the summer season, enhancing heat exchange between the deep and surface ocean. The response of winter water to changing wind patterns has already been observed (Anilkumar et al. 2006; Sabu et al. 2020), although the direct mixing mechanisms were not studied. These results confirm that the properties of winter water will change in response to wind through its impact on turbulent mixing. However, there are many interacting and opposing processes. Stratification is expected to continue to increase (Sallée et al. 2021), suppressing the vertical extent of mixing. Our observation show that heat fluxes may nevertheless be enhanced under strong stratification (Fig 9b). Secondly, as the UCDW warms (Auger et al. 2021), the gradient between UCDW and the overlying winter water might be expected to increase, enhancing heat flux via DDC in some subpolar regions. Reduced ice cover would simultaneously decrease the seasonal stratification that results from sea ice melt, allowing heat to be more readily transported to the surface layer, where it inhibits further ice growth (Martinson 1990). Warmer and reduced thickness of the austral summer winter water layers will likely result

in warmer intermediate waters that are subducted beneath the ACC (Evans et al. 2018), thereby impacting water mass transformation and the thermohaline circulation.

Previous work has emphasized the importance of variations in surface salinity linked to sea ice in regulating the rate of water mass transformation in the subpolar Southern Ocean (Abernathey et al. 2016; Pellichero et al. 2018). Here, we add that changes in the mechanisms that drive heat flux can contribute to increasing the buoyancy of CDW and the transformation to AAIW before it reaches the mixed layer. Observations show that the Southern Ocean is warming (Auger et al. 2021), however interannual variability in the winter water layer south of Australia has been observed to be greater than the long term trend (Auger et al. 2021, their Figure 4b). Nevertheless, the shoaling and warming trend of the UCDW has been linked to increased stratification at the base of the winter water layer reducing mixing and the loss of heat from UCDW to overlying waters and the atmosphere (Auger et al. 2021). The increase in stratification is likely linked to freshwater forcing (Marshall et al. 2014; Armour et al. 2016; Lecomte et al. 2017). This work quantifies the contribution of turbulent mixing and its sensitivity to the driving mechanisms in regulating heat fluxes between these two water masses. An increase in the stratification at the base of the winter water may reduce the ability of DDC to drive heat fluxes (as seen in the Ross Sea where stratification is strong), however an increase in the temperature gradient enhances the potential for heat flux via turbulent mixing. While DDC may not contribute significantly to the global energy balance (as per van der Boog et al. 2021), it is identified here as an important mechanism driving fluxes of heat between UCDW and the winter water and is therefore important for water mass transformation in the subpolar Southern Ocean.

Acknowledgments. I. Giddy received support from the Oppenheimer Memorial Trust, NRF-SANAP (SNA170506229906), iAtlantic Horizon 2020 grant (818123) and the STINT-NRF Mobility Grant (STNT180910357293). S. Swart: Wallenberg Academy Fellowship (WAF 2015.0186), Swedish Research Council (VR 2019-04400); and the grants of S-A. Nicholson and S. Swart: NRF-SANAP (SNA170522231782, SANAP200324510487). I. Fer received support from the Research Council of Norway, through the AROMA project, grant number 294396. The authors would like to thank the captain and crew of the SA Agulhas II and the assistance of Sea Technology Services for the deployment, retrieval and piloting of the Slocum.

Data availability statement. The glider and dissipation data will be made available upon publication. ERA5 data are generated using Copernicus Climate Change Service Information, available online (www.ecmwf.int/en/forecasts/datasets/archive-datasets/reanalysis-datasets/era5). Biogeochemical Argo data were collected and made freely available by the Southern Ocean Carbon and Climate Observations and Modeling (SOCCOM) Project funded by the National Science Foundation, Division of Polar Programs (NSF PLR -1425989 and OPP-1936222), supplemented by NASA, and by the International Argo Program and the NOAA programs that contribute to it.http://www.argo.ucsd.edu(link is external), http://argo.jcommops.org(link is external)). The code used to produce the results of the paper will be made available via Zenodo.

APPENDIX A

Quality Control Measures for Dissipation Rate Estimates

Here we describe the quality control procedures applied to each of dissipation estimates from both shear probes respectively, in order to identify dissipation estimates that are deemed untrustworthy. Data that does not pass the QC is masked before the analysis. First, the MR internal clock has a tendency to drift over time. The Slocum clock was used to correct for a 17 second drift in the MR clock over the period of the deployment.

QC1. The servo-controlled battery positioning of the Slocum creates vibrations that may affect the quality of turbulence measurements. The servo was deactivated during the up-casts, but not during the down-casts due to a piloting error. To correct for the servo caused vibrations, segments during which the servo was on (identified as segments during the dive where the pitch changed) were filtered out from the dataset.

QC2. The glider is within 20 m of an inflection point. When the glider inflects, the angle of attack and estimate of glider speed is uncertain. Mechanical vibrations necessary to change the glider pitch at inflection also contaminate the measurements.

QC3. Histograms of the glider angle of attack (AOA), pitch, roll and speed were used to diagnose the glider flight metrics. AOA and glider speed through the water are estimated from the hydrodynamic model of (Merckelbach et al. 2010), implemented in Gerd Krahmans GEOMAR software. Outliers were hand selected and masked. If the glider angle of attack is too steep, the data is also not reliable. Data where the gliders AOA was greater than modular 5 degrees was masked. Pitch angles less that —15^o— and greater than —30^o— were also masked as too steep or too shallow pitch angles. Notice that the pitch and AOA was more consistent on the climbs because the servo control was not deactivated. When the flow past the sensor was less than 0.25 m s^{-1} the data was masked. Rapid changes in pitch and roll are also unreliable, so data where ΔRoll and ΔPitch was greater than 1 was masked.

QC4. The shear spectra was averaged over increasing levels of dissipation and compared to the empirical Nasmyth spectra to determine the noise level of the data. The Figure of Merit, which is a metric for the mean absolute deviation from Nasmyth (Wolk et al. 2002), and data where the FOM is >1.5 is masked. For increasingly weaker dissipation, the threshold is relaxed, such that for dissipation data between 10^{-10} and 10^{-11} W kg^{-1}, a mask is applied where FOM > 2, and for values greater than 10^{-11} W kg^{-1}, FOM ¿ 2.5.

QC5. All dissipation values greater than $1x10^{-4}$ W kg^{-1} are masked as these values are too high to be detectable by the shear probes and can be assumed to be noise.

QC6. Remaining suspect dissipation estimates were hand-selected and masked.

QC7. Finally, to derive one estimate of dissipation from the two shear probes, we compared the dissipation estimates of the shear probes with each other. If their ratio was larger than 5, we selected the minimum value of the two, otherwise the average of the two was taken.

References

Abernathey, R. P., I. Cerovecki, P. R. Holland, E. Newsom, M. Mazloff, and L. D. Talley, 2016: Water-mass transformation by sea ice in the upper branch of the Southern Ocean overturning. *Nature Geoscience*, **9 (8)**, 596–601, https://doi.org/10.1038/ngeo2749.

730 Anilkumar, N., and Coauthors, 2006: Fronts, water masses and heat content variability in the
731 Western Indian sector of the Southern Ocean during austral summer 2004. *Journal of Marine*
732 *Systems*, **63 (1-2)**, 20–34, https://doi.org/10.1016/j.jmarsys.2006.04.009.

733 Armour, K. C., J. Marshall, J. R. Scott, A. Donohoe, and E. R. Newsom, 2016: Southern Ocean
734 warming delayed by circumpolar upwelling and equatorward transport. *Nature Geoscience*, **9 (7)**,
735 549–554, https://doi.org/10.1038/ngeo2731.

736 Auger, M., R. Morrow, E. Kestenare, J.-B. Sallée, and R. Cowley, 2021: Southern Ocean in-situ
737 temperature trends over 25 years emerge from interannual variability. *Nature Communications*,
738 **12 (1)**, 514, https://doi.org/10.1038/s41467-020-20781-1.

739 Baker, M. A., and C. H. Gibson, 1987: Sampling Turbulence in the Stratified Ocean: Statistical
740 Consequences of Strong Intermittency. *Journal of Physical Oceanography*, **17 (10)**, 1817–1836,
741 https://doi.org/10.1175/1520-0485(1987)017⟨1817:STITSO⟩2.0.CO;2.

742 Bebieva, Y., and K. Speer, 2019: The Regulation of Sea Ice Thickness by Double-Diffusive
743 Processes in the Ross Gyre. *Journal of Geophysical Research: Oceans*, **124 (10)**, 7068–7081,
744 https://doi.org/10.1029/2019JC015247.

745 Bebieva, Y., and M. Timmermans, 2016: An examination of double-diffusive processes in a
746 mesoscale eddy in the Arctic Ocean. *Journal of Geophysical Research: Oceans*, **121 (1)**, 457–
747 475, https://doi.org/10.1002/2015JC011105.

748 Belcher, S. E., and Coauthors, 2012: A global perspective on Langmuir turbulence in
749 the ocean surface boundary layer. *Geophysical Research Letters*, **39 (18)**, https://doi.org/
750 10.1029/2012GL052932.

751 Bouffard, D., and L. Boegman, 2013: A diapycnal diffusivity model for stratified environ-
752 mental flows. *Dynamics of Atmospheres and Oceans*, **61-62**, 14–34, https://doi.org/10.1016/
753 j.dynatmoce.2013.02.002.

754 Boyer Montégut, C., G. Madec, A. Fischer, A. Lazar, and D. Iudicone, 2004: Mixed layer depth
755 over the global ocean: An examination of profile data and a profile-based climatology. *Journal*
756 *of Geophysical Research: Oceans*, **109**, https://doi.org/10.1029/2004JC002378.

Brainerd, K. E., and M. C. Gregg, 1995: Surface mixed and mixing layer depths. *Deep Sea Research Part I: Oceanographic Research Papers*, **42 (9)**, 1521–1543, https://doi.org/10.1016/0967-0637(95)00068-H.

Dohan, K., and R. E. Davis, 2011: Mixing in the Transition Layer during Two Storm Events. *Journal of Physical Oceanography*, **41 (1)**, 42–66, https://doi.org/10.1175/2010JPO4253.1.

du Plessis, M. D., S. Swart, L. C. Biddle, I. S. Giddy, P. M. S. Monteiro, C. J. C. Reason, A. F. Thompson, and S. Nicholson, 2022: The Daily-Resolved Southern Ocean Mixed Layer: Regional Contrasts Assessed Using Glider Observations. *Journal of Geophysical Research: Oceans*, **127 (4)**, https://doi.org/10.1029/2021JC017760.

Evans, D. G., J. D. Zika, A. C. Naveira Garabato, and A. J. G. Nurser, 2018: The Cold Transit of Southern Ocean Upwelling. *Geophysical Research Letters*, **45 (24)**, https://doi.org/10.1029/2018GL079986.

Fer, I., A. K. Peterson, and J. E. Ullgren, 2014: Microstructure Measurements from an Underwater Glider in the Turbulent Faroe Bank Channel Overflow. *Journal of Atmospheric and Oceanic Technology*, **31 (5)**, 1128–1150, https://doi.org/10.1175/JTECH-D-13-00221.1, URL https://journals.ametsoc.org/view/journals/atot/31/5/jtech-d-13-00221_1.xml.

Foster, T. D., and E. C. Carmack, 1976: Temperature and Salinity Structure in the Weddell Sea. *Journal of Physical Oceanography*, **6 (1)**, 36–44, https://doi.org/10.1175/1520-0485(1976)006⟨0036:TASSIT⟩2.0.CO;2.

Giddy, I., S. Swart, M. du Plessis, A. F. Thompson, and S. Nicholson, 2021: Stirring of Sea-Ice Meltwater Enhances Submesoscale Fronts in the Southern Ocean. *Journal of Geophysical Research: Oceans*, **126 (4)**, https://doi.org/10.1029/2020JC016814.

Goodman, L., E. R. Levine, and R. G. Lueck, 2006: On Measuring the Terms of the Turbulent Kinetic Energy Budget from an AUV. *Journal of Atmospheric and Oceanic Technology*, **23 (7)**, 977–990, https://doi.org/10.1175/JTECH1889.1.

Gordon, A. L., and B. A. Huber, 1984: Thermohaline stratification below the Southern Ocean sea ice. *Journal of Geophysical Research*, **89 (C1)**, 641, https://doi.org/10.1029/JC089iC01p00641.

Gordon, A. L., and B. A. Huber, 1990: Southern ocean winter mixed layer. *Journal of Geophysical Research*, **95 (C7)**, 11 655, https://doi.org/10.1029/JC095iC07p11655.

Gregg, M., E. D'Asaro, J. Riley, and E. Kunze, 2018: Mixing Efficiency in the Ocean. *Annual Review of Marine Science*, **10 (1)**, 443–473, https://doi.org/10.1146/annurev-marine-121916-063643.

Guthrie, J. D., I. Fer, and J. Morison, 2015: Observational validation of the diffusive convection flux laws in the Amundsen Basin , Arctic Ocean. *Journal of Geophysical Research: Oceans*, **120 (12)**, 7880–7896, https://doi.org/10.1002/2015JC010884.

Guthrie, J. D., I. Fer, and J. H. Morison, 2017: Thermohaline staircases in the Amundsen Basin: Possible disruption by shear and mixing. *Journal of Geophysical Research: Oceans*, **122 (10)**, 7767–7782, https://doi.org/10.1002/2017JC012993.

Hersbach, H., and Coauthors, 2018: ERA5 hourly data on single levels from 1979 to present. Copernicus Climate Change Service (C3S) Climate Data Store (CDS).

Hoppema, M., 2004: Weddell Sea is a globally significant contributor to deep-sea sequestration of natural carbon dioxide. *Deep Sea Research Part I: Oceanographic Research Papers*, **51 (9)**, 1169 – 1177, https://doi.org/https://doi.org/10.1016/j.dsr.2004.02.011.

Inoue, R., H. Yamazaki, F. Wolk, T. Kono, and J. Yoshida, 2007: An Estimation of Buoyancy Flux for a Mixture of Turbulence and Double Diffusion. *Journal of Physical Oceanography*, **37 (3)**, 611–624, https://doi.org/10.1175/JPO2996.1.

Kelley, D. E., 1990: Fluxes through diffusive staircases: A new formulation. *Journal of Geophysical Research*, **95 (C3)**, 3365, https://doi.org/10.1029/JC095iC03p03365.

Lecomte, O., H. Goosse, T. Fichefet, C. de Lavergne, A. Barthélemy, and V. Zunz, 2017: Vertical ocean heat redistribution sustaining sea-ice concentration trends in the Ross Sea. *Nature Communications*, **8 (1)**, 258, https://doi.org/10.1038/s41467-017-00347-4.

Marshall, J., K. C. Armour, J. R. Scott, Y. Kostov, U. Hausmann, D. Ferreira, T. G. Shepherd, and C. M. Bitz, 2014: The ocean's role in polar climate change: asymmetric Arctic and Antarctic responses to greenhouse gas and ozone forcing. *Philosophical Transactions of the Royal Society*

A: Mathematical, Physical and Engineering Sciences, **372 (2019)**, 20130 040, https://doi.org/10.1098/rsta.2013.0040.

Martinson, D. G., 1990: Evolution of the southern ocean winter mixed layer and sea ice: Open ocean deepwater formation and ventilation. *Journal of Geophysical Research*, **95 (C7)**, 11 641, https://doi.org/10.1029/JC095iC07p11641.

McDougall, T. J., and P. M. Barker, 2011: *Getting started with TEOS-10 and the Gibbs Seawater (GSW) Oceanographic Toolbox*. Trevor J McDougall, Battery Point, Tas.

Merckelbach, L., D. Smeed, and G. Griffiths, 2010: Vertical Water Velocities from Underwater Gliders. *Journal of Atmospheric and Oceanic Technology*, **27 (3)**, 547–563, https://doi.org/10.1175/2009JTECHO710.1.

Middleton, L., E. C. Fine, J. A. MacKinnon, M. H. Alford, and J. R. Taylor, 2021: Estimating Dissipation Rates Associated With Double Diffusion. *Geophysical Research Letters*, **48 (15)**, https://doi.org/10.1029/2021GL092779.

Muench, R. D., J. T. Gunn, and D. M. Husby, 1990: The Weddell-Scotia confluence in midwinter. *Journal of Geophysical Research*, **95 (C10)**, 18 177, https://doi.org/10.1029/JC095iC10p18177.

Nasmyth, P. W., 1970: *Oceanic turbulence*. University of British Columbia, URL 10.14288/1.0302459, publisher:.

Nicholson, S.-A., D. B. Whitt, I. Fer, M. D. du Plessis, A. D. Lebéhot, S. Swart, A. J. Sutton, and P. M. S. Monteiro, 2022: Storms drive outgassing of CO2 in the subpolar Southern Ocean. *Nature Communications*, **13 (1)**, 158, https://doi.org/10.1038/s41467-021-27780-w.

Osborn, T. R., 1980: Estimates of the Local Rate of Vertical Diffusion from Dissipation Measurements. *Journal of Physical Oceanography*, **10 (1)**, 83–89, https://doi.org/10.1175/1520-0485(1980)010⟨0083:EOTLRO⟩2.0.CO;2.

Paulson, C. A., and J. J. Simpson, 1977: Irradiance Measurements in the Upper Ocean. *Journal of Physical Oceanography*, **7 (6)**, 952–956, https://doi.org/10.1175/1520-0485(1977)007⟨0952:IMITUO⟩2.0.CO;2.

Pellichero, V., J.-B. Sallée, C. C. Chapman, and S. M. Downes, 2018: The southern ocean meridional overturning in the sea-ice sector is driven by freshwater fluxes. *Nature Communications*, **9 (1)**, 1789, https://doi.org/10.1038/s41467-018-04101-2.

Pellichero, V., J.-B. Sallée, S. Schmidtko, F. Roquet, and J.-B. Charrassin, 2017: The ocean mixed layer under Southern Ocean sea-ice: Seasonal cycle and forcing. *Journal of Geophysical Research: Oceans*, **122 (2)**, 1608–1633, https://doi.org/10.1002/2016JC011970.

Polzin, K. L., J. M. Toole, and R. W. Schmitt, 1995: Finescale Parameterizations of Turbulent Dissipation. *Journal of Physical Oceanography*, **25 (3)**, 306–328, https://doi.org/10.1175/1520-0485(1995)025⟨0306:FPOTD⟩2.0.CO;2.

Roach, L. A., and Coauthors, 2020: Antarctic Sea Ice Area in CMIP6. *Geophysical Research Letters*, **47 (9)**, https://doi.org/10.1029/2019GL086729.

Sabu, P., S. A. Libera, R. Chacko, N. Anilkumar, M. Subeesh, and A. P. Thomas, 2020: Winter water variability in the Indian Ocean sector of Southern Ocean during austral summer. *Deep Sea Research Part II: Topical Studies in Oceanography*, **178**, 104 852, https://doi.org/10.1016/j.dsr2.2020.104852.

Sallée, J.-B., and Coauthors, 2021: Summertime increases in upper-ocean stratification and mixed-layer depth. *Nature*, **591 (7851)**, 592–598, https://doi.org/10.1038/s41586-021-03303-x.

Scheifele, B., S. Waterman, and J. R. Carpenter, 2021: Turbulence and Mixing in the Arctic Ocean's Amundsen Gulf. *Journal of Physical Oceanography*, **51 (1)**, 169–186, https://doi.org/10.1175/JPO-D-20-0057.1.

Schmidtko, S., G. C. Johnson, and J. M. Lyman, 2013: MIMOC: A global monthly isopycnal upper-ocean climatology with mixed layers: MIMOC. *Journal of Geophysical Research: Oceans*, **118 (4)**, 1658–1672, https://doi.org/10.1002/jgrc.20122.

Shaw, W. J., and T. P. Stanton, 2014: Dynamic and Double-Diffusive Instabilities in a Weak Pycnocline. Part I: Observations of Heat Flux and Diffusivity in the Vicinity of Maud Rise, Weddell Sea. *Journal of Physical Oceanography*, **44 (8)**, 1973–1991, https://doi.org/10.1175/JPO-D-13-042.1.

Shibley, N. C., and M. Timmermans, 2019: The Formation of Double-Diffusive Layers in a Weakly Turbulent Environment. *Journal of Geophysical Research: Oceans*, **124 (3)**, 1445–1458, https://doi.org/10.1029/2018JC014625.

Shibley, N. C., M.-L. Timmermans, J. R. Carpenter, and J. M. Toole, 2017: Spatial variability of the Arctic Ocean's double-diffusive staircase: The Arctic's Double-Diffusive Staircase. *Journal of Geophysical Research: Oceans*, **122 (2)**, 980–994, https://doi.org/10.1002/2016JC012419.

Shih, L. H., J. R. Koseff, G. N. Ivey, and J. H. Ferziger, 2005: Parameterization of turbulent fluxes and scales using homogeneous sheared stably stratified turbulence simulations. *Journal of Fluid Mechanics*, **525**, 193–214, https://doi.org/10.1017/S0022112004002587.

Song, H., J. Marshall, J. Campin, and D. J. McGillicuddy, 2019: Impact of Near-Inertial Waves on Vertical Mixing and Air-Sea CO $_2$ Fluxes in the Southern Ocean. *Journal of Geophysical Research: Oceans*, **124 (7)**, 4605–4617, https://doi.org/10.1029/2018JC014928.

St. Laurent, L., and R. W. Schmitt, 1999: The Contribution of Salt Fingers to Vertical Mixing in the North Atlantic Tracer Release Experiment*. *Journal of Physical Oceanography*, **29 (7)**, 1404–1424, https://doi.org/10.1175/1520-0485(1999)029⟨1404:TCOSFT⟩2.0.CO;2.

Talley, L. D., and Coauthors, 2019: Southern Ocean Biogeochemical Float Deployment Strategy, With Example From the Greenwich Meridian Line (GO-SHIP A12). *Journal of Geophysical Research: Oceans*, **124 (1)**, 403–431, https://doi.org/10.1029/2018JC014059.

Thompson, A. F., A. Lazar, C. Buckingham, A. C. Naveira Garabato, G. M. Damerell, and K. J. Heywood, 2016: Open-Ocean Submesoscale Motions: A Full Seasonal Cycle of Mixed Layer Instabilities from Gliders. *Journal of Physical Oceanography*, **46 (4)**, 1285–1307, https://doi.org/10.1175/JPO-D-15-0170.1.

Toole, J. M., 1981: Sea ice, winter convection, and the temperature minimum layer in the Southern Ocean. *Journal of Geophysical Research*, **86 (C9)**, 8037, https://doi.org/10.1029/JC086iC09p08037.

Turner, J., 1973: *Buoyancy effects in Fluids*. Cambridge University Press, Cambridge.

van der Boog, C. G., H. A. Dijkstra, J. D. Pietrzak, and C. A. Katsman, 2021: Double-diffusive mixing makes a small contribution to the global ocean circulation. *Communications Earth & Environment*, **2 (1)**, 46, https://doi.org/10.1038/s43247-021-00113-x.

Whalen, C. B., J. A. MacKinnon, L. D. Talley, and A. F. Waterhouse, 2015: Estimating the Mean Diapycnal Mixing Using a Finescale Strain Parameterization. *Journal of Physical Oceanography*, **45 (4)**, 1174–1188, https://doi.org/10.1175/JPO-D-14-0167.1.

Wijesekera, H. W., 2005: Upper ocean heat and freshwater budgets in the eastern Pacific warm pool. *Journal of Geophysical Research*, **110 (C8)**, C08 004, https://doi.org/10.1029/2004JC002511.

Wilson, E. A., S. C. Riser, E. C. Campbell, and A. P. S. Wong, 2019: Winter Upper-Ocean Stability and Ice–Ocean Feedbacks in the Sea Ice–Covered Southern Ocean. *Journal of Physical Oceanography*, **49 (4)**, 1099–1117, https://doi.org/10.1175/JPO-D-18-0184.1.

Wolk, F., H. Yamazaki, L. Seuront, and R. G. Lueck, 2002: A New Free-Fall Profiler for Measuring Biophysical Microstructure. *Journal of Atmospheric and Oceanic Technology*, **19 (5)**, 780–793, https://doi.org/10.1175/1520-0426(2002)019⟨0780:ANFFPF⟩2.0.CO;2.

Young, I. R., and A. Ribal, 2019: Multiplatform evaluation of global trends in wind speed and wave height. *Science*, **364 (6440)**, 548–552, https://doi.org/10.1126/science.aav9527.

Paper IV

Sea-ice impacts inter-annual variability in phytoplankton phenology and carbon export in the Weddell Sea

I. Giddy, S-A. Nicholson, B. Y. Queste, S. Thomalla, S. Swart
Geophysical Research Letters, **in review** (2022)

Sea-ice impacts inter-annual variability in phytoplankton phenology and carbon export in the Weddell Sea

I.S. Giddy[1,2,3], S-A. Nicholson[3], B. Queste[2], S. Thomalla[1,3], S. Swart[1,2],

[1]Department of Oceanography, University of Cape Town, Rondebosch, South Africa
[2]Department of Marine Sciences, University of Gothenburg, Gothenburg, Sweden
[3]Southern Ocean Carbon-Climate Observatory (SOCCO), CSIR, Cape Town, South Africa

Key Points:

- High-resolution glider observations are used to characterize multi-year phytoplankton bloom phenology in the Antarctic Marginal Ice Zone
- Years with greater sea-ice volume drive deeper mixing and support higher magnitude blooms
- Phytoplankton community composition and water column density stratification impact the strength of particulate carbon export flux

Corresponding author: Isabelle Giddy, isgiddy@gmail.com

Abstract

Carbon export from the ocean surface to depth is an important component of the biological carbon pump, a key regulator of the world's climate. The Antarctic Marginal Ice Zone accounts for 15% of Southern Ocean primary production, however, limited observations mean that the variability and drivers of primary production and its link to export are poorly constrained. Using a combination of gliders, biogeochemical Argo floats and satellite observations, we show that years with more sea-ice formation over winter result in more intense phytoplankton blooms (∼30% greater average daily Primary Production) and export to 100 m (∼50% higher daily carbon export) the following summer, but these increases were not reflected in the long term carbon export beyond the deepest winter mixed layer depth. These results suggest that if Antarctic sea-ice continues to decline, the biological carbon pump may become weaker, with implications for climate and Antarctic ecosystems.

Plain Language Summary

Algae in the ocean surface take up carbon dioxide from the atmosphere through photosynthesis and transfer it to the deep ocean when they die and sink. This process is key to maintaining a habitable planet and is known as the biological carbon pump. The seasonally ice-covered ocean around Antarctica is one of the most active areas for algal growth, but also a region of rapid climate change. Because of the difficulty in taking measurements in this remote region, the physical and biological processes that control the growth and sinking of algae and its response to changing sea-ice remain uncertain. In this study, we use a combination of satellites and autonomous robots to elucidate the role of sea-ice on the biological carbon pump. We find that sea-ice impacts algal growth by its influence on the light and nutrient conditions needed for photosynthesis. Predicting the amount of algae that sinks, although influenced by sea-ice conditions, is more complex and linked to the greater marine ecosystem. The evidence suggests that the species of algae, zooplankton grazing, and the rate at which dead algae breaks down are important and should be a focus point for further research.

1 Introduction

The Antarctic Marginal Ice Zone (MIZ) undergoes the surface ocean's largest transformation by the annual growth and retreat of sea-ice (Parkinson, 2019). One of the most productive oceanic regions (Arrigo et al., 2008; Ardyna et al., 2017), the MIZ accounts for $\sim$ 15% of Southern Ocean (SO) primary production (PP) (Taylor et al., 2013), that supports a diverse food-web dominated by krill, marine birds, seals and whales (Massom & Stammerjohn, 2010), and drives the biological carbon pump, through the downward transport of particulate organic carbon (POC) from the surface ocean to the interior.

The phenology of phytoplankton blooms in the Antarctic MIZ has been relatively well-observed since the satellite era and the introduction of under ice biogeochemical Argo (BGC-Argo) floats (Thomalla et al., 2011; Ardyna et al., 2017; Uchida et al., 2019; Arteaga et al., 2020; von Berg et al., 2020). Here, the seasonal range of PP is 2-3 times greater than in other SO regions in response to the high seasonality of solar irradiance and sea-ice (Ardyna et al., 2017). Although blooms initiate while still under light-limited conditions ($<$1 Ein m^{-2} day^{-1}) (Arteaga et al., 2020; Hague & Vichi, 2021), sea-ice melt enhances the rate of PP by generating a shallow freshwater lens and retaining phytoplankton in a higher average light environment (Smith & Nelson, 1985; Smith & Comiso, 2008; Thomalla et al., 2011; Lester et al., 2021). Ice melt also deposits iron (Arrigo et al., 2008; Lannuzel et al., 2016), which can temporarily enhance PP. However, in the SO, the major supply of iron is from depth, when winter mixing deepens the mixed layer beyond the ferricline and entrains a large reservoir of iron to support seasonal growth (Tagliabue et al., 2014; Llort et al., 2015; Nicholson et al., 2016, 2019; Ardyna et al., 2017).

PP is connected to the export of POC into the ocean interior through biological and physical processes, with only a small fraction of the organic carbon fixed by PP in the surface ultimately reaching the ocean interior (Martin et al., 1987; Giering et al., 2014; Henson et al., 2019). Particles are exported from the surface layer by sinking via the biological gravitational pump or by direct transport through the physical injection pump (Boyd et al., 2019). In the MIZ, the seasonal shoaling of the mixed layer traps particles beneath the thermocline, however most export occurs towards the end of the bloom season (Moreau et al., 2020) and strong stratification by sea-ice melt suppresses vertical transport along isopycnals (Giddy et al., 2021). The biological gravitational pump is therefore thought to be more important in this region. The export efficiency of the biological gravitational pump is regulated by particle formation and rates of sinking (aggregation, fragmentation, ballasting, senescence, grazing, viral lysis) and remineralization (microbial activity, chemical dissolution), themselves factors that largely depend on rates of PP and the community composition (Bach et al., 2019; Henson et al., 2019).

Globally, the upper ocean is predicted to continue to stratify into the 21st century (Kwiatkowski et al., 2020; Sallée et al., 2021). In the Antarctic MIZ, the resultant reduction in vertical nutrient fluxes may decrease PP (Arteaga et al., 2020), but conversely, decreased sea-ice cover may lengthen the bloom season and increase net PP (Henson et al., 2021). Sinking organic carbon that is remineralized within the Circumpolar Deep Water layer accounts for about half of the carbon sink in the Weddell Sea (Naveira Garabato et al., 2017; MacGilchrist et al., 2019), suggesting that changes in the biological carbon pump here can have a disproportionate impact on the global carbon cycle. However, how changes in PP translate to POC export remains unclear and an area of active research (e.g. Belcher et al., 2019; Arteaga et al., 2020; Moreau et al., 2020).

This study aims to understand the link between PP and carbon export in the SO MIZ. We focus on a region in the North Eastern Weddell Sea (Figure 1a,b) that is covered by sea-ice in the winter. First, we harness two decades of satellite observations and two profiling floats to contextualise two years of phytoplankton blooms that were observed between 2018 and 2020, at sub-daily resolution using gliders (referred to as SG2018 and SG2019 respectively; Figure 1c,d). We highlight the likely physical controls on the interannual variability in bloom phenology. Second, we use the glider data to link the biological and physical processes that control the export of POC to the underlying Upper Circumpolar Deep Water (UCDW), from where dissolved organic carbon has the potential to be sequestered into the ocean's abyss (Hoppema, 2004; MacGilchrist et al., 2019).

2 Methods

2.1 Phenology metrics

Using 23 years of satellite observations together with two BGC-Argo floats (WMO ID:5904397 and 5904467), we describe phytoplankton blooms by duration (days) and magnitude - the maximum surface chlorophyll-a (chl-a) achieved in the season (mg m^{-3}). Bloom initiation and termination are defined using chl-a thresholds, following Hopkins et al. (2015), where bloom initiation is the prepeak minimum concentration plus 5% of the range between the prepeak minimum and peak concentration, while the bloom termination is the postpeak minimum concentration plus 5% of the range between the peak and postpeak minimum concentration. The peak of the bloom identifies the annual chl-a maximum, wherein an annual cycle is defined from July to the following June. The duration is determined as the number of days between bloom initiation and termination. Since integrated chl-a over the bloom duration was linearly correlated with bloom magnitude, (Figure S1; $r^2 = 0.83$; $p < 0.001$), we use only bloom magnitude and duration as the key metrics characterizing interannual bloom variability.

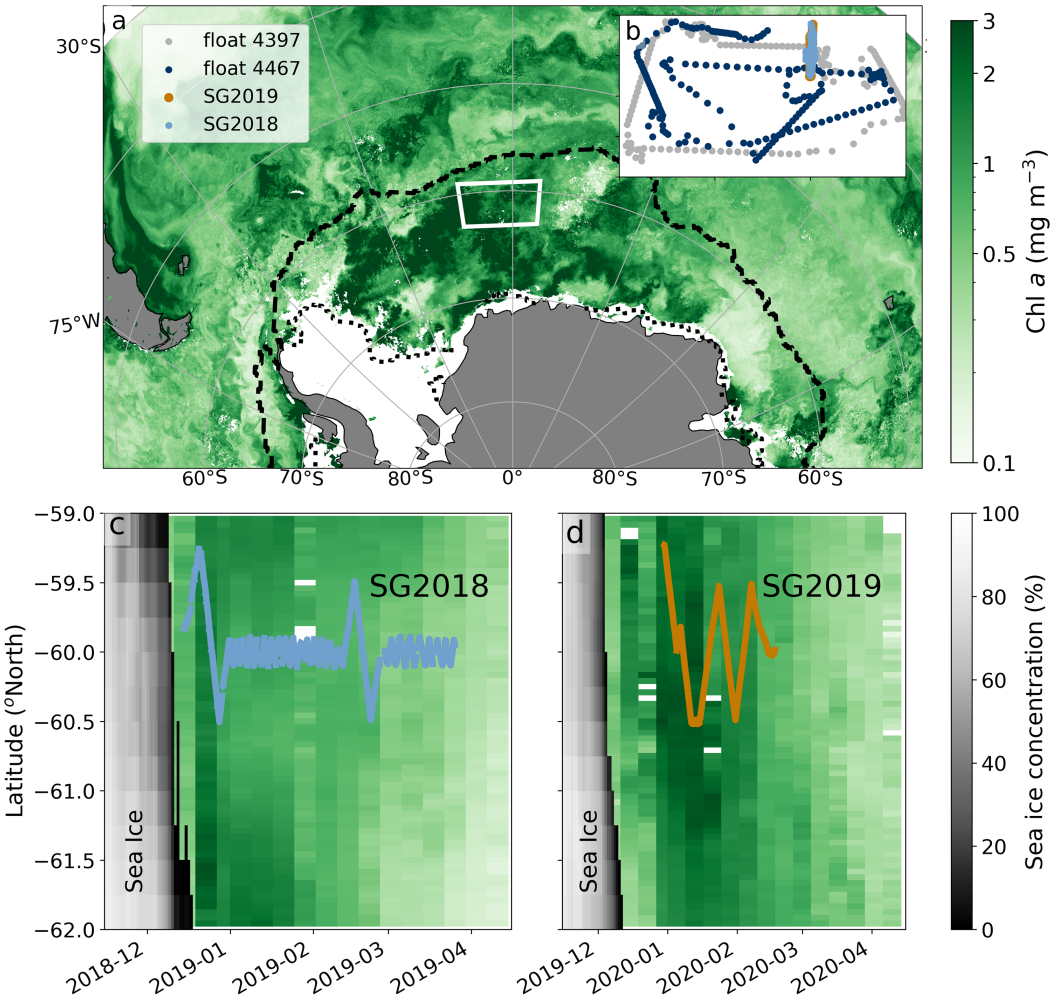

Figure 1. a) Average satellite chlorophyll-*a* concentration (Ocean Color-Climate Change Initiative) during austral summer (Dec 2019- Feb 2020) in the Atlantic sector of the Southern Ocean. The maximum and minimum sea-ice extents (National Snow and Ice Data Center) are shown in the dashed and dotted black lines, respectively. The study region is demarcated by the inlaid white box b), which shows the sampling trajectories of the two BGC-Argo, floats WMO ID:5904397 (during 2015-2020, dark blue) and WMO ID: 5904467(during 2014-2019, grey), and the two Seagliders (SG2018, during Dec 2018-March 2019, light blue) and SG2019 (Dec 2019 - Feb 2020, orange). c) Hovmöller plot for the latitudinal extent (averaged across longitude) of the study region of sea-ice concentration (Sea Ice Concentration Climate Data Record, OSI 430b) and satellite chlorophyll-*a* during the (c) 2018-2019 summer season for the SG2018 deployment (latitudinal trajectory shown in blue), and (d) for the 2019-2020 summer for the SG2019 deployment (orange).

2.2 Seasonal physical environmental conditions

Here we define key metrics used to characterise physical environmental conditions of the study region. The onset of sea-ice melt is defined as the date when sea-ice concentration first decreased and remained below 95% of the annual maximum. Mean annual sea-ice volume is computed as ice area (from sea-ice concentration) multiplied by the ice thickness, and averaged in time. A threshold for seasonal wind increase is defined as the first day in which wind stress reached 10% greater than the median wind stress after the annual minimum wind stress (using the same definition for an annual cycle as in section 2.1). The day when net heat flux (Q_{net}) rises above (drops below) + 10 W m^{-2} (positive into the ocean/negative out of the ocean) is also compared to bloom initiation and termination. Photosynthetically Active Radiation (PAR) is correlated with net heat flux ($r^2 = 0.86$; Figure S2) so is not assessed separately. Sea-ice and atmospheric variables are averaged to the same temporal resolution as the satellite chl-*a* observations for comparison ($\sim$ 8-day). Finally, all satellite products are averaged within the bounding box indicated in Figure 1b (-10 to 5 ^{o}E and -62 to -59 ^{o}S).

The mixed layer depth (MLD) is defined as the depth at which the density changes by 0.03 kg m^{-3} compared to a reference density at 10 m (de Boyer Montégut, 2004). MLD_{max} is the annual winter mixed layer maximum derived from the BGC-Argo floats (WMO ID: 5904397 and 5904467) from 2014-2018 and 2015-2020 respectively.

2.3 Primary Production

PP is estimated using the spectrally-resolved Carbon-based Productivity model (CbPM; Westberry et al., 2008) applied to the glider profiles (see Text S1 for a description of glider data processing). The CbPM estimates PP as a function of carbon biomass and phytoplankton growth rate, where carbon is estimated from backscatter with phytoplankton carbon, $C_{phyto} = 13000 \times bbp_{700}$ - 3.5 $\times$ 10^{-4} (Behrenfeld et al., 2005) and growth rate from the chl-*a*:C_{phyto} ratio and surface PAR. However, glider PAR was only available during the 2018 deployment (SG2018). To extend the PP analysis to the 2019 glider deployment (SG2019), Moderate Resolution Imaging Spectrometer/Aqua (MODIS) satellite PAR was co-located with both gliders. Glider PAR was comparable with satellite PAR ($r^2 = 0.44$, gain = 0.9; Figure S3) giving us confidence to use satellite PAR during SG2019 when no in situ PAR was available.

2.4 Aggregate Particulate Organic Carbon Export

We use high resolution optical backscatter measurements from the gliders to estimate POC export. Glider backscatter profiles are separated into a "small" particle baseline signal (7-point running minimum followed by a running maximum) and a "large" particle "spike" signal (all residuals above the baseline), following Briggs et al. (2011). After bin-averaging profiles of backscatter in the vertical to 10 m with a 50 m rolling mean, and binning profiles to 2-days with a 2-day running mean in time, carbon flux events are identified as follows. First, using a 10-day moving window over each glider dataset, the time of maximum spike for each depth level is identified. Linear regressions are then fit between the depth of each maximum spike and time. Only regressions with $r^2 > 0.4$ are identified as flux events. Finally, the linear regression fits are used to estimate the sinking speed of large particles (Δdepth/Δtime) (Figure S4). Large particle backscatter is converted to POC, and multiplied by the derived bulk sinking speeds (with individual export events ranging between 48 and 88 m day^{-1} and an average sinking rate of 65 m day^{-1}) to estimate aggregate POC flux (equation 4, Briggs et al., 2011). Export is estimated at 100 m, as the depth horizon most commonly used to estimate export in models (Buesseler & Boyd, 2009). Export efficiency (E_{eff}) is defined as the ratio of export at 100 m to PP, using PP values from 2 days earlier. A lag of 2 days was chosen based on the average sinking rates of aggregates. Similarly, transfer efficiency (T_{eff}) is defined

as the ratio of export at 170 m (the deepest winter mixed layer, Moreau et al., 2020) to export at 100 m from 2 days earlier. We also estimate T_{eff} from the rate of flux attenuation by fitting the aggregate POC profiles identified as export events to Martins Curve (Martin et al., 1987):

$$F_z = f_{z_0} \times (z/z_0)^{-b}, \quad (1)$$

where F_z is the carbon flux with depth, f_{z_0} is the flux at a reference depth z_0, z is depth, and b is the attenuation coefficient, with smaller $-b$ representing faster attenuation rates and a lower T_{eff}.

All data used and their processing is described in Supplementary Texts 1 and 2.

3 Results and Discussion

3.1 Characteristics and drivers of bloom phenology in the Weddell Sea

The efficiency of the biological pump is associated with bloom phenology, which is mediated by nutrient availability, light and mortality (Behrenfeld & Boss, 2014; Arteaga et al., 2018). Here, we assess the drivers of bloom phenology in the north eastern Weddell Sea to determine what sets the upper limits of PP in this region. Our results demonstrate that the initiation of the seasonal bloom was in close proximity to sea-ice melt (within 8 - 32 days of each other), with 61% of the onset in bloom initiation attributed to the onset of ice melt (Figure 2a,b; S5a). While it is appreciated that this analysis does not directly test Sverdrup's Critical Depth Hypothesis (Sverdrup, 1953), it's relevance is inferred by the association of sea-ice melt with the shoaling of the mixed layer in the light-limited MIZ (Pellichero et al., 2017), together with an increasing trace of chl-*a* observed in the satellite record (Figure 2a). In addition, for the instances where we had reliable MLD data from the BGC-Argo deployments, bloom initiations (determined as in section 2.1) were coincident with a shoaling of the MLD and support the likelihood of enhanced growth associated with a seasonal shoaling of the mixed layer, also noted by (von Berg et al., 2020). As such, top-down controls of bloom initiation that evoke the role of zooplankton grazing (e.g. Dilution-Recoupling Hypothesis; Behrenfeld & Boss, 2014; Arteaga et al., 2020), are unlikely. This result is further supported by the finding of Moreau et al. (2020) in the Antarctic MIZ, that phytodetritus (and not fecal pellets from grazing) compose the majority of carbon export during the initial stages of the summer bloom. An investigation of bloom termination found that the timing was more variable than bloom initiation. In the satellite record, bloom initiation varied by 48 days from the earliest to the latest date of initiation, while bloom termination varied by 72 days (Figure 2a, S5). In addition to greater variability, the drivers of bloom termination are also less well understood than those of bloom initiation. Here we assessed the seasonally variable physical parameters of wind stress, PAR, heat flux, and ice formation as potential drivers of bloom termination, but found no significant correlations (Figure 2b, S2; S5c,d). As such, we conclude that bloom termination is most likely driven by the depletion of nutrients and trace metals (Boyd et al., 2005; Krause et al., 2019), grazing (Moreau et al., 2020; Kauko et al., 2021), bacteria, and viruses (Biggs et al., 2021), which were not measured as part of this study.

By far the most prominent characteristic of interannual variability in bloom phenology is that of bloom magnitude (Figure 2a), which ranged from a very meagre seasonal maximum of 0.4 mg m^{-3} (2010) to a seasonal maximum as high as 2.8 mg m^{-3} (2005). Previous studies have identified nutrient availability as the leading driver of variability in bloom magnitude (Llort et al., 2015; Ardyna et al., 2017). In the northern edge of the Weddell Sea, the outcropping of warm and salty UCDW (located between 100 and 200 m in the winter) is enriched with dissolved iron (Klunder et al., 2011, their Figure 5). We found a strong relationship between the depth of winter mixing and the maximum chl-*a* achieved during the following summer from BGC-Argo float data (Figure 2c;

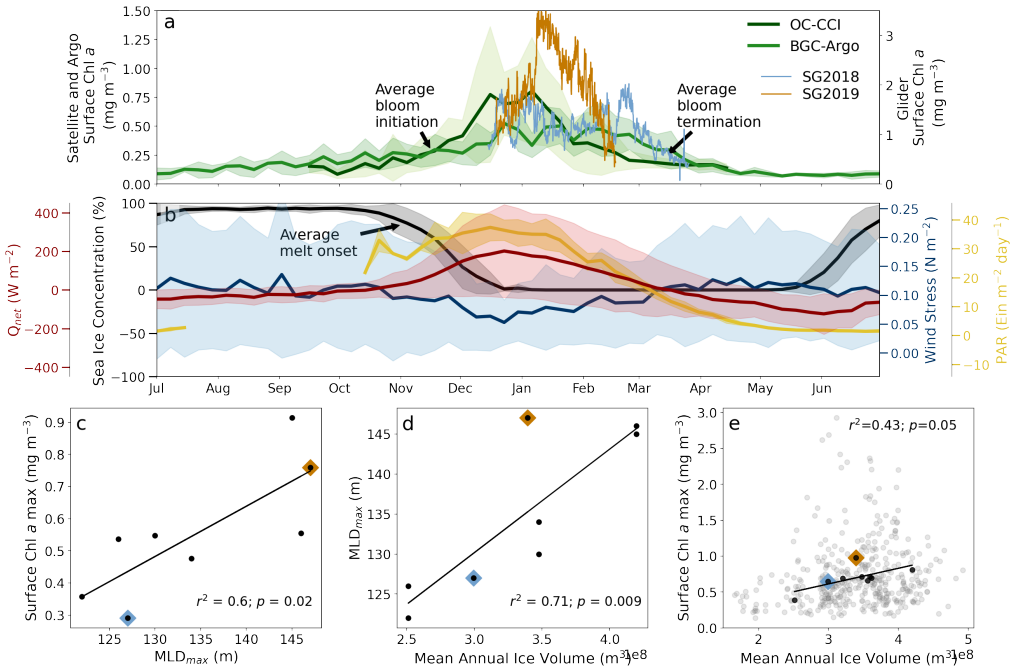

Figure 2. a) Climatologies of satellite-observed surface chl-*a* (OC-CCI; 1997-2020, dark green) and mean of two BGC-Argo floats (WMO ID:5904397 and 5904467; 2016-2019; light green). Glider observations of surface chl-*a* during the 2018-19 summer season (light blue, SG2018) and the 2019-20 summer season (orange, SG2019). Float and glider chl-*a* are averages over the top 20 m. The climatological bloom initiation and termination dates are indicated. b) Climatologies over the same time period of sea-ice concentration (black), Qnet (red), wind stress (blue) and Photosynthetically Active Radiation (yellow). The sea-ice melt onset is indicated. Shading in panels (a) and (b) represent one standard deviation. Linear regressions of c) the deepest winter mixed layer with the following summers' maximum chl-*a* as observed by the BGC-Argo floats (2015-2019); d) the total annual ice volume with the deepest winter mixed layer (2015-2019) and e) the annual ice volume with annual maximum chl-*a* from OC-CCI (2011-2020): the grey dots are values per degree latitude and longitude, the black dots are a spatial average of the study region. The regression applies to the spatial average. The blue and orange diamonds correspond to the years of the glider deployments (2018-19 and 2019-20, respectively).

$r^2 = 0.6$; $p = 0.02$), indicating a likelihood that dissolved iron delivery through winter entrainment of UCDW determines the summer bloom maxima.

One of the primary drivers of deep winter mixing in the ice-impacted oceans is brine rejection from sea-ice formation (McPhee & Morison, 2001; Wilson et al., 2019). A metric for sea-ice formation and brine rejection was approximated using the mean annual ice volume. This mechanistic link was supported by the significant relationship ($r^2 = 0.71$; $p = 0.009$) observed between MLD_{max} (measured by the floats) and a box average of annual ice volume overlying the trajectory of the floats (Figure 2d). Years in which there was a higher annual ice volume also tended to be coincident with higher magnitude summer blooms (Figure 2e; $r^2 = 0.47$; $p = 0.04$). Extending this analysis to the ice-impacted SO (Figure S6), we find that sea-ice volume is an important driver of bloom magnitude, specifically along the coast of Antarctica and in some open-ocean regions, most notable in the central Weddell Sea, Ross Sea and off East Antarctica ($\sim 45^o$). Although there is evidence of spatial variability likely associated with an interplay between light and nutrient limitation (e.g., 30% of the ice-impacted region where $r^2 > 0.25$), we note regions with highest bloom amplitudes on average (85^{th} percentile of bloom peak magnitudes) are strongly correlated to ice volume, $r^2 > 0.5$). Furthermore, a higher volume of meltwater may enhance summer stratification (although stratification is also a function of heat flux into the ocean), which was positively and significantly related to bloom magnitude (Figure S7b, $r^2 = 0.47$; $p = 0.06$). While not directly accounted for, ice volume is linked to iron accumulation within the sea-ice and release thereof (Lannuzel et al., 2016) and as such, iron delivery from sea-ice may also contribute to part of the observed variability, albeit minor in comparison with that originating from the winter entrainment of UCDW (e.g. Annett et al., 2017). These multiple lines of evidence point towards the key role that sea-ice formation plays in determining the interannual variability in magnitude of phytoplankton blooms through its modulation of both nutrient and light supply.

3.2 The fate of particulate organic carbon

In the Antarctic MIZ, changes in the fraction of carbon fixed by photosynthesis that is exported to the ocean interior has the potential to impact climate (Fogwill et al., 2020). To infer how the biological carbon pump here might respond to different surface conditions, we link surface processes to the fate of sinking organic carbon by coupling the analysis of phytoplankton phenology in section 3.1 to two distinct years of seasonal blooms (Figure 2a) that were observed by gliders (Figure 1, SG2018 and SG2019). The bloom captured by SG2018 was longer and of a lower magnitude (max chl-a=2.0 mg m^{-3}, 133 days, of which the glider sampled 101 days), while in contrast, the bloom captured by SG2019 was shorter and of higher magnitude (max chl-a=3.7 mg m^{-3}, 77 days of which the glider sampled 51 days, Figure 1c,d; 2a; S5). Correspondingly, the maximum winter MLD was 20 m deeper preceding the higher magnitude bloom in 2019 compared with 2018 (Figure 2c).

Modeled rates of PP reflect the characteristics of surface chl-a (Figure 1a), and were $\sim$30% lower during 2018-19 (mean = 1741 $\pm$ 628 mg C m^{-2} day^{-1}, Figure 3a) compared to 2019-20 (mean = 2496 $\pm$ 616 mg C m^{-2} day^{-1}; Figure 3b). Differences in PP between the two years translated into even bigger differences ($\sim$50%) in daily export rates at 100 m (mean = 151 $\pm$ 60 mg C m^{-2} day^{-1} and 306 $\pm$ 97 mg C m^{-2} day^{-1} respectively, Figure 3a,b). Thus, these metrics classify the Weddell Sea MIZ as a region of High Productivity, Low Export, as defined by Henson et al. (2019, see Figure S7), with a similar E_{eff} between the two years (mean = 0.09 $\pm$ 0.05 in 2018-19 and 0.12 $\pm$ 0.03 in 2019-20; S8b). However, we found that E_{eff} is sensitive to the choice of the PP model (Figure S9c). We elected to implement the CbPM in this study, but note that while the magnitude of E_{eff} would be different, the relative changes between the two years would not differ if another model was used. Similarly, E_{eff} is sensitive to the method used to compute export. There

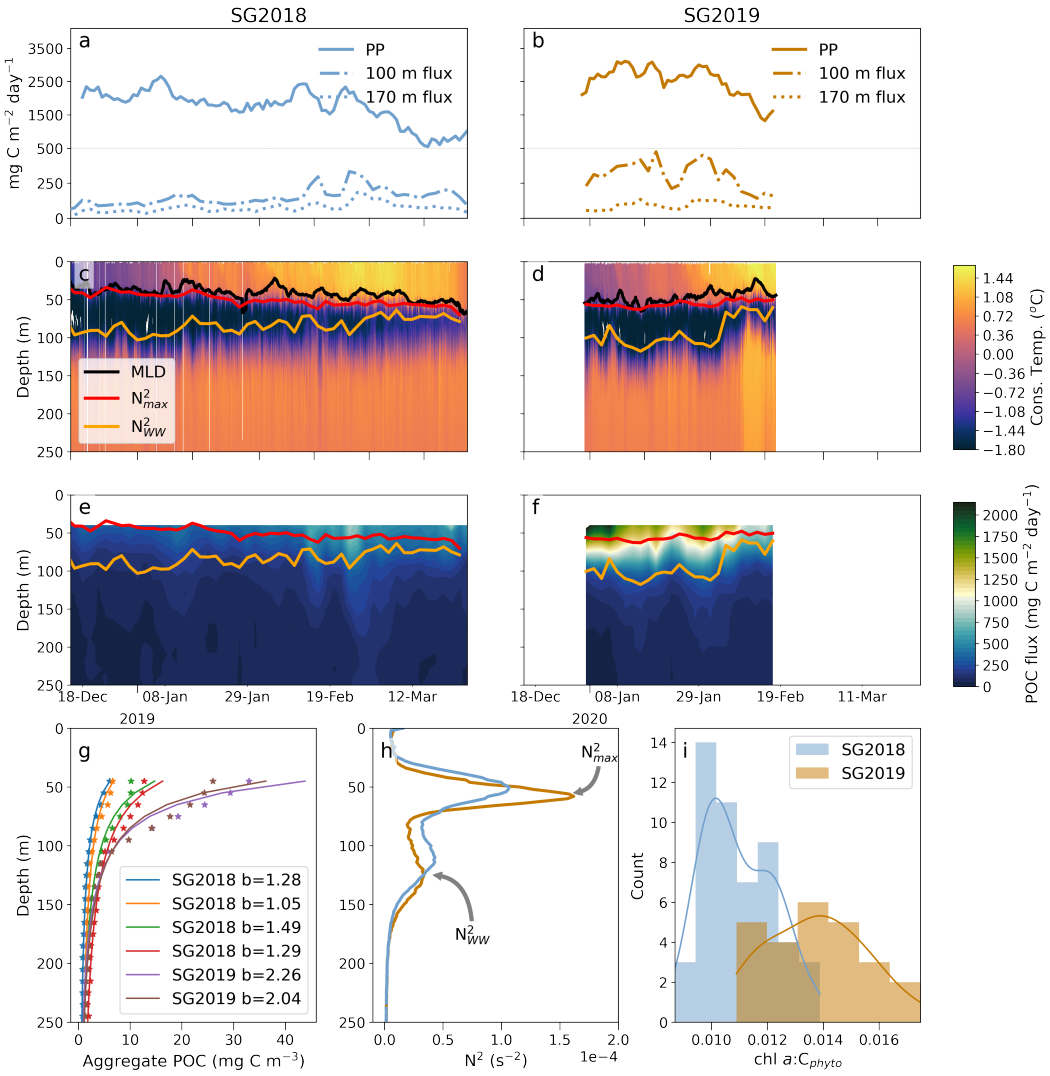

Figure 3. a) Integrated primary production in the upper 200 m smoothed by 4 days (solid line), export at 100 m (dash-dot line) and export at 170 m (dotted line) from glider deployments in (a) the 2018-19 and (b) the 2019-20 productive seasons. Note the change in scale of the y-axis between 0-500 m and 500-3500 m, indicated by the faint grey line, to emphasise variability in the smaller values. Vertical sections of conservative temperature in (c) 2018-19 and (d) 2019-20. Marked on both (c, d) are the MLD (black line), the depth of maximum stratification (N^2_{max}) (red line), and the depth of the Winter Water N^2_{max} (orange line). Vertical sections of large particle Particulate Organic Carbon flux during (e) 2018-19 and (f) 2019-20. Values above 40 m are missing as a result of the 50 m rolling mean applied to the dataset (see section 2.4). g) Martin Curve fits during flux events. h) Mean vertical stratification profiles corresponding to SG2018 (blue) and SG2019 (orange). i) Histograms of average mixed layer chl-a:C$_{phyto}$ ratio in SG2018 and SG2019. .

are large uncertainties in the absolute numbers, associated with uncertainty in large-particle POC to backscatter ratio and sinking speed. Nevertheless, relative differences should be more robust.

When we extended this analysis to the T_{eff} ($export_{170m}$:$export_{100m}$), we found that T_{eff} was inverted, with a higher T_{eff} in 2018-19 (0.05 ± 0.01) than in 2019-20 (0.03 ± 0.01; Figure S8c); a result also reflected in the flux attenuation rate, which was slower in 2018-19 (-1.3 ± 0.2) than in 2019-20 (-2.2 ± 0.06, Figure 3g). This translates to similar daily export rates to 170 m between the two years (2018-19: 73 ± 32 mg C m^{-2} day^{-1} and 2019-20: 90 ± 26 mg C m^{-2} day^{-1}; Figure 3a,b). As such, an additional factor that will change the estimate of E_{eff} is the choice of depth horizon for export.

Variability in flux attenuation rates (Figure 3g) suggest that remineralization rates, which are known to account for a large proportion of variability in T_{eff} (Belcher et al., 2016; Bach et al., 2019), contrasted across the two years and may explain the similarity in export to 170 m despite differences in PP. The rate of remineralization is primarily controlled by (1) temperature (Marsay et al., 2015), (2) variation in sinking rates associated with size and porosity of aggregates (Bach et al., 2019) and the ratio between particle and water density (Condie, 1999), and (3) microbial degradation influenced by functional activity and community structure, POC composition (labile, semi-labile, recalcitrant) (Cavan et al., 2018) and grazing load (Cavan et al., 2015; Henson et al., 2019). We assume the effect of temperature is negligible as the interannual variability in temperature is small compared to latitudinal variability (Figure 3c,d).

Large cells (notably diatoms with additional ballast; Tréguer et al., 2018), would be expected to sink faster, escaping microbial degradation and hence drive a higher T_eff and lower attenuation rate. As expected, a deeper winter MLD prior to the summer bloom would likely result in an increase in iron supply, thereby supporting a higher magnitude bloom as seen in 2019-20 (Figure 2c,d). A typical community composition response to high iron and light availability leads to a dominance of diatoms (Smetacek et al., 2012). Although we did not directly measure community composition, chl-a:C_{phyto} ratios have been used to infer changes in community composition, with a higher chl-a:C_{phyto} typically indicating a larger proportion of diatoms (Cetinić et al., 2015). As such, there were likely more diatoms in the community during 2019-20 than during 2018-19. However, the sinking rates were not significantly different between the two years (mean = 65 m day^{-1}; S4), and the predicted diatom-dominated bloom was counter-intuitively characterized by a faster attenuation rate (Figure 3g). The higher chl-a:C_{phyto} may also represent a higher ratio of fresh, labile phytoplankton in SG2019 compared to "older", more refractory particulate matter in SG2018 that could contribute to the observed higher transfer efficiency compared to that in SG2019 (Cavan et al., 2018). An alternative interpretation of the chl-a:C_{phyto} pertains to changes in the bacterial load of the system (i.e. that the species were the same in both years but that there was less carbon from bacteria in the year with a higher ratio). We argue that this is unlikely, as higher production is often associated with higher bacterial load (Henson et al., 2019).

Changes in density with depth can also influence the sinking rate of particles through two mechanisms. Firstly, when a sinking particle encounters denser water, the relative density between water and particle is reduced and the buoyancy force on the particle increases, decreasing its sinking velocity (Condie, 1999). Secondly, under conditions where the thermocline deepens at a rate faster than the sinking speed of the particles, particles may be re-entrained into the mixed layer (Lacour et al., 2019; D'Asaro, 2008; Noh & Nakada, 2010). If, through these mechanisms, particles are retained within the thermocline, they would be exposed to a longer period of remineralization in the upper ocean, thus reducing export to depth. Indeed, the accumulation of particles within the thermocline is a strong feature of the bloom in 2019-20 (Figure 3f), and particles appear to follow isopycnals, while those in 2018-19 do not (Figure 3e). Additionally, the level of stratification in 2019-20 is greater than in 2018-19 (N^2_{max} = 1.6e^{-3} s^{-1} and 1e^{-3} s^{-1},

respectively; Figure 3h). While a diatom-dominated community might be expected to sink faster, the larger density change with depth observed in 2019-20 may slow particle sinking rates, resulting in the relatively similar sinking rates across the two years and the reduced T_{eff} for 2019-20.

Finally, remineralization rates and flux attenuation may be influenced by bacterial load and grazing (e.g. Cavan et al., 2015). Thus, the faster remineralization rates observed in 2019-20 could be a result of higher grazing pressure within the upper 200 m. This is feasible as grazing by zooplankton has been demonstrated to account for ∼90% of the fate of phytoplankton in this region (Moreau et al., 2020), although grazing is not constrained in this study.

4 Conclusions

Glider measurements of both physical (temperature and salinity) and biological (chl-*a* and carbon) variables enable the simultaneous quantification of PP, export, and water column density at scales of hours to days. These results, complemented by BGC-Argo and satellite observations, have revealed the complexity of interactions grounded in sea-ice characteristics (formation, duration, melt) that currently govern PP and carbon export in the Weddell Sea. Firstly, we find empirical evidence, from both floats and satellites, that increased winter sea-ice formation drives deeper winter mixing, which in turn leads to more intense phytoplankton blooms in the following season, likely due to nutrient and iron entrainment. Secondly, our two seasons of glider data provide preliminary evidence that more of these intense blooms lead to higher carbon export at 100 m, suggesting a potential positive impact of sea-ice on the biological carbon pump. However, higher 100 m export was attenuated more quickly with depth and did not translate to substantially higher export past 170 m, the depth of deepest winter mixing (with high flux attenuation rates relative to global averages greater than 1 Marsay et al., 2015). This inverse relationship between E_{eff} and T_{eff} that was observed in the 2019-20 bloom period confirms that estimating export from a uniform depth of 100 m risks overestimating export for this region (Palevsky & Doney, 2018) as carbon export was found to change considerably between 100 m and 170 m (the maximum winter MLD). Altogether, this suggests that more intense blooms and carbon export events may not lead to enhanced long-term carbon storage, although more data are needed to confirm this initial finding. Targeted observational campaigns to constrain uncertainties in the variability of sea ice formation and the drivers of remineralization (e.g. through the incorporation of imaging platforms and Acoustic Doppler Current Profilers on gliders), are important to improving predictions on how the carbon sink in the subpolar gyres of the Southern Ocean responds to changes in the surface ocean.

Acknowledgments

This work was supported by the following grants of S. Swart: Wallenberg Academy Fellowship (WAF 2015.0186), Swedish Research Council (VR 2019-04400); S.Swart and S. Thomalla: STINT-NRF Mobility Grant (STNT180910357293); S.-A. Nicholson and S. Swart: NRF-SANAP (SNA170522231782, SANAP200324510487); S.Thomalla: CSIR Parliamentary Grant. I.S Giddy acknowledges the support of the NRF-SANAP (SNA170506229906) and iAtlantic Horizon 2020 grant (818123), as well as the Oppenheimer Memorial Trust PhD fund. This work would not have been possible without the valuable fieldwork aboard the RV SA Agulhas II, her captain and crew for deployment of gliders; Andy Thompson and the glider piloting team at Caltech for their contributions to the ROAM-MIZ project, including glider SG643 and its associated data. The authors would like to thank Nathan Briggs for advice regarding the calculation of particulate organic carbon export, Hannah Joy-Warren for feedback at the final stages of the manuscript and constructive comments from an anonymous reviewer.

Open Research

All data used in this study is freely available online. Biogeochemical Argo data were collected and made freely available by the Southern Ocean Carbon and Climate Observations and Modeling (SOCCOM) Project funded by the National Science Foundation, Division of Polar Programs (NSF PLR -1425989 and OPP-1936222), supplemented by NASA, and by the International Argo Program and the NOAA programs that contribute to it. The Argo Program is part of the Global Ocean Observing System. The following links will access data from the particular SOCCOM floats used in this study on the Argo system (`ftp://ftp.ifremer.fr/ifremer/argo/dac/aoml/5904397`; `ftp://ftp.ifremer.fr/ifremer/argo/dac/aoml/5904467`). The results in this paper contain modified Copernicus Climate Change Service information 2021. Neither the European Commission nor ECMWF is responsible for any use that may be made of the Copernicus information or data it contains. The glider data is archived with the National Center for Environmental Information and is available at the following url `https://www.ncei.noaa.gov/access/metadata/landing-page/bin/iso?id=gov.noaa.nodc:0244004`. The code that was used in the analysis of this paper is also made available via Github and Zenodo (`10.5281/zenodo.5655923`). The code used to compute the glider-CbPM was adapted from L. Arteaga's script available on Github: `https://zenodo.org/badge/latestdoi/368542675`.

References

Annett, A. L., Fitzsimmons, J. N., Séguret, M. J., Lagerström, M., Meredith, M. P., Schofield, O., & Sherrell, R. M. (2017). Controls on dissolved and particulate iron distributions in surface waters of the Western Antarctic Peninsula shelf. *Marine Chemistry*, *196*, 81–97. doi: 10.1016/j.marchem.2017.06.004

Ardyna, M., Claustre, H., Sallée, J.-B., D'Ovidio, F., Gentili, B., van Dijken, G., ... Arrigo, K. R. (2017). Delineating environmental control of phytoplankton biomass and phenology in the Southern Ocean: Phytoplankton Dynamics in the SO. *Geophysical Research Letters*, *44*(10), 5016–5024. doi: 10.1002/2016GL072428

Arrigo, K. R., van Dijken, G. L., & Bushinsky, S. (2008). Primary production in the Southern Ocean, 1997–2006. *Journal of Geophysical Research*, *113*(C8), C08004. doi: 10.1029/2007JC004551

Arteaga, L., Boss, E., Behrenfeld, M. J., Westberry, T. K., & Sarmiento, J. L. (2020). Seasonal modulation of phytoplankton biomass in the Southern Ocean. *Nature Communications*, *11*(1), 5364. doi: 10.1038/s41467-020-19157-2

Arteaga, L., Haëntjens, N., Boss, E., Johnson, K. S., & Sarmiento, J. L. (2018). Assessment of Export Efficiency Equations in the Southern Ocean Applied to Satellite-Based Net Primary Production. *Journal of Geophysical Research: Oceans*, *123*(4), 2945–2964. doi: 10.1002/2018JC013787

Bach, L. T., Stange, P., Taucher, J., Achterberg, E. P., Algueró-Muñiz, M., Horn, H., ... Riebesell, U. (2019). The Influence of Plankton Community Structure on Sinking Velocity and Remineralization Rate of Marine Aggregates. *Global Biogeochemical Cycles*, *33*(8), 971–994. doi: 10.1029/2019GB006256

Behrenfeld, M. J., Boss, E., Siegel, D. A., & Shea, D. M. (2005). Carbon-based ocean productivity and phytoplankton physiology from space: Phytoplankton growth rates and ocean productivity. *Global Biogeochemical Cycles*, *19*(1). doi: 10.1029/2004GB002299

Behrenfeld, M. J., & Boss, E. S. (2014). Resurrecting the Ecological Underpinnings of Ocean Plankton Blooms. *Annual Review of Marine Science*, *6*(1), 167–194. doi: 10.1146/annurev-marine-052913-021325

Belcher, A., Henson, S. A., Manno, C., Hill, S. L., Atkinson, A., Thorpe, S. E., ... Tarling, G. A. (2019). Krill faecal pellets drive hidden pulses of particulate organic carbon in the marginal ice zone. *Nature Communications*, *10*(1), 889.

421 doi: 10.1038/s41467-019-08847-1
422 Belcher, A., Iversen, M., Manno, C., Henson, S. A., Tarling, G. A., & Sanders, R.
423 (2016). The role of particle associated microbes in remineralization of fecal
424 pellets in the upper mesopelagic of the Scotia Sea, Antarctica. *Limnology and*
425 *Oceanography*, *61*(3), 1049–1064. doi: 10.1002/lno.10269
426 Biggs, T. E. G., Huisman, J., & Brussaard, C. P. D. (2021). Viral lysis modifies
427 seasonal phytoplankton dynamics and carbon flow in the Southern Ocean. *The*
428 *ISME Journal*. doi: 10.1038/s41396-021-01033-6
429 Boyd, P. W., Claustre, H., Levy, M., Siegel, D. A., & Weber, T. (2019). Multi-
430 faceted particle pumps drive carbon sequestration in the ocean. *Nature*,
431 *568*(7752), 327–335. doi: 10.1038/s41586-019-1098-2
432 Boyd, P. W., Strzepek, R., Takeda, S., Jackson, G., Wong, C. S., McKay, R. M.,
433 ... Ramaiah, N. (2005). The evolution and termination of an iron-induced
434 mesoscale bloom in the northeast subarctic Pacific. *Limnology and Oceanogra-*
435 *phy*, *50*(6), 1872–1886. doi: 10.4319/lo.2005.50.6.1872
436 Briggs, N., Perry, M. J., Cetinić, I., Lee, C., D'Asaro, E., Gray, A. M., & Rehm, E.
437 (2011). High-resolution observations of aggregate flux during a sub-polar North
438 Atlantic spring bloom. *Deep Sea Research Part I: Oceanographic Research*
439 *Papers*, *58*(10), 1031–1039. doi: 10.1016/j.dsr.2011.07.007
440 Buesseler, K. O., & Boyd, P. W. (2009). Shedding light on processes that con-
441 trol particle export and flux attenuation in the twilight zone of the open
442 ocean. *Limnology and Oceanography*, *54*(4), 1210–1232. doi: 10.4319/
443 lo.2009.54.4.1210
444 Cavan, E. L., Giering, S. L. C., Wolff, G. A., Trimmer, M., & Sanders, R. (2018).
445 Alternative Particle Formation Pathways in the Eastern Tropical North Pa-
446 cific's Biological Carbon Pump. *Journal of Geophysical Research: Biogeo-*
447 *sciences*, *123*(7), 2198–2211. Retrieved from `https://onlinelibrary.wiley`
448 `.com/doi/abs/10.1029/2018JG004392` doi: 10.1029/2018JG004392
449 Cavan, E. L., Le Moigne, F. A. C., Poulton, A. J., Tarling, G. A., Ward, P., Daniels,
450 C. J., ... Sanders, R. J. (2015). Attenuation of particulate organic carbon flux
451 in the Scotia Sea, Southern Ocean, is controlled by zooplankton fecal pellets.
452 *Geophysical Research Letters*, *42*(3), 821–830. doi: 10.1002/2014GL062744
453 Cetinić, I., Perry, M. J., D'Asaro, E., Briggs, N., Poulton, N., Sieracki, M. E., &
454 Lee, C. M. (2015). A simple optical index shows spatial and temporal
455 heterogeneity in phytoplankton community composition during the 2008
456 North Atlantic Bloom Experiment. *Biogeosciences*, *12*(7), 2179–2194. doi:
457 10.5194/bg-12-2179-2015
458 Condie, S. (1999). Settling regimes for non-motile particles in stratified waters. *Deep*
459 *Sea Research Part I: Oceanographic Research Papers*, *46*(4), 681–699. doi: 10
460 .1016/S0967-0637(98)00085-5
461 de Boyer Montégut, C. (2004). Mixed layer depth over the global ocean: An exam-
462 ination of profile data and a profile-based climatology. *Journal of Geophysical*
463 *Research*, *109*(C12), C12003. doi: 10.1029/2004JC002378
464 D'Asaro, E. A. (2008). Convection and the seeding of the North Atlantic bloom.
465 *Journal of Marine Systems*, *69*(3-4), 233–237. doi: 10.1016/j.jmarsys.2005.08
466 .005
467 Fogwill, C. J., Turney, C. S. M., Menviel, L., Baker, A., Weber, M. E., Ellis, B., ...
468 Cooper, A. (2020). Southern Ocean carbon sink enhanced by sea-ice feed-
469 backs at the Antarctic Cold Reversal. *Nature Geoscience*, *13*(7), 489–497. doi:
470 10.1038/s41561-020-0587-0
471 Giddy, I., Swart, S., du Plessis, M., Thompson, A. F., & Nicholson, S. (2021).
472 Stirring of Sea-Ice Meltwater Enhances Submesoscale Fronts in the South-
473 ern Ocean. *Journal of Geophysical Research: Oceans*, *126*(4). doi:
474 10.1029/2020JC016814
475 Giering, S. L. C., Sanders, R., Lampitt, R. S., Anderson, T. R., Tamburini,

C., Boutrif, M., ... Mayor, D. J. (2014). Reconciliation of the carbon budget in the ocean's twilight zone. *Nature*, *507*(7493), 480–483. doi: 10.1038/nature13123

Hague, M., & Vichi, M. (2021). Southern Ocean Biogeochemical Argo detect under-ice phytoplankton growth before sea ice retreat. *Biogeosciences*, *18*(1), 25–38. doi: 10.5194/bg-18-25-2021

Henson, S., Cael, B. B., Allen, S. R., & Dutkiewicz, S. (2021). Future phytoplankton diversity in a changing climate. *Nature Communications*, *12*(1), 5372. doi: 10.1038/s41467-021-25699-w

Henson, S., Le Moigne, F., & Giering, S. (2019). Drivers of Carbon Export Efficiency in the Global Ocean. *Global Biogeochemical Cycles*, *33*(7), 891–903. doi: 10.1029/2018GB006158

Hopkins, J., Henson, S. A., Painter, S. C., Tyrrell, T., & Poulton, A. J. (2015). Phenological characteristics of global coccolithophore blooms: Coccolithophore bloom phenology. *Global Biogeochemical Cycles*, *29*(2), 239–253. doi: 10.1002/2014GB004919

Hoppema, M. (2004). Weddell Sea is a globally significant contributor to deep-sea sequestration of natural carbon dioxide. *Deep Sea Research Part I: Oceanographic Research Papers*, *51*(9), 1169–1177. doi: 10.1016/j.dsr.2004.02.011

Kauko, H. M., Hattermann, T., Ryan-Keogh, T., Singh, A., de Steur, L., Fransson, A., ... Moreau, S. (2021). Phenology and Environmental Control of Phytoplankton Blooms in the Kong Håkon VII Hav in the Southern Ocean. *Frontiers in Marine Science*, *8*, 623856. doi: 10.3389/fmars.2021.623856

Klunder, M., Laan, P., Middag, R., De Baar, H., & van Ooijen, J. (2011). Dissolved iron in the Southern Ocean (Atlantic sector). *Deep Sea Research Part II: Topical Studies in Oceanography*, *58*(25-26), 2678–2694. doi: 10.1016/j.dsr2.2010.10.042

Krause, J. W., Schulz, I. K., Rowe, K. A., Dobbins, W., Winding, M. H. S., Sejr, M. K., ... Agustí, S. (2019). Silicic acid limitation drives bloom termination and potential carbon sequestration in an Arctic bloom. *Scientific Reports*, *9*(1), 8149. doi: 10.1038/s41598-019-44587-4

Kwiatkowski, L., Torres, O., Bopp, L., Aumont, O., Chamberlain, M., Christian, J. R., ... Ziehn, T. (2020). Twenty-first century ocean warming, acidification, deoxygenation, and upper-ocean nutrient and primary production decline from CMIP6 model projections. *Biogeosciences*, *17*(13), 3439–3470. doi: 10.5194/bg-17-3439-2020

Lacour, L., Briggs, N., Claustre, H., Ardyna, M., & Dall'Olmo, G. (2019). The Intraseasonal Dynamics of the Mixed Layer Pump in the Subpolar North Atlantic Ocean: A Biogeochemical-Argo Float Approach. *Global Biogeochemical Cycles*, *33*(3), 266–281. doi: 10.1029/2018GB005997

Lannuzel, D., Vancoppenolle, M., van der Merwe, P., de Jong, J., Meiners, K., Grotti, M., ... Schoemann, V. (2016). Iron in sea ice: Review and new insights. *Elementa: Science of the Anthropocene*, *4*, 000130. doi: 10.12952/journal.elementa.000130

Lester, C. W., Wagner, T. J. W., McNamara, D. E., & Cape, M. R. (2021). The Influence of Meltwater on Phytoplankton Blooms Near the Sea-Ice Edge. *Geophysical Research Letters*, *48*(2). doi: 10.1029/2020GL091758

Llort, J., Lévy, M., Sallée, J.-B., & Tagliabue, A. (2015). Onset, intensification, and decline of phytoplankton blooms in the Southern Ocean. *ICES Journal of Marine Science*, *72*(6), 1971–1984. doi: 10.1093/icesjms/fsv053

MacGilchrist, G. A., Naveira Garabato, A. C., Brown, P. J., Jullion, L., Bacon, S., Bakker, D. C. E., ... Torres-Valdés, S. (2019). Reframing the carbon cycle of the subpolar Southern Ocean. *Science Advances*, *5*(8), eaav6410. doi: 10.1126/sciadv.aav6410

Marsay, C. M., Sanders, R. J., Henson, S. A., Pabortsava, K., Achterberg, E. P.,

& Lampitt, R. S. (2015). Attenuation of sinking particulate organic carbon flux through the mesopelagic ocean. *Proceedings of the National Academy of Sciences*, *112*(4), 1089–1094. doi: 10.1073/pnas.1415311112

Martin, J. H., Knauer, G. A., Karl, D. M., & Broenkow, W. W. (1987). VERTEX: carbon cycling in the northeast Pacific. *Deep Sea Research Part A. Oceanographic Research Papers*, *34*(2), 267–285. doi: 10.1016/0198-0149(87)90086-0

Massom, R. A., & Stammerjohn, S. E. (2010). Antarctic sea ice change and variability – Physical and ecological implications. *Polar Science*, *4*(2), 149–186. doi: 10.1016/j.polar.2010.05.001

McPhee, M., & Morison, J. (2001). Under-ice Boundary Layer. In *Encyclopedia of Ocean Sciences* (pp. 3071–3078). Elsevier. doi: 10.1006/rwos.2001.0146

Moreau, S., Boyd, P. W., & Strutton, P. G. (2020). Remote assessment of the fate of phytoplankton in the Southern Ocean sea-ice zone. *Nature Communications*, *11*(1), 3108. doi: 10.1038/s41467-020-16931-0

Naveira Garabato, A. C., MacGilchrist, G. A., Brown, P. J., Evans, D. G., Meijers, A. J. S., & Zika, J. D. (2017). High-latitude ocean ventilation and its role in Earth's climate transitions. *Philosophical Transactions of the Royal Society A: Mathematical, Physical and Engineering Sciences*, *375*(2102), 20160324. doi: 10.1098/rsta.2016.0324

Nicholson, S.-A., Lévy, M., Jouanno, J., Capet, X., Swart, S., & Monteiro, P. M. S. (2019). Iron Supply Pathways Between the Surface and Subsurface Waters of the Southern Ocean: From Winter Entrainment to Summer Storms. *Geophysical Research Letters*, *46*(24), 14567–14575. doi: 10.1029/2019GL084657

Nicholson, S.-A., Lévy, M., Llort, J., Swart, S., & Monteiro, P. M. S. (2016). Investigation into the impact of storms on sustaining summer primary productivity in the Sub-Antarctic Ocean: Storms Sustain Summer Primary Production. *Geophysical Research Letters*, *43*(17), 9192–9199. doi: 10.1002/2016GL069973

Noh, Y., & Nakada, S. (2010). Estimation of the particle flux from the convective mixed layer by large eddy simulation. *Journal of Geophysical Research*, *115*(C5), C05007. doi: 10.1029/2009JC005669

Palevsky, H. I., & Doney, S. C. (2018). How Choice of Depth Horizon Influences the Estimated Spatial Patterns and Global Magnitude of Ocean Carbon Export Flux. *Geophysical Research Letters*, *45*(9), 4171–4179. doi: 10.1029/2017GL076498

Parkinson, C. L. (2019). A 40-y record reveals gradual Antarctic sea ice increases followed by decreases at rates far exceeding the rates seen in the Arctic. *Proceedings of the National Academy of Sciences*, *116*(29), 14414–14423. doi: 10.1073/pnas.1906556116

Pellichero, V., Sallée, J.-B., Schmidtko, S., Roquet, F., & Charrassin, J.-B. (2017). The ocean mixed layer under Southern Ocean sea-ice: Seasonal cycle and forcing. *Journal of Geophysical Research: Oceans*, *122*(2), 1608–1633. doi: 10.1002/2016JC011970

Sallée, J.-B., Pellichero, V., Akhoudas, C., Pauthenet, E., Vignes, L., Schmidtko, S., ... Kuusela, M. (2021). Summertime increases in upper-ocean stratification and mixed-layer depth. *Nature*, *591*(7851), 592–598. doi: 10.1038/s41586-021-03303-x

Smetacek, V., Klaas, C., Strass, V. H., Assmy, P., Montresor, M., Cisewski, B., ... Wolf-Gladrow, D. (2012). Deep carbon export from a Southern Ocean iron-fertilized diatom bloom. *Nature*, *487*(7407), 313–319. doi: 10.1038/nature11229

Smith, W. O., & Comiso, J. C. (2008). Influence of sea ice on primary production in the Southern Ocean: A satellite perspective. *Journal of Geophysical Research*, *113*(C5), C05S93. doi: 10.1029/2007JC004251

Smith, W. O., & Nelson, D. M. (1985). Phytoplankton Bloom Produced by a Receding Ice Edge in the Ross Sea: Spatial Coherence with the Density Field. *Sci-*

ence, *227*(4683), 163–166. doi: 10.1126/science.227.4683.163

Sverdrup, H. U. (1953). On Conditions for the Vernal Blooming of Phytoplankton. *ICES Journal of Marine Science*, *18*(3), 287–295. doi: 10.1093/icesjms/18.3.287

Tagliabue, A., Sallée, J.-B., Bowie, A. R., Lévy, M., Swart, S., & Boyd, P. W. (2014). Surface-water iron supplies in the Southern Ocean sustained by deep winter mixing. *Nature Geoscience*, *7*(4), 314–320. doi: 10.1038/ngeo2101

Taylor, M. H., Losch, M., & Bracher, A. (2013). On the drivers of phytoplankton blooms in the Antarctic marginal ice zone: A modeling approach: Marginal Ice Zone phytoplankton blooms. *Journal of Geophysical Research: Oceans*, *118*(1), 63–75. doi: 10.1029/2012JC008418

Thomalla, S. J., Fauchereau, N., Swart, S., & Monteiro, P. M. S. (2011). Regional scale characteristics of the seasonal cycle of chlorophyll in the Southern Ocean. *Biogeosciences*, *8*(10), 2849–2866. doi: 10.5194/bg-8-2849-2011

Tréguer, P., Bowler, C., Moriceau, B., Dutkiewicz, S., Gehlen, M., Aumont, O., ... Pondaven, P. (2018). Influence of diatom diversity on the ocean biological carbon pump. *Nature Geoscience*, *11*(1), 27–37. doi: 10.1038/s41561-017-0028-x

Uchida, T., Balwada, D., Abernathey, R., Prend, C. J., Boss, E., & Gille, S. T. (2019). Southern Ocean Phytoplankton Blooms Observed by Biogeochemical Floats. *Journal of Geophysical Research: Oceans*, *124*(11), 7328–7343. doi: 10.1029/2019JC015355

von Berg, L., Prend, C. J., Campbell, E. C., Mazloff, M. R., Talley, L. D., & Gille, S. T. (2020). Weddell Sea Phytoplankton Blooms Modulated by Sea Ice Variability and Polynya Formation. *Geophysical Research Letters*, *47*(11). doi: 10.1029/2020GL087954

Westberry, T., Behrenfeld, M. J., Siegel, D. A., & Boss, E. (2008). Carbon-based primary productivity modeling with vertically resolved photoacclimation:Carbon-based Porduction Model. *Global Biogeochemical Cycles*, *22*(2). doi: 10.1029/2007GB003078

Wilson, E. A., Riser, S. C., Campbell, E. C., & Wong, A. P. S. (2019). Winter Upper-Ocean Stability and Ice–Ocean Feedbacks in the Sea Ice–Covered Southern Ocean. *Journal of Physical Oceanography*, *49*(4), 1099–1117. doi: 10.1175/JPO-D-18-0184.1

Supporting Information for "Sea-ice impacts inter-annual variability in phytoplankton phenology and carbon export in the Weddell Sea"

I.S. Giddy[1,2,3], S-A. Nicholson[3], B. Queste[2], S. Thomalla[1,3], S. Swart[1,2],

[1]Department of Oceanography, University of Cape Town, Rondebosch, South Africa

[2]Department of Marine Sciences, University of Gothenburg, Gothenburg, Sweden

[3]Southern Ocean Carbon-Climate Observatory (SOCCO), CSIR, Cape Town, South Africa

Contents of this file

Introduction In the supplementary text (S1 and S2), the data used for the main analyses and their processing and QC are described. The supplementary figures provide additional information pertaining to choices made in the analysis, intermediate steps in the methodology, as well as figures from which values are referenced to in the main text. The supplementary figures are in the order in which they are referred to in the main manuscript.

Text S1. Glider and float observations

Two Seagliders (SG643 from CalTech and SG640 from the University of Gothenburg), referred to in the text as SG2018 and SG2019 respectively, to differentiate between the

years in which they sampled, were deployed over consecutive austral summers in December 2018 and 2019 at 60^{o}S, 0^{o}E (Figure 1c, d). SG2018 profiled for 102 days (within the demarcated study region), while SG2019 profiled for 119 days with only the last 51 days of sampling being within the demarcated study region and retained for this analysis. The seasonal evolution measured by the gliders are compared directly with one another despite their contrasting sampling scales ($\sim$20 km vs 100 km for SG2018 and SG2019, respectively), as both gliders were able to resolve the phenological features of the bloom due to the mean seasonal modulation being spatially widespread (as evident in Figure 1 c, d).

The gliders sampled temperature, conductivity (salinity), 700 nm optical backscatter, chlorophyll *a* fluorescence, and Photosynthetically Active Radiation (PAR; only SG2018) nominally at 0.2 Hz resulting in a vertical resolution of 0.2–1.5 m in the upper 400 m. Bad salinity and temperature profiles were removed manually before smoothing using a 5-point running mean, and then converted to absolute salinity and conservative temperature using the Gibbs Seawater toolbox (McDougall & Barker, 2011). Fluorescence was converted to chlorophyll *a* (chl *a*) using the provided factory scale constant (0.0121) and then calibrated to co-located in situ CTD bottle samples that were processed on board with acetone extracted fluorometry. To calibrate chl *a* for both glider missions, we used all available bottle samples (December 2018, October 2019 and February 2020 - corresponding to the deployment of SG643, and the deployment and retrieval of SG640). We did not have access to bottle samples at retrieval of SG643 in March 2019 due to ship constraints. The regression resulted in a scale factor of 0.425, $r^2 = 0.78$; which was applied to both SG643 and SG640. Following scaling of fluorescence, the data was quenching-corrected following

Thomalla, Ogunkoya, Vichi, and Swart (2017). Raw optical backscattering was converted to volume scattering at angle (124^o) and wavelength (700 nm) specific to the sensors. The volume-scattering function of seawater was calculated according to Zhang, Hu, and He (2009) and subtracted from the profiles to yield scattering due to particles only. The result was multiplied by 2π and the angle-dependent scale factor, 1.076 for the ECO FLBB optical scattering sensors and, finally added to the backscattering co-efficient of seawater to yield the optical backscattering coefficient bbp_{700}. A deep blank was removed from the backscattering data by subtracting the 5^{th} percentile of optical backscatter between 200 and 400 m.

PAR (μV) was scaled to μEin m^{-2} s^{-1} and corrected for the factory dark count. The top 5 m of PAR measurements were deemed unreliable and removed, following which the profile was algebraically recalculated using an exponential equation from 80 m to the surface to derive surface PAR values. The light attenuation coefficient, k_d, was computed from the vertical PAR profiles. Note that the PAR sensor is scalar allowing for the use of both dive and climb profiles.

To derive daily integrated PAR used in the Primary Production model and for comparison to satellite MODIS PAR (section S2), the following steps were followed:

1. Select only midday (or as near to midday) profiles from the glider observations, based on the midpoint of daylength (the average time between dives was 2.5 $\pm$ 1 hour during the mission, meaning that the glider surfaced at least once or twice during midday hours).

2. PAR with units μEin m^{-2} s^{-1} was then converted to Ein m^{-2} h^{-1} (divide by 1e6 and multiply by 3600s). This value is the glider estimate of amplitude of a daily sinusoidal curve of light.

3. Using sunrise and sunset as 0 and pi, and the daylength as the period of a sinusoidal curve, we extrapolate from the single daily PAR value, and integrate under the curve to derive a daily average PAR (Ein m^{-2} day^{-1}).

Finally, all the data were gridded by profile in the horizontal and binned to 1 m resolution in the vertical. All the glider data were prepared for analysis using GliderTools (Gregor et al., 2019).

Additionally, we used two Biogeochemical-Argo floats that profiled within the study site (Figure 1b) from December 2014 to July 2019 (WMO ID: 5094397) and January 2015 to February 2020 (WMO ID: 5094467), generating 9 years of seasonal cycle data. For all the float variables only data with a quality control flag of 1 or 2 were used (good or probably good).

Text S2. Satellite and Reanalysis Products

Sea-ice concentration products OSI-450 (1997-2015) (OSI-450., 2017) and OSI-430-b (2016-2019) (OSI-430-b, 2019), distributed by EUMETSAT Ocean and Ice Satellite Application Facility (Lavergne et al., 2019), were extracted at daily resolution. Thin sea-ice thickness, distributed by the University of Bremen, was extracted for the available time period (2011-2020). The product is retrieved daily from observations of the L-band microwave sensor SMOS (Soil Moisture and Ocean Salinity) (Huntemann et al., 2014). The maximum and minimum sea-ice extents in 2019 and 2020 are taken from the Sea Ice Index data product, provided by the National Snow and Ice Data Center (Fetterer, 2017). Zonal and Meridional winds as well as longwave, shortwave, sensible, and latent heat fluxes, were retrieved from ERA5 reanalysis at 6-hourly intervals (Hersbach et al., 2018). Chl *a* was extracted at 8-daily resolution from the Ocean Color Climate Change Initiative (OC-CCI)

v5.0 product, distributed by the European Space Agency (Sathyendranath et al., 2019). MODIS Daily Mean PAR was extracted from the 8-daily 4 km resolution product from 2002 to 2020. The daily product was used from 2019 to 2020 and co-located with the glider positions (`https://oceandata.sci.gsfc.nasa.gov/directaccess/MODIS-Aqua/Mapped/Daily/4km/par/`).

Figure S1.

Figure S2.

Figure S3.

Figure S4.

Figure S5.

Figure S6.

Figure S7.

Figure S8.

Figure S9.

References

Behrenfeld, M. J., Boss, E., Siegel, D. A., & Shea, D. M. (2005). Carbon-based ocean productivity and phytoplankton physiology from space: Phytoplankton growth rates and ocean productivity. *Global Biogeochemical Cycles*, *19*(1). doi: 10.1029/2004GB002299

Behrenfeld, M. J., & Falkowski, P. G. (1997). Photosynthetic rates derived from satellite-based chlorophyll concentration. *Limnology and Oceanography*, *42*(1), 1–20. doi: 10.4319/lo.1997.42.1.0001

Fetterer, F. K. K. M. W. S. M. W. A. (2017). *Sea Ice Index, Version 3.* Boulder,

Colorado USA. NSIDC: National Snow and Ice Data Center. (Type: dataset) doi: 10.7265/N5K072F8

Gregor, L., Ryan-Keogh, T. J., Nicholson, S.-A., du Plessis, M., Giddy, I., & Swart, S. (2019). GliderTools: A Python Toolbox for Processing Underwater Glider Data. *Frontiers in Marine Science*, *6*, 738. doi: 10.3389/fmars.2019.00738

Henson, S., Le Moigne, F., & Giering, S. (2019). Drivers of Carbon Export Efficiency in the Global Ocean. *Global Biogeochemical Cycles*, *33*(7), 891–903. doi: 10.1029/2018GB006158

Hersbach, H., Bell, B., Berrisford, P., Biavati, G., Horányi, A., Muñoz Sabater, J., ... Thépaut, J.-N. (2018). *ERA5 hourly data on single levels from 1979 to present.* Copernicus Climate Change Service (C3S) Climate Data Store (CDS). Retrieved 2021-02-15, from 10.24381/cds.adbb2d47

Huntemann, M., Heygster, G., Kaleschke, L., Krumpen, T., Mäkynen, M., & Drusch, M. (2014). Empirical sea ice thickness retrieval during the freeze-up period from SMOS high incident angle observations. *The Cryosphere*, *8*(2), 439–451. doi: 10.5194/tc-8-439-2014

Lavergne, T., Sørensen, A. M., Kern, S., Tonboe, R., Notz, D., Aaboe, S., ... Pedersen, L. T. (2019). Version 2 of the EUMETSAT OSI SAF and ESA CCI sea-ice concentration climate data records. *The Cryosphere*, *13*(1), 49–78. doi: 10.5194/tc-13-49-2019

McDougall, T. J., & Barker, P. M. (2011). *Getting started with TEOS-10 and the Gibbs Seawater (GSW) Oceanographic Toolbox.* Battery Point, Tas.: Trevor J McDougall. (OCLC: 724024071)

OSI-430-b. (2019). *Global sea-ice concentration interim climate data record 2016 onwards*

(v2.0), [Online]. EUMETSAT Ocean and sea-ice Satellite Application Facility. Norwegian and Danish Meteorological Institutes.

OSI-450. (2017). *Global sea-ice concentration climate data record 1979-2015 (v2.0), [Online].* EUMETSAT Ocean and sea-ice Satellite Application Facility. Norwegian and Danish Meteorological Institutes. Retrieved from doi:10.15770/EUM_SAF_OSI_0008

Platt, T., & Sathyendranath, S. (1993). Estimators of primary production for interpretation of remotely sensed data on ocean color. *Journal of Geophysical Research*, *98*(C8), 14561. doi: 10.1029/93JC01001

Sathyendranath, S., Brewin, R., Brockmann, C., Brotas, V., Calton, B., Chuprin, A., ... Platt, T. (2019). An Ocean-Colour Time Series for Use in Climate Studies: The Experience of the Ocean-Colour Climate Change Initiative (OC-CCI). *Sensors*, *19*(19), 4285. doi: 10.3390/s19194285

Thomalla, S. J., Ogunkoya, A. G., Vichi, M., & Swart, S. (2017). Using Optical Sensors on Gliders to Estimate Phytoplankton Carbon Concentrations and Chlorophyll-to-Carbon Ratios in the Southern Ocean. *Frontiers in Marine Science*, *4*, 34. doi: 10.3389/fmars.2017.00034

Westberry, T., Behrenfeld, M. J., Siegel, D. A., & Boss, E. (2008). Carbon-based primary productivity modeling with vertically resolved photoacclimation:Carbon-based Porduction Model. *Global Biogeochemical Cycles*, *22*(2). doi: 10.1029/2007GB003078

Zhang, X., Hu, L., & He, M.-X. (2009, March). Scattering by pure seawater: Effect of salinity. *Optics Express*, *17*(7), 5698. doi: 10.1364/OE.17.005698

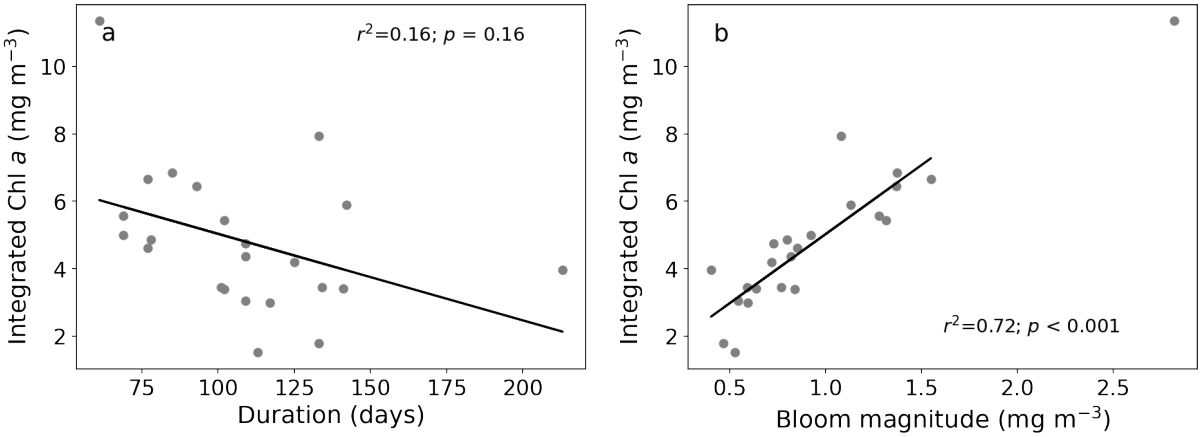

Figure S1. Linear regressions between (a) bloom duration and (b) bloom magnitude and seasonally integrated chl a (between bloom initiation and termination).

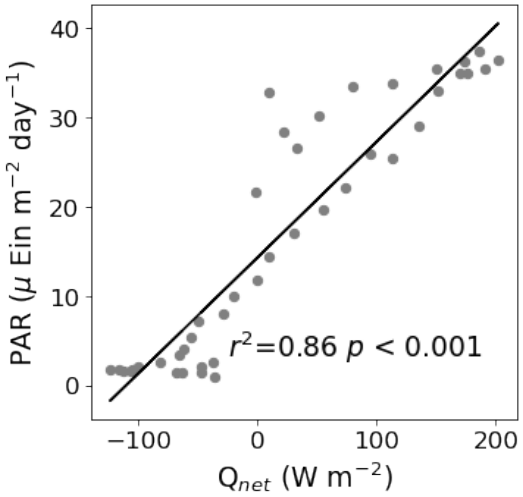

Figure S2. Pearsons' r correlation between Q_{net} and light (Photosyntheically Active Radiation)

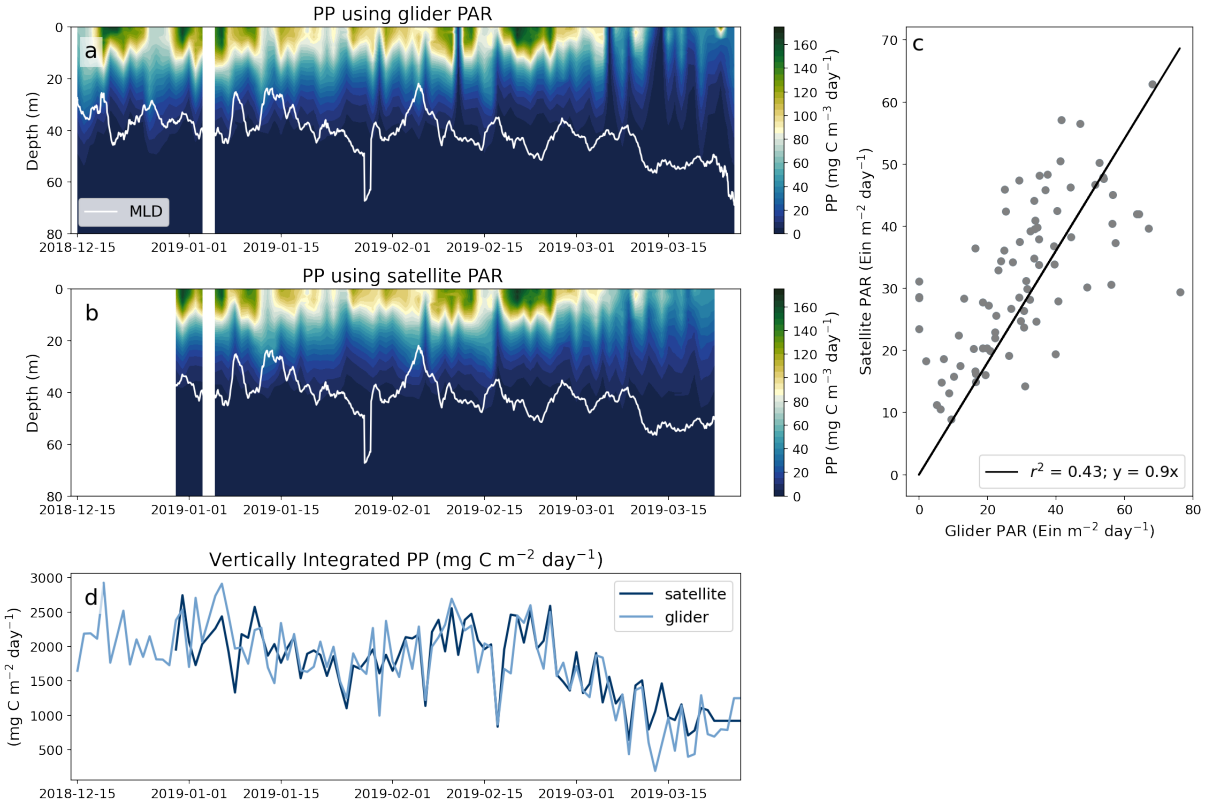

Figure S3. Primary production (PP) computed from the spectrally resolved CbPM a) using Photosynthetically Active Radiation (PAR) from MODIS-Aqua and b) using surface PAR measured by SG2018. c) Regression between glider-measured PAR and MODIS-Aqua PAR. d) Comparison between vertically-integrated primary production estimated using corrected satellite PAR (dark blue) and glider PAR (light blue).

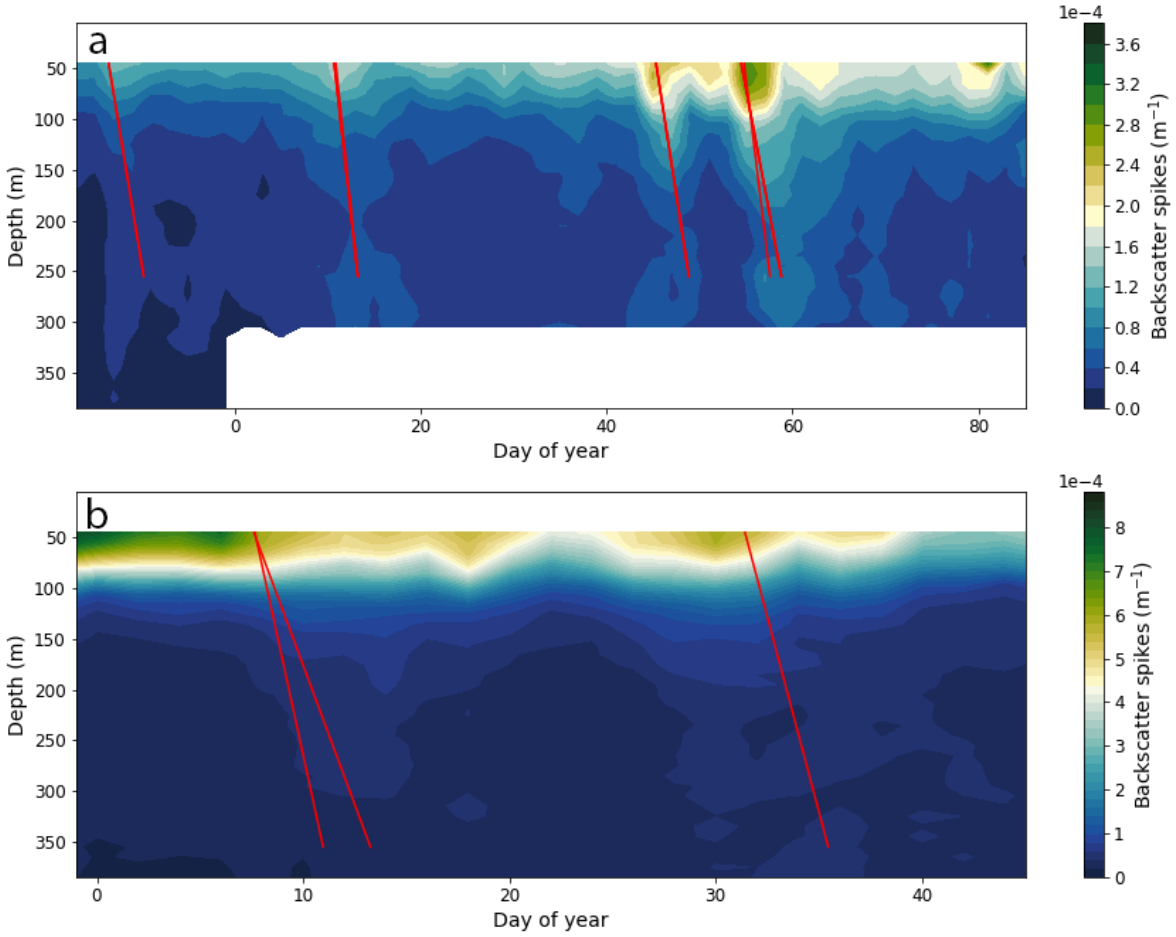

Figure S4. Visual representation of export events identified in the study based on large particle backscatter. (a) SG2018 and (b) SG2019. The upper 40 m is masked as a result of a 50 m rolling mean that was applied to the data. An export event (identified by the red lines) is derived from fitting linear regressions fitted between the depth of each maximum spike and time in 10 day moving windows. Only regressions with $r^2 > 0.4$ were identified as export events.

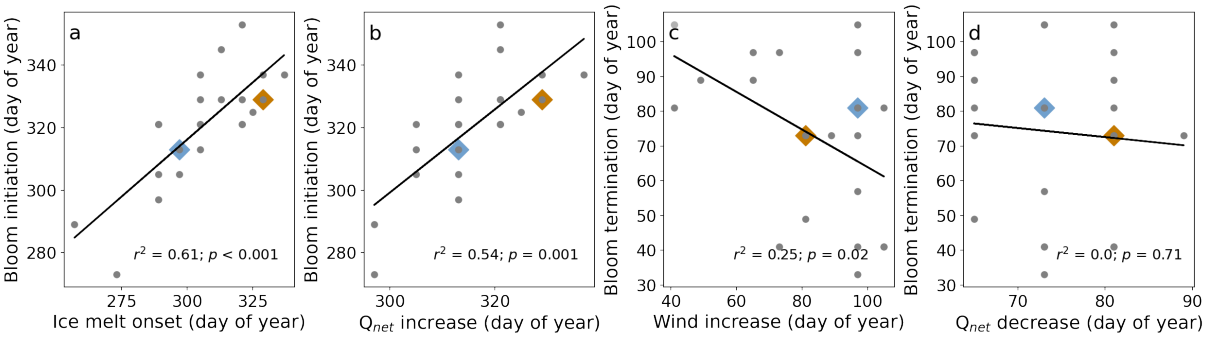

Figure S5. Assessed drivers of bloom initiation and termination. Linear regression between a) ice melt onset and bloom initiation, b) day that Q_{net} switches to positive into the ocean and bloom initiation, c) wind increase threshold and bloom termination and d) day that Q_{net} switches to negative into the ocean and bloom termination. Blue and orange diamonds indicate the years in which SG2018 and SG2019 sampled.

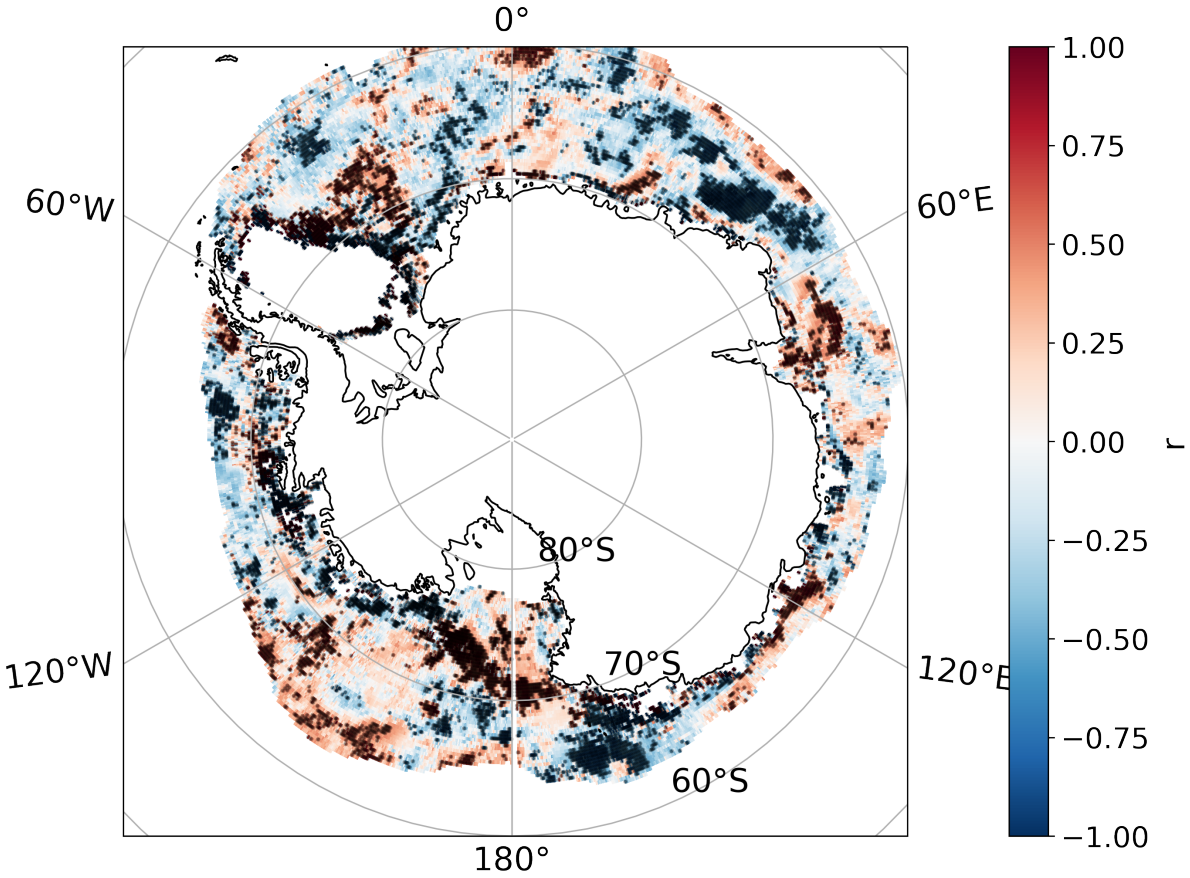

Figure S6. Map of the correlation (r) between mean annual ice volume and the following summer's maximum chl-*a* between 2011 and 2020. Pixels where $r^2 > 0.25$ are marked with a blue x. This equates to ∼30% of the ice-impacted Southern Ocean on average. Note the missing data in the western Weddell Sea due to annual ice cover.

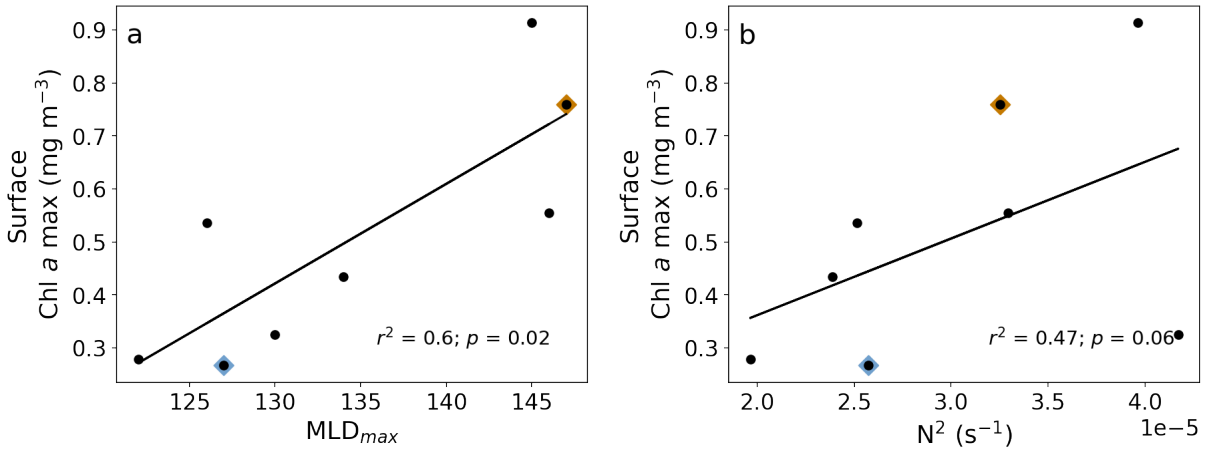

Figure S7. Linear regressions between a) winter MLD$_{max}$ and the maximum summer chl *a* magnitude and b) summer stratification and the maximum summer chl *a* magnitude. Blue and orange diamonds indicate the years in which SG2018 and SG2019 sampled.

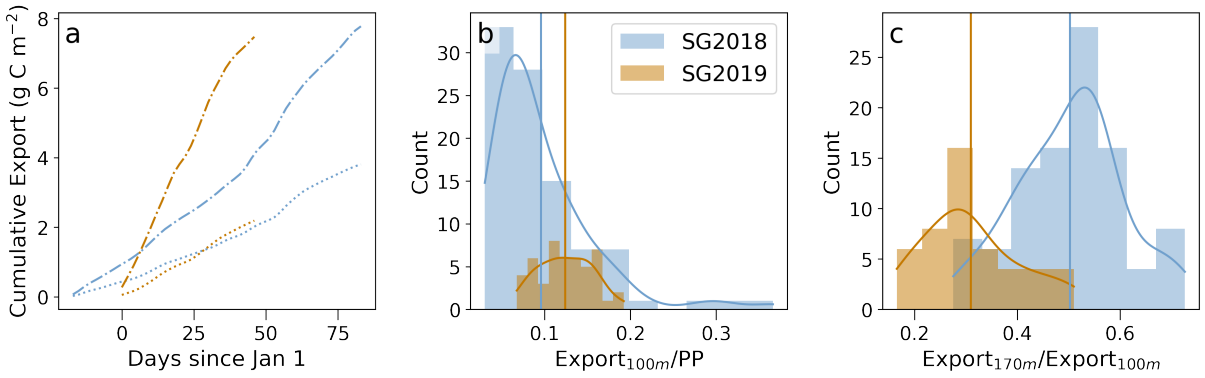

Figure S8. a) Seasonal cumulative export at 100 m (dash-dot lines) and 170 m (dotted lines) for SG2018 (blue) and SG2019 (orange) respectively. b) Histogram of export efficiency at 100 m for the SG2018 (blue) and SG2019 (orange). c) Histogram of transfer efficiency at 170 m for SG2018 (blue) and SG2019 (orange).

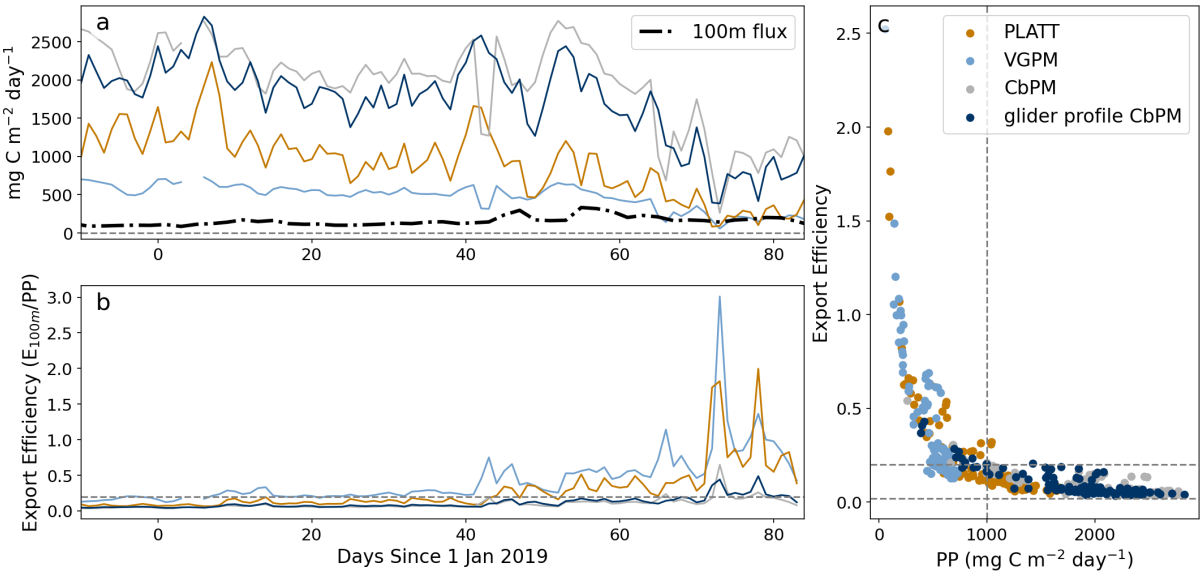

Figure S9. Multi-model analysis of primary production and export efficiency during SG2018. a) Daily rates of primary production based on the standard Vertically Generalized Production Model (VGPM; Behrenfeld & Falkowski, 1997) (light blue), the Platt model (Platt & Sathyendranath, 1993) (gold), the standard CbPM model (Behrenfeld et al., 2005) (grey) and the spectrally-resolved CbPM model (Westberry et al., 2008) (dark blue; selected for use in this study). The dash-dot line shows export to 100 m. b) Export efficiency computed from the different models. c) Export efficiency compared to primary production for the different models. The grey dashed vertical and horizontal lines represent changes in export regimes as defined by Henson et al. (2019), where points with an export efficiency above 0.2 and primary production below 1000 mg C m^{-2} day^{-1} are defined as high-export, low-production regimes at one extreme, and points lying below 0.02 on the y-axis and primary productivity above 1000 mg C m^{-2} d^{-1} are defined as high-production low-export regimes.